

TECHNISCHE UNIVERSITÄT MÜNCHEN

MAX-PLANCK-INSTITUT FÜR PHYSIK
Werner-Heisenberg-Institut

Study of Backgrounds in the CRESST Dark Matter Search

Karoline Julia Schäffner

Vollständiger Abdruck der von der Fakultät für Physik der Technischen Universität München zur Erlangung des akademischen Grades eines

Doktors der Naturwissenschaften (Dr. rer. nat.)

genehmigten Dissertation.

Vorsitzender: Univ. - Prof. Dr. Björn Garbrecht

Prüfer der Dissertation: 1. Hon. - Prof. Allen C. Caldwell, Ph.D.
2. Univ. - Prof. Dr. Stefan Schönert

Die Dissertation wurde am 03.07.2013 bei der Technischen Universität München eingereicht und durch die Fakultät für Physik am 22.07.2013 angenommen.

Abstract

There is strong evidence that dark matter makes up roughly 85% of all the matter in the universe. However, the exact nature of this non-luminous matter remains unknown and its detection poses one of the most exciting challenges in experimental particle and astroparticle physics today. Among the variety of theoretical models proposed for dark matter, Weakly Interacting Massive Particles (WIMPs) are a favored candidate. WIMPs offer the correct relic abundance in the early universe and arise naturally from extensions to the Standard Model of particle physics.

The CRESST experiment aims at direct detection of WIMPs via their elastic scattering off target nuclei in scintillators operated at millikelvin temperatures. When a particle interacts inside these cryogenic detectors it produces both light and phonon signals; by simultaneously measuring the two signal channels the particle can be identified. The amount of produced scintillation light depends on the particle, so knowledge of the light-to-phonon ratio (light yield) for different particles is a powerful tool for background discrimination. In the latest CRESST run an excess of events in the WIMP search region was observed which cannot be explained solely by the known sources of background. WIMPs have been considered as one possible explanation for the excess, but the background levels are too high and the uncertainties in the background model are too large to permit a clear determination.

The major objectives of the work described in this dissertation were to gain a better understanding of the backgrounds in CRESST and to study how to reduce them from their present levels, with the broader aim of clarifying the nature of the observed excess. A major background contribution in the energy region of interest was identified as coming from the metal clamps used to hold the scintillators in place. On the basis of this study, different clamp designs were developed and tested in the CRESST test facility at Gran Sasso with the goal of minimizing clamp-related background in future runs. The results of these studies are presented.

Complementary to reducing backgrounds, a more accurate description of the light-to-phonon ratio for different background sources is essential. It is shown here for the first time that there exists an energy dependence in the light yield for α -particles in the CRESST detectors. This is demonstrated for CaWO_4 and CdWO_4 crystals and the experimental findings are described by a phenomenological model. Results are also presented from the application of a semi-empirical model to describe the light yield distribution of electrons/gammas and α -particles observed in the measurement; the light yield distribution of nuclear recoils is also examined. Applying this model to CRESST would enable a more physically accurate description of the data — a worthwhile gain.

Überblick

Astronomische Beobachtungen deuten darauf hin, dass etwa 85% der im Universum vorhandenen Materie aus einer bisher nicht näher identifizierten Materieform besteht, welche weder der elektromagnetischen noch der starken Wechselwirkung unterliegt. Eine mögliche Erklärung dieser sogenannten Dunklen Materie beruht auf der Annahme schwach wechselwirkender und massiver Teilchen, sogenannter WIMPs (Weakly Interacting Massive Particle), welche in Erweiterungen des Standardmodells der Elementarteilchen vorkommen. Die direkte Beobachtung dieser bisher rein hypothetischen Teilchen stellt eine der drängendsten, aber auch der experimentell anspruchsvollsten Aufgaben der heutigen Teilchen- und Astroteilchenphysik dar.

Das CRESST-Experiment versucht, WIMPs anhand ihrer elastischen Streuung an Kernen szintillierender Kristalle nachzuweisen, welche als Tieftemperaturkalorimeter betrieben werden. In diesen Kalorimetern werden koinzident zwei Signalkanäle ausgelesen: Phononen und Szintillationslicht. Die Messung des Szintillationslichtes erlaubt, die Art des wechselwirkenden Teilchens zu identifizieren und Untergrund effizient zu unterdrücken. In der letzten Messperiode wurden bei CRESST Ereignissen nachgewiesen, welche nicht als bekannte Untergrundereignisse interpretiert werden können. Jedoch ist die Untergrundrate im relevanten Energiebereich noch relativ hoch und die Unsicherheit in der Modellierung des Untergrundes zu groß, um WIMPs als eindeutige Ursache dieser Ereignisse ansehen zu können.

Im Rahmen der vorliegenden Dissertation wurden mögliche Ursachen der vorhandenen Untergrundereignisse untersucht und die metallischen Halteklammern der Kristalle als deren Hauptquelle identifiziert. Neue Konzepte für die Halteklammern wurden entwickelt und in einem eigens dafür im Gran Sasso Untergrundlabor aufgebauten Testkryostaten untersucht.

Neben einer Verringerung des Untergrundes ist die genaue Kenntnis einer eventuellen Energieabhängigkeit der Szintillationsausbeute zur Reduktion systematischer Unsicherheiten von essentieller Bedeutung für die Identifikation etwaiger Untergrundereignisse. Für die bei CRESST verwendeten CaWO_4 - sowie CdWO_4 -Kristalle wurde erstmals eine Energieabhängigkeit der Lichtausbeute von Alphateilchen festgestellt. Die experimentellen Daten wurden anhand eines phänomenologischen Modells beschrieben. Des Weiteren wurde ein semi-empirisches Modell auf die Beschreibung der energieabhängigen Ausbeute des Szintillationssignals von Alphateilchen, Elektronen und Gammastrahlung angewandt. Auch die Lichtausbeute von Kernrückstößen wurde untersucht. Dieses Modell würde eine einfachere und physikalisch motivierte Beschreibung der gewonnenen Daten ermöglichen — ein wertvoller Gewinn.

Contents

1. Dark Matter	1
1.1. Evidence for Dark Matter	1
1.1.1. Galactic and Cluster Scale	1
1.1.2. Cosmic Scale	2
1.2. Dark Matter Candidates	3
1.3. Detection Experiments for WIMPs	5
1.3.1. Accelerator Experiments	5
1.3.2. Indirect Searches	5
1.3.3. Direct Searches	7
1.4. Direct Detection of WIMPs	11
1.4.1. Detection Rate	11
1.4.2. Low Energy	12
1.4.3. Recoil Spectrum	12
2. The CRESST Experiment	17
2.1. Background and Background Reduction	17
2.1.1. Muons	17
2.1.2. Gammas and Electrons	19
2.1.3. Radon	21
2.1.4. Neutrons	21
2.2. Experimental Set-up	22
2.3. Detector Principle	23
2.3.1. Overview	25
2.3.2. Cryogenic Calorimeters	25
2.4. Two-channel Detection	27
2.4.1. Scintillating Absorbers	27
2.4.2. Cryogenic Light Detector	28
2.4.3. Light/Phonon Discrimination	29
2.4.4. Target Nuclei for Dark Matter Search	33
2.5. Scintillating Surrounding	34
2.6. Advantages of CRESST Detectors	38
2.6.1. Remarks on Detector Performance	38
2.6.2. Alternative Scintillating Materials	43
2.7. Summary and Conclusions from Run 32	43

3. Detection Principle	47
3.1. Heat Capacity	47
3.1.1. Dielectrics and Semiconductors	47
3.1.2. Metals	48
3.1.3. Superconducting Metals	48
3.2. Transition Edge Sensor (TES)	49
3.3. Relaxation Processes	50
3.4. Thermal Coupling	51
3.4.1. Kapitza Coupling	51
3.4.2. Electron-phonon Coupling	52
3.4.3. Thermal Coupling to the Heat Bath	54
3.5. Signal Formation Model for Cryogenic Calorimeters	54
4. Detector Operation and Data Analysis	59
4.1. SQUID-based Readout	59
4.2. Data Acquisition	60
4.2.1. Bias Supply Chain	62
4.2.2. Signal Readout Chain	62
4.2.3. Heater Chain	62
4.3. Data Preparation	63
4.3.1. Pulse Parameters	63
4.3.2. Pulse Height Evaluation	65
4.3.3. Energy Calibration	68
4.4. Cuts	72
4.4.1. Stability Cut	72
4.4.2. Peak Position	72
4.4.3. Right-left Baseline	74
4.4.4. Onset-delay in Event	74
4.4.5. Pulse Amplitude	74
4.4.6. RMS of the Template Fit	76
5. Detailed Examination of Background	77
5.1. Motivation	77
5.2. Observations from Run 31	78
5.2.1. Foil Covered Clamps	79
5.2.2. Araldite Covered Clamps	83
5.2.3. Pure Metal Clamps	87
5.2.4. Summary from Run 31 Data	92
5.3. Observations from Run 32	92
5.3.1. Clamp Manufacturing	93
5.3.2. Results	94

5.4.	Origin of the Low Energy Alpha-background	96
5.4.1.	Clamp Bulk Material	97
5.5.	Origin of the Pb-recoil Background in Run 32	100
5.5.1.	Silver Coating of Clamps	100
5.5.2.	Implantation of Daughters of Rn-222	101
5.5.3.	Time Dependence of Pb-recoil Events in Run 32	103
5.6.	Relaxation Events	106
5.7.	Secondary Backgrounds	108
5.7.1.	Sputtering on the Clamps	108
5.7.2.	Sputtering on the Scintillating and Reflective Foil	108
5.7.3.	Conclusion	109
6.	Development of New Clamping Concepts	111
6.1.	Overview	111
6.2.	Bulk Material	112
6.2.1.	Requirements	112
6.2.2.	NOSV Copper	112
6.2.3.	Tin	114
6.2.4.	Production of CuSn6	118
6.3.	Reflective Coverage of Clamps	119
6.3.1.	Etching	120
6.3.2.	Passivating	120
6.3.3.	Sputtering	120
6.4.	Scintillating Coating of Clamps	121
6.4.1.	Motivation	121
6.4.2.	Set-up to Study Scintillation Efficiencies	123
6.4.3.	ZnO Layer	124
6.4.4.	Plastic Scintillator	125
6.4.5.	Summary	126
6.5.	Crystal-clamp Interface	127
6.5.1.	Calcium Tungstate Balls	127
6.5.2.	Calcium Tungstate Half-cylinders	128
6.5.3.	NOSV Half-cylinders	128
6.5.4.	Pure Metal Concept	130
7.	Results for Different Clamp Concepts	133
7.1.	Test-facility at Gran Sasso	133
7.2.	Detector Module	134
7.2.1.	Crystal and Light Detector	134
7.2.2.	Holder Design	135
7.3.	Results of Tested Concepts	135
7.3.1.	Calcium Tungstate Balls	137

7.3.2.	Calcium Tungstate Half-cylinders	141
7.3.3.	NOSV Copper Half-cylinders	148
7.3.4.	Pure Metal Clamps	151
7.4.	Résumé	152
8.	Low Energy Alpha Analysis	155
8.1.	Motivation	155
8.2.	Interaction of Ionizing Particles in Matter	156
8.2.1.	Stopping of Charged Particles	156
8.2.2.	Scintillation Response to Highly Ionizing Particles	158
8.3.	Experimental Arrangement	161
8.3.1.	Detector Module	161
8.3.2.	Degraded Alpha Source	162
8.4.	Data Description Model	164
8.4.1.	Fitting the Electron/Gamma-event Distribution	164
8.4.2.	Fitting the Alpha-particle Distribution	166
8.4.3.	Maximum Likelihood Fit	167
8.5.	Results from Calcium Tungstate	169
8.5.1.	Fitting the Gamma- and Alpha-particle Distribution	169
8.5.2.	Qualitative Agreement of Data and Fit	173
8.5.3.	Comparison to Run 32	173
8.5.4.	Statistical Error of the QF	175
8.6.	Results from Cadmium Tungstate	175
8.6.1.	Fitting the Gamma- and Alpha-particle Distribution	175
8.6.2.	Qualitative Agreement of Data and Fit	177
8.6.3.	Statistical Error of the Fit	179
8.7.	Summary	179
9.	Semi-empirical Description of Quenching Factors	181
9.1.	Semi-empirical Method	182
9.2.	Stopping Powers for Ions in Calcium Tungstate	183
9.3.	Fitting the Data	185
9.3.1.	Mean of the Distribution of Electron/Gamma-events	185
9.3.2.	Mean of the Distribution of Alphas and Nuclear Recoils	185
9.4.	Results for Alpha-particles	186
9.4.1.	Qualitative Agreement of Data and Fit	186
9.4.2.	Discussion and Interpretation	188
9.5.	Results for O-, Ca- and W-recoils	189
9.5.1.	Neutron Source	190
9.5.2.	Discussion on Results	190
9.5.3.	Qualitative Agreement of Data and Fit	194
9.5.4.	Statistical Error of the QF	194

9.6. Summary and Outlook	197
10.Conclusion and Perspective	199
Appendices	203
A. Test Cryostat at Gran Sasso	203
A.1. Underground Site	203
A.2. Dilution Refrigerator	203
A.3. Electronics and DAQ	206
A.4. Performance	206
A.4.1. Conditions for Detector Operation	206
A.4.2. Long Term Stability	207
A.4.3. Gamma-background	207
B. Alternative Scintillators	211
B.1. Cadmium Tungstate	212
B.1.1. Properties	212
B.1.2. Experimental Set-up	214
B.1.3. Light Output at Low Temperatures	214
B.1.4. Event Discrimination	216
B.1.5. Radioactivity in Cadmium Tungstate	217
B.1.6. Neutrino Physics and Perspectives	219
B.2. Cesium Iodide	221
B.2.1. Experimental Set-up	221
B.2.2. Light Output at Low Temperatures	221
B.2.3. Performance of the Phonon Channel	222
C. Sputtering	225
C.1. Energy Spectrum of Sputtered Set of Ions	225
C.2. Energy Spectrum of Sputtered O-, C- and H-Ions	227
C.3. Conclusion and Outlook	227
D. Calculation of Quenched Bands	229
E. Description of the Electron/Gamma-distribution	231
Bibliography	234
Acknowledgments	245

1. Dark Matter

Today, experimental data from studying the universe on both cosmological and galactical scales provides overwhelming evidence that our universe cannot be understood without the participation of non-luminous matter which is not composed of baryons or other known particles, the so-called *dark matter*.

In the field of astrophysics dark matter is necessary for a conclusive understanding of our universe, starting from the formation of structures in the early universe extending to its past and future evolution. For particle physics the nature of dark matter is of central importance to clarify the presence of new physics in form of new particles beyond the standard model. Thus, the nature of the so far still unknown dark matter particle has an important impact on the physics of the smallest and the largest observable length scales.

The fact that the variety of dark matter candidates motivated by cosmology and particle physics is constantly increasing visualizes how little is actually known about their identity. There are numerous experiments following different strategies for detection, among them the CRESST-II (Cryogenic Rare Event Search with Superconducting Thermometers) experiment, aiming for a direct detection of dark matter in form of Weakly Interaction Massive Particles (WIMPs).

In the first part of this chapter, evidences for the existence of dark matter from experimental observations are summarized. In section 1.2 dark matter candidates are introduced, focusing on WIMPs. Section 1.3 gives an overview on the different detection methods for WIMPs and in section 1.4 the implications for the direct detection of WIMPs in CRESST detectors are discussed.

1.1. Evidence for Dark Matter

1.1.1. Galactic and Cluster Scale

In 1933, the first evidence for a non-luminous form of matter in the universe came from F. Zwicky. He determined the velocities of the galaxies in the Coma cluster by Doppler shift measurements of spectral lines. From these velocities he determined the mass of the cluster using the virial theorem and compared it to the mass estimated by the number of stars visible in the cluster. The velocity dispersion found was far too large to arise from the gravity of luminous matter only and thus, F. Zwicky postulated an invisible form of matter to account for the missing mass of the cluster [Zwi33].

Later, in 1970, further evidence also came from V.C. Rubin and W. Ford who measured the *rotation curves* of the galaxies in the cluster M31 [RF70]. Higher resolution

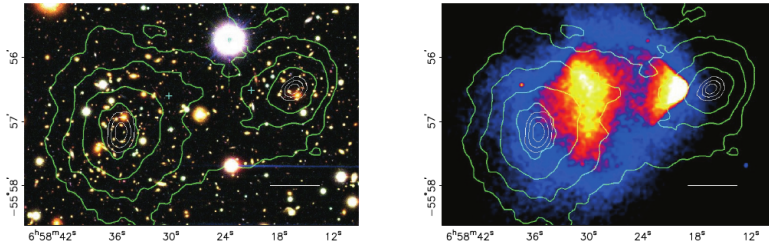


Figure 1.1. – Images of the Bullet cluster taken in the visible range of the spectrum (left) and in the X-ray spectrum (right). The total mass distribution as inferred from an analysis of the gravitational lensing effect is shown in form of green contours in both plots. Pictures taken from [Clo+06].

HI observations (21 cm line of the hyper fine transition of molecular hydrogen) carried out by A. Bosma also revealed that the rotation curves for the majority of the spiral galaxies remain flat beyond the optical disk [Bos81]. These observations provide strong arguments for an additional matter contribution.

In 2006, another strong evidence of dark matter was discovered in the Bullet cluster [Clo+06]. Two galaxy clusters collided leading to a separation of their components, the stars and the gas clouds, because in comparison to stars, gas clouds experience a friction when traversing each other. Figure 1.1 shows a picture of the colliding clusters in the visible and the X-ray spectrum together with the distribution of the total mass according to calculations based on the gravitational lensing effect (green contour lines). In typical galaxy clusters, the center of mass is expected in the position of the hot gas since it contributes the most to its total mass. However, D. Clowe et al. found an offset in the center of mass and the distribution of the hot gas (see figure 1.1). This strongly argues for an additional contribution of matter which is not affected by frictional processes, the dark matter.

1.1.2. Cosmic Scale

Evidence for dark matter on the cosmic scale comes from observations of the Cosmic Microwave Background (CMB). The CMB was emitted about 400,000 years after the Big Bang at the time when the universe became transparent due to the decoupling of the photons from the cosmic plasma.

Today's spectrum of the CMB was very precisely measured by the WMAP (Wilkinson Microwave Anisotropy Probe) collaboration. The temperature variations found are in the order of 10^{-5} . The CMB spectrum is a kind of snapshot of the matter distribution in the early universe at the time of last scattering. Thus, a measurement of these temperature variations as carried out by WMAP allows one to determine values for the different constituents of the universe. Due to a gravitational red-shifting of the photons

the cosmic background radiation is nowadays observable in the microwave band.

The Standard Model of cosmology allows us to theoretically describe the compositions of the universe. The Friedman equation connects the expansion of the universe to its curvature and density in form of matter and dark energy. The total density of the entire universe is given by: $\Omega_{\text{matter}} + \Omega_{\text{curvature}} + \Omega_{\text{dark-energy}} = 1$, whereas the matter contribution is the sum from all present matter species as baryons, neutrinos, non-baryonic matter in form of dark matter and others.

From the last seven-year WMAP data the different contributions to the total energy density of the universe being the non-baryonic dark matter Ω_m , baryonic matter Ω_b and dark energy Ω_Λ are constraint to be [Kom+11]:

- $\Omega_\Lambda = 0.728^{+0.015}_{-0.016}$
- $\Omega_m = 0.277 \pm 0.014$
- $\Omega_b = 0.0456 \pm 0.0016$

Furthermore, the curvature-term is also determined from the WMAP data to $-0.0133 < \Omega_{\text{curvature}} < 0.0084$, meaning that the universe is flat to a good approximation.

To summarize, the major part of the universe is made of dark energy and its nature is completely unknown. The contribution of matter to the total density in the universe is only one fourth and most of it is of non-baryonic form. Thus, the so far unknown dark matter is five times more prevalent than baryonic matter.

1.2. Dark Matter Candidates

Before discussing dark matter candidates it is meaningful to list the requirements on a dark matter particle as obtained from experimental observations:

- it has to be *neutral* as it was not detected via absorption or emission of electromagnetic radiation
- it is expected to have a *mass* since all evidences rely on gravitational interactions
- it has to be *color neutral* since no participation in the strong interaction has been observed
- it has to *only rarely interact with ordinary matter* since it was not yet detected in a direct dark matter search
- it has to be *stable on cosmological time scales* since it was present in the early universe and is still observed today

Further properties of dark matter candidates based on models used to describe our universe should be mentioned:

- its properties have to be consistent with observations and models of the Big Bang nucleosynthesis
- from cosmology the *temperature at the time of the decoupling of matter and radiation* is set as it is important in order to allow for a correct structure formation
- *weak interaction* is possible but not necessary, however, this would be the detection channel for direct dark matter experiments

The lists set requirements and constrains on dark matter candidates, but do not pin down a certain type. In order to look for possible candidates one naturally starts with the known particles from the Standard Model of particle physics (SM). However, most of SM particles are unstable with life times shorter than the age of the universe. The only SM particles that might be considered as a dark matter candidate are *neutrinos*. However, current upper bounds for the mass of the neutrino together with their relic density $\Omega_\nu \simeq m_\nu/47eV \lesssim 0.012$ [Nak10] show that the contributions from the neutrinos are too small. Furthermore, the neutrino is relativistic and therefore, to present knowledge cannot be responsible for the structure formation.

The need for new physics beyond the Standard Model does not only come from the dark matter, but also from unsolved problems in particle physics as the gauge hierarchy problem (GHP), the neutrino mass problem and the strong CP violation problem, all arguing for an extension of the Standard Model of particles.

Today, the favored and most studied dark matter candidate are the *WIMPs* (Weakly Interacting Massive Particles), since this class of hypothetical particles with a mass in the GeV-TeV scale and an interaction via the W and Z gauge bosons shows the correct relic density. This means that the dark matter observed today can be explained by dark matter in form of WIMPs existing as a thermal relic from the early universe. Furthermore WIMPs appear in many particle theories and have an interaction channel for direct detection in physics experiments.

In order to allow for particles as WIMPs, extensions have to be introduced to the Standard Model of particles involving new physics on the weak scale. Alongside many other theories, the theory of supersymmetry (SUSY) is an elegant way, on the one hand, to solve the gauge hierarchy problem and on the other hand to provide several new electrically neutral particles that are good candidates for dark matter. In SUSY every Standard Model particle has a new partner particle of same gauge interactions and same quantum number but a different spin of $1/2$, meaning that the super partners of bosons are fermions and vice versa. The conservation of the quantum number (R-parity) is responsible for the fact that the lightest SUSY particle (LSP) cannot decay into a Standard Model particle thus, providing suitable dark matter candidates.

Two interesting candidates for dark matter exist within the Minimal Supersymmetric Standard Model (MSSM): the *gravitino* and the lightest candidate of the so-called *neutralinos* [BG06]. The gravitino is the super partner of the graviton and not a WIMP.

The lightest neutralino can be realized by a superposition of the super partners of W, Z, photon and Higgs boson, and is a prototypical WIMP dark matter candidate.

It deserves a mention that there are many further interesting theories and dark matter candidates, which, however are beyond the scope of this short introduction. The interested reader is recommended to have a look at [Ber+10b], [Fen10], [BG06] and references for a more profound picture on the wide topic of dark matter candidates.

Since CRESST-II aims for a direct detection of dark matter in form of WIMPs, the following sections exclusively are based on WIMP dark matter.

1.3. Detection Experiments for WIMPs

If dark matter consists of WIMPs, there are three main fields existing on how WIMPs can be found and studied: the search for new particles at colliders, the search for annihilation products, referred to as indirect detection, and the search for direct interactions of WIMPs in earth bound experiments.

This section gives a short overview on the aforementioned detection methods and on the status of main experiments working in the respective area.

1.3.1. Accelerator Experiments

Accelerator experiments as the Large Hadron Collider (LHC) at CERN (Conseil Européen pour la Recherche Nucléaire) have some chance to probe the existence of dark matter particles in form of WIMPs since the mass of WIMPs is expected to be in the region of $M_{weak} \sim 100$ GeV, the scale to be probed at LHC.

However, the direct production of WIMPs is not visible at colliders as LHC or Tevatron. Also mono-jet or mono-photon signals from XXj and $XX\gamma$ at LHC are indistinguishable from background such as Zj and $Z\gamma$ [FST06], [Fen10]. Thus, the detection channel at LHC relies on an indirect production. This means, in the framework of SUSY and if R-parity is conserved, in high energy collisions pairs of squarks and gluinos can be produced which finally decay to the color-neutral LSP, the neutralino WIMP. These LSPs are observable in form of missing mass and momentum [Ber+10b].

Nonetheless, the observation of missing mass would only mean that the particle is stable enough to exit the detector and of course, does not imply that such new particles have to be necessarily dark matter. Thus, collider observations can only be a complementary way to study the nature of WIMP dark matter.

1.3.2. Indirect Searches

Another way to detect WIMPs are indirect searches which rely on the pair annihilation or decays of the dark matter particles. There are various secondary particles from annihilation processes possible: photons from the meV to the TeV-scale, antiparticles, and neutrinos. Since the expected energies of the annihilation products are about a tenth of

the WIMP mass, it is a challenging task to observe these products in form of photons, antimatter and neutrinos in astrophysical experiments.

Photons In order to detect photons produced by WIMP pair annihilation, ground-based atmospheric Čerenkov telescopes as well as space-based experiments such as FERMI are existing. Since WIMPs are not charged, mono-energetic photons $XX \rightarrow \gamma\gamma$ can only be produced via a loop-induced process and are highly suppressed. In the dominant processes the WIMP annihilates or decays into secondary particles which finally emit photons. Thus, the observable photon signals are expected to follow a continuous distribution over a wide energy range. So far no definite signals were detected by such experiments and only upper limits on dark matter annihilation cross section could be set [Cir12].

Antimatter Promising and interesting particles that can also be signals from WIMP annihilation are positrons [JKG96]. Different experiments, among them the Payload for Antimatter/Matter Exploration and Light-nuclei Astrophysics (PAMELA [Adr+09]), the Fermi Large Area Telescope (Fermi-LAT [Ack+12]) and most recently the Alpha Magnetic Spectrometer (AMS-02 [Agu+13]) observe an excess in the cosmic positron fraction which cannot originate only from interactions between the cosmic-ray nuclei and atoms in the interstellar medium. As confirmed recently by AMS-02, these observations can only be explained by new physical phenomena as an astrophysical object but also by particle physics in form of a dark matter annihilation process [Agu+13].

It remains to be seen if the astrophysical background of these experiments is understood sufficiently well in order to give a definite and conclusive answer on the role of dark matter in the near future.

Neutrinos As also shown in the following section, WIMPs may also be detected by scattering off a nucleus. Thus, after scattering and if their final velocity is less than the escape velocity, they can be trapped gravitationally in the center of a gravitational potential as for example the sun (via spin-dependent interaction) or the earth (via spin-independent interaction). Given the situation that the capture and annihilation of WIMPs is in equilibrium, there might be an increased flux of neutrinos from the center of the sun or the earth from WIMP annihilation processes. Huge earth-bound experiments as the Super-Kamioka Nucleon Decay Experiments (Super-Kamiokande, [Tan+11]), the IceCube Neutrino Observatory, and the Antarctic Muon and Neutrino Detector Array (AMANDA) [Abb+12] look for an excess of neutrinos from the sun and set nowadays the most stringent bounds on the spin-dependent cross section for WIMPs with masses above $200 \text{ GeV}/c^2$. Furthermore, these experiments are competitive to direct searches in the WIMP mass range from $50 \text{ GeV}/c^2$ to $5 \text{ TeV}/c^2$ [Abb+12]. So far no significant excess over the expected atmospheric neutrino background has been observed.

For the spin-independent interaction cross section the situation is somewhat different as direct searches obtain higher sensitivities, in particular for low mass WIMPs. Thus, there is a gainful complementarity between indirect and direct searches.

1.3.3. Direct Searches

WIMPs have a small but finite probability of elastic scattering with a nucleus through the process $X SM \rightarrow X SM$ [Ber+10b]. The challenges of such experiments comprise highly sensitive detectors in order to measure the expected small recoil energies combined with an ultra-low background. A detailed discussion on the requirements for a direct detection of WIMPs, as aimed in CRESST, is given in section 1.4. In this section only a short overview of existing direct dark matter searches and their status is given.

The field of direct WIMP searches is very active and numerous experiments are existing all over the world with the prospect of, due to an enormous technological progress, increasing in size and sensitivity within the next decade. Direct searches are based on a single- or on a two-channel readout choosing from the detection of light-, charge- or phonon-signals created by the scattering event, depending on the actual target material. One channel sets the actual energy of the recoiling nucleus and in the case a second channel is used, it gives the possibility of identifying the nature of the interacting particle, a powerful tool in order to discriminate signal events from common background.

Direct searches can be subdivided into two main classes: direct dark matter experiments using liquid noble gases and experiments using solid cryogenic detectors.

Liquid Noble Gas Detectors

Liquid noble gases as xenon (Xe), argon (Ar) and neon (Ne) are considered as target materials and two different concepts are followed in order to operate such detectors. Single phase detectors only measure the light produced in the liquid gas by the scattering events while using PMTs, whereas in the double phase detectors so-called time projection chambers (TPCs) are used. In such TPCs the scintillation light signal and the ionization charge signal are measured simultaneously allowing for a background identification via light/charge discrimination, a background rejection via fiducialization and a multi-scatter identification. Furthermore, the design of such detectors easily allows to realize experiments on the ton-scale. A large target mass is of advantage in the scope of searching for very rare scattering events.

At present, the most stringent limit on WIMP dark matter comes from XENON100 collaboration, excluding spin-independent WIMP-nucleon cross sections for WIMP masses above $8 \text{ GeV}/c^2$ with a minimum of $2.0 \cdot 10^{-45} \text{ cm}^2$ at $m_\chi = 55 \text{ GeV}/c^2$ [Apr+12]. Recently, the XENON collaboration is working on setting up XENON1T, which will use 1 ton of LXe as fiducial mass and is aiming to study interaction cross section down to $2.0 \cdot 10^{-47} \text{ cm}^2$. Besides XENON, two additional experiments working with LXe detectors should be mentioned.

The LUX collaboration is using a LXe TPC with 100 kg fiducial mass which, after commissioning is ready to be moved in the underground at the Sanford Underground Research Facility (SURF) [Ake+13]. In Japan, another single phase LXe detector from the XMASS collaboration is in operation. Results from XMASS are expected only after reducing the present background level [Sek+10].

There are two experiments to be mentioned using LAr as target for WIMP scattering: DarkSide and ArDM. The DarkSide experiment is currently under construction and aims in its first phase (DarkSide-50) to operate about 50 kg of target mass [Aki+12]. A sensitivity of $2.0 \cdot 10^{-45} \text{ cm}^2$ for a WIMP mass of $100 \text{ GeV}/c^2$ is expected in three years of data taking. As DarkSide, also the ArDM utilizes a double-phase LAr detector with 850 kg of target mass [Mar+11]. The detector was first commissioned at CERN and in 2012 moved to Canfranc underground laboratory in Spain. Currently the detector is under installation.

For liquid noble gases the most interesting time is yet to come. So far no hint for dark matter was found in noble gas detectors. In the next years many experiments with target masses close to the ton-scale will start operation with the goal to reach even higher sensitivities and the hope to finally detect the dark matter particle.

Cryogenic Detectors

In this work the class *cryogenic detectors* is used in order to describe solid state detectors for dark matter search operated at low temperatures. As in the case of the liquid noble gas detectors they can be subdivided into single- and two-channel detection experiments. There is a wide choice of target materials available, ranging from semiconductors as silicon (Si) and germanium (Ge) via various intrinsic and extrinsic inorganic scintillators as sodium iodide (NaI), cesium iodide (CsI), calcium tungstate (CaWO_4), zinc tungstate (ZnWO_4) and cadmium tungstate (CdWO_4) as well as pure sapphire crystals.

Cryogenic detectors are very sensitive devices providing a low energy threshold and an excellent energy resolution and thus, are very suitable for the direct detection of WIMPs, in particular in the low-mass region.

Two-channel Detection The CRESST-II experiment rejects common background events from signal events via light/phonon discrimination, whereas the Cryogenic Dark Matter Search (CDMS II) and the Edelweiss collaboration (Expérience pour Détecter Les Wimps En Site Souterrain) simultaneously detect phonon and ionization signals in order to distinguish nuclear recoil events, as also expected from WIMPs, from the common e/γ -background.

The CDMS collaboration uses silicon and germanium as target material and recently published data [Ang+13] from a total raw exposure of 140.2 kg-days from eight Si detectors. In the data they find three possible WIMP-candidate events which cannot be explained by known background. From a likelihood analysis a WIMP mass of $8.6 \text{ GeV}/c^2$

and a WIMP nucleon interaction cross section of $1.9 \cdot 10^{-41} \text{ cm}^2$ is preferred. Former limits of CDMS II for Ge detectors from standard and low-threshold analyses are statistically compatible with the latest result [Ang+13].

In 2012, the Edelweiss collaboration published results from four germanium detectors and an exposure of 113 kg-days collected in 2009-2010. They do not find any evidence for a nuclear-recoil signal which could be attributed to a WIMP interaction. Their limit for a $10 \text{ GeV}/c^2$ WIMP is $1.0 \cdot 10^{-41} \text{ cm}^2$ on a spin-independent WIMP nucleon cross section [Arm+12]. With new generation detectors the Edelweiss collaboration aims to lower the energy threshold as well as to increase in target mass. This will allow them to probe lower regions in the cross section versus mass parameter space, in particular in the region of interest for low-mass WIMPs [Arm+12].

The CRESST-II experiment, which will be explained in more detail in chapter 2 and chapter 3, uses mainly scintillating CaWO_4 crystals as target.¹ Latest results from a total net exposure of about 730 kg-days collected by eight detectors have been published in 2012 [Ang+12]. We find an excess of events, at a statistical significance of more than 4σ , which cannot be explained by known background. One possible origin of these events are WIMPs. For the two likelihood maxima WIMP masses of $25.3 \text{ GeV}/c^2$ and $11.6 \text{ GeV}/c^2$ as well as corresponding nucleon interaction cross sections of $1.6 \cdot 10^{-42} \text{ cm}^2$ and $3.7 \cdot 10^{-41} \text{ cm}^2$ are found. An elaborated overview on CRESST results and conclusions is presented in section 2.7. In figure 2.19 the CRESST results are shown in the WIMP parameter space, together with the results from other direct searches as discussed in this paragraph.

Single-channel Detection In the context of direct searches also two experiments should be mentioned which instead use a single-channel approach in order to detect WIMP scattering events.

Since more than a decade, the former DAMA/NaI and the present DAMA/LIBRA collaboration located at the Gran Sasso National Laboratory in Italy is observing an annual modulation signal of single hit-events in their detector which can be interpreted as a dark matter modulation signal. DAMA/LIBRA is using the scintillator Na(Tl) as target material and low-background PMTs detect the light produced by particle interactions in these crystals. Since always two tubes are connected to each of the crystals (9.7 kg) which are operated in coincidence, they arrive at the sensitivity of single-photoelectron detection. If considering the data taken before the upgrade (DAMA/NaI) and taken afterwards (DAMA/LIBRA), the cumulative exposure is 1.17 ton-years, corresponding to 13 annual cycles [Ber+10a]. The collaboration confirms, with a statistical significance of 8.9σ , the observation of an annual modulation (phase of 147 ± 7 days which is consistent with the annual modulation dark matter signature, expected to be about 153 days) [Ber+10a].

¹CRESST-II is the upgrade phase of CRESST-I. For simplicity, the term CRESST will be used instead of CRESST-II throughout this work.

Another experiment in the field is CoGeNT (Coherent Germanium Neutrino Technology). The CoGeNT detector, consisting of an ultralow-noise germanium detector (440 g) with the ability to reject surface backgrounds, is operated in the Soudan Underground Laboratory (SUL). The low energy threshold (about 0.5 keV) of this detector makes it a suitable tool for the study of, in particular, low-mass WIMPs. In 2011, the CoGeNT collaboration published results from the first 56-days of data taking where they find an excess of events above the anticipated background below 2 keV in ionization energy [Aal+11a]. The cumulative exposure, taken in 442 live days, showed a modulation with a significance of about 2.8σ in the low-energy region and satisfies the needs of a dark matter annual modulation signal. After an interruption due to a fire in the experimental hall at SUL in 2011, CoGeNT is now again taking data. Next generation CoGeNT detectors aim for a higher target mass, lower background and lower threshold and fulfill the requirements in order to search for annual modulation in the region of WIMP mass and nucleon cross section favored by DAMA/LIBRA [Aal+13].

Summary and Prospects

Dark matter searches are facing very exciting and interesting years. The picture, in particular comparing results from liquid noble gas detectors and cryogenic detectors is controversial.

On the one hand side there are indications for WIMP scattering events present in DAMA/LIBRA, CoGeNT, CRESST-II and CDMS II in the region of low WIMP masses ($\mathcal{O}(10 \text{ GeV}/c^2)$) and on couplings in the range of 10^{-41} cm^2 to 10^{-42} cm^2 . On the other hand side the XENON100 collaboration set the most stringent limits in the last years, in particular at higher WIMP masses.² Similar results are expected from LUX.

Commonly, the status of various dark matter experiments is shown on a plot of the WIMP nucleon cross section versus WIMP mass. Examining such a plot, the signal regions from afore mentioned experiments which see scattering events that may be interpreted as WIMP signals appear all in the same region, both in WIMP masses and couplings. Moreover, the exclusion limits of experiments that so far did not see any evidence as for example XENON100 and Edelweiss are not very stringent in this low-mass region. When going to smaller WIMP masses of only few $\mathcal{O}(10 \text{ GeV}/c^2)$ the WIMP nucleon cross section for these experiments rises rapidly, being equivalent to a decrease in their experimental sensitivity (see figure 2.19).

Taking into account the theoretical uncertainties on parameters such as for example the velocity distribution of the WIMPs or their assumed density, their is at present no unsolvable contradiction between the null results from XENON10 and XENON100 and the possibly positive results from aforementioned experiments.

For the future it is most important that dark matter searches are carried out with reasonable care. Experiments have to reduce their present background, gain an even more

²The best XENON limit for WIMP masses below $10 \text{ GeV}/c^2$ was set by XENON10 excluding cross sections above $7.0 \cdot 10^{-42} \text{ cm}^2$ for a WIMP mass of $7 \text{ GeV}/c^2$ [Ang+11].

profound understanding of their detectors, increase in sensitivity and, where appropriate, also in target mass. Without any doubt, the discovery of WIMPs would start a new era of physics and thus, this path has to be trod carefully.

1.4. Direct Detection of WIMPs

In the case that the dark matter observed in the universe is made out of WIMPs, they are expected to be bound gravitationally in galaxies and galaxy clusters in the form of for example a spherical isothermal halo. In order to be able to detect WIMPs, their density in the galactic halo has to be sufficiently high. In an earth bound detector WIMPs will very rarely scatter *elastically off nuclei*. For WIMP velocities smaller than the galactic escape velocity, interactions with the nucleus will happen coherently. The energy transferred to the particular recoiling nucleus from a WIMP scattering can be measured. This is the detection channel for all direct dark matter experiments, as previously mentioned.

As shown in the next two sections, only very low events rates as well as small recoil energies are expected from WIMP-nucleon scattering. In section 1.4.3 the recoil energy spectrum for WIMP interactions in CaWO_4 , the CRESST target material, is calculated.

1.4.1. Detection Rate

A first rough estimation of the total event rate R for a detector with a number of target nuclei $n_{\text{target}} = M_{\text{target}}/m_N$ (m_N is the mass of the nucleus and M_{target} is the mass of the target), a given WIMP flux of ϕ_χ and an elastic scattering cross section σ is

$$R = n_{\text{target}} \phi_\chi \sigma. \quad (1.1)$$

With the flux of WIMPs penetrating the target defined as

$$\phi_\chi = \frac{\rho_\chi}{m_\chi} v \quad (1.2)$$

where m_χ is the WIMP mass, ρ_χ the WIMP density and v their velocity, the total interaction rate R can be calculated as

$$R = \frac{M_{\text{target}}}{m_N} \frac{\rho_\chi}{m_\chi} v \sigma. \quad (1.3)$$

Inserting typical values in equation (1.3) [Huf10], the expected total rate per kilogram detector target and per year in a CRESST detector is $\mathcal{O}(10 \text{ kg}^{-1} \text{ year}^{-1})$.

This is a very low rate and sets a challenge for direct dark matter experiments. The common background has to be reduced as far as possible (underground laboratory, shieldings, radiopure materials) and an active background discrimination might be used in order to distinguish signal events from common background. The active background suppression used in CRESST is explained in chapter 2.

1.4.2. Low Energy

The energy transferred to the recoiling target nucleus in a WIMP scattering event mainly depends on the masses of the WIMP and the target nuclei involved as well as on their velocities.

WIMP masses are expected to be $\mathcal{O}(10 \text{ GeV}/c^2)$ [Ber+10b]. The velocity of the WIMPs has to be smaller than the escape velocity, otherwise they could not be bound to our Milky Way. In the simplest model, the velocity of WIMPs in the galactic rest frame can be approximated to be in the order of the velocity of the sun $v_{\odot}=220 \text{ km/s}$ and the process of WIMP-nucleon scattering can be described in the non-relativistic limit. The recoil energy E_r transferred in the scattering process can be calculated as

$$E_r = \frac{\mu_N^2 v^2 (1 - \cos\Theta)}{m_N} \quad (1.4)$$

where v is the relative speed, Θ is the scattering angle in the center of mass frame and μ is the reduced mass of the WIMP-nucleus system given by

$$\mu = \frac{m_{\chi} m_N}{m_{\chi} + m_N}. \quad (1.5)$$

The transferred energy is maximal, in the case that the mass of the WIMP and the mass of the target nucleus are identical. Assuming $m_{\chi} = m_N$, an angle $\Theta = \pi$ and a velocity of $v \approx 10^{-3}c$ the maximal energy $E_{r,max}$ can be expressed as

$$E_r = \frac{1}{2} m_{\chi} v^2 \approx \frac{1}{2} m_{\chi} c^2 10^{-6} = \frac{1}{2} \left(\frac{m_{\chi}}{\text{GeV}/c^2} \right) \text{keV}. \quad (1.6)$$

The maximal energy transfers expected from WIMP-nucleon scattering are in the order of a few 10 keV. This means direct detection experiments have to provide a very low energy threshold in order to detect such low recoil energies.

1.4.3. Recoil Spectrum

For dark matter experiments, apart from the total event rate, the spectral shape of the expected event distribution is of central importance. The differential recoil energy spectrum can be calculated by differentiating equation (1.3) with respect to the recoil energy E_r while also taking into account that the WIMPs do not all have the same velocity and are rather described by a velocity distribution $f(v)$. Thus, the differential rate can be written as the integral

$$\frac{dR}{dE_r} = \frac{\rho_{\chi}}{m_N m_{\chi}} \int_{v_{min}}^{\infty} d^3 v f(\vec{v}) v \frac{d\sigma(\vec{v}, E_r)}{dE_r} \quad (1.7)$$

and v_{min} is the minimal velocity above which a WIMP can transfer the considered energy to a nucleus given by

$$v_{min} = \sqrt{\frac{E_r m_N}{2\mu^2}} \quad (1.8)$$

where μ is the reduced mass of the WIMP-nucleus system as stated in equation (1.5).

Scattering Cross Section

The WIMP-nucleus cross section has two contributions: a spin-independent (SI) and a spin-dependent (SD). The spin-dependent part involves a coupling of WIMPs to the net spin of the particular target nucleus of the detector whereas the spin-independent contribution accounts for the scalar interactions. Since the target nuclei of a CRESST detector have a net spin of zero, the spin-dependent contribution can be neglected. The spin-independent cross section can be formulated as [Ber+10b]

$$\frac{d\sigma_{SI}}{dE_r} = \frac{m_N \sigma_0 F^2(E_r)}{2\mu^2 v^2} \quad (1.9)$$

where $F(E_r)$ denotes the nuclear form factor expressed as a function of the recoil energy E_r and σ_0 is the point-like total scattering cross section of the nucleus. The form factor will be explained in more detail in a subsequent paragraph. Since the cross section σ_0 depends on the given target nuclei, it is common to use a normalized cross section $\sigma_{\chi N}$ for a comparison between the different direct dark matter searches. Following [DFS98], the WIMP-nucleon scalar cross section is defined as

$$\sigma_{\chi N} = \left(\frac{1 + m_\chi/m_N}{1 + m_\chi/m_P} \right)^2 \frac{\sigma_0}{A^2} \quad (1.10)$$

with the proton mass m_P and the atomic mass number of the target A .

By means of the previous definitions, equation (1.7) can be rewritten as

$$\frac{dR}{dE_r} = \frac{\rho_\chi}{2m_\chi \mu_N^2} \sigma_0 F^2(E_r) \int_{v_{min}}^{\infty} d^3v \frac{f(\vec{v})}{v}. \quad (1.11)$$

Velocity Distribution

So far, the integral over the velocity distribution in equation (1.7) was not commented. Assuming an isothermal halo model, the velocity distribution for the WIMPs in the galactic rest frame can be described by a Maxwell-Boltzmann distribution

$$f(\vec{v}) = N \left(\frac{3}{2\pi w^2} \right)^{\frac{3}{2}} \exp\left(-\frac{3v^2}{2w^2}\right) \quad (1.12)$$

with the normalization factor N given by [LS96]

$$N = \left(\operatorname{erf}(z) - \frac{2}{\sqrt{\pi}} z \exp(-z^2) \right)^{-1} \quad (1.13)$$

with

$$z^2 = \frac{3v_{esc}^2}{2w^2}. \quad (1.14)$$

In the isothermal sphere model w is the root mean square velocity of the WIMPs given by the simple relation $w = \sqrt{\frac{3}{2}}v_\infty$ where v_∞ is the asymptotic value for the rotational velocities [DFS98]. The measured rotational velocity of our solar system is $v_\odot = 220 \pm 20 \text{ km sec}^{-1}$. Thus, w yields a value of $270 \pm 25 \text{ km sec}^{-1}$. The escape velocity v_{esc} of the Milky Way has a value of 554 km sec^{-1} [Smi+07].

Form Factor

Before the differential event rate can be calculated, the last remaining term in equation (1.7), the *form factor*, has to be discussed. The form factor describes the effect of the finite size of the nucleus. At low enough energies the nucleus can, to a good approximation, be described as a point-like object. At higher momentum transfers, however, the substructures of the nucleus play a role and have to be accounted for. Formally, the form factor is given as a Fourier transform of the matter density of the nucleus.

In dark matter searches a simple model for the form factor initially developed by R. Helm [Hel56] and later worked out by [Eng91] is used. In this model the nucleus is described by the convolution of two density functions ρ_0 and ρ_1

$$\rho(\vec{r}) = \int \rho_0(\vec{r}') \rho_1(\vec{r} - \vec{r}') d^3 r' \quad (1.15)$$

where ρ_0 describes the constant density of a sphere with radius r and ρ_1 accounts for the decrease of the density towards the edges of this sphere, known as the skin-effect.

The Fourier transformation of the density ρ can be written as

$$F(\vec{q}) = 3 \frac{j_1(qR_0)}{qR_0} \exp\left(-\frac{1}{2}q^2 s^2\right) \quad (1.16)$$

where q is the momentum transferred in the scattering process given by $q = \sqrt{2m_N E_r}$, $j_1(qR_0)$ is the first spherical Bessel function and s is the thickness parameter for the surface of the nucleus ($s \simeq 1 \text{ fm}$).

This description is a good and simple approximation for the form factor. However, as shown in [Sch10], by using a different evaluation of the nuclear radius as suggested by Lewin and Smith [LS96], an improved description can be achieved. Thus, for the calculation of the differential event rate shown in this work the Helm form factor with

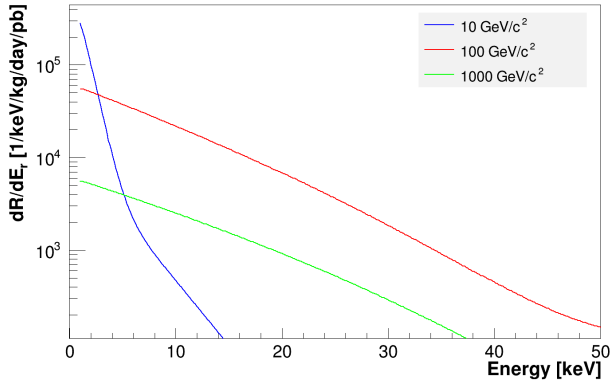


Figure 1.2. – The differential event rate for WIMP masses of $10 \text{ GeV}/c^2$, $100 \text{ GeV}/c^2$ and $1000 \text{ GeV}/c^2$ in CaWO_4 while using a Helm form factor with Lewin/Smith parametrization. The rates are given in units of a WIMP-nucleon cross section of 1 pb .

the parametrization of Lewin/Smith is used. To summarize, the differential event rate shown in figure 1.2 was calculated, as explained before, according to the following assumptions:

- a Maxwell-Boltzmann distribution for the velocity distribution of the WIMPs
- a Helm form factor with Lewin/Smith parametrization
- an energy threshold of the detector of 0 keV
- target material is calcium tungstate (CaWO_4 , sum over individual compounds)
- normalized to an exposure of 1 kg-day

The spectra depicted in figure 1.2 are shown for three different WIMP masses and are given in units of a WIMP-nucleon cross section of 1 pb . The differential event rate shows no prominent features, the rate above energies of 50 keV is not significant and the overall expected event rates are very low. The current interaction cross section $\sigma_{\chi N}$ is expected to be in the order of 10^{-7} pb leading to event rates $R \lesssim 0.1 \text{ kg}^{-1} \text{ day}^{-1}$ [Sch10].

Thus, as mentioned before, the requirements on the direct detection experiments comprise very low background conditions, a method to distinguish background events from signal events, long measuring times as well as large target masses in order to have a realistic chance to detect dark matter particles in form of WIMPs in an earth bound experiment.

2. The CRESST Experiment

The CRESST-II experiment is located in an underground laboratory in central Italy. The experiment is designed to directly detect dark matter in the form of WIMPs using cryogenic calorimeters operated at millikelvin temperatures. As shown in the previous chapter, the main challenges for a direct dark matter search are the anticipated low event rates and the low energy deposits expected for possible dark matter candidates.

In this chapter, the main sources of radioactive background in CRESST (section 2.1) and ways to shield them are discussed. Section 2.2 introduces the experimental set-up and section 2.3 gives a short overview on the detection technology. Section 2.4 points out the advantages of a two-channel detection technique in terms of event discrimination and identification. The importance of a complete scintillating surrounding of the detectors used in CRESST is discussed (section 2.5). The last section, section 2.7, focuses on the latest results of the CRESST experiment.

2.1. Background and Background Reduction

As only about ten WIMP interactions per kilogram of target material and per year are expected in an energy range of a few $\mathcal{O}(10 \text{ keV})$ (see section 1.4), the reduction and suppression of the radioactive background from natural decay chains, man-made radioactivity and cosmic rays is a key requirement.

This section gives an overview of possible background sources and introduces measures that have been taken in CRESST in order to suppress them as far as possible.

2.1.1. Muons

Cosmic radiation arriving at the Earth's atmosphere consists mainly of protons (90%), the remaining part are α -particles, electrons, and a small fraction of lighter elements such as lithium, beryllium, and boron. Due to high energy collisions in the upper layers of the atmosphere, cosmic rays produce a long cascade of lighter particles that decay further to muons, electrons, positrons, and photons. At sea level, muons are the most numerous and penetrating component of the cosmic rays, inducing background events in the detectors through different processes. First, muons can directly deposit energy in the detector when traversing it. They can also produce secondary electrons, gammas and spallation products in surrounding materials that may reach the detector.

For this reasons, it is essential to minimize the muon flux in the vicinity of the detectors by setting up the experiment in a deep underground site. The CRESST experiment

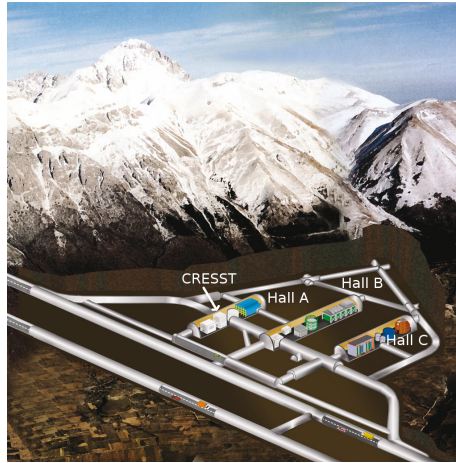


Figure 2.1. – Scheme of the LNGS underground laboratory. The three main experimental halls are hosted next to a 10 km long highway tunnel (Traforo del Gran Sasso) [LNG12].

is located in the Laboratori Nazionali del Gran Sasso (LNGS) in central Italy which is operated by the Istituto Nazionale di Fisica Nucleare. A scheme of the underground laboratory extending over a total area of 18000 m² and subdivided in three main experimental halls (hall A, hall B, and hall C) is shown in figure 2.1. The lab is accessible via a highway tunnel which connects Rome and the Adriatic sea passing the Gran Sasso mountains. At present, LNGS hosts 18 experiments in the field of astroparticle physics and nuclear astrophysics [LNG12]. A minimum rock overburden of 1400 m of dolomite rock (equivalent to about 3150 meter of water) reduces the cosmic muon flux at LNGS by six orders of magnitude to a rate of about $\mathcal{O}(1 \text{ h}^{-1} \text{ m}^{-2})$ [Amb+95].

In order to identify muon background events, the CRESST experiment is equipped with a *muon veto* consisting of 20 plastic scintillator panels each read out by a PMT (see figure 2.2). The panels cover a solid angle of 98.7% around the detectors and whenever a muon is detected coincident events in the detectors are rejected.

By defining a veto time-window around the veto signal, secondary particles with short decay times ($\tau_{1/2} < 1 \text{ s}$) can also be discarded. However, if the decay time of the secondary particles is long ($\tau_{1/2} \gg 1 \text{ s}$), signals associated with their decay cannot be vetoed in this way. Reactions that can produce long lived isotopes are [Arp92]:

- *muon capture*:
a negative muon can be captured by a proton from of a nucleus while leaving the nucleus in an excited state. Its de-excitation may be accompanied by the emission of one or more neutrons, gammas, and betas.

- *nuclear reaction via inelastic, electromagnetic scattering:*
the muon inelastically scatters on a nucleus leaving the nucleus in an excited state. The nucleus de-excites via the emission of gammas and betas.
- *spallation:*
the high energy muon can hit a heavy nucleus and subsequently the nucleus will emit a large number of protons and neutrons

Out of these reactions, spallation neutrons generated by cosmic ray muons interacting in rock, in the shielding of the detectors, or in the detectors themselves are the most dangerous background.

Interacting neutrons deposit their energy via elastically scattering off target nuclei; the same is expected from WIMPs (see section 1.4). Hence, it is necessary for rare event searches to identify the muon induced neutron background in a reliable way. Detailed information on muon induced neutrons in CRESST can be found in [Sch10].

2.1.2. Gammas and Electrons

Another background originates from members of the natural decay chains of ^{238}U and ^{232}Th and from the natural isotope ^{40}K that are present in, for example, the surrounding rock, mainly producing gammas and electrons with energies up to 2.6 MeV. The computed integral gamma flux from all natural chains at LNGS is about $\mathcal{O}(1\text{ s}^{-1}\text{cm}^{-2})$ [Arp92].

In order to reduce this environmental background massive shields made out of materials with a high atomic number and high density are adopted, since such materials have a good stopping power for gamma radiation.

In CRESST, a shield of 20 cm of low background *lead* (24 t of weight) encloses the detectors (see figure 2.2). However, lead is not a very clean material having regard to its intrinsic radioactivity. The radioactive isotope ^{210}Pb from the ^{238}U chain contributes in a significant way to the low energy background. It decays in several steps to ^{206}Pb by emitting α -, β -, and γ -radiation, furthermore producing bremsstrahlung and X-rays. To suppress background induced by ^{210}Pb , a 14 cm thick *copper shield* (10 t of weight) is installed between the lead shield and the detector modules (see figure 2.2). The copper used for this shield is electrolytically refined, such as oxygen free high conductive (OFHC) copper, known for its very low level of intrinsic radioactivity [Heu95]. As copper has a large cross section for neutron capture the exposure to cosmic radiation, during its production and storage, is kept as little as possible. Except for this constraint, copper is a very suitable material to be used, also for manufacturing detector holders or any other structures inside the experimental volume.

Whenever lead cannot be shielded by internal copper layers *Roman lead* can be utilized. This lead comes from old wrecks of Roman ships sunk in the Mediterranean sea or near Britain. The content of ^{210}Pb is five orders of magnitude lower than in common

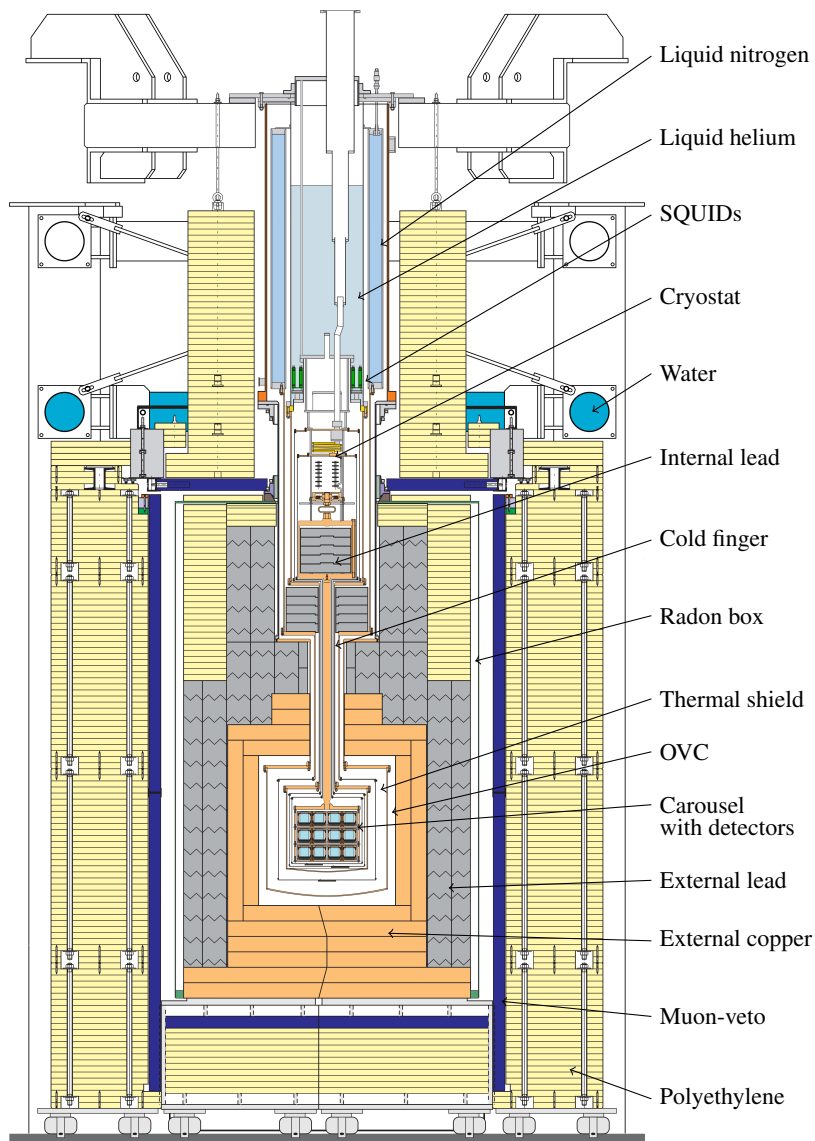


Figure 2.2. – Scheme of the CRESST set-up. See text for discussion.

lead due to the overburden of water which prevented that the lead, as well as its chemical contaminations were activated by cosmic ray neutrons during the last 2000 years [Ale+98]. Furthermore, the amount of naturally abundant radioactive isotopes had time to decay.

2.1.3. Radon

A dangerous background source for all rare event searches is the airborne radioactivity coming from radon. ^{222}Rn is part of the ^{238}U decay chain and decays via α -decay into ^{218}Po with a half-life of 3.825 days [MPG06]. It is present not only in dwellings, but also in underground laboratories as it can be washed or diffused out from surrounding rock. ^{222}Rn and its progenies produce a variety of α - and β -particles that may produce gamma radiation by bremsstrahlung or by nuclear reactions.

The radon activity at LNGS amounts to about 50 Bq per cubic meter of air [Arp92]. This value depends considerably on seasonal variations and of course on the internal ventilation situation of the laboratory. In order to provide a radon free zone in the vicinity of the detectors, the lead and copper shields are surrounded by an air-tight box, the so called *radon box* (figure 2.2). This container is constantly flushed and kept under over pressure with pure nitrogen gas coming from a liquid nitrogen storage dewar.

As discussed in section 2.5, background coming from radon, especially its progeny ^{210}Po , has to be kept at a minimal level. Investigations of the backgrounds present in the latest CRESST run (Run 32) and elaborated in this thesis showed, it is in particular the α -emitter ^{210}Po which introduces a dangerous nuclear-recoil background in the relevant energy range of interest. Hence, all copper pieces used for detector holders and other structures in the vicinity of the detectors are etched in nitric acid to remove surface contaminations and afterwards are stored in flow boxes flushed with clean nitrogen gas to avoid further adsorption of radon gas on the surfaces.

The assembling of the detectors for the upcoming run is carried out in a dedicated flow box system only flushed with radon-cleaned air, kindly provided by the CUORE collaboration. Its measured radon contamination is in the range of mBq/m^3 of air. Also the mounting of the detectors in the cryostat is done while respecting measures of radon prevention. A structure similar to a tent, which also is flushed with deradonized air during the whole mounting process, is build around the copper structure onto which the detectors are mounted.

2.1.4. Neutrons

Energetic neutrons interact in a similar way as WIMPs are supposed to: both scatter off target nuclei elastically. Neutrons, therefore, are considered a very severe background source as they can mimic a dark matter signal.

The neutron background present at Gran Sasso mainly comes from (α , n)-reactions on light elements as well as from fission of ^{238}U in the rock or in the concrete used to

cover the walls of the laboratory. In addition, high energetic neutrons can be induced by muons in the surrounding but the flux expected from this source is very small in comparison. Aglietta et al. found for the Mont Blanc Underground Laboratory (5200 meter of water equivalent), that the neutron flux generated by cosmic-ray muons is roughly three orders of magnitude lower than that induced by natural activity [Agl+89].

The measured neutron flux in hall A at LNGS is about $19.4 \text{ h}^{-1} \text{ m}^{-2}$ for an energy interval of [1-2500] keV and $10.1 \text{ h}^{-1} \text{ m}^{-2}$ for the interval from [2.5-25] MeV [Bel+89]. In order to prevent this background in CRESST, a *neutron shield* is installed outside of the lead and copper shields (see figure 2.2). It consists of a 45 cm thick (10 t in weight) polyethylene (PE) structure and in addition of containers filled with PE granulate or water, at the less accessible positions of the experimental set-up. PE and water work as moderator that slows down neutrons to thermal energies, in the range of some meV. These thermal neutrons can no longer produce a measurable signal in the detector.

However, there are further mechanisms for neutron production that cannot be avoided by the present PE shielding in CRESST. First, muons can produce neutrons in the lead and copper shielding itself and second, contaminations of for example ^{238}U in the lead can also produce neutrons by fission reactions.

To shield against these neutrons, an additional moderator has to be installed within the gamma shielding (Pb- and Cu-shields). For the new run, additional 5 cm of PE are implemented inside the OVC, the outer vacuum chamber (see figure 2.2) of the cryostat. The PE is of high-purity, especially a low content of ^{238}U and ^{232}Th is indispensable to avoid (α , n)-reactions within the PE.

2.2. Experimental Set-up

CRESST detectors are operated around 10 mK. Such low temperatures are provided by a commercial ^3He -/ ^4He -dilution refrigerator (Oxford Instruments). The refrigerator, as well as its storage tanks for liquid nitrogen and liquid helium (upper half in figure 2.2), are made from standard materials that do not fulfill particular requirements in terms of radiopurity. A special design has been chosen to ensure low background by separating most of the components of the cryostat from the experimental volume.

The detectors are mounted onto a copper structure, referred to as *carousel* which is located in a low background *cold box*. A picture of the carousel with detectors mounted is shown in figure 2.3. It has no line of sight to the non-radiopure materials of the cryostat's dilution unit as additional 20 cm of high purity lead (Boliden lead and Plombum lead) are mounted directly below the mixing chamber of the refrigerator. The thermal and mechanical connection between the cryostat and the carousel with the detectors is provided by a 1.5 m long copper rod, the *cold finger*.

The cold box consists of five thermal shields: an outer vacuum chamber (OVC) at ambient temperature, a first thermal shield sunk at the liquid nitrogen dewar of the cryostat, an inner vacuum chamber anchored at liquid helium temperature and two additional ra-



Figure 2.3. – The carousel is made out of NOSV copper and can house up to 33 complete detector modules (equivalent to a target mass of about 10 kg) and consists of 12 towers. The flanges for the different thermal shields are visible in the upper part of the picture.

diation shields at 600 mK and 80 mK. Both the cold finger and the radiation shields are made from radiopure copper, which has been etched and electro-polished to remove any kind of surface contaminations and to reduce the probability of re-contamination.

Low temperature detectors are very sensitive to mechanical vibrations. External vibrations from the laboratory and surrounding are attenuated as the whole cryostat rests on air dampers and has no mechanical connection to the Pb- and Cu-shielding. Mechanical vibrations introduced by the cryostat (boiling of liquids, 1K-pot) are damped by mounting the carousel onto a spring loaded plate which is directly fixed onto the cold finger.

The cryostat is located in a three floor building. To avoid disturbances due to electromagnetic interferences a Faraday cage surrounds the experimental volume (ground floor) as well as the detector electronics for readout and biasing (first floor). On the ground floor, the Faraday cage houses also a class 100 clean room to provide clean conditions for mounting and dismounting detectors in the carousel. Part of the first floor is outside the clean room and allows easy access for servicing the cryostat and maintaining the detector electronics. The second floor includes work space, a flow box system for detector assembling as well as a computing area.

2.3. Detector Principle

In CRESST massive *cryogenic calorimeters* are used as particle detectors. The basic detection process within a calorimeter is the temperature rise caused by a particle interaction in an absorber and its conversion into a measurable electrical signal.

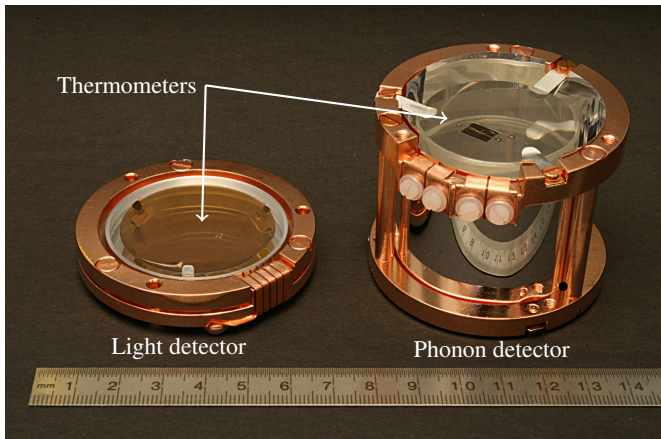


Figure 2.4. – On the left hand side a light detector in its copper holder is shown. A CaWO_4 crystal also mounted in its copper holder and surrounded by a reflective foil is visible on the right hand side. The thermometers (TES) are indicated on the surface of both detectors. The phonon detector together with its light detector forms a so-called detector module.

The first scientist to propose the use of low temperature bolometers for the study of nuclear phenomena was F. E. Simon in 1935 [Sim35]. The research on superconducting bolometers started in 1938 and it was H. D. Andrews who, for the first time detected α -particles from a polonium source in a superconducting bolometer made out of niobium nitride [AFW49]. In the following years, considerable effort was put into the development of these low temperature detectors having a wide range of applications such as infrared astronomy, fast spectroscopy, material analysis, and plasma diagnostics.

The use of large cryogenic detectors for the search of rare events such as neutrinoless double-beta decay and electron decay was proposed by E. Fiorini and T. O. Niinikoski only in 1983 [FN84]. Nowadays, cryogenic calorimeters and bolometers are widespread in the field of rare event searches.

Cryogenic calorimeters are very suited for dark matter searches as they combine an excellent energy resolution with a low energy threshold. The absorbers can be chosen from a wide range of materials. This allows a study of WIMP interactions in different target materials, which is an advantage in particular in the case of a positive WIMP-signal (see appendix B).

2.3.1. Overview

In this section, only a short overview on the type of detectors used in the CRESST experiment is given. A detail description of their working principle and a model for the signal formation in low-temperature calorimeters is the topic of study in chapter 3.

As mentioned before, the CRESST detectors are cryogenic calorimeters that are operated at about 10 mK. A picture of a CRESST detector module is depicted in figure 2.4: on the right hand side the absorber crystal is shown in its copper holder. The absorbers are massive, inorganic scintillators. WIMPs are expected to scatter elastically off nuclei in these crystals. The energy deposited by a particle interaction leads to a temperature rise ΔT in the absorber crystal, which is detected by a thermometer located on the absorber. The thermometers belong to the *transition-edge sensors* (TES, see figure 2.4).

A TES consists of a superconducting thin film which is operated in its transition between the normalconducting and the superconducting phase. In this way a tiny temperature excursion ΔT (\mathcal{O} (μK)) caused by a particle interaction is detected by measuring the change in resistance ΔR . A transition curve from a TES is shown in figure 3.1. The point where the sensor is stabilized within the transition is referred to as the *operating point*.

The second detector shown in figure 2.4 is a *light detector*. The light detector allows the discrimination of background events from potential dark matter signal events by measuring the scintillation light emitted from the absorber crystal as a consequence of a particle interaction. The light detector typically consists of a sapphire wafer coated with a thin layer of silicon used as light absorber. The light detector is also operated as a calorimeter and equipped with a TES. Light detector and absorber crystal are facing each other and are enclosed by a scintillating and reflective housing. Such a set-up of light detector and phonon detector we refer to as *detector module*.

In the following the basic components of a cryogenic calorimeter are introduced before explaining the two-channel detection used in CRESST.

2.3.2. Cryogenic Calorimeters

Schematically, a calorimeter consists of an absorber characterized by its heat capacity C , a thermometer and a thermal link with heat conductance G to a heat bath of constant temperature T_B (see figure 2.5). Particles interacting in the absorber and depositing an energy ΔE cause a temperature rise measured by the thermometer given by

$$\Delta T = \frac{\Delta E}{C}. \quad (2.1)$$

Via the thermal link to the heat bath the temperature of the absorber relaxes back to equilibrium. The time constant τ for the relaxation process is given by the decay time

$$\tau = \frac{C}{G}. \quad (2.2)$$

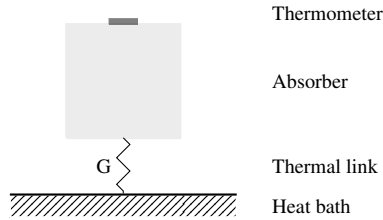


Figure 2.5. – Scheme of a basic calorimeter: particles interacting in the absorber deposit an amount of energy ΔE . The energy deposit leads to a temperature rise ΔT that is measured by the thermometer. Via the thermal link G the calorimeter relaxes back to heat bath temperature T_B .

In this simple model the signal consists of an instantaneous temperature rise ΔT and an exponential decay with the time constant τ .

However, this model does not sufficiently describe the real situation as the thermal resistances between the subsystems (thermometer, absorber) cannot be neglected at temperatures below 100 mK. In addition, the temperature rise is measured in the thermometer which is not in equilibrium with the absorber. The two main effects that influence the signal shape are:

Thermalization Process An interaction in the absorber is followed by a relaxation process, also known as thermalization. For the shape of the signal, it is important where in the calorimeter the thermalization takes place. This can happen in the bulk of the absorber or on its surfaces, in the thermometer or in other areas of the calorimeter as impurities or defects in the absorber crystal.

Thermal Couplings The mutual but finite couplings between the different subsystems lead to a temperature gradient in the calorimeter and introduce new time constants. The different thermal couplings that have to be considered are the electron-phonon coupling, the phonon-phonon coupling at boundaries between different materials (Kapitza coupling), and the already mentioned coupling to the heat bath.

For the moment we restrict ourselves to this simple explanation and return to the experimental set-up of the CRESST experiment. Thereafter, chapter 3 gives a more elaborate description of the detector concept and explains in detail the signal formation model for cryogenic calorimeters as used in CRESST.

2.4. Two-channel Detection

The overall rate of events in a CRESST detector module after putting all passive shielding in place is in the order of 10^4 events/kg/year, only taking into account an energy region from 10 keV to 40 keV.

In order to distinguish signal events from common background, the additional readout of the simultaneous produced scintillation light in the absorber provides a very sensitive tool. Employing this technique, nuclear recoils, which are also expected to be produced by WIMP interactions, are discriminated against the e/γ -background by the quenched ratio of light-to-phonon signal. This technique allows for an event-by-event discrimination and is discussed in more detail in the following sections.

2.4.1. Scintillating Absorbers

Since CRESST-II, the CRESST collaboration moved from a single- to a two-channel readout of detectors. Additional to the phonon signal also the scintillation light produced in the target from an incident particle is detected. The light/phonon discrimination implies to definitely use a scintillator as target material.

In a scintillator a fraction of the initial energy of the interacting particle is converted into scintillation photons. There are organic and inorganic scintillating materials existing, but for the application as a CRESST dark matter detector, only inorganic materials are considered.

In an inorganic scintillator, the emission of scintillation light can be itemized by a sequence of processes [Rod97]:

- interaction of the incident particle by creating electrons and holes
- relaxation of primary electrons and holes via the production of secondary particles as electrons, holes, photons or other electronic excitations
- thermalization of the low-energy secondary products resulting in e-h pairs with energies in the range of the band gap energy of the material
- energy transfer from the e-h pairs to the luminescences centers of the scintillator
- emission of scintillation photons from these luminescences centers

Depending on the way the luminescences centers are available in the material, scintillators are sub-divided into intrinsic and extrinsic scintillating materials [Rod97].

As previously mentioned, in CRESST mainly calcium tungstate crystals (CaWO_4) are used as target. CaWO_4 crystals belong to the class of dielectric, inorganic and intrinsic scintillators. The maximum scintillation emission wavelength at room temperature is in the range of 420 nm to 425 nm [Zde+05].



Figure 2.6. – Scintillating CaWO_4 crystals excited by UV light. The scintillation light is in the blue regime of the visible spectrum. One front surface is mechanically roughened to facilitate the escape of scintillation light from the crystal.

For coherent scattering there is an enhancement in the WIMP-nucleon interaction cross section $\sigma_{\chi N} \propto A^2$ (see equation (1.10)). Thus, CaWO_4 crystals, due to the presence of tungsten, are a suitable target material.

These crystals have a cylindrical shape (40 mm in diameter and height) and weigh about 300 g each. Two of these crystals are depicted in figure 2.6. For e/γ -interactions, about 1-2% of the deposited energy in the crystal is detected in the form of scintillation light. CaWO_4 crystals are non-hygroscopic and there is no degradation of the scintillation light output for events at the surface of the crystal detectable. Hence, the full volume of the absorber is utilized for dark matter search, a definition of a fiducial volume, as present in XENON or CDMS is not necessary ([Apr+10; Ahm+10]).

Besides CaWO_4 , zinc tungstate (ZnWO_4) has also been investigated and tested in the latest CRESST run. ZnWO_4 crystals have a lower level of intrinsic radioactivity and the amount of produced scintillation light is expected to be higher than in CaWO_4 , two requisites which would allow us to increase the sensitivity of the experiment. Detailed investigations on ZnWO_4 can be found in [Bav09; Zim12].

2.4.2. Cryogenic Light Detector

In order to detect the scintillation light from the absorber crystals, cryogenic *light detectors* have been developed. Such a light detector consists of a thin sapphire disc ($d=460\ \mu\text{m}$) with a diameter of 40 mm, equal to the diameter of the crystal. As pure sapphire is transparent for the blue scintillation light of CaWO_4 , a $1\ \mu\text{m}$ thick layer of silicon is epitaxially grown onto the sapphire disc. This type is called a SOS (*silicon-on-sapphire*) absorber. Besides the SOS-type pure silicon wafers are also used as light absorbers. A CaWO_4 crystal with its light detector is depicted in figure 2.4.

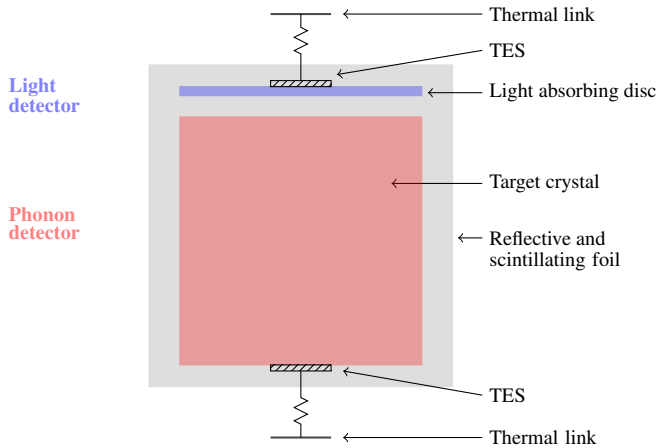


Figure 2.7. – Schematic drawing of a CRESST detector module.

The working principle of the light detectors is very similar to that of the absorber crystals: scintillation photons get absorbed in the silicon layer and produce phonons. These phonons are absorbed in the thermometer and lead to a temperature rise of the electron system of the TES - the finally detected light signal. The dimensions and structure of the TES are optimized for the purpose of light detection.

These light detectors are sensitive enough to measure energy deposits down to 10 eV. Information on the development and design, the optimization, and the performance of light detectors can be found in [Fra02; Pet05; Pan08; Huf10] and [Tan11].

2.4.3. Light/Phonon Discrimination

Each crystal is paired with a cryogenic light detector and together they form a *detector module*. A schematic drawing thereof can be seen in figure 2.7. The front surface of the crystal, facing the light detector, is mechanically roughened to prevent trapping of scintillation light by total reflection on the surface of the crystal. Both detectors are surrounded by a highly reflective polymeric foil which also scintillates (see section 2.5).

The experimental set-up allows a measurement of two coincident signals: the phonon signal and the light signal. The phonon signal provides an accurate and very precise measurement of the energy deposition in the crystal, approximately independent of the type of interacting particle.¹ The light signal allows one to identify the type of interacting particle, as the amount of scintillation light strongly depends on it.

¹The measured energy in the crystal is perfectly independent of the particle, when the small fraction of the energy, escaping in form of scintillation light, is taken into account.

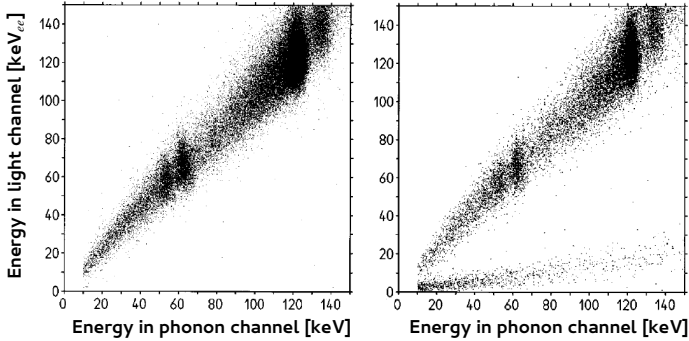


Figure 2.8. – In both plots the energy from the light channel is plotted versus the energy in the phonon channel. The detector was irradiated with a ^{57}Co γ -source as well as with electrons from a ^{90}Sr -source. Gammas and electrons from these sources as well as from background sources appear in a band with a slope close to unity by normalization. Exposing the detectors to an external neutron source (right plot) results in a second band with a significantly reduced slope. Clearly, electron and gamma events are separated from neutron events. Plot from [Meu+99].

The parameter describing this behavior is the *quenching factor* QF . It is defined as the ratio of scintillation light produced by an interacting particle of type X to the scintillation light produced by a gamma of the same energy:

$$QF^X(E_{dep}) = \frac{\text{light produced by particle of type } X \text{ when depositing } E_{dep}}{\text{light produced by gamma when depositing } E_{dep}} \quad (2.3)$$

where X denotes the type of particle and E_{dep} the amount of energy deposited in the absorber crystal. Even though quenching factors have been studied in many different scintillating materials and under different experimental conditions, there is no fundamental theory so far that enables one to calculate and predict the quenching factor for a special material and different interacting particles. Only semi-empirical models like the one proposed by Birks are available [Bir64].

Both plots in figure 2.8 show the energy in the light channel plotted versus the energy in the phonon channel for a detector irradiated with a ^{57}Co γ -source as well as with electrons from ^{90}Sr . Gammas and electrons appear in a band with a slope equal to unity by definition.

While exposing the detector to a neutron source a second band appears (see right plot in figure 2.8). This band is attributed to neutron interactions in the CaWO_4 crystal which, in comparison to gammas and electrons, produce about ten times less light. The constant slope of the two bands in figure 2.8 suggests that the amount of scintillation light is proportional to the total deposited energy.

particle type	1/QF
γ , electrons	1
α -particles	4.5
O-recoils	9.6
Ca-recoils	15.7
W-recoils	25.6

Table 2.1. – Inverse values of quenching factors taken from [Ang+12]. The QF for α -particles is derived directly from the background data of Run 32. The QF for oxygen is determined by a neutron calibration which took place during the data taking of Run 32. For the Ca- and W-recoils the QF s are determined by dedicated experiments [Huf+].

The difference in the light yield for gammas and neutrons can be understood by having a closer look on the modes of interactions of these particles in solid materials like CaWO_4 : gammas and electrons interact electromagnetically (mainly via photoelectric-effect and Compton scattering) and thus deposit their energy in the electron system of the absorber which excites the luminescence centers of the scintillator. Neutrons instead deposit their energy mainly by elastic scattering on target nuclei. The excitation of the luminescence centers via the nuclear channel is less efficient. It is worth mentioning that the more heavy the recoiling nucleus, the less scintillation light at same deposited energy is emitted.

In order to distinguish background events from signal events the corresponding QF s of the different background sources have to be known. In CaWO_4 the main measurable recoil energies from *neutrons* due to kinematic reasons come from the oxygen and calcium nuclei, given the spectrum from typical sources. Therefore, the QF s of oxygen and calcium recoils have to be known to identify the neutron background.

Another common background in rare event searches comes from α -particles. The investigation of the quenching factor for low-energy α -particles in CaWO_4 is a major topic of this work and will be discussed in detail in chapter 8.

The QF for α -particles at MeV-energies can be determined directly from Run 32 data.² The presence of α -emitters from natural decay-chains in the crystals itself allow for a calculation of the QF at MeV-scale directly from the background data. The QF for oxygen recoils as for example induced by neutrons is determined from a neutron calibration which was carried out during Run 32. The QF for calcium recoil events cannot be determined from the neutron calibration data due to limitations imposed by detector resolution and available statistics. The same is valid for tungsten recoils. Dedicated experiments were carried out to measure QF s for calcium and tungsten recoils [Huf+]. Amongst others, a determination of the QF s for O-, Ca- and W-recoils in CaWO_4 should be achieved by a low-temperature scattering facility, set up at the tandem accel-

²The latest CRESST Run we refer to as Run 32. The Run 32 lasted from May 2009 until April 2011.

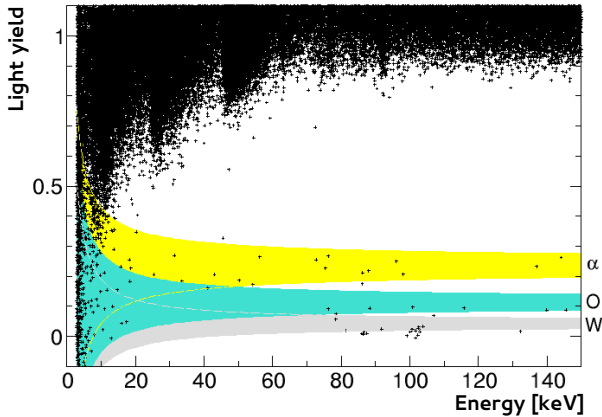


Figure 2.9. – Data in the light yield-energy plane for a detector module operated during the last CRESST run. The electron and gamma background events appear at a light yield around 1 by definition. The yellow band indicates where α -particles are expected. The turquoise and grey band illustrate the region of oxygen and tungsten recoils, respectively. The calcium band is located between the oxygen and tungsten band and is stripped for clarity. Plot from [Ang+12].

erator Maier-Leibnitz- Laboratorium (MLL) at Technical University of Munich [Str13].

Table 2.1 summarizes the inverse values of CRESST quenching factors [Ang+12]. Corresponding to these values, characteristic bands can be assigned to the different types of interacting particles.

A more common way of illustrating the CRESST data is through a plot in the *light yield-energy plane*. The *light yield* (LY) of an event is defined as the ratio of the energy measured with the light detector (keV_{ee}) to the energy measured with the phonon detector. Figure 2.9 shows the light yield-energy plane for a detector module operated during the last CRESST run. The highly populated band at a light yield of about 1 is attributed to the e/γ -background. The yellow band indicates the region expected for α -particle interactions. The turquoise and grey band illustrate the region of oxygen and tungsten recoils respectively. The boundaries of each band are chosen such that the central 80% of the events of a certain type are expected to be within these boundaries.

When discussing the discrimination power of background events from potential signal events there are two main aspects to be considered: firstly, it is of advantage if interactions from WIMPs and from common background sources take place on different nuclei in the case of a compound target material. However, this constraint depends purely on the physics of the interaction of WIMPs in the target material, especially on their actual mass. In other words, in the case of very light WIMPs, the main measurable contributions from scatterings in a CaWO_4 crystal are, due to kinematic reasons,

expected to come from oxygen. However, neutrons, depending on their actual energy spectrum, will also produce mainly oxygen and calcium recoils. By contrast, a heavy WIMP due to the A^2 proportionality in the cross section is expected to mainly produce detectable tungsten-recoils. Therefore, in section 2.4.4 the particular nuclei in CaWO_4 absorbers, to which a WIMP during an interaction may transfer its energy are discussed.

Secondly, the different bands have to be separated to allow for a reliable identification. However, at lower energies the bands start to overlap. The width of the bands is mostly set by the energy resolution of the light detector. Thus, an improvement of the resolution of the light detector would increase the sensitivity of the experiment.

In summary, the ability of measuring light and phonon signals is a powerful tool to discriminate radioactive backgrounds from potential signal events. In a detector with a finite energy resolution the discrimination ability is dominated by the radioactive backgrounds still present in the experimental set-up. The most dominant background are gammas and electrons both coming from the surrounding materials of the experiment and from the CaWO_4 crystals themselves.³

Furthermore, radioactive decay products from radon present on the parts surrounding the detectors can lead to a background in the α -band as well as to nuclear recoil events showing very little associated light signals since the recoiling Pb-nuclei have a high mass number (see section 2.5 for a detailed discussion on this background). The latter is a dangerous background as it can mimic WIMP interactions.

2.4.4. Target Nuclei for Dark Matter Search

As presented in the previous section, various backgrounds (electrons/gammas, neutrons, α -particles) appear in different bands in the light yield-energy plane. Thus, an event-by-event based particle identification is possible.

In this section it is discussed where WIMP interactions are expected in the light yield-energy plane. As shown in section 1.4, WIMPs are expected to interact via elastic scattering off target nuclei. The A^2 proportionality in the interaction cross section enhances the interaction probability on heavy target nuclei. In the case of CaWO_4 , WIMPs are therefore anticipated to mainly interact on the tungsten nuclei ($A_W \approx 184$).

Due to a finite energy threshold of the detectors, the latter assumption has to be looked at in more detail, in particular taking into account the actual mass of the WIMP. For heavy WIMPs the energy transferred to the heavy tungsten-nuclei is efficient and allows for detection. For low mass WIMPs the energies transmitted to the tungsten nuclei might be too low to be detectable, while the energy transmitted to a calcium or oxygen nucleus may be still in the detectable range.

Figure 2.10 illustrates this behavior: the expected rate of WIMP scatterings on the different target nuclei is plotted as a function of the WIMP mass for recoil energies in

³The intrinsic radioactivity present in our CaWO_4 crystals varies between the crystals since they are produced by different crystal-growth institutions. The main contamination comes from isotopes of the natural decay chains ^{238}U and ^{232}Th , the α -emitter ^{211}Bi from the ^{235}U -chain and a contamination with ^{147}Sm .

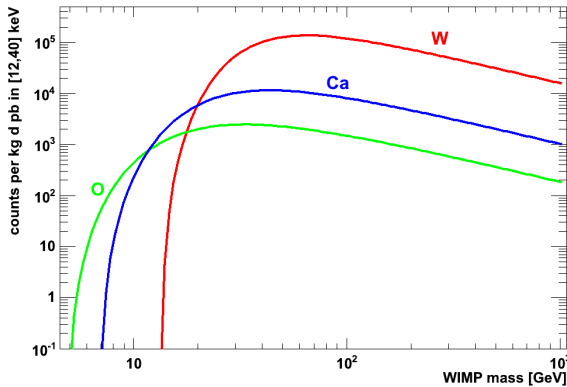


Figure 2.10. – The expected rate of WIMP scatterings off the three target nuclei in CaWO_4 , for a sensitive energy range of 12 keV to 40 keV and a cross-section of 1 pb, as a function of the WIMP mass. Plot from [Ang+12].

the range of [12,40] keV. The lower energy bound reflects a typical energy threshold of a detector. The upper energy bound is set to 40 keV since, due to form factor effects, nearly no WIMP scatterings are expected at energies above this value (see section 1.4.3 and [Sch10] for a discussion on form factors).

For WIMP masses larger than 30 GeV, tungsten recoils completely dominate possible dark matter signals. In the case of WIMP masses below 20 GeV, the calcium and oxygen recoils start to become relevant and finally at WIMP masses around 10 GeV, the scatterings off tungsten are completely below threshold and only scatterings off calcium and oxygen are detectable. Therefore, in CRESST all three types of recoils are considered for dark matter analysis. This allows to be sensitive to a large range of WIMP masses (see section 2.6).

2.5. Scintillating Surrounding

The main component of the housing is a *reflective and scintillating* polymeric foil (Radiant Mirror Film VM2002 by 3M). On the front surfaces of the cylindrical housing two additional rings, made out of plastic scintillator material (BC408 from Saint Gobain) are used to guide the foil around the crystal. Furthermore, the rings feature a special shape that helps to have a defined enclosing in the area of wire bonds and the metal clamps utilized to keep the crystals in position.

It is of crucial importance that the surrounding material is not only reflective but also scintillating in order to discriminate background due to α -decaying isotopes on the surface of the housing of the detectors.

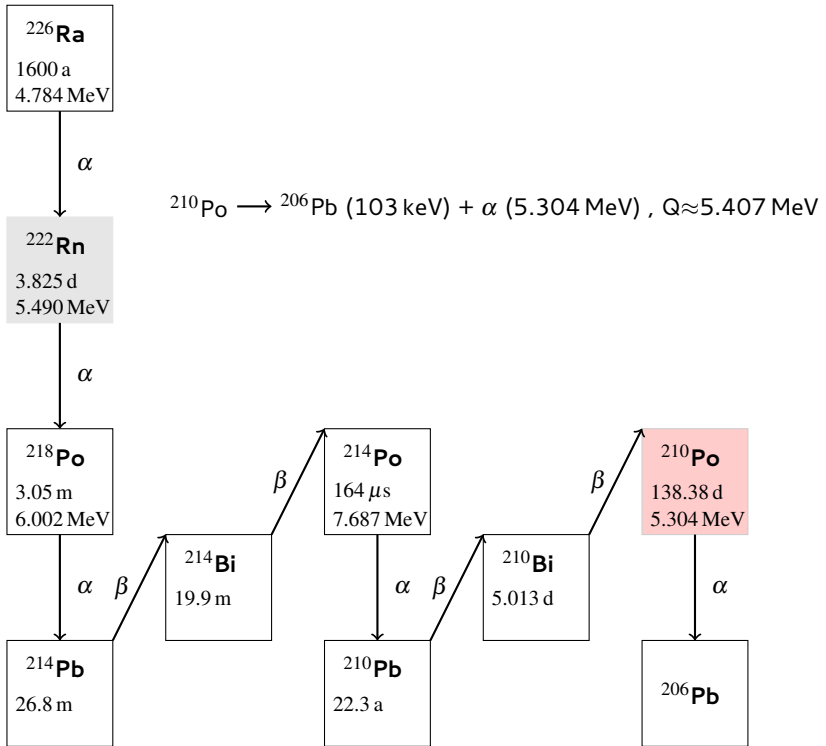


Figure 2.11. – Decay chain of ^{222}Rn . The half-lives and decay energies are taken from [MPG06]. In the decay of ^{210}Po , a recoil energy of 103 keV is transferred to the daughter nucleus ^{206}Pb .

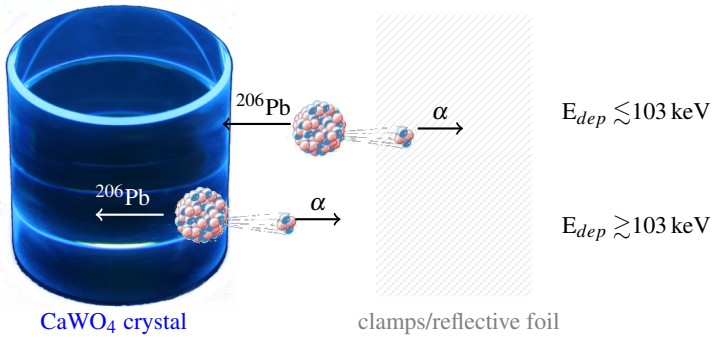


Figure 2.12. – Background events introduced by the decay of the ^{210}Po isotope. ^{210}Po can sit on the surface or even be implanted in the detector as well as its surrounding materials. When a decay of ^{210}Po takes place in the clamp/reflective foil, the maximum kinetic energy of a ^{206}Pb nucleus recoiling the CaWO_4 is 103 keV. In the case where the ^{210}Po -decay takes place on the surface of the crystal the detected energy is ≥ 103 keV.

The main source for this kind of background is ^{222}Rn . Radon is present in ambient air and if there is no special radon-prevention undertaken, radon and/or its progenies may deposit on the detector and its surrounding. In figure 2.11 the decay chain of ^{222}Rn is shown including the ^{210}Po isotope. Figure 2.12 illustrates background introduced by ^{210}Po . ^{210}Po is an α -emitter and decays to stable ^{206}Pb via the emission of an α -particle with an energy of 5.304 MeV (see figure 2.11). The recoiling lead nucleus carries the rest of the Q-value, namely about 103 keV and leaves the center of mass in the opposite direction than the α -particle (see figure 2.12). The following two situations are important:

^{210}Po Contamination on/in the Surrounding Materials In the case that the ^{210}Po is present on/in the housing material of the detectors, the recoiling lead nucleus can hit the crystal whereas the α -particle escapes in the opposite direction (upper case in figure 2.12). Due to its high mass, the recoiling lead nucleus has a similar quenching factor as W-recoils and consequently appears either in or slightly below the tungsten band. Thus, these background events can mimic WIMP signals.

If the ^{210}Po nucleus sits on the surface, the full recoil energy of 103 keV is deposited in the CaWO_4 crystal; in the case where ^{210}Po is implanted in the surrounding the ^{206}Pb nucleus loses part of its initial energy by traversing the surrounding. Therefore, the (detectable) energies of lead nuclei can range from 103 keV down to threshold energy.

A rejection of ^{206}Pb -events is achieved by using scintillating materials for all parts surrounding the detector. In this way the α -particle produces additional light that is

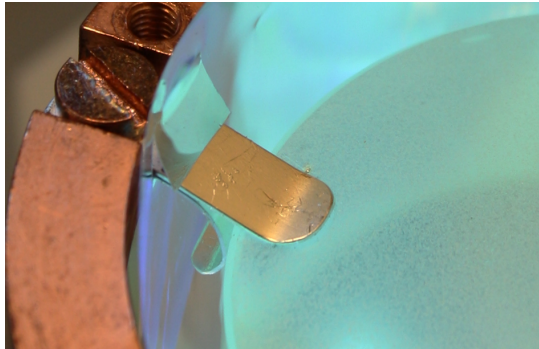


Figure 2.13. – Photography of a crystal mounted with silver coated bronze clamps. One of in total six pairs of clamps is visible. The metal clamps are the only not scintillating parts in the vicinity of the detectors. They are found to be the origin of ^{210}Po -related background observed in Run 32.

detected simultaneously with the ^{206}Pb -recoil in the crystal. This additional light shifts the event to higher light yields away from the region where WIMP interactions are expected.

^{210}Po Contamination on/in the Crystal In the case where ^{210}Po sits on the surface of the crystal, or is implanted into the crystal, the situation is different (see lower case in figure 2.12). The full energy of the lead nucleus of 103 keV is detected in the case where the ^{210}Po -nucleus is implanted in the crystal plus a possible contribution from the α -particle. The overall detected energy is ≥ 103 keV and thus far above the energy range relevant for WIMP search.

In the last CRESST run the only non-scintillating material present inside the detector housing were the six pairs of metal clamps used to hold the detectors in position. These clamps are made out of bronze and are coated with a thin layer of silver to improve light reflection (see figure 2.13). Three additional clamps are needed to fix the light detector in its holder.

In earlier CRESST runs, clamps coated with a scintillator were already introduced to prevent background from α -emitters. However, the plastic coverage of the clamps gave rise to events attributed to thermal relaxation processes in the plastic. These events are characterized by a different pulse-shape in comparison to normal events. In these detectors relaxation events could be observed in a wide energy range down to threshold energy (see chapter 5). At higher energies, the relaxation events can be distinguished from good particle-events with high significance. However, approaching the energy threshold (small amplitudes) the differences in pulse-shape are less pronounced and a contribution of relaxation events to the signal region cannot be completely excluded.

In order to avoid such relaxation events in Run 32 only pure metal clamps have been used. As a consequence lead recoil events (produced via the mechanism explained before) have been observed in Run 32 and some of them have leaked into the WIMP region. These Pb-recoils have been accounted for in the analysis [Ang+12], but a significant reduction of the present background is essential for an upcoming run.

The scope of the work presented in this thesis is an investigation and description of the backgrounds existing in CRESST. A significant reduction of the background allows us to also reduce possible consequences of uncertainties in a particular background model.⁴ Furthermore, a reliable identification of a positive signal can only be achieved when the detector physics related to present backgrounds is completely understood.

Background from α -emitters and related Pb-recoil events coming from the clamps are investigated in detail (see chapter 5). After having identified the origin of the different background sources, measures taken to avoid them in a future run are introduced.

The development of new clamping concepts as well as related measurements carried out in the test facility at the Laboratori Nazionali del Gran Sasso are the topic of the study in chapter 6 and chapter 7.

2.6. Advantages of CRESST Detectors

2.6.1. Remarks on Detector Performance

Energy Measurement of the Phonon Channel Even though the target crystals used in CRESST consist of massive dielectric absorbers, they provide a very accurate measurement of the deposited energy in the crystal combined with an excellent energy resolution. In figure 2.14 the low energy spectrum of the phonon detector called Verena is shown. The dominant feature around 50 keV is attributed to a contamination of ^{210}Pb in the crystal (also see decay scheme in figure 2.11).

Not only the 46.5 keV of the gamma transition can be observed but also the energy of the accompanying β -spectrum. Due to the slow time response of the detectors, the gamma and the electron cannot be resolved but rather the summed energy of both particles is measured. Therefore, a β -spectrum with a sharp line at precisely 46.5 keV extending up to the Q-value of the decay at 63.5 keV is visible.

Furthermore, the copper fluorescence line (8.05 keV) is observed at 8.2 keV with a resolution of about 300 eV (FWHM) [Ang+09]. Another γ -line from the decay of ^{41}Ca (3.61 keV) is found at 3.6 keV.

The accurate determination of the deposited energy in the target crystals is an outstanding advantage of the CRESST detector technique in the wide field of dark matter experiments.

⁴In other words, in the case of the absence of background, the model to describe it does not matter.

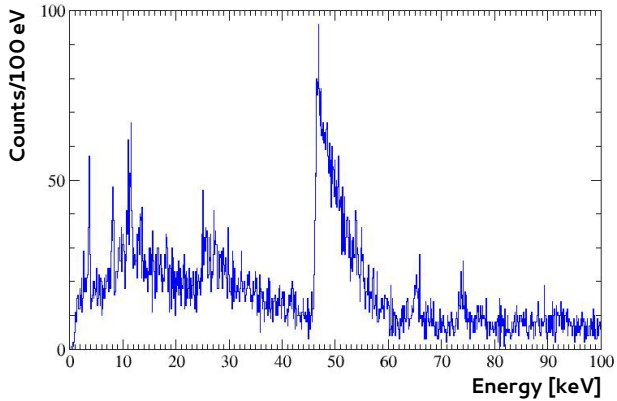


Figure 2.14. – Energy spectrum of the phonon detector Verena [Ang+09]. The γ -line at 46.5 keV from the decay of ^{210}Pb is visible together with its accompanied β -spectrum. The fluorescence line of copper ($K_{\alpha}=8.05$ keV) as well as the γ -transition from ^{41}Ca (3.61 keV) can be observed in the spectrum.

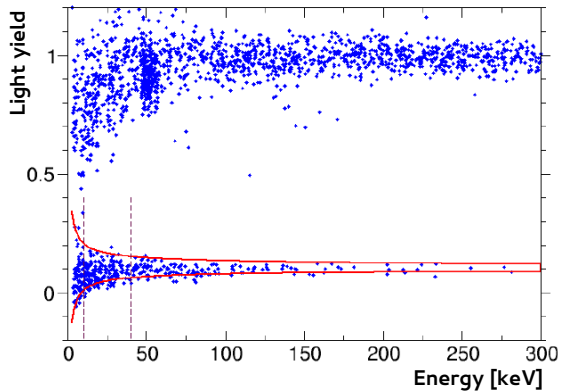


Figure 2.15. – Data in the light yield-energy plane for a CRESST detector module obtained by a neutron calibration (AmBe-source). The band at a LY around 1 is due to e/γ -interactions. The band at lower LY is associated to neutron interactions [Ang+12].

Rejection of Gamma Background Neutron induced nuclear recoils appear in a band clearly separated from the e/γ -band. In figure 2.15 the light yield is plotted versus energy for a conventional CRESST detector module as obtained by a calibration measurement with an AmBe neutron source. The band at a light yield around 1 is caused by e/γ -background. The lower band is due to nuclear recoils induced by neutrons. The bands are well separated and demonstrate the good discrimination power of CRESST. The solid red lines mark the central 80% probability band calculated for oxygen recoils. This means that 10% of the events are expected above the upper and 10% are expected below the lower boundary. The vertical dashed lines mark the region relevant for WIMP search.

At energies above 100 keV the distribution of the events induced by neutrons fits particularly well to the calculated band since, due to kinetic reasons, the neutrons mainly scatter off the oxygen-nuclei. At lower energies the distribution also contains calcium- and tungsten recoils. The actual contributions of O-, Ca- and W-recoils depend on the spectral distribution of the neutrons from the calibration source.

To this end, the discrimination between e/γ -events and nuclear recoil-events is limited by the e/γ -leakage into the region of interest. Therefore, in CRESST the lower bound of the WIMP sensitive region (acceptance region) E_{acc}^{min} is defined such that only one event from e/γ -leakage is expected in the acceptance region in the whole data set. Values for E_{acc}^{min} range from 10.2 keV to 19.0 keV in Run 32 for the different modules [Ang+12]. The upper bound E_{acc}^{max} is set to 40 keV as no significant WIMP recoils are expected at higher energies.

Large Dynamic Range Another remarkable feature of CRESST calorimeters is their wide sensitivity range. CRESST detectors are optimized to be most sensitive in the range ≤ 100 keV. Nonetheless, also energies up to 5 MeV or higher can be detected and an accurate energy can be assigned to these events mainly caused by α -particle interactions.

A reliable energy calibration over a wide energy range provides the possibility to identify the different α -lines and thus to determine the intrinsic impurity level of the crystals.

Aside from the study of radioactive contaminations present in a crystal, one can use this technique for nuclear physics, for example to investigate rare nuclear decays. In 2004, using CaWO_4 as target, the natural α -decay of the ^{180}W isotope was observed for the first time ($T_{1/2} = (1.8 \pm 0.2) \cdot 10^{18}$ y, $Q = (2516.4 \pm 1.1(\text{stat.}) \pm 1.2(\text{sys.}))$ keV) [Coz+04].

In figure 2.16 the light-phonon-plane for a CaWO_4 absorber in Run 28 is shown. There are three bands indicated: the e/γ -band, the α -band and the band where nuclear recoils are expected, as for example O-recoils induced by neutrons. These discrete lines in the α -band can be attributed to radioactive isotopes, which are mainly members of the natural decay chains.

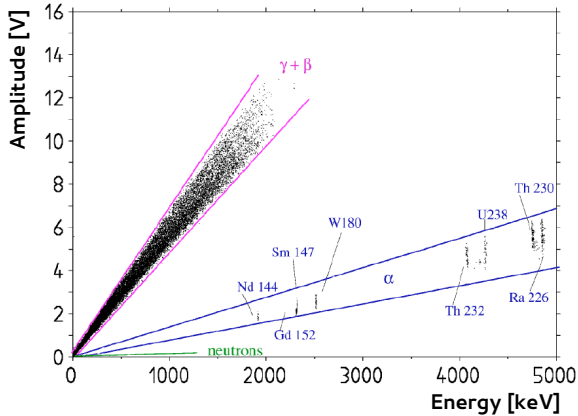


Figure 2.16. – Pulse amplitude in the light detector plotted vs. energy in the phonon detector of a CaWO_4 crystal. Energies up to 5 MeV can be identified. In the α -band different discrete lines appear. In these data the natural α -decay of ^{180}W was observed for the first time ever [Coz+04].

Multi Target Approach In comparison to other dark matter searches, as XENON (using liquid xenon as target [Apr+10]) or CDMS (using pure germanium and silicon [Ahm+10]), CRESST detectors are intrinsic multi target detectors. This is advantageous because WIMP interactions will be detectable on the different target nuclei of the compound material (see section 2.4.4 and figure 2.10) and therefore being sensitive to a wide range of possible WIMP masses. Even very low mass WIMPs ($\mathcal{O}(10 \text{ GeV})$) will give a measurable signal when scattering off oxygen nuclei.

The opportunity to employ diverse scintillators will be particularly important for the confirmation of a positive WIMP signal (see section 1.4). In addition, different scintillators provide further information to understand and reduce background.

Room for Improvement The phonon detectors are sensitive down to energies of about 2 keV. The detection threshold of the light detectors on an absolute energy scale is as low as 9 eV to 10 eV, corresponding to three and less photons. In terms of defining the WIMP sensitive region it is not only the detection threshold of the light and phonon detector that determines the WIMP sensitivity, but also the discrimination efficiency at which the dominant e/γ -background can be suppressed at low energies.

Every band has an energy dependent width. In theory, the width of a band is given by the energy resolution of both the light and the phonon detector. Due to the small fraction of energy emitted in the form of scintillation light, the resolution of the phonon detectors is about an order of magnitude better (on the keV_{ee} -scale). Therefore, the width of the bands depends essentially on the performance of the light detector.

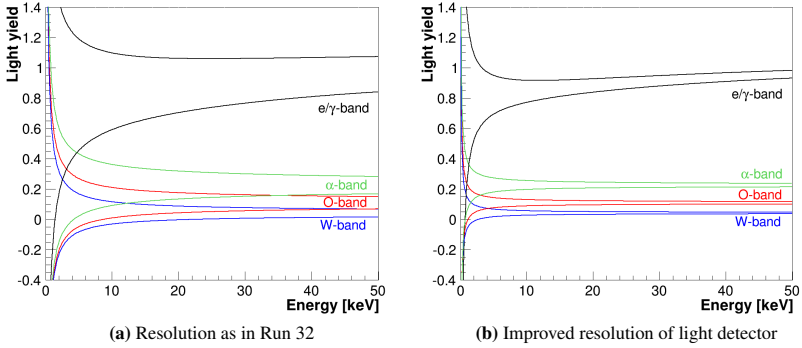


Figure 2.17. – Light yield-energy plane showing the e/ γ -band as well as the regions where α -particles and O- and W-recoil events are expected. In CRESST detectors the width of the bands is mainly limited by the resolution of the light detector. In the left plot the bands are plotted using typical CRESST values from the detector module Rita in Run 32. In right plot the resolution of the light channel was improved by a factor of five resulting in a better separation of the bands.

In figure 2.17 data is plotted in the light yield-energy plane for two different situations. In figure 2.17 (a) the bands for e/ γ -events, α -particles and O- and W-recoils are shown using typical CRESST-values for the energy resolution. In figure 2.17 (b) the energy resolution of the light detector is artificially set to be five times better than in the left plot.⁵ The bands in the right plot are better separated from each other and allow for a more reliable discrimination of incident particles, especially at low energies. Note, the boundaries are chosen as 1.28σ central boundary lines, meaning that 80% of events of the corresponding type are expected within these boundaries.

The lower bound E_{acc}^{min} of the WIMP acceptance region depends on the resolution and on the level of the e/ γ -background to be suppressed. In the case of an increased resolution, E_{acc}^{min} will also be shifted to lower energies. A lower threshold would also rise the WIMP count rate as the featureless spectrum is expected to rise exponentially at lower energies (see section 1.4).

Summing up, the present performance of the light detector allows us to some extent to distinguish O- and W-recoils in the acceptance region but an improvement of the energy resolution of the light detector would increase the sensitivity of the experiment. The following theses give an overview of the theoretical and experimental work done so far on this topic [Fra02; Pet05; Pan08; Huf10; Tan11].

⁵The resolution of the light detector is increased by a factor 5. The resolution of the phonon detector remains unchanged. The parameter S_0 is given by $S_0 = (\sigma_0^P)^2 + (\frac{1}{5}\sigma_0^L)^2$ and S_1 is divided by a factor of 25. S_2 for Rita in Run 32 was zero. Detailed explanation on the meaning of the parameters are given in section 8.4.

2.6.2. Alternative Scintillating Materials

Another possibility to improve the discrimination efficiency and thus the sensitivity of the experiment is to use scintillating materials with a higher light output. In a conventional CaWO_4 crystal only up to 2% of the deposited energy in the crystal are detected in form of scintillation light in the light detector.

So far a number of crystals, including ZnWO_4 , CaMoO_4 , CdWO_4 and titanium doped Al_2O_3 have been investigated as new target materials for CRESST in [Bav+08; Bav09; Zim12; Kle10] and within this work (see appendix B). When looking for alternative target materials, certain criteria should be taken into account:

- the material should be a scintillator with a high light output at low temperatures
- the overall level of intrinsic radioactive contaminations should be as low as possible, preferable lower than in currently used CaWO_4 crystals
- the new target material should be easy available to allow for a constant and reproducible supply
- when aiming to test for heavy WIMPs a target material with at least one heavy nucleus (WIMP interaction cross section scales $\propto A^2$) in the compound is required.
- the material should not suffer from surface effects that result in a position dependence of the phonon or light signals. Observations of such a behavior would be a criterion for exclusion of the respective material.

In the framework of this thesis, CdWO_4 and a CsI (pure) have been studied with the focus on the light output at low temperatures, the intrinsic radioactivity and the performance as a conventional CRESST detector. Results from these studies are presented in appendix B.

2.7. Summary and Conclusions from Run 32

Run 32 took place from June 2009 until April 2011. From the 18 detector modules mounted in the cryostat at Gran Sasso, ten modules were completely functional with both a phonon and light detector operational. One of these modules was equipped with a ZnWO_4 crystal and was excluded from the analysis because of uncertainties in the quenching factor for this material. Another module had a very bad performance with almost no sensitivity in the WIMP search region and was also not taken into account for the final analysis. The collected data from the eight remaining detector modules after cuts corresponds to a net exposure of 730 kg-days.

The region sensitive for WIMP interactions (*acceptance region*) is defined in the following way: to be sensitive to a wide range of possible WIMP masses all three

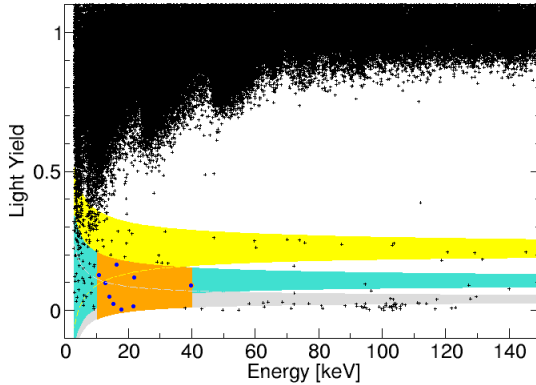


Figure 2.18. – Data in the light yield-energy plane for a detector module operated during Run 32. The colored bands indicate the region where α -particles (yellow), oxygen recoils (turquoise) and tungsten recoils (grey) are expected. The WIMP search region (acceptance region) is colored in orange and the observed events in this region are visualized as blue spots. The highly populated band at a light yield of around 1 is due to e/γ -interactions [Ang+12].

kinds of nuclear recoils are considered (oxygen, calcium and tungsten). The recoil-energy range of interest has an upper bound at 40 keV as no significant WIMP signal is expected at higher energies. The lower energy boundary is set by electrons and gammas leaking into the nuclear recoil region due to the finite resolution of the detectors. The e/γ -leakage can be calculated based on a fit of the observed e/γ -distribution. The lower bound E_{acc}^{min} is set such that only one leakage event is allowed per module in the whole data set. Hence, the value of E_{acc}^{min} is characteristic for each detector module, as it depends on its energy resolution, the level of intrinsic radioactivity as well as the e/γ -background from the surrounding of the experiment. Values for E_{acc}^{min} range from 10.2 keV to 19.0 keV.

In figure 2.18 the data of one detector module named Rita/Steven (ch51/ch52) from Run 32 is shown in the the light yield-energy plane. The colored areas show where α -particles (yellow), oxygen recoils (turquoise) and tungsten recoils (grey) are expected. The calcium band is not plotted. In orange the acceptance region is shown together with the events observed in this region (blue dots).

A maximum likelihood analysis is used to estimate the relevant backgrounds in the acceptance region, coming from e/γ -leakage, leakage from α -particles, neutrons and lead recoil events from ^{210}Po . The results from the likelihood analysis also leave room for a possible WIMP signal. In total we observe 67 events in all eight detector modules in the acceptance regions. To clarify if the observed events are compatible with the considered backgrounds, a likelihood ratio test is performed. The analysis results in a statistical significance for positive signals of more than 4σ . Therefore, the observed

	M1	M2
e/γ -events	8.00 ± 0.05	8.00 ± 0.05
α -events	$11.5^{+2.6}_{-2.3}$	$11.2^{+2.5}_{-2.3}$
Neutron events	$7.5^{+6.3}_{-5.5}$	$9.7^{+6.1}_{-5.1}$
Pb events	$15.0^{+5.2}_{-5.1}$	$18.7^{+4.9}_{-4.7}$
Signal events	$29.4^{+8.6}_{-7.7}$	$24.2^{+8.1}_{-7.2}$
m_χ [GeV]	25.3	11.6
σ_{WN} [pb]	$1.6 \cdot 10^{-6}$	$3.7 \cdot 10^{-5}$

Table 2.2. – Results of the maximum likelihood fit taking into account known background sources as well as a contribution from a possible WIMP signal. The event numbers are given in counts. The WIMP mass and interaction cross-section are shown for both of the two maxima M1 and M2 of the likelihood function. Except for the e/γ -events the errors shown correspond to a 1σ confidence interval. The statistical error for e/γ s is small as they are present with high statistics [Ang+12].

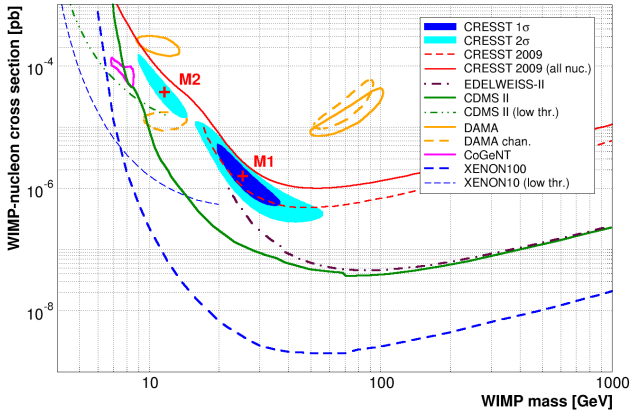


Figure 2.19. – The identified signal region (M1 and M2) from the Run 32 CRESST data in the WIMP parameter space. The 1σ (blue) and 2σ (cyan) contours have been calculated with respect to the global likelihood maximum M1. Experimental upper limits are shown from XENON100 [Apr+12], XENON10 [Ang+11], CDMS II [Ahm+10] and Edelweiss-II [Arm+12]. The favored regions associated with the data from DAMA/LIBRA (orange, 90% C.L., [Sav+09]) and CoGeNT (magenta, 90% C.L., [Aal+11b]) are also shown.

events do not seem to be explained by the sources of known background but rather an additional origin of these events has to be considered. One possibility are WIMPs.

The results of the maximum likelihood fit including the considered backgrounds as well as a possible WIMP signal are summarized in table 2.2. The likelihood function has two maxima, the global maximum M1 and the only slightly disfavored relative maximum M2 (see figure 2.19). The fact that there are two maxima can be attributed to the different target nuclei that are present in the compound material CaWO_4 . Principally both maxima give the same WIMP energy spectrum, only the composition of the participating target nuclei changes. In the case of M1 the WIMP is heavy enough to produce tungsten recoils that can be detected. About 69% of the recoils happen on tungsten, about 25% on calcium and only 7% of the recoils are on oxygen. In the case of M2 only scatterings on calcium (48%) and on oxygen nuclei (52%) are observed. The derived WIMP masses for the two maxima correspond to low mass WIMPs with a mass of $m_\chi = 25.3 \text{ GeV}$ and $m_\chi = 11.6 \text{ GeV}$ for M1 and M2 respectively.

There is no intention to declare the direct detection of WIMPs but rather consider them as one valid hypothesis to explain the excess of background events. As the overall background levels in Run 32 are still too high and the uncertainties in the background model are too large, the major goal of the next run is to clarify if the excess above known background events still remains after a significant reduction of the present background.

3. Detection Principle

In order to distinguish background events from potential signals events in the CRESST experiment, the scintillation light produced by an interaction in the target crystal is detected simultaneously with the temperature signal. Both detectors, the phonon and the light detector, are operated as cryogenic calorimeters. A basic description of a cryogenic calorimeter was already given in section 2.3. In this chapter, the principle and the detection concept of such kind of detectors is discussed in detail.

In section 3.1 the heat capacities of the different detector components are explained. Section 3.2 discusses the thermometer type used in order to read out the detectors. The relaxation processes and thermal couplings involved in the process of the signal formation are studied in section 3.3 and section 3.4. Finally, section 3.5 introduces the model used to describe the detected signals; a basic understanding on this model is given.

3.1. Heat Capacity

The heat capacity plays a crucial role for low temperature calorimeters as it limits the amplitude of the temperature signal ΔT that can be obtained. The heat capacity results from the different possible excitations of the various components of a thermodynamic system at a certain temperature.

3.1.1. Dielectrics and Semiconductors

In non-magnetic dielectric absorbers the heat capacity is dominated by the lattice specific heat. At low temperatures the heat capacity, due to the excitations of phonons, can be very well described by the Debye-model [Deb12]:

$$c_{ph} = \frac{12\pi^4}{5} n_a k_B \left(\frac{T}{\Theta_D} \right)^3 = AT^3 \quad (3.1)$$

where c_{ph} is the lattice specific heat, n_a is the number of lattice atoms per mole, Θ_D is the material's Debye temperature and A is a material constant. Due to the T^3 dependence, the phononic heat capacity is very small at temperatures in the millikelvin regime and therefore dielectric materials are very suitable as absorbers for massive calorimeters.

In the CRESST experiment mainly large calcium tungstate crystals (CaWO_4) are used as absorbers. They have a cylindrical shape (40 mm in diameter and height) and weigh about 300 g each.

3.1.2. Metals

For metals the electronic contribution has to be taken into account. Conducting electrons in a metal can be described as a Fermi gas and the specific heat is given by

$$c_{el} = \frac{\pi^2}{2} n_e k_B \frac{T}{T_F} = \gamma T \quad (3.2)$$

where c_{el} is the electronic specific heat, n_e is the number of conducting electrons per mole and T_F is the Fermi temperature.

Hence, the total specific heat of a metal such as for example the thermometers used in the CRESST experiment, is

$$c = \gamma T + AT^3 \quad (3.3)$$

where γ and A are constants which only depend on the material [Pob92]. Below temperatures of about 1 K the phononic specific heat becomes negligible in most metals and the electronic component dominates due to its linear dependency.

3.1.3. Superconducting Metals

The specific heat of the lattice is not affected by the transition in the superconducting state. The electronic specific heat, however, has a discontinuity at the critical temperature T_c where the conducting electrons start to form *Cooper pairs*. This second order phase transition results in [BCS57]

$$c(T_c) = 2.43\gamma T_c \quad (3.4)$$

where c denotes the electronic part of the specific heat in the superconductor.

At temperatures below the critical temperature T_c , the electronic component of the specific heat decreases exponentially. This is a direct consequence of the energy gap representing the binding energy of Cooper pairs. Below $T_c/2$, the Bardeen-Cooper-Schrieffer-(BCS) theory of superconductivity allows to describe the electronic specific heat by

$$c = 1.34\gamma T_c \left(\frac{\Delta}{k_B T} \right)^{\frac{3}{2}} \exp\left(\frac{-\Delta}{k_B T} \right) \quad (3.5)$$

where Δ is the superconducting energy gap and T_c the critical temperature of the superconductor. At temperatures well below T_c ($\sim T_c/10$) the electronic part of the specific heat becomes negligible in comparison to the remaining phononic contribution.

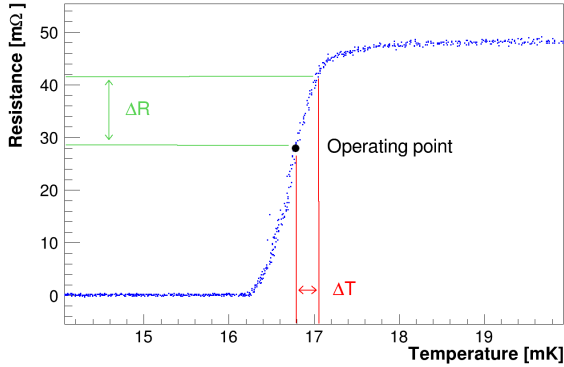


Figure 3.1. – Typical transition curve of a TES tungsten film. An operation of the thermometer in its transition from the normalconducting to the superconducting state allows the detection of tiny excursions in temperature ΔT by measuring the change in resistance ΔR of the TES.

3.2. Transition Edge Sensor (TES)

As mentioned in section 2.3, in CRESST transition edge sensors (TES) are used as thermometers to read out the large dielectric absorbers. A transition curve of such a sensor can be seen in figure 3.1. The steepness of the transition curve of the TES allows the detection of small temperature changes ΔT ($\mathcal{O}(\mu\text{K})$) caused by particle interactions in the absorber by measuring the change in resistance ΔR .

In the case of a conventional CRESST detector, the TES is made out of a thin tungsten film (200 nm) which is evaporated onto the surface of the absorber crystal and extends over an area of $(6 \times 8) \text{ mm}^2$. In addition, a TES is equipped with contact pads made out of aluminum. The connection between the contact pads of the sensor and the detector holder is made using aluminum bond wires having a diameter of $25 \mu\text{m}$ (see figure 3.2). Also the thermal link consisting of a gold wire bond (diameter of $25 \mu\text{m}$) is visible. This thermal link is bonded onto a long and thin gold structure which extends across the tungsten film. It allows the sensor after a particle interaction in the absorber to relax back to equilibrium.

In order to stabilize the TES at its operating point, a heater is used. It consists of a gold stitch bond which is bonded to the same gold structure on the TES as also used for the thermal link. In this way a stabilization of the TES in an operating point within a few μK is practicable.

The TES is fabricated using thin film technology and photo-lithography. A tungsten film evaporated onto the surface of the crystal is etched to the desired shape. Pattern of gold and aluminum structures is carried out by two subsequent lift-off processes.

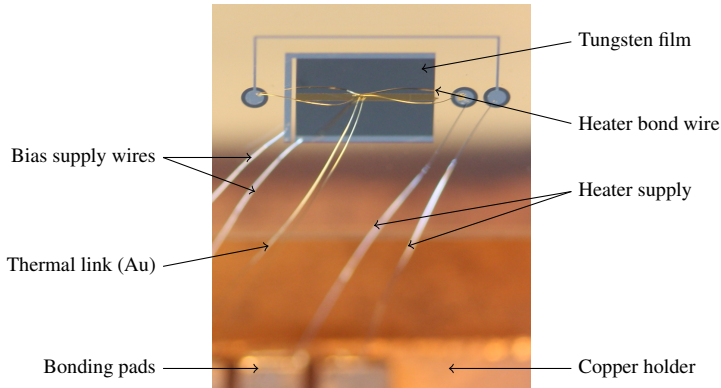


Figure 3.2. – Picture of a TES evaporated onto the surface of the crystal. The bias supply wires are used to bias the tungsten film. The heater allows for the stabilization of the TES in an adequate operating point within the transition. The thermal link connects the sensor to the heat bath.

The aluminum pads are produced via an evaporation process, the gold stripe instead is produced by sputtering. Both aluminum and gold are processed after the tungsten film evaporation.

3.3. Relaxation Processes

All particle interactions in the absorber, irrespective of whether through electron or nuclear recoils, create high frequency phonons $\mathcal{O}(\text{THz})$. The energies of these phonons are of a few meV. These phonons are called *non-thermal phonons* as thermal energies in the temperature range of the detector operation (approximately 10 mK) are very small ($E \approx k_B T \approx 1 \mu\text{eV}$).

The spectra of these phonons depend on the type of interacting particle. Ionizing radiation shows an almost mono-energetic distribution whereas phonons produced by nuclear recoils have a very broad frequency distribution. However, these phonon populations are not stable and decay very fast to a distribution with a mean frequency of few 100 GHz [Prö+95]. This very rapid initial decrease of the phonon frequency is driven by a frequency-dependent anharmonic decay rate ($\propto \nu^5$). With this decay differences in the spectra are washed out very quickly.

The fast initial decay is followed by a much slower process and the average phonon frequency distribution remains quasi constant for a few milliseconds. During this time the phonons spread ballistically over the volume of the absorber. Only few elastic scatterings on the surface are necessary until they are homogeneously distributed over the volume of the crystal.

A further thermalization in the large absorbers can be achieved via:

Direct Absorption of Phonons in the TES If non-thermal phonons enter the thermometer they get absorbed by the free electrons of the tungsten film very quickly thereby heating the electron system of the metal film. The heated TES may relax back to equilibrium temperature as a part of the energy thermalized in the electron system can be re-emitted into the absorber as thermal phonons. However, the dominant process at these low temperatures is relaxation via the thermal link to the heat bath.

Thermalization by Inelastic Scattering on the Crystal Surface Phonons that thermalize in the absorber before being absorbed by the TES lead to an increase in the absorbers' temperature. As in the case of a direct absorption in the TES, the absorber also relaxes back to equilibrium temperature via the thermal link but on a longer time scale.

Loss of Phonons via Metal Clamps Metal clamps are used to fix the crystals in their copper structure. Phonons that leave the absorber via these metal clamps are lost and do not contribute to the signal.

3.4. Thermal Coupling

An energy deposition in the absorber is followed by relaxation processes which result in different temperatures of the sub-systems (phonons in absorber, phonons in TES, electrons in TES) of the calorimeter. These temperature differences lead to a heat flow between the sub-systems until equilibrium conditions are reached again. To gain a more accurate understanding of the time-dependence of the signals, the couplings between the different sub-systems of the calorimeter have to be studied.

3.4.1. Kapitza Coupling

Phonons hitting a boundary between two materials experience a boundary resistance. The phonons can be transmitted from material 1 into material 2 or can be reflected back into material 1 depending on the given transmission probability.

The energy flux $\dot{Q}_{1 \rightarrow 2}$ due to phonons crossing the absorber-thermometer interface is given by [Prö+95]:

$$\dot{Q}_{1 \rightarrow 2} = \left\langle \frac{E}{V} \right\rangle \left(\frac{1}{2} \right) \langle v_{\perp} \alpha \rangle \quad (3.6)$$

where $\langle E/V \rangle$ is the average thermal energy density in the absorber and v_{\perp} is the group velocity of the phonons normal to the interface. The transmission probability is denoted by α and $\langle \dots \rangle$ accounts for an average over all modes and wave vectors of the phonons.

Equation (3.6) can be used for the calculation of both the energy transmission for thermal and non-thermal phonons. Only the thermal energy density $\langle E/V \rangle$ has to be replaced by the energy density of the non-thermal phonons. The value for $\langle v_{\perp} \alpha \rangle$ calculated for the thermal population can also be used for the non-thermal phonons as, due to isotope or surface scattering, their wave vectors' distribution is the same.

The Kapitza conductance G_K for thermal phonons between two materials can be calculated: the evaluation of the energy flux has to be carried out in both directions, from material 1 into material 2 and vice versa. The Kapitza conductance G_K for the absorber-thermometer interface thus is given by [Prö+95]:

$$G_K = \frac{\dot{Q}_{1 \rightarrow 2}(T + \Delta T) - \dot{Q}_{2 \rightarrow 1}(T)}{\Delta T} = \frac{C}{2V} \langle v_{\perp} \alpha \rangle \propto T^3 \quad (3.7)$$

where C/V is the heat capacity per unit volume of the absorber. The T^3 dependence of the coupling comes from the T^3 term in the phonon heat capacity of the absorber. The heat capacity of phonons in the thermometer is very small and can be neglected.

Equation 3.7 describes the energy flux via one single interface. In CRESST this applies for detectors where the TES is directly evaporated onto the surface of the crystal.

More sophisticated detectors are fabricated as composite detectors [Kie07], wherein the TES is deposited onto a small crystal ((10 x 20 x 1) mm³) made out of CaWO₄. This so-called carrier is glued onto the absorber using a small amount of epoxy resin.

In this case, the Kapitza conductance between the CaWO₄-absorber and TES has to take a plurality of interfaces into account: CaWO₄-absorber → glue layer, glue layer → CaWO₄-carrier and CaWO₄-carrier → W-film. For the evaporated tungsten film and the glue layer the assumption of strong phonon scattering on imperfections and isotopes is valid because of the high concentration of defects. If there is a strong phonon scattering present, the energy distribution of the phonons is according to their density of states and $\langle v_{\perp} \alpha \rangle$ can be used for the transmission probability. The Kapitza resistance for composite detectors is the sum of the Kapitza resistances of the interface absorber-glue, glue-carrier and carrier-thermometer. Note, in the case that no scattering takes place, the transmission probability (absorber - thermometer) has to be calculated for every single phonon taking into account the epoxy layer.

3.4.2. Electron-phonon Coupling

For a complete understanding of the signal formation, the coupling of the phonons to the electrons of the thermometer G_{ep} has to be taken into account.

The electron-phonon coupling is dominated by the frequency dependence of the mean free path of the phonons l_p . Pippard found that l_p can be described by the product $l_e p$, where l_e is the mean free path of the electrons and p is the phonon wave vector.

The mean free path of the electrons is dominated by scattering on crystal defects and impurities and therefore is temperature independent. The temperature dependence of the mean free path of the phonons is set by their wave vector p .

limiting cases	longitudinal phonons	transversal phonons
thermal:		
$pl_e \ll 1$	$\frac{1}{l_L} = \frac{4}{15} C \frac{v^2 l_e}{v_L^3}$	$\frac{1}{l_T} = \frac{1}{5} C \frac{v^2 l_e}{v_T^3}$
non-thermal:		
$pl_e \gg 1$	$\frac{1}{l_L} = \frac{\pi}{6} C \frac{v}{v_L^2}$	$\frac{1}{l_T} = C \frac{1}{v_T^2 l_e}$

Table 3.1. – Formulations for the mean free path for longitudinal and transversal phonons for the thermal and the non-thermal case according to Pippards' model [Pip55].

Table 3.1 summarizes the mean free path formulations for longitudinal and transversal phonons according to Pippards' model [Pip55] where v_L and v_T are the speed of sound for the longitudinal and transverse modes, v is the phonon frequency, C denotes a material constant and p is the phonon wave vector. Two limiting cases are important and should be discussed:

Thermal Phonons At low enough temperatures the limit $pl_e \ll 1$ applies. The coupling in this case is dominated by the transversal phonons as the speed of sound for transversal phonons is generally smaller than that of longitudinal phonons [Har79].

The temperature-dependence of the electron-phonon scattering times and thus their coupling in a clean three-dimensional system is $\propto T^3$ [DiT+92]. An ideal system which does not show impurities or defects is in this case, referred to as a *clean system*. For a typical metal thin film such as, for example, the TES a disordered system has to be considered instead. For a simple metal with a spherical Fermi surface the electron-phonon coupling behaves like $G_{ep} = (T^4/\Theta_D^2) \cdot B(T)$ where Θ_D is the Debye temperature and $B(T)$ introduces the effect of disorder [LG91; DiT+92]. Disorder in this case accounts for the effect of lattice defects, impurity atoms and boundaries in thin metal films on the electron-phonon scattering rates. At low temperatures $B(T) \propto T$ resulting in $G_{ep} \propto T^5$. This T^5 dependence leads to a thermal decoupling of the electron system in the thermometer from the phonons system in the thermometer and thus the absorber.

Non-thermal Phonons For high phonon frequencies $pl_e \gg 1$ applies. Dominantly longitudinal phonons interact with electrons as their mean free path for inelastic scattering (absorption) is $l_L \propto v^{-1}$. Thus, longitudinal non-thermal phonons are absorbed very efficiently in the metal film and in this way transfer energy to the electron system of the thermometer.

Due to the afore mentioned decoupling of thermal phonons ($G \propto T^5$), the electron system of the thermometer film can heat up substantially relative to the absorber. Hence,

the sensitivity of the detector is rather limited by the heat capacity of the metal film of the thermometer than by the heat capacity of the absorber. The major influence of the absorber on the sensitivity of the detector is related to its phonon transport properties, for example by the velocity of sound in the absorber.

3.4.3. Thermal Coupling to the Heat Bath

The thermal coupling of the thermometer to the heat bath is defined by a gold wire bond or a thin film gold structure. The relaxation time is given by $\tau = C/G$ where C denotes the heat capacity and G the heat conductance. G can be calculated from the Wiedemann-Franz law

$$G = \frac{LT}{R} \quad (3.8)$$

where L is the Lorenz number ($L=24.5 \text{ nW}\Omega/\text{K}^2$) and R the residual electrical resistance at low temperatures T .

3.5. Signal Formation Model for Cryogenic Calorimeters

All effects explained so far are the basis to develop a signal formation model for cryogenic calorimeters used in CRESST. A schematic picture of the model that will be discussed in this section can be seen in figure 3.3. A detailed and quantitative description is given in [Prö+95]. Here we will restrict ourselves to the basic concept and understanding of this model.

The detector can be considered to consist of three different subsystems: the electrons and phonons in the thermometer and the phonons in the absorber. All systems are thermally weakly coupled to each other. Each of the subsystems can be characterized by its temperature T and its heat capacity C .

The phonon system of the absorber and the phonon system of the thermometer are thermally coupled via the Kapitza coupling G_K . In the thermometer, the coupling between the phonons and electrons is described by the electron-phonon coupling G_{ep} . The calorimeter is coupled to the heat bath via a thermal link G_{eb} on the thermometer and via the copper structure of the detector holder introducing a parasitic thermal conductance G_{ab} . A simplification can be introduced by combining G_K and G_{ep} to:

$$G_{ea} = \left(\frac{1}{G_{ep}} + \frac{1}{G_K} \right)^{-1} \quad (3.9)$$

representing the coupling between the phonon system of the absorber and the electron system of the thermometer.

After an interaction in the absorber, part of the high frequency phonons will thermalize in the absorber. In our model this is described by a power input $P_a(t)$ into the

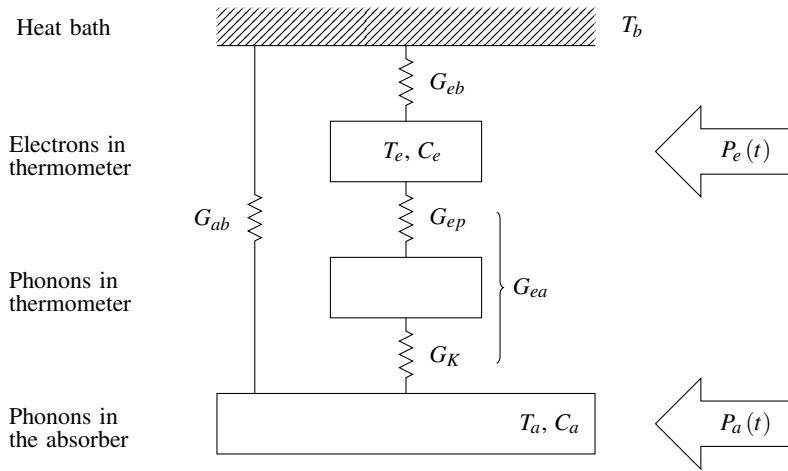


Figure 3.3. – Scheme of a thermal model for cryogenic calorimeters. T_e and T_a are the temperatures of the electron system in the thermometer and the phonon system in the absorber. T_b is the temperature of the heat bath. C_e and C_a represent the heat capacities of the electrons in the thermometer and the absorber. P_e and P_a are the energy flows from the non-thermal phonons and thermal phonons into them. G_{eb} , G_{ea} and G_{ab} are the couplings of the different subsystems.

thermal phonon system of the absorber. The non-thermal phonons which enter the thermometer and get absorbed efficiently by its electron system are modeled by another time-dependent power input $P_e(t)$. $P_e(t)$ and $P_a(t)$ decay exponentially and are given by:

$$P_e(t) = P_0 e^{-\frac{t}{\tau_n}}, \quad P_a(t) = \frac{1-\varepsilon}{\varepsilon} P_0 e^{-\frac{t}{\tau_n}}, \quad P_0 = \frac{\varepsilon \Delta E}{\tau_n} \quad (3.10)$$

where P_0 is the initial power input into the thermometer and ΔE is the energy deposited by an interacting particle in form of non-thermal phonons in the absorber during the time τ_n . ε represents the fraction of high frequency phonons that thermalize in the thermometer and $(1-\varepsilon)$ expresses the fraction of phonons thermalized in the absorber.

The overall time constant of the thermalization process results from the thermalization of phonons in the absorber τ_a and in the thermometer τ_e . Hence, the life time of the non-thermal phonon population τ_n is given by:

$$\tau_n = \left(\frac{1}{\tau_e} + \frac{1}{\tau_a} \right)^{-1}. \quad (3.11)$$

The time constant τ_a is governed by inelastic processes mainly happening at the surface of the absorber and is therefore proportional to the ratio of volume and surface area of

the absorber ($\tau_a \propto V_a/O_a$). The time constant for the thermalization in the thermometer is given by:

$$\tau_e = \frac{2V_a}{\bar{\eta}A\langle v_{\perp}\alpha \rangle} \propto \frac{V_a}{A} \quad (3.12)$$

with $\bar{\eta}$ expressing the probability for an absorption of the high frequency phonons in the thermometer, with α being the probability of transmission from the absorber to the thermometer and v_{\perp} the phonon group velocity normal to the surface. τ_e depends linearly on the volume of the absorber V_a and is indirect proportional to the area of the absorber-thermometer interface A .

In the case of a composite detector, the dependence on V_a allows to identify different classes of events by pulse-shape analysis [Kie07].

Using the time constants τ_e and τ_a we can define the fraction ε of phonons that finally thermalize in the thermometer as:

$$\frac{\tau_e}{\tau_a} = \frac{\varepsilon}{1 - \varepsilon} \quad \Rightarrow \quad \varepsilon = \frac{\tau_a}{\tau_e + \tau_a}. \quad (3.13)$$

The power input $P_a(t)$ and $P_e(t)$ can be formulated as two coupled differential equations for the temperature of the electrons in the thermometer T_e and the temperature of the phonons present in the absorber T_a . The heat capacity of the absorber and the thermometer are denoted as C_a and C_e respectively; T_b is the temperature of the heat bath.

$$C_e \frac{dT_e}{dt} + (T_e - T_a)G_{ea} + (T_e - T_b)G_{eb} = P_e(t) \quad (3.14)$$

$$C_a \frac{dT_a}{dt} + (T_a - T_e)G_{ea} + (T_a - T_b)G_{ab} = P_a(t) \quad (3.15)$$

The measured thermometer signal is defined as

$$\Delta T_e(t) \equiv T_e(t) - T_b. \quad (3.16)$$

Given the initial conditions

$$T_a(t=0) = T_e(t=0) = T_b \quad (3.17)$$

the equations have the following solution [Prö+95] for a thermometer signal $\Delta T_e(t)$

$$\Delta T_e(t) = \Theta(t) \left[A_n \left(e^{-t/\tau_n} - e^{-t/\tau_m} \right) + A_t \left(e^{-t/\tau_e} - e^{-t/\tau_n} \right) \right]. \quad (3.18)$$

Equation (3.18) describes a superposition of two exponential pulses. The first component is referred to as the non-thermal component as it describes the direct absorption of non-thermal phonons in the thermometer. Phonons that thermalize in the absorber are described by the second component. The amplitudes of the two components are denoted with A_n and A_t for the non-thermal and the thermal component, respectively.

After a particle interaction we assume an instantaneous and homogeneous distribution of non-thermal phonons in the absorber. In equation (3.18) this phonon distribution is expressed by the step function $\Theta(t)$.

The three different time constants present in equation (3.18) are

- τ_n : the effective time constant for the thermalization of non-thermal phonons (life time of non-thermal phonons),
- τ_t : the thermal relaxation time constant of the absorber temperature (influenced by the heat capacity of the absorber),
- τ_{in} : the intrinsic thermal relaxation time constant of the thermometer (influenced by the coupling to the heat bath),

whereas τ_{in} and τ_t are given by

$$\tau_{in} \approx \frac{C_e}{G_{ea} + G_{eb}}, \quad \tau_t \approx \frac{C_a}{G_{eb}G_{ea}/(G_{eb} + G_{ea}) + G_{ab}}. \quad (3.19)$$

At low temperatures the thermal component is strongly suppressed due to the weak thermal coupling between the electrons and the phonons in the thermometer and the dominant signal component is the non-thermal one.

The time constant τ_{in} can be influenced by changing the thermal coupling G_{eb} of the thermometer. Depending on the ratio of τ_{in} to τ_n , the detector can be operated in two different ways:

Calorimetric Mode In the case $\tau_n \ll \tau_{in}$ the detector integrates the power input $P_e(t)$ and the amplitude of the non-thermal component A_n corresponds to the total energy absorbed in the thermometer ($A_n \approx -\epsilon\Delta E/C_e$). In this calorimetric mode τ_n describes the rise time of both signal components whereas τ_{in} denotes the decay time of the non-thermal component and τ_t is the decay time of the thermal component.

Bolometric Mode For $\tau_n \gg \tau_{in}$ the flux of the non-thermal phonons is measured. The amplitude of the non-thermal component A_n is given by the power input and essentially the total thermal coupling of the thermometer ($A_n \approx P_0/(G_{ea} + G_{eb})$). In this case τ_n is the decay time of the non-thermal component and the rise time of the thermal component, τ_{in} is the rise time of the non-thermal component and τ_t determines the decay time of the thermal component.

Figure 4.6 shows an averaged pulse from a crystal operated in the bolometric mode and fitted with two exponential components modeling the non-thermal and the thermal contribution of the event.

4. Detector Operation and Data Analysis

In the previous chapter, the physical processes that are responsible for the temperature change in the thermometer after a particle event and thus a change of the resistance of the metal film have been explained. Section 4.1 focuses on the readout of these resistance changes. In section 4.2, an overview is given on all the electronic components necessary for detector operation and data acquisition.

For each detected pulse several parameters are extracted. In particular, the pulse height of each pulse is determined using a template fit which is finally converted to the deposited energy in the calibration procedure. All these aspects are related to data analysis and summarized in section 4.3. Section 4.4 gives an overview of the cuts applied to the data to remove classes of invalid pulses. The cuts are selected regarding the relevance of the analyses done within this work and not in sense of a general dark matter analysis.

4.1. SQUID-based Readout

The resistance changes of the thermometer film are so small that a conventional way of measuring a resistance signal by simply detecting the voltage drop across the metal film is not feasible with a conventional amplifier. Instead, a very precise tool for measuring small current variations, a SQUID (Superconducting Quantum Interference Device) is used. The basic scheme of the readout circuit is shown in figure 4.1. The circuit is laid-out as a parallel circuit biased with a constant current I_B ($\mathcal{O}(\mu A)$). In the branch parallel to the thermometer film R_T there is a superconducting coil (input coil) as well as two identical shunt resistances each with half the value of R_S . The current through the input coil is

$$I_{Sq} = \frac{I_B R_T(T)}{R_T(T) + R_S}. \quad (4.1)$$

A change of the resistance of the thermometer ΔR_T leads to a change of the branching ratio of the current. For $\Delta R_T \ll R_T$ the change of the current in the input-coil branch

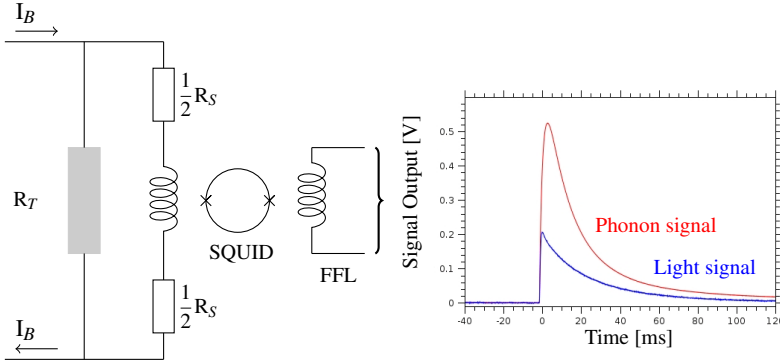


Figure 4.1. – Readout scheme used to convert the change of the resistance of the TES to a voltage signal as shown on the left hand side of this picture. Each light- and phonon channel has its own SQUID-based readout circuit.

can be expressed as:

$$\begin{aligned}
 \Delta I_{sq} &= \frac{dI_{sq}}{dR_T} \Delta R_T \\
 &= \frac{I_B R_S}{(R_T + R_S)^2} \Delta R_T \\
 &= \frac{I_B R_S}{(R_T + R_S)^2} \frac{dR_T}{dT} \Delta T \propto \Delta T.
 \end{aligned} \tag{4.2}$$

For small ΔR_T the change of the current ΔI_{sq} is thus proportional to the temperature change of the thermometer.

The input coil converts current to magnetic flux which is then measured by the SQUID. In order to obtain a linear response a FLL-setup (Flux-Locked-Loop) is used to keep the flux through the SQUID coil always constant. The feedback reacts on any change in flux seen by the SQUID coil and transforms this variation in a voltage signal at the output of the SQUID FLL - the final recorded voltage pulse (see figure 4.1).

4.2. Data Acquisition

A simplified block diagram of the electronics set-up is shown in figure 4.2. Different colors are chosen for the three main chains: in blue the *signal readout chain* and in red the *heater chain* needed for detector stabilization and control. The detector *bias supply chain* is colored in black.

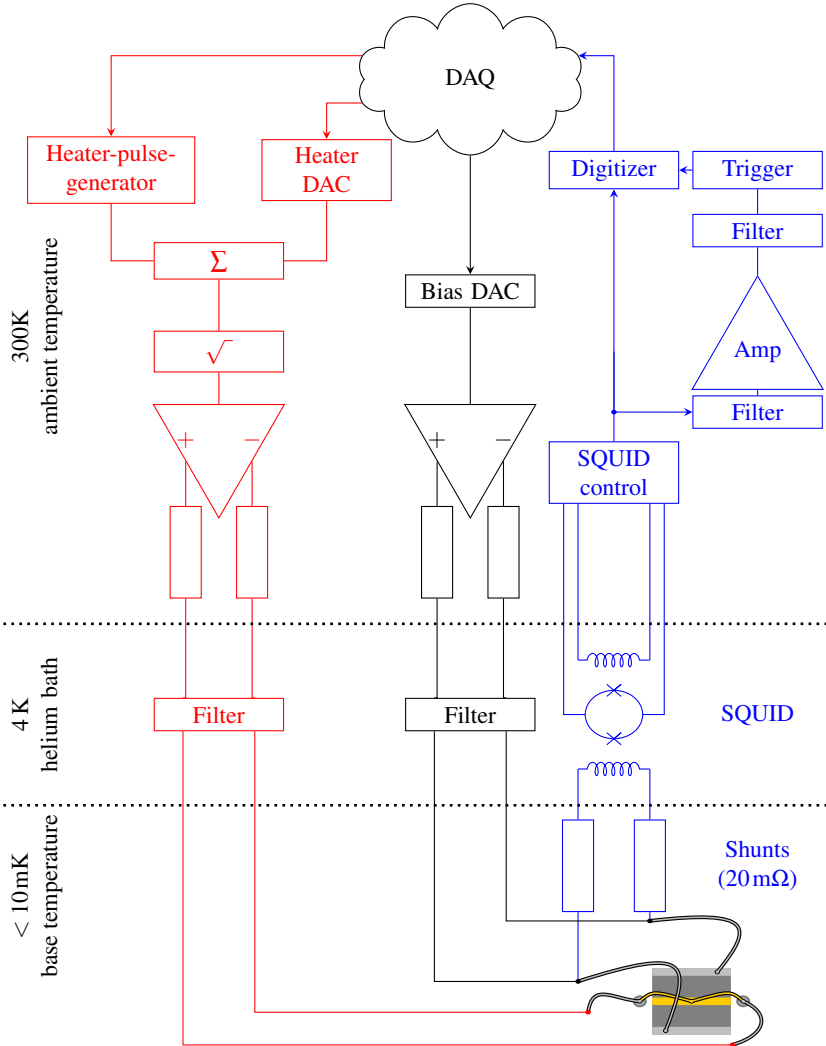


Figure 4.2. – Simplified diagram of essential components of the DAQ system. The readout circuit containing the SQUID and the trigger electronics is shown in blue. The detector bias is shown in black; the heater system for detector stabilization and the test pulse generator is plotted in red. The thermometer exhibits the design used to read out the target crystals. Taken from [Kie12].

4.2.1. Bias Supply Chain

The bias current for the readout of the detectors is provided by floating current sources mounted at room temperature. The detectors are operated close to the base temperature of the cryostat, whereas the SQUIDs are located in the liquid helium bath of the cryostat at 4.2 K. In the leads running from the current sources down to the detectors low pass filters (cutoff at 10 kHz) are inserted to reduce high frequency interferences.

4.2.2. Signal Readout Chain

The voltage output signals from the FLL-unit are split into two parallel branches. In one branch the signals are continuously digitized using a 16 bit transient digitizer, which is sampling every 40 μ s. In the other branch, the signals are first filtered and amplified before they are AC-coupled to a trigger module. The trigger is activated when the signal exceeds a pre-defined value which then stops digitization of the signal after a certain number of post trigger samples has been recorded. In Run 32, each record consisted of 8192 samplings (total record length: 328 ms). The first quarter of such a record (2048 samplings) is called the pre-trigger region as the samples have been buffered before the actual trigger signal arrived. The pre-trigger region is used to evaluate the baseline of each record whereas the remaining three-quarters contain the actual signal pulse.

It does not matter which channel from a detector module did activate the trigger as always its partner is also read out. In this way a record always contains both the phonon signal and the coincident light signal.

4.2.3. Heater Chain

Each thermometer film is equipped with a heater structure which, in the case of an absorber crystal, is realized in form of a stitch bond. The stitch bond is made onto the thin gold structure (thermal coupling) of the TES using a gold wire with a diameter of 25 μ m (see figure 4.2).

The heater serves two different purposes utilizing a superposition of two different voltage signals. Firstly, to stabilize the thermometer (TES) in its operating point within the superconducting transition, a *quasi-constant current* is used. This almost constant heating current is regulated by a computer controlled DAC which outputs a variable voltage that is proportional to the desired heating current.

Secondly, pulse-shaped signals called *heater pulses* are injected in certain time intervals. They are necessary in order to extend the energy calibration over a wide energy range including, in particular, the WIMP search region. The heater pulses are generated with a wave form generator. A pulser attenuator allows to adjust the pulse height individually for each detector. The sum of both parts, the constant heating current and the pulses, are sent through an analogue square-rooter. Finally, a set of resistors defines the total heating current before being sent through the respective detector heater.

Control Pulses for the Stabilization of the Thermometer The requirements on the quality of the stabilization mechanism of the thermometer depend on the temperature range of detector operation. Particle interactions in a CRESST detector module typically lead to temperature variations in $\mathcal{O}(\mu\text{K})$. Therefore, the control mechanism has to provide a precision that is stable on this level.

For stabilization, high-current heater pulses (*control pulses*) are sent at intervals of six seconds in order to drive the TES completely out of its superconducting transition. In this way, the final voltage signal from the SQUID of a control pulse reflects the distance between the operating point and the top of the transition curve. This gives the possibility to control the position of the operating point by adjusting the power applied to the heater to keep the output voltage from the control pulses constant.

Test Pulses for the Energy Calibration Along with the control pulses, so-called *test pulses* are sent to the detector. A sequence of up to twelve pulses of different amplitudes is fired with a waiting time of 30 seconds between pulses. These heater pulses are used to extend the energy calibration down to low energies where no external gamma sources can be applied.¹ They also allow us to check the detector response over time and correct for possible variations. Last but not least the smallest test pulses are used to test the trigger efficiency in the low energy part. Section 4.3.3 describes the procedure used to calibrate the detectors in a range from 5 keV to 2000 keV .

4.3. Data Preparation

Some basic parameters are assigned to each detected pulse already by the DAQ, other main parameters are calculated offline. A list of these pulse parameters is given in section 4.3.1. The pulse height of each detected pulse is determined by a template fit. Finally, an energy corresponding to the respective deposited energy in the detectors has to be assigned. The corresponding calibration procedure is explained in section 4.3.3.

4.3.1. Pulse Parameters

A typical phonon and light signal from a CRESST detector module can be seen in figure 4.3. From such raw pulses and some parameters recorded by the DAQ, a collection of different parameters is calculated during data processing.

time since start The time difference between the start of the data file and the trigger signal of the event. In the case of analyzing a set of subsequent data files the start refers to the starting time of the first data file.

¹CRESST aims to detect WIMPs by recoil energies $\mathcal{O}(10\text{keV})$ and hence requires a calibration procedure in this energy range. The cold box enclosing the detectors is made out of 12 mm thick copper, a barrier which cannot be penetrated by X-rays from an external calibration source. Test pulses are used instead.

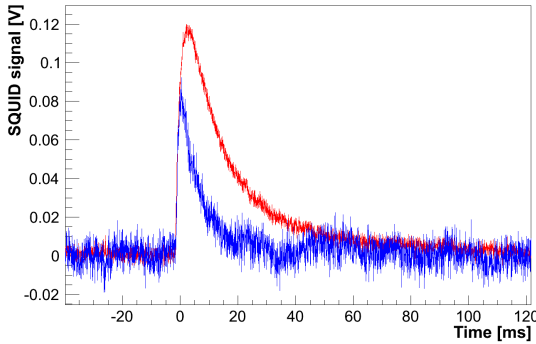


Figure 4.3. – Coincident pulse as recorded with a CRESST detector. The phonon and light signals are colored in red and blue respectively. This event deposited about 30 keV in the crystal.

amplitude of test pulse The parameter that indicates for each test pulse the amplitude in volts injected to generate this pulse.

onset delay in event This parameter describes the time difference between the first trigger and the subsequent triggers in the same event for all participating detectors.

base line The average level of the SQUID output voltage signal without the presence of a pulse is called base line. A tilted line is fitted in the pre-trigger region to determine the base line and a possible tilt due to pile up. All pulses are shown with a base line of 0. This means that when calculating the pulse height of an event the base line is subtracted.

RMS in base line The root-mean-square deviation of the sampled pulse from the fitted base line.

pulse height A first simple evaluation of the maximum voltage level of the pulse after filtering with a 50-sample moving average.

onset-channel The first sample with a value that reaches 10% of the pulse height.

rise time In this program defined as the time between the onset of a pulse and a signal level of 50% of the pulse height parameter.

decay time The time between the onset of a pulse and the sample when the pulse has decayed to $1/e$ of the maximum pulse height.

peak position The total rise time of the pulse from the onset to the pulse maximum.

right-left baseline The difference between the average level of the last 50 samples and the first 50 samples of a record.

4.3.2. Pulse Height Evaluation

Since the energy of an event is related to its pulse height, the accurate evaluation of the pulse height is of utmost importance.

The pulse height determination by searching the maximum of a filtered pulse has a tendency to pick upward going noise fluctuations leading to an overestimation of the actual pulse height. If one prefers that a pulse height of 0 V corresponds to zero energy another method has to be chosen.

Another important attribute is the shape of the pulse. It probes the position of the operating point within the transition. Close to the operating point the transition curve is expected to behave linear, meaning that $\Delta R \propto \Delta T$ and hence small pulses within this linear region of the transition reveal an unaltered pulse shape. When going to higher energies, the response of the thermometer may start to be non-linear and as a consequence, the shape of the pulses changes. Therefore, the pulse height determination by the moving average in the non-linear range of the transition is not meaningful.

A simple *template fit* in the time domain permits us to take into account the non-linearity effect of the transition curve and allows an unbiased measure of the pulse height of an event. The algorithm that combines all these pre-conditions is the *template fit*, also known as *standard event fit*. In the following, the term pulse height will be only attributed to the parameter determined with the moving average procedure. The term *amplitude* will be used instead for the pulse height as determined by the template fit.

Template Fit

The idea behind the template fit is to create an appropriate *template pulse*, scale and shift in time for this template to best fit the data. The template pulse is averaged from a set of $\mathcal{O}(100)$ pulses out of a narrow pulse-height distribution at low energies. The pulses to build the template have to be still in the linear-response-region of the detector. Commonly, a set of 122 keV γ -pulses (^{57}Co -calibration) is used. A template pulse represents a pulse with reduced noise level due to averaging and is created separately for both the particle pulses and the heater pulses injected for calibration reasons.

Three free parameters can be varied during the fit: the baseline offset, the shift of the onset of the pulse and the amplitude of the pulse that is scaled in order to best fit the data. From deviations between fitted pulses and real data pulses, RMS values are

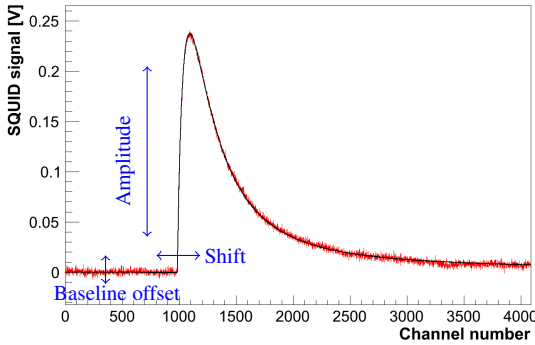


Figure 4.4. – Real data of a particle pulses (about 30keV) together with the result from a template fit (black line). The three parameters that can be varied to best match template and data pulse are indicated in form of blue colored arrows.

calculated for each pulse. The RMS value is a measure of the deviation between fit and data and it is minimized in order to find the best fit.

Truncated Template Fit

The determination of the amplitude of pulses by the template fit only works reliably within the linear regime of the transition. As higher energetic particles drive the thermometer into its non-linear range they suffer a change in pulse-shape. An indication of non-linearity is the pronounced increase in the RMS of the fit starting at a certain pulse height (typically around 200 keV, see left plot in figure 4.5). The change of the pulse shape is responsible for the dramatic decrease of the fit quality.

The region of interest for WIMP search is below 40 keV, hence non-linearities at energies above $\mathcal{O}(100 \text{ keV})$ are not relevant. Nonetheless, for characterizing background sources and the general performance of detectors, it is also advantageous to reconstruct higher energy pulses. This can be obtained by using a *truncated fit*: only the linear part of the high-energy pulse will be considered and fitted with the low-energy template pulse. The limit, from where the pulse is not considered anymore but its shape is extrapolated using the template pulse we refer to as *truncation limit* (see figure 4.5). This method works well as long as a sufficient number of samplings remain in the linear region. With the truncated fit energies up to some MeV can be reconstructed reliably.²

²This only applies for detectors with a transition curve which does not show abnormal structures as e.g. steps or discontinuities.

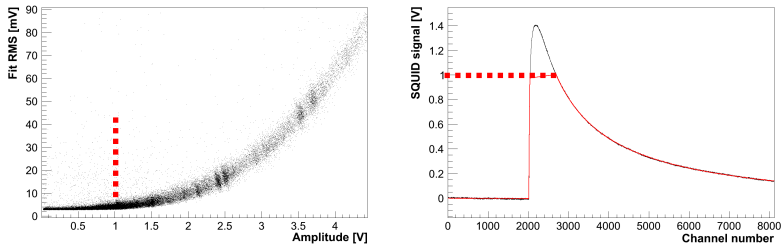


Figure 4.5. – Pulses exceeding the linear range of the transition suffer a change in pulse shape and cannot be fitted with the low-energy-template. An indication of the decrease of the fit quality is the prominent increase in the Fit RMS (left plot). Using a truncated template fit allows to reconstruct high energetic pulses as only the linear part of the pulse is considered for fitting. In the right plot such a truncated template is shown (red solid line). The limit where the extrapolation of the pulse starts is referred to as truncation limit (in this plot ≈ 1 V).

Correlated Template Fit

The CRESST detectors measure two signals simultaneously - the energy deposited in the crystals and the simultaneous emission of scintillation light. In comparison to the light signals the phonon signals are quite robust and clean. The light signals are smaller in amplitude and more noisy and therefore their fit is less reliable. The situation can be improved by performing a *correlated fit*. The template pulses for the correlated fit are produced out of the same set of pulses for both the light and phonon channel. Thus, the relative timing of the light/phonon signal is identical to common coincident pulses and trigger walk effects are suppressed.³ The correlated fit increases the quality of the amplitude determination as it enables us to determine the onset of even very small light pulses due to the known relative timing of phonon and light signals. The best fit is found by minimizing the sum of the RMS values of both signals.

Fit with Two Exponentials

Besides the template fit another procedure can be used to determine the exact amplitude of the signals. It fits two exponential components (see equation 3.18) independently to each pulse. As with the template fit, high-energy pulses are fitted respecting the truncation limit. The fit algorithm needs a lot more computing time, is less stable and thus is mainly used to determine additional pulse parameters, in particular the thermal decay time of template pulses.

³Trigger walk describes the dependence of the trigger time on the pulse height. Trigger walk would render the advantages of having a fixed relative timing useless.

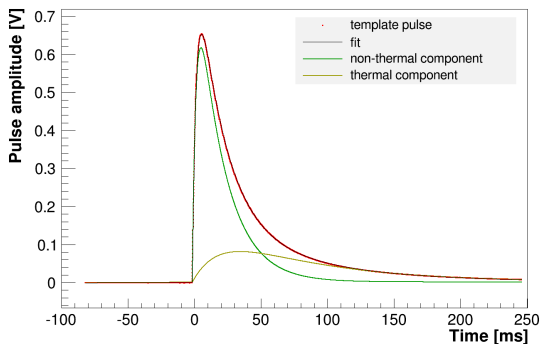


Figure 4.6. – Template pulse of the phonon detector Rita fitted with two exponential components. The non-thermal and the thermal contribution are indicated. The sum of both results in the fit to the pulse (black solid line).

Figure 4.6 shows the result of such a fit to the template pulse of the phonon detector Rita. The non-thermal and the thermal component are indicated as well as the sum of both (black line).

4.3.3. Energy Calibration

In order to obtain the absolute energy of the events a calibration with an external radiation source is required.⁴ Furthermore, the energy calibration has to be extended down to the low energy range of the detectors. This is done with the help of heater pulses, as explained previously. The calibration procedure is described in the following text.

Cobalt Calibration

The source used for calibration is an external ^{57}Co γ -source that is only applied during calibration. ^{57}Co shows two prominent lines at 122.1 keV and at 136.5 keV. As mentioned before, a lower-energetic source cannot be used as the barrier of 12 mm of solid copper from thermal shielding has to be penetrated. In figure 4.7 the energy spectra from a CRESST detector module is depicted, including the spectrum of the phonon channel (red-color) and the light channel (blue-color), respectively. The response of the detectors to the 122.1 keV gammas is used to fix the energy scale.

⁴In the case of a crystal showing a high intrinsic radioactive contamination with e.g. ^{210}Pb , also an intrinsic γ -line can be used for calibration.

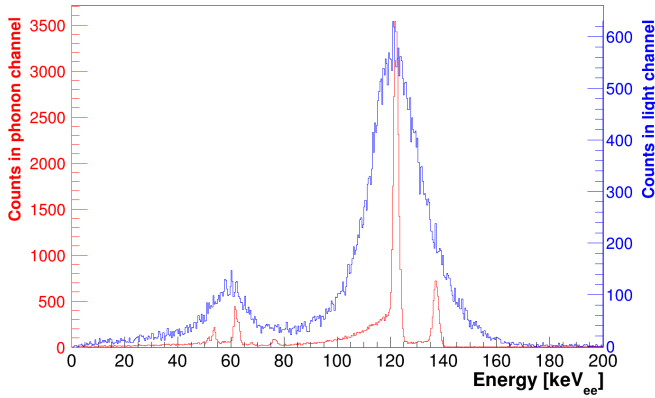


Figure 4.7. – Energy spectra of a CRESST detector module during a calibration with an external ^{57}Co γ -source. The energy is converted in keV_{ee} (electron-equivalent). This means that in the case of the light channel, an equivalent energy of 122.1 keV_{ee} is assigned to the peak in the energy spectrum (blue color) due to the scintillation light detected while irradiating the target crystal with ^{57}Co . The phonon detector nicely separates the two distinct lines from the ^{57}Co -source whereas the relative resolution of the light detector is not sufficient to resolve the line spectrum.

Phonon Detector The 122.1 keV gammas when being absorbed in the crystal lead to a discrete line. An energy of 122.1 keV is assigned to the fitted peak-value and provides an absolute point of the detector response function. The small energy fraction which is emitted in the form of scintillation light is not taken into account for the phonon detector. Note, the energy deposit of a neutron in the crystal is, due to the even smaller fraction of emitted scintillation light, slightly off-scale. However, this effect is neglected in the following analyses.

The energy scale of the phonon detector gives the total energy deposited from an interaction in the absorber and is quasi independent of the particle type.

Light Detector The 122 keV_{ee} peak in the light detector corresponds to the amount of scintillation light produced by the absorption of a 122 keV gamma in the target crystal. This means an equivalent energy is assigned to the peak in the spectrum. Furthermore, the type of particle used for calibrating is essential as the amount of produced scintillation light strongly depends on this. In the case of calibrating with gammas the subscript ee (electron-equivalent) is added to the energy scale to visualize that the scale is only valid for electron recoils. For other particle types the respective quenching factors have to be considered (see section 2.4.3). Note, the intrinsic energy resolution of the light detector is better than the energy resolution of the phonon detector.

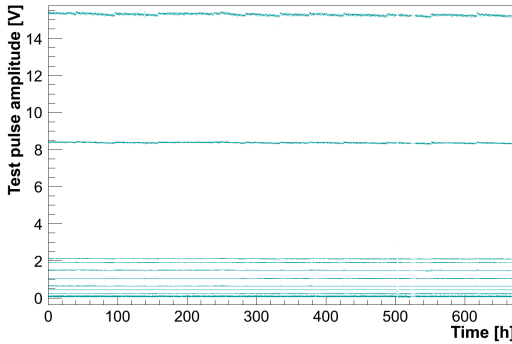


Figure 4.8. – A set of test pulses of different amplitudes are injected via the heater structure into the detector. The measured values of test pulse amplitudes are plotted versus time.

Calibration with Heater Pulses

The cobalt calibration probes the detector response at one certain energy (122 keV) and is a reference only for the actual time of the calibration run. To ensure stable and reliable conditions during the whole data taking phase a procedure is needed that allows to extend the calibration down to lower/higher energies. Furthermore, time-dependent changes of the detector response should be also detectable.

These requirements can be met additionally by using a heater calibration. The heater pulses (test pulses) are injected into the thermometer in regular intervals of 30 s via a dedicated heater structure. Instead of one single amplitude a sequence of up to twelve test pulses with different amplitudes are sent to the heater structure. As for particle pulses, a correlated and truncated template fit is carried out to determine the exact pulse amplitude.

In order to obtain a linear dependence of the injected voltage signal and the reconstructed pulse amplitude, the heater pulses are sent through a square rooter before arriving at the heaters of the detectors. The square rooter is necessary to decouple the quasi-constant current from the injected heater pulses because the energy of a heater pulse should not change if the constant heating varies over time due to stabilization issues. However, without a square-rooter the heating power is proportional to the square of the current and thus to the square of the sum of the input signals. By using a square-rooter the relation between the constant heating current and the heater pulses is linearized, namely simple the sum of both signals. There are now two different aspects to be commented on in more detail:

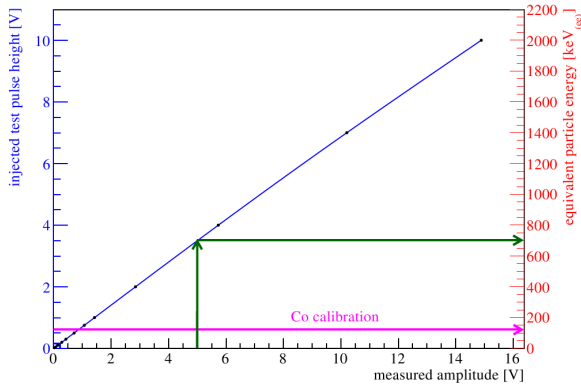


Figure 4.9. – As black points, the amplitude of injected test pulses is plotted vs. the measured amplitude. A low-order polynomial is fitted to the points to acquire a continuous response function (blue line). To convert the test pulse height into an equivalent energy (right scale), the cobalt calibration (pink arrow) is used. The evaluation of the transfer function allows one to assign to any measured amplitude the corresponding particle energy at the time of the particle event. The green arrows mark a certain particle-event. The pulse signal has a reconstructed amplitude of 5 V corresponding to an energy deposition in the crystal of 700 keV. Illustration from [Sch10].

Variations in Time The injected test pulses allow us to probe the detector response over the time window of a measurement. Figure 4.8 shows the detector response for such a sequence of test pulses versus time. In between two test pulses of the same amplitude, up to five/six minutes may pass by. In order to know the response of the detector also in between these discrete points, *splines* are fitted to the test pulses of each amplitude.

Continuous Response Function The test pulses by themselves just allow for a probing of the detector response at discrete pulse amplitudes (energies). To obtain a continuous response function of the detector over the whole energy range of interest the discrete points are fitted with a polynomial. In figure 4.9 an example of a response function is illustrated. The rather linear dependence of the measured pulse amplitude on the height of injected heater pulses is clearly visible.

Energy Transfer Function (Heater Calibration) The final step is the absolute energy calibration of the heater. The energy injected by the heater is proportional to the amplitude of the injected voltage pulse. This proportionality constant is determined by the calibration measurement with a ^{57}Co γ -source. Once this proportionality is determined, the energy of each injected heater pulse is known and can be used to establish

a relation between the amplitude of the detector response and the injected energy. The pink arrow in figure 4.9 indicates this relation.

The transfer function is quantified by the CPE-value (Convert Pulse amplitude to Energy):

$$\text{CPE} = \frac{\text{particle energy [keV]}}{\text{injected test pulse amplitude [V]}}. \quad (4.3)$$

4.4. Cuts

For a CRESST dark matter analysis a list of basic quality cuts is applied to ensure the validity of the data. In the following sections, only a subset of these cuts will be explained in more detail. The cuts described below are selected with regard to measurements carried out in the framework of this thesis. A detailed description of the CRESST dark matter analysis can be found in [Lan08; Sch10; Pfi10; Rei11] and [Ang+12].

4.4.1. Stability Cut

The *stability cut* rejects periods where the detectors were not running stably at their operating points. As already discussed, control pulses are sent every few seconds to the detector heater. A PI-controller realized in software keeps the SQUID output signal of these control pulses at a pre-defined value by adjusting the quasi-constant heating current. However, external disturbances (for example vibrations, heavy work in the underground site, maintenance jobs) can drive the detectors out of their operating points. When the control pulse height leaves the region where the detector is considered to be stable, the data between the last stable control pulse and the next stable control pulse are discarded.

4.4.2. Peak Position

A class of events that has to be identified and removed from the data are direct hits of the thermometer film as well as interactions in the small carrier substrate in the case of a composite design for the phonon detector (see section 3.4). Both types of events can be spotted by their exceptional pulse shape. Figure 4.10 (j) gives an example of such kind of events which are characterized by their fast rise and decay times in comparison to interactions in the absorber crystal.

The peak position is the total rise time of the pulse from the onset to the pulse maximum and thus gives a good measure for removing such pulses. The limits for this cut have to be set conservative enough not to remove real absorber hits. Especially in the low energy regime, small pulse amplitudes are approaching the baseline noise level and differences in pulse-shape are becoming less prominent. Furthermore, pulses that do not decay within a record may still show a signal above threshold when the precedent pre-trigger is over. Such pulses reveal a peak-position-value that is well separated

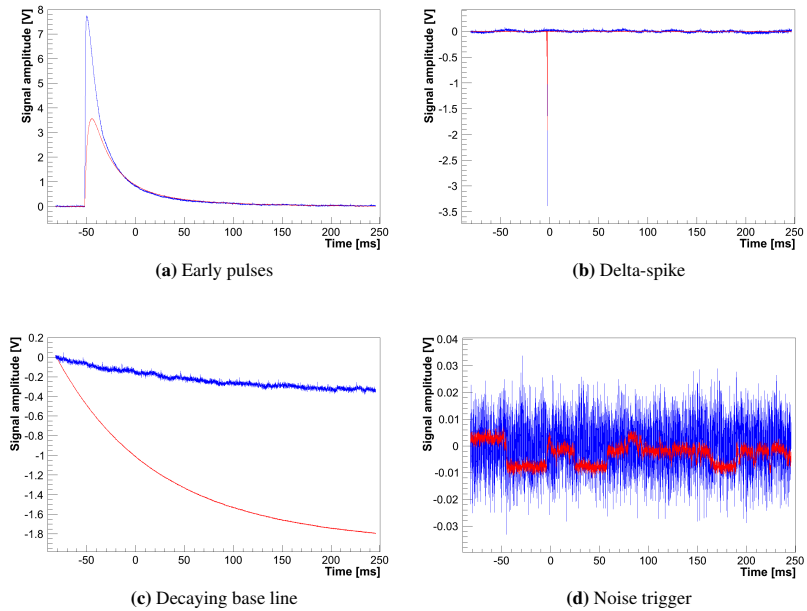


Figure 4.10. – Examples of invalid events that can be removed by a cut on the *peak-position* parameter. Red colored events correspond to phonon signals, blue events are light signals.

from normal pulses. In addition, delta-spikes are artificial signals that have an instantaneous rise and can also be identified and rejected by the peak position parameter (see figure 4.10 (a) and (b)).

A decaying baseline (figure 4.10 (c)) is the result of very large pulses that do not decay within one record length and due to their still high signal levels, reactivate the trigger. They show a "peak" at the very beginning of the record and can be removed by cutting on this parameter. Moreover, in many cases extra noisy baselines as shown in figure 4.10 (d) may also be removed by cutting on the peak position parameter.

4.4.3. Right-left Baseline

The right-left baseline parameter is used to remove for example SQUID resets, flux quantum losses, and pile-up events (see figure 4.10 (e) to (h)). Pile-up events are not considered for analysis since at present the reconstruction of the pulses does not foresee two pulses in the same record. Due to the low event-rates in the main CRESST experiment, pile-up events are quite rare and do not add a relevant dead-time contribution. However, measurements in the test-facility have to cope with a factor of ten higher rate and an increase in the loss in measuring time due to pile-up. Therefore, it is planned to implement the treatment of pile-up events for future analyses.

There is a continuous variation of the right-left baseline parameter as the amplitude of the pulses changes, resulting in a right-left baseline parameter being larger for higher pulse-amplitudes. If only a removal of SQUID resets and flux quantum losses is intended, an energy-independent weak cut on this parameter can be also applied since these invalid pulses show a clear discontinuity from the continuous distribution.

4.4.4. Onset-delay in Event

If particles directly hit the light detector, the phonon detector does not see any signal and therefore these events are referred to as *light-only events* (see figure 4.10 (i)). Light-only events are not of interest for further analysis and can be removed from the data set by cutting on the *onset-delay in event* parameter. In a light-only event the light detector triggers whereas the phonon detector does not trigger at all. In this case the onset-delay for the phonon detector is at its maximum value. These events can easily be removed by neglecting all events around this maximum.

4.4.5. Pulse Amplitude

Since the energy range of interest for most of the measurements carried out on detector optimization is in $\mathcal{O}(100\text{ keV})$, high energy events from for example α -particles (figure 4.10 (g)) or high energetic gammas can be discarded from the data. To do so a cut on the pulse amplitude (typically below $300\text{ keV}_{(ee)}$) is carried out. To remove noise only events as well as tiny pulses that disappear in the baseline noise a lower limit on

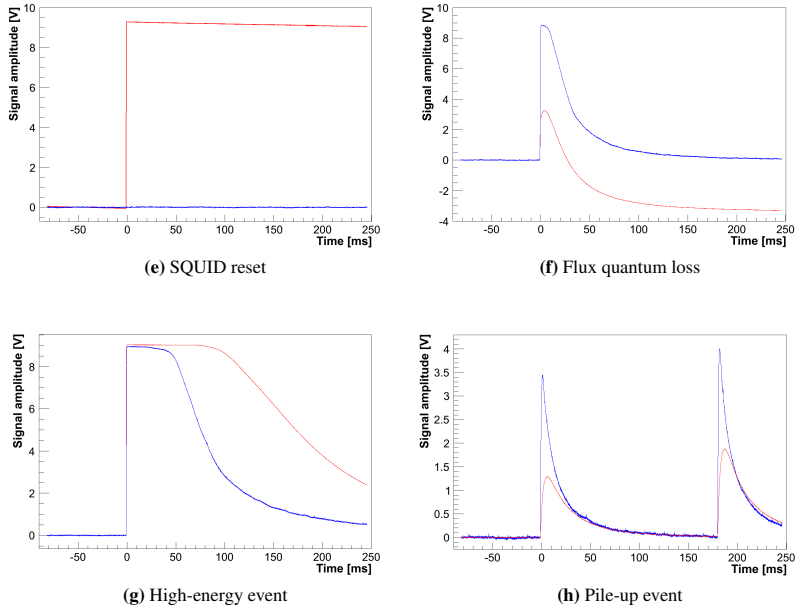


Figure 4.10. – Invalid pulses that can be rejected by cutting on the *right-left baseline* parameter.

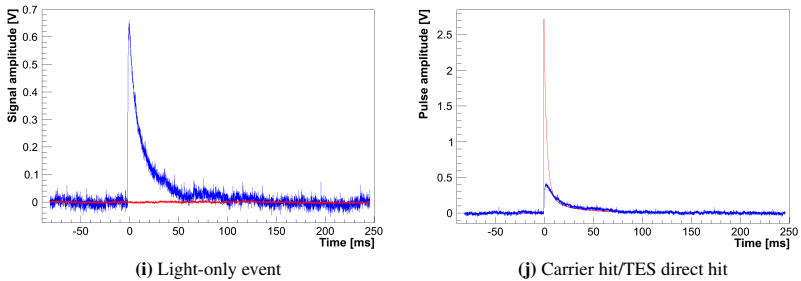


Figure 4.10. – Light only events can be removed by a cut on the *onset-delay in event* parameter. A particle interaction in the carrier (composite detector) or a direct interaction in the thermometer of the crystal lead to very fast pulses which can be rejected by the parameter *peak position*.

the pulse amplitude is set for the phonon detector. For the light detector no lower limit is set as it might remove events which are expected to show very little or no light signal.

4.4.6. RMS of the Template Fit

The cut on the RMS of the template fit is a *general cut* on the pulse-shape of the recorded events. All signals that have a different shape in comparison to the template pulse will be discarded by cutting on this parameter. This includes artificial or noise pulses with a completely different shape as well as also pulses with a strongly tilted baseline or just a higher detector noise (microphonics, electromagnetic interferences).

Typically the limits for the RMS cut are chosen tight for the phonon detectors but quite weak for the light detector to not remove any events expected which show only little or no light within the resolution of the light detector.

5. Detailed Examination of Background

Chapter 5 focuses on a closer study of background events observed in the CRESST data, in particular of Run 32. Section 5.1 comments on the motivation for a profound investigation of the present backgrounds of the experiment, especially in the light of a future CRESST run. Besides e/γ -events and neutrons from the surroundings of the experiment, a significant part of the background is coming from the clamps that hold the target crystals in position. Section 5.2 and section 5.3 give a detailed summary of the observations made in Run 31 and Run 32 while using different clamp-types. The backgrounds introduced by various clamp designs are documented and categorized.

Alpha-particles from the decay of ^{210}Po as well as the corresponding Pb-recoils are making part of the clamp introduced background. It was found that the α -emitter can be located on the surface of the clamp but also can be present in its bulk material. Therefore, section 5.4 is dedicated to study the origin of the α -background coming from the clamp material, whereas section 5.5 discusses the origin of the observed ^{206}Pb -recoil background.

Furthermore, relaxation events are found whenever a plastic-interface is used between the clamp and the crystal. Section 5.6 summarizes this class of background events. Surface sputtering effects may be caused by heavy energetic recoiling nuclei as for example produced by the decay of ^{210}Po . Such secondary backgrounds are the topic of section 5.7.

5.1. Motivation

In Run 32, after about two years of data taking, a net exposure of 730 kg-days was collected. An excess of events has been observed which cannot be explained by known background as accounted for in a likelihood analysis. These "extra" events allow for an interpretation as positive WIMP signals. Corresponding WIMP parameters have been derived (see section 2.7) and are listed in table 2.2.

However, the arguments for a positive WIMP signal are not solid enough since the uncertainties of the model used for describing the background are still very large (see table 2.2). The high background present within and around the acceptance region is responsible for these large uncertainties. In the acceptance region the contribution from considered backgrounds and the contribution from a possible WIMP signal are at the same level. This illustrates that a clear understanding of the data requires a reduction of the present background. In order to reduce the present background its origin has to be investigated.

The study of background sources observed in the Run 32 data while using bare metal clamps was a main topic of this thesis. In addition, measures to avoid or eliminate them have been developed for a future CRESST run. Observations made in Run 31 data while utilizing different clamp types are used in order to get a better understanding of possible backgrounds introduced via these particular clamp types. Results from these investigations are presented in the following section (see section 5.2). These findings, together with the observations made from the Run 32 data, are the basis for the development of future clamp concepts (see chapter 6).

5.2. Observations from Run 31

Run 31 took place from August 2008 to December 2008. The clamps that were used to keep the crystals in their copper structure were of three different types. In figure 5.1 photographs of the various types are shown: the leftmost picture shows a bronze clamp covered with a reflective foil. This foil consists of a multi-layers structure deposited onto a carrier foil. Coincidentally, this foil is also a scintillator. The central picture shows a bronze clamp covered with a thin layer of reflective aluminum and an additional layer of scintillating epoxy resin. The last picture shows a bare bronze clamp only covered with a thin layer of aluminum.¹ All detector modules use conventional CaWO_4 crystals as absorbers. A *set of clamps* consists of *six pairs of clamps*, and every pair consists of a clamp holding the crystal on its lateral surface and one clamp holding the flat surface of the crystal (see the rightmost picture in figure 5.1).

Three categories of clamp induced backgrounds have been identified:

- *no light events* from micro-fracturing of the crystal, as for example due to a too tight holding of the crystal by the clamps
- events with a *different pulse-shape* due to energy releases in the material in touch with the crystal (e.g. the plastic coverage of the clamps). As phonons have to transverse a material border, changes in pulse-shape are expected.
- events with no or only little associated light caused by a recoiling nucleus escaping from the most upper surface layer or the surface of the clamp material

¹In total nine modules with foil covered clamps, seven modules with Araldite covered clamps and one module with bare metal clamps have been mounted in the cryostat. The nine operational modules include seven modules with foil covered clamps, one module with epoxy covered clamps and one module with bare metal clamps.

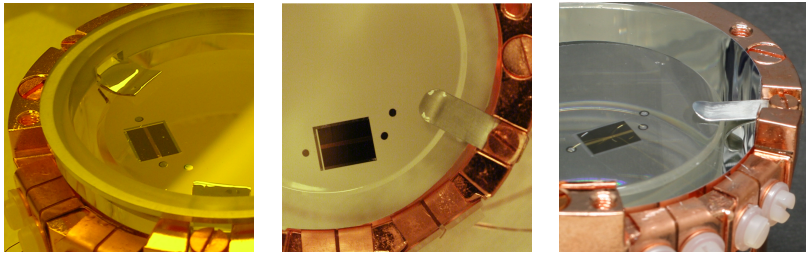


Figure 5.1. – Three different clamp designs were used in Run 31. In the leftmost picture a bronze clamp covered with a reflective and scintillating foil is visible. A clamp covered with aluminum and a thin layer of a scintillating epoxy resin on top is shown in the central picture. The rightmost picture shows bare bronze clamps covered with a layer of aluminum.

5.2.1. Foil Covered Clamps

Clamp Manufacturing

The detector module *K07/David* was equipped with foil covered clamps in Run 31.² The clamps consist of bronze (CuSn6) of a thickness of (0.35-0.4) mm. After machining, the clamps have been etched to remove surface radioactivity from the machining process.³

In a next step the clamps were covered with a reflective and scintillating foil (Radiant Mirror Film VM2002; 3M[®] company). This polymeric, multi-layer foil has a thickness of (60-70) μm and is also used for the housing of the detector modules. A thin layer of epoxy resin (Araldite[®] 2012) was used to fix the still unfitted foil on the metal clamp. As a final step the already attached foil was cut to the desired shape to best shield the metal clamp but not to cover more of the crystals' surface area than needed. The foil does not cover the complete clamp surface as it is folded around the clamp via its short edge (see the leftmost picture in figure 5.1). A small slit on each side is present; the clamp material/gluing layer may have a line of sight to the surface of the crystal.

Data Analysis

The data selection has been done by applying some of the cuts already presented and discussed in section 4.4. The stability cut removes the periods from the data when the detectors were not in their operating points. On both channels a cut on the right-left baseline and the peak-position parameter was applied to remove invalid pulses. In order

²In this notation K07 refers to the name of the CaWO_4 crystal and David is the name of the corresponding light detector.

³Piranha etch is an acid solution used to remove organic remnants and to etch copper surfaces. One liter of solution consists of 700 ml H_2O , 150 ml 95% H_2SO_4 and 150 ml of 35% H_2O_2 .

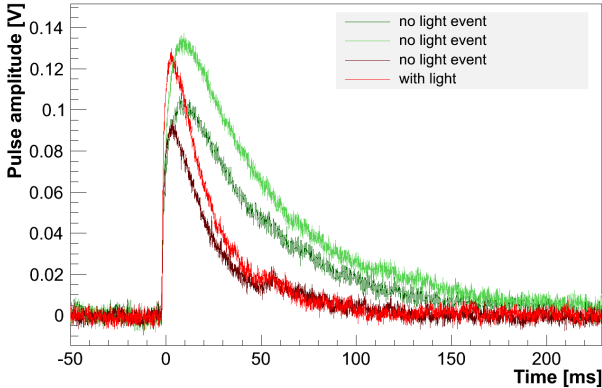


Figure 5.2. – The two different classes of observed no light events in the module K07/David are shown. The red colored pulse is a typical pulse out of the e/γ -band distribution having an associated light signal. The dark red pulse belongs to the class of no light events which acquire the pulse-shape of normal particle-pulses. The pulses shown in green color also have no associated light signal but belong to the class of no light events showing varying decay times (as clearly visible in the plot).

to reject the direct hits of the thermometer film, a weak cut on the onset-channel of the phonon detector was applied. A weak cut on the Fit RMS of the light detector has been applied whereas no cut on the Fit RMS of the phonon detector was carried out not to remove events with a different pulse-shape. A total net exposure after cuts of about 6.12 kg-days was accomplished for the module K07/David.⁴

Results

An event detected in the phonon-detector with no correlated signal in the light detector is referred to as *no light event*. In total, 25 no light events have been observed in an energy range from 15 keV to 400 keV. When having a closer look at the pulse-parameters of no light signals, two classes can be identified: one set of pulses shows the same shape as normal particle pulses, as for example from calibration with a ^{57}Co γ -source. A second class of no light events is characterized by varying decay times and a slower rise time. In figure 5.2, these two different classes of no light events are shown.

A cut on the *decay time* allows us to remove the class of no light events showing longer decay times. From the total number of 25 no light events, four events have a

⁴The data files from Run 31 considered for the analysis presented in this work include all files from *bck_073* to *bck_110* for the three modules (K07/David, Rita/Steven and Sabine/Josef).

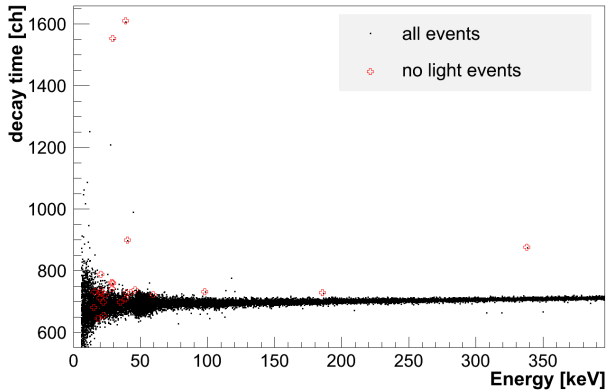


Figure 5.3. – Decay time versus energy for the detector module K07/David. No light events are marked with a red cross. The four events with longer decay time can be rejected from the other events by applying a weak cut on the decay time parameter.

longer decay time and can be identified and removed from the data set (see figure 5.3).⁵ However, the remaining 21 events cannot be rejected by any cut on a pulse parameter.

Interpretation

One possible explanation for **events with different pulse-shape** are relaxation processes taking place in the scintillating and reflective polymeric foil that covers the metal clamp and constitutes the interface between the crystals and the clamp. The polymeric foil is mainly made out of the polymer PEN (Poly(ethylene 2,6-naphthalate)). It is attached onto the metal clamp using a small amount of epoxy resin (Araldite[®] 2012).

There are two different mechanisms of possible relaxation phenomena to be mentioned. Firstly, the sandwich design of metal clamp-glue-polymeric foil when being cooled down from room temperature to 10 mK leads to stress on boundary areas between different materials due to a difference in the thermal expansion coefficient. This may lead to micro-cracking of the plastic in the case that the tensile strength is exceeding the fracture limit of the material. Such cracking, if happening very close to the contact area of the crystal, might be the origin for events with longer decay time. Phonons created due to relaxation processes in the foil are expected to lead to events with different pulse-shape since phonon-propagation in plastic is expected to be slow.

⁵A rejection of events with different pulse-shape is valid as WIMPs are expected to scatter off the tungsten nuclei in the CaWO₄ crystal. Changes in pulse-shape are neither observed nor expected from recoiling nuclei.



Figure 5.4. – Some of the crystals using foil-covered clamps in Run 31 showed micro-fractures at the surface where the clamps were in contact with the crystal. The fissures are not only present at the surface but extend also sideways and into the volume of the crystal.

Furthermore, the phonons have to transverse material borders and hence, the Kapitza coupling, taking into account the heat capacity of the PEN/glue layer, may also influence the pulse-shape of these events.

Plastic when being cooled down below its glass transition temperature (T_g) starts to change from its rubbery-like behavior and gets stiffer until it reaches properties as known from solids like glass.⁶ A polymer consists of long chains of molecules that - at moderate temperatures - are highly mobile and allow the plastic material to be flexible and soft. At low temperatures the chains loose their possibility to move. In the case of applying high surface stress, such as for example, in the form of compressional stress by a very tight holding of the crystal, this might end in fracturing of the polymeric foil. Since the compressional stress is highest at the contact area between the polymeric foil and the crystal, the released mechanical energy is suggested to be also transmitted into the crystal resulting in events with different pulse-shape and no associated light signal. Fracturing processes are not accompanied by scintillation light as the breaking of atomic bonds does not result in an energy transfer to the luminescence centers, neither in plastics nor inorganic scintillators.

An explanation for **particle-like no light events** can be found by looking at the findings made in measurements as early as during CRESST-I.⁷ Pure Al_2O_3 crystals (without light detectors) have been used as absorbers and puzzling observations have been made in the first runs using this detector set-up: the rate of observed events was or-

⁶Around T_g polymers change from elastic and rubber-like behavior to a solid being very hard and brittle. The stiffness of polymers can increase by a factor of up to 10^3 [MR01]. The T_g for PEN is around 125 °C.

⁷CRESST-I is the first phase of the CRESST experiment. During CRESST-I sapphire crystals (not a scintillator material) have been used as target and only the phonon-signal was read out.

ders of magnitude higher than expected. The huge number of detected events which completely resembled those from particle events (observed with calibration sources) originated from micro-cracking or micro-fracturing of the sapphire crystals themselves. The crystals were held in their copper structures using small sapphire balls that were pressed against the sapphire crystal by plastic clamps made from Delrin[®]. The clamp was closed tightly to avoid vibrations that would result in microscopic frictional effects disturbing the detector operation (*microphonics*). Since the balls provided just a tiny contact area this led to high compressional stress at the contact surface and to cracking of the sapphire crystals. Observations under the microscope revealed small fractures extending sideways and into the volume of the absorber crystal as well as in the sapphire balls themselves. Investigations on these fracture processes can be found in [Åst+06].

The foil-covered clamps used in Run 31 also fixed the crystals very tightly: already the metal-sheets used for producing the clamps were quite stiff. Furthermore, the coverage of the metal clamps with the scintillating foil provided an additional increase in stiffness. The polymers of the foil as well as the epoxy resin used to attach the foil to the clamp adopt the properties of glassy solids, when being cooled down to millikelvin-temperatures. An examination of the CaWO_4 crystals held by foil covered clamps under the microscope demonstrated the presence of fractures right at the surface of the crystal which was in contact with the clamps. From the surface fractures small fissures also extend into the volume of the crystal (see figure 5.4). Hence, the origin of the 21 observed no light events with pulse-shape like particle pulses can be attributed to the micro-fracturing of the CaWO_4 crystals.

To summarize, too tight clamping is responsible for the main fraction of observed no light events in the detector module K07/David. An additional four out of the 25 no light events provide a different pulse shape. These four events very likely result from relaxation processes due to compressional stress in the scintillating foil right at the point where it touches the crystal.

5.2.2. Araldite Covered Clamps

Clamp Manufacturing

In Run 31 the detector module *Rita/Steven* was equipped with metal clamps covered with Araldite[®] 2011. The raw material of the clamps, as in the case of the foil-covered clamps, was a specially produced bronze. Before applying a thin layer of highly reflective aluminum by a Magnetron-sputtering process, the clamps have been treated with Piranha etch.

In order to allow for an active background discrimination, a scintillating coating was applied onto the surface of the aluminum covered clamps. The substance used is an epoxy resin called Araldite[®] 2011. In dedicated experiments it was found that this epoxy resin is a scintillator at mK-temperatures. Araldite 2011, mixed with resin and catalyst, was heated up to 60 °C to obtain lower viscosity. The resin was applied onto

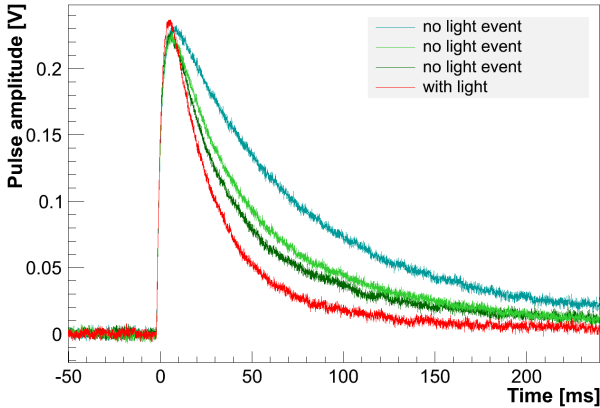


Figure 5.5. – Different classes of no light events seen by the phonon channel in the module Rita/Steven. The red pulse is an e/γ -event. The pulses in light and dark green showing varying decay times belong to one class of no light events. The turquoise pulse is an example for another category of no light events being characterized by even longer decay times.

the clamps by dipping and thereafter stripping it off using a thin and clean PE-HD foil. This technique allows us to apply homogeneous layers of $\mathcal{O}(100\ \mu\text{m})$ onto the clamp surface, which was measured by micro-meter calipers.

Data Analysis

The data selection includes a stability cut, a cut on the right-left baseline parameter on both channels as well as a cut on the peak position parameter to remove the carrier events and direct hits of the thermometer in the phonon detector Rita.⁸ Again, a cut on the RMS of the fit is only applied to the light detector data not to remove possible events introduced by the clamps. The total net exposure (after cuts) amounts to 6.7 kg-days.

Results

In total, within an energy range of 15 keV to 400 keV, 54 no light events have been observed in the detector module Rita/Steven. The pulse-shape of most of the no light events (50 events out of total 54) does not resemble the one of ordinary particle pulses, as for example from a calibration source. Moreover, the class of no light events with different pulse-shapes can be divided into two sub-classes.

⁸The phonon detector Rita is a composite detector. Its TES is evaporated onto a small carrier substrate ($10 \times 20 \times 1\ \text{mm}^3$) which is glued onto the large crystal.

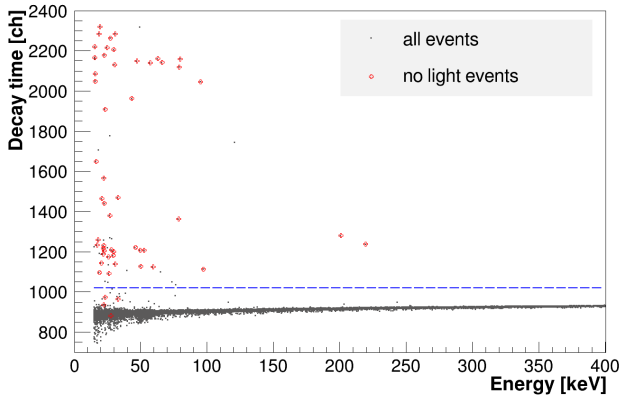


Figure 5.6. – Decay time versus energy for the detector module Rita/Steven. Out of 54 no light events 50 events can be rejected by a weak cut on the decay time parameter (blue dotted line).

In figure 5.5 a selection of no light events is shown. The pulses illustrated in light and dark green belong to the group of no light events showing different decay times and a slower rise time in comparison to particle pulses (red pulse). The turquoise pulse is characterized by an even longer decay time.

No light events revealing clearly different pulse-shapes can be identified and rejected by a weak cut on the decay time (see figure 5.6; blue dotted line).

However, four of the 54 events lie slightly above or inside the distribution of ordinary particle events and cannot be excluded (below blue dotted line). Even by applying a strong cut on the RMS of the fit of the phonon channel, these events cannot be removed from the data set. Note, the events above the blue dotted line which are not indicated as no light events are due to pile-up. This means that within one record a second event (few ms) took place changing the decay time parameter.

The origin of the no light events with different pulse-shapes and the origin of the four events revealing the shape of ordinary particle pulses is discussed in the following.

Interpretation

As in the case of the detector module K07/David, the clamp-crystal interface of Rita was provided by a plastic layer. No light events with the observed profile may have their origin in relaxation processes happening in the plastic. This is plausible because events coming from the plastic are expected to suffer a change in their pulse-shape as already explained. In the detector module Rita/Steven the overall fraction of no light events showing a characteristic pulse-shape is by far larger than in K07/David.



Figure 5.7. – A bronze clamp covered with aluminum and a thin layer of the scintillating epoxy resin Araldite® 2011, as used for the detector module Rita/Steven. A part of the coverage which was in contact with the crystal was removed while dismantling the detector. See text for further explanations.

The cause might be attributed to the particular properties of the epoxy resin. Thin Araldite® 2011 layers are quite flexible and soft and after coating the surface of the clamp, showed a rubber-like and slightly sticky behavior. Due to these properties the overall contact area of clamp and crystal is larger at room temperature. Since only relaxation events that happen very close to or in the contact area are expected to be seen in the detector, a larger contact area may increase the number of detectable events from relaxation processes.

The appearance of micro-fissures in the Araldite layer at low temperatures can be the explanation of no light events revealing slightly longer decay times (green-colored pulses in figure 5.5).⁹ This is compatible with the observations made in the detector module K07/David utilizing foil-covered clamps as discussed in the previous section.

Furthermore, the slight cohesive behavior of the epoxy layer leads to an interconnection between these layers and the CaWO_4 crystal, as verified while dismantling the detector after the measurement. The coverage from several clamps was damaged while being disassembled. The part of the epoxy-aluminum layer which was in contact with the crystal was completely stripped from the bronze clamp (see figure 5.7). The obviously tight interconnection generates additional stress right at the crystal-clamp contact area due to the different thermal expansion coefficients of the materials involved. Besides creating micro-fissures in the coverage layer which appear in the data in the form of relaxation events, this particular arrangement can also give rise to microscopic friction effects (microphonics): the plastic coverage - due to its higher shrinkage - might occasionally "hop" in relation to the crystal.

Events from friction processes are expected to be pure thermal events. As discussed in section 3.5, a particle event from a CRESST calorimeter can be modeled by fitting

⁹Fracturing processes produce events that resemble ordinary particle pulses with respect to their pulse-shape composition (thermal- and non-thermal component). However, they are characterized both by a longer rise and decay time as signals have to pass from one material (plastic coverage) to the other (crystal).

two exponentials to the pulse: a non-thermal component and a thermal component. In figure 5.8 an ordinary particle-event, a no light event with a slightly different pulse-shape (green pulses in figure 5.5) and a no light event belonging to the turquoise-colored class of events are shown together with a two-exponential fit. The particle-pulse and the no light event with a slightly different decay time parameter show a similar composition of the non-thermal (violet solid line) and the thermal component (ocher solid line). The no light event from the turquoise-colored class of pulses has a different composition and is described by only one slow component. Therefore, the no light events showing very long decay times (turquoise-pulse in figure 5.5) are suggested to be the result of such friction effects.

However, a definite statement on the origin of the two different classes of no light events with varying pulse-shapes cannot be given since only one module equipped with this type of clamps was operational in Run 31. However, as only one class of no light events with a different pulse-shape is found for modules equipped with foil-covered clamps, the second class of events in Rita/Steven suggest to be induced by the particular coating.

The four no light events, resembling the pulse-shape of ordinary particle pulses probably are caused by micro-fracturing of the CaWO_4 crystal due to a too tight holding. The bronze material used for this type of clamps is the same as used for the production of the foil-covered clamps. Additional tightness is provided by the epoxy layer on the bronze clamp. The number of no light events revealing the shape of particle pulses is reduced in comparison to the module K07/David. This could be understood as the added amount of plastic coverage onto the springy metal clamp is in $\varnothing(100\ \mu\text{m})$ for the Araldite-covered clamps whereas in the case of the foil-covered clamps (K07/David), the applied plastic layers add up to thicknesses of 200-250 μm . The mechanical properties of the clamps at low temperatures are strongly influenced by this added plastic coverage. The thicker the plastic layer, the more stiff the clamps get and as a consequence, the clamping strength of the crystal is increased. This might explain the smaller number of no light events in the module Rita/Steven in comparison to K07/David (4 events in Rita/Steven, 21 events in K07/David). This conclusion is supported by the fact that no visible cracks (see figure 5.4) could be observed at Rita's crystal-clamp contact areas. Table 5.1 gives a summary of the results obtained from the foil-covered clamps and the Araldite covered clamps.

5.2.3. Pure Metal Clamps

Clamp Manufacturing

The module *Sabine/Josef* was equipped with pure metal clamps that consist of the same bronze material as used for the previously mentioned designs. The clamp surface was cleaned by Piranha etch before a thin layer of reflective aluminum was applied.

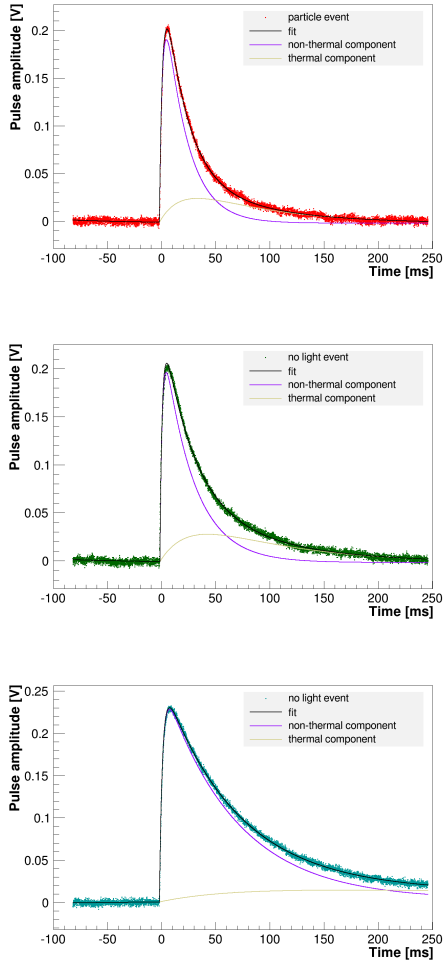


Figure 5.8. – A fit consisting of two exponential components was applied to an ordinary particle-event (first picture), a no light event showing a slightly longer decay time (green-colored class of pulses in figure 5.5; second picture) and a no light event from the turquoise-colored class (third picture). The composition of the non-thermal and the thermal component to the total signal is similar for the first two pulses. The no light event from the turquoise-colored class of pulses shows a completely different composition and is almost described by one slow component only. Thus, it can be interpreted as a pure thermal signal.

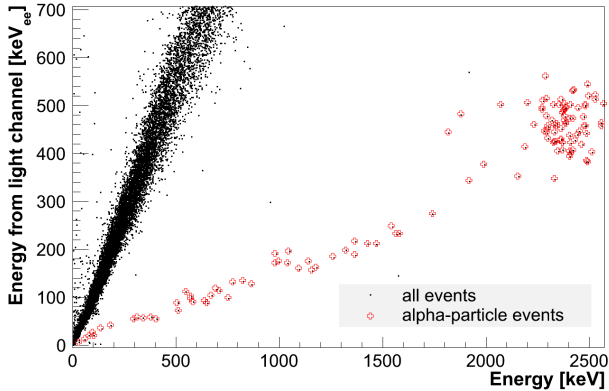


Figure 5.9. – The energy in the light channel is plotted versus the energy in the phonon channel for the detector module Sabine/Josef. The highly populated band is the e/γ -band. The events marked in red belong to α -particle interactions in the crystal. The energy spectrum of the α -particles is continuous and goes down to zero energy. α -particles that do not appear as a line spectrum at the particular energy of the decay are referred to as degraded alphas.

Data Analysis

An electric interference on the light signals results in a reduced overall net exposure in comparison to the modules Rita/Steven and K07/David of 4.91 kg-days after cuts. The basic cuts comprise the stability cut, a cut on the right-left baseline parameter in both channels, as well as, a cut on the peak position to remove direct hits of the TES in the phonon channel. The energy interval for this module can be reconstructed in a range from 15 keV to 3000 keV. A wide energy range demonstrates the observed performance of the pure metal clamps in a consistent way.

Results

In the analyzed data a new effect appeared which, in the case of the clamp designs already discussed, could not be observed and therefore can only be attributed to this particular design. In the data a significant number of so-called *degraded α -particles* is found. Degraded α -particles summarize a class of α -events that do not show the full energy of the α -decay (typically $\mathcal{O}(\text{MeV})$) but rather a continuous energy spectrum ranging from the nominal Q-value of the decay down to energy threshold.

In figure 5.9 this observation is demonstrated. The events marked with a red cross appear in the band where α -particle interactions are expected. The α -events are uniformly distributed over the whole energy range. The population of events around

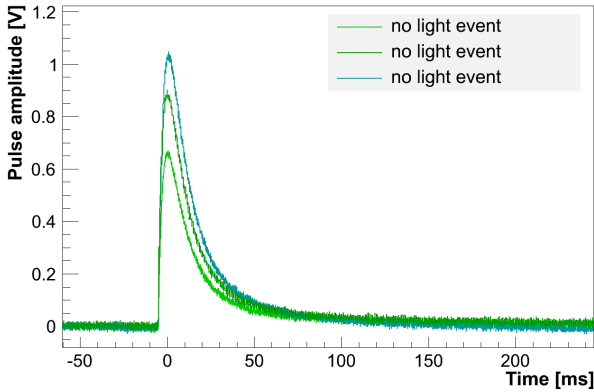


Figure 5.10. – Events with no associated light signal in the detector module Sabine/Josef. The three pulses correspond to deposited energies of 85 keV, 113 keV and 136 keV.

2300 keV is attributed to an internal radioactive contamination in the CaWO_4 crystal from ^{147}Sm .^{10,11} Internal α -contaminations show up as a line spectrum since the full energy of the α -particle is deposited within the crystals. Thus, the degraded α -particles must have another origin which allows the α -particle to lose a part of its initial energy before being detected in the crystal.

In addition to degraded α -events another class of background events is observed. In the data set, three events without a correlated light signal are found. The three events have energies of about 86 keV, 113 keV and 136 keV and perfectly resemble the shape of ordinary particle pulses as for example from a calibration source. All three events are shown in figure 5.10. In figure 5.11 data in the light yield-energy plane is shown with the three no light events marked in red. The distribution of events around a light yield of 0.2 belongs to the degraded α -events.

Here it is important to note that in the whole data set of the module Sabine/Josef, no events with a different pulse-shape (longer rise/decay times) are observed.

¹⁰The line from the α -decay of ^{147}Sm is present in all CaWO_4 crystals. Seemingly the contamination is introduced already during the production procedure of the crystals or even present in the raw materials used to grow the crystals. Any intrinsic, low rate α -contamination is in principle not a dangerous background as it shows up far away from the WIMP-signal region.

¹¹The resolution of the α -line from ^{147}Sm in figure 5.9 is very weak as the phonon detector Sabine due to its limited linear range of the transition does not allow for a precise energy reconstruction in the MeV-range.

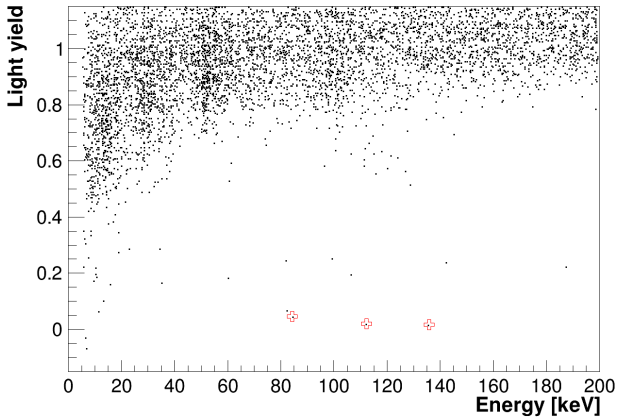


Figure 5.11. – Data in the light yield-energy plane for the detector module Sabine/Josef. Three no light events are marked in red. The band at a light yield of about 1 is the e/γ -band. Around a light yield of 0.2 the degraded α -particles are visible. The event at a LY value of 0.1, slightly above the no light event at around 85 keV, shows a small correlated light signal.

Interpretation

The degraded α -events can only be emitted from a non-scintillating surface material in the vicinity of the detector as any scintillating material would add additional light to the detected events. In other words, an α -particle that escapes from a scintillating surface produces scintillation light which is detected, due to the slow response time of the light detector, together with the scintillation light emitted from the CaWO_4 crystal when hit by the α -particle. Therefore, the degraded α -event would not appear in the α -band, but would be shifted to higher light yields in direction of the e/γ -band.¹²

In the detector Sabine/Josef the degraded α -events lie perfectly in the α -band and since the bare metal clamps are the only non-scintillating material in the detectors' surrounding they must be the origin for the observed α -particles. Alpha-particles that deposit energies in the keV-range have to lose most of their energy inside the clamp material. Therefore, the radioactive α -contamination is present in the *bulk* of the clamp material. A similar mechanism was explained in section 2.5 (see figure 2.12) for α -particles emitted from the isotope ^{222}Rn , present in ambient air.

The recoiling nucleus leaves the center of mass in the opposite direction to the α -particle. Its energy depends on the Q-value of the decay; in the case of ^{210}Po (^{222}Rn

¹²Depending on the energy of the degraded α -particle and the light yield of the scintillator, degraded α -events can lie slightly below, inside or even above the e/γ -band. In order to render α -particle induced backgrounds from the surrounding of the detector harmless, it is aimed to move them up in light yield as far as possible.

decay-chain (see figure 2.11)), the recoil energy of the ^{206}Pb -nucleus is approximately 103 keV. In this energy range the effective range of heavy nuclei in solids is a few 10 nm. Therefore, the decay has to happen in the uppermost surface layer of the clamp to still allow the nucleus to escape from the clamp material. The energies deposited in the crystal range from their maximum recoil energy down to zero energy, depending on the fraction of the initial energy lost in the clamp material.

As discussed in the following section, the α -background is in fact caused by a contamination in the bulk of the bronze material originating from radon adsorption during and before the production process of the bronze. Thus, lead recoil events with energies up to about 103 keV are expected. In total three no light events are observed: the event at 136 keV cannot be attributed to the class of lead-recoil events since it shows a far higher energy than the ^{206}Pb recoil can achieve from the decay. Following this argumentation it cannot be excluded that the event at around 113 keV is due to a lead-recoil as no recoil anti-quenching was taken into account in the analysis. This means when calibrating the phonon detector the small amount of energy which leaves the crystal in form of scintillation light was not taken into account. Thus, events with very small associated light signals appear at a slightly higher energy in the phonon channel. The third event appears at 85 keV and is suggested to result from a Pb-nucleus which was slightly implanted in the aluminum coated clamp.

However, the two higher energetic no light events (113 keV and 136 keV) should, within the sensitivity of the light detector show a correlated light signal in the case they result from recoiling nuclei. Therefore, a reasonable explanation for the presence of these no light events is once more a microscopic fracturing process of the CaWO_4 crystal.

5.2.4. Summary from Run 31 Data

In Run 31 three different clamp-designs have been used. The different designs introduced background events: no light events from micro-fracturing of the crystals resembling the pulse-shape from ordinary particle pulses, no light events showing different pulse-shapes from relaxation events taking place in the plastic interface between crystal and clamp and degraded α -events from a radioactive contamination in the bulk material of the clamps. Table 5.1 lists the results obtained from the analyses of Run 31 data.

5.3. Observations from Run 32

A general summary on the results of Run 32 in the scope of the dark matter data analysis was given in section 2.7. In this section the analysis of the data is focused on background events coming from the clamps. All operational detector modules in Run 32 were equipped with the same type of clamps and high statistics was achieved in about two years of data taking.

	Foil-covered clamp	Araldite-covered clamp	Pure-metal clamp
Module	K07/David	Rita/Steven	Sabine/Josef
Exposure [kg-days]	6.1	6.7	4.9
Energy range [keV]	15-400	15-400	15-3000
Total number of no light events	25	54	3
No light events with <i>different</i> pulse-shape	4	50	0
No light events with pulse-shape of particle pulses	21	4	3

Table 5.1. – Results obtained from the analyses of the data from Run 31 concerning background events introduced by the three different clamp-designs used.

5.3.1. Clamp Manufacturing

In order to prevent plastic materials coming into contact with the crystals, the clamps in Run 32 were only *pure metal clamps*. However, the raw material was the same as used in Run 31. To avoid fracturing of the crystals due to a too firm tightening, the thickness of the bronze metal sheets used for the production of the clamps was adjusted. Two different thicknesses were used for the six pairs of clamps needed for each phonon detector. The clamps fitting the lateral surfaces as well as the top front surface are made out of bronze sheets having a thickness of (0.30-0.32) mm. The clamps on the bottom front surface which carry the weight of the crystal are made out of sheets with a thickness of (0.40-0.45) mm to sustain plastic deformation.

After manufacturing, the clamps underwent a chemical cleaning treatment. First, the clamps were etched in Piranha solutions (for 4 min), afterwards the surface of the clamps was treated by a electro-polishing process.¹³ The particular shape of the clamps results in a non defined field in the electro-polishing bath which caused blackish remnants close to the holes used to fix the clamp. Therefore, another short etching step (Piranha, 60 sec) was introduced after the electro-polishing process. A thorough rinsing using deionized water was carried out after each cleaning procedure.

To ensure a good light reflection, the cleaned bronze clamps have been covered with a thin layer of silver ($5.5 \pm 1.5 \mu\text{m}$) by an electro-plating process.¹⁴

¹³Polygrat-Electrolyte E104 was used for electro-polishing. The process was carried out for 4 min at 7 V.

¹⁴The silver-plating solution is called "Glanzsilberbad SCANDIA 360" from Heimerle+Meule. The silver electrodes have been classified as "Reinst-Silber". Plating took 6 min at 0.6 V/1.2 A.

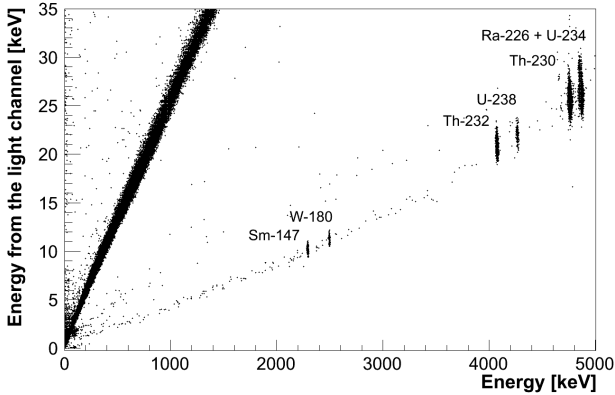


Figure 5.12. – The energy in the light channel is plotted versus the energy in the phonon channel for Rita/Steven in Run 32. The highly populated band is the e/γ -band. The degraded α -events (less populated band) extend over an energy range up to 5 MeV and within their continuous distribution also some discrete lines from internal α -emitters are visible. Between these bands another distribution of events is visible. They can be attributed to be induced by radon on/in the scintillating surrounding and/or the surface of the crystal (see section 2.5 for further information).

5.3.2. Results

As all detectors were equipped with the same type of clamps the observations and results can be demonstrated by choosing one single representative detector module.

In all detectors a prominent number of degraded alpha events is observed. At the same time, a distinct number of nuclear recoils from recoiling lead nuclei is detected.

The detector Rita/Steven reconstructs energies up to some MeV and is therefore a perfect candidate to demonstrate the degraded α -event mechanism. Figure 5.12 depicts the energy from the light channel versus the energy in the phonon channel. As usual, the band with the high density of events is the e/γ -band. Another far less populated band is observed where α -particle interactions are expected. The α -band is plotted for an energy range up to 5 MeV. Within the continuous distribution of degraded α -events shown in figure 5.12 discrete lines are also visible, corresponding to an intrinsic radioactive contamination of the crystal with ^{147}Sm , ^{180}W , ^{232}Th , ^{238}U , ^{230}Th , ^{266}Ra , and ^{234}U . At energies higher than 5 MeV even more discrete lines from intrinsic α -emitters appear.

The degraded α -events appear in the region expected for α -particle interactions, meaning that these degraded alphas have lost part of their energy in a non-scintillating surface - the bronze clamps. The clamps are coated with a silver layer of approximately $5.5 \pm 1.5 \mu\text{m}$ thickness. The projected range of α -particles of 5.5 MeV (e.g. from ^{210}Po)

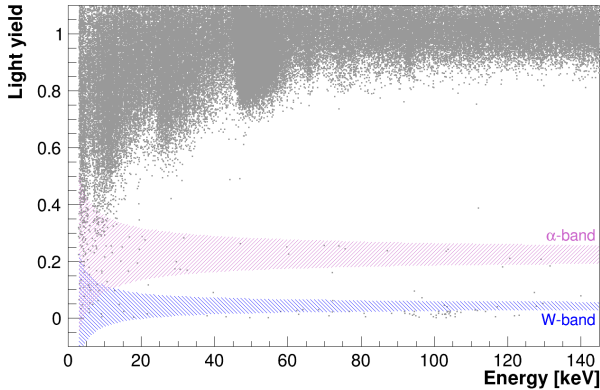


Figure 5.13. – Data in the light yield-energy plane for Rita/Steven in Run 32. The violet and blue shaded areas indicate the regions where α -particle interactions and tungsten recoil-events are expected. The presence of degraded α -events going down to threshold energy is visible. The events slightly below the W-band are ^{206}Pb recoiling nuclei originating from the α -emitter ^{210}Po .

in silver is $11.7\ \mu\text{m}$ [Zie+12].¹⁵ As degraded alphas are observed down to threshold energy, the α -contamination cannot only come from the silver coverage but must have also a contribution coming from the bulk material (CuSn6) of the clamp, as also confirmed by Monte Carlo simulation [Buc11].

In figure 5.13 the data of the detector module Rita/Steven is shown in the light yield-energy plane. The violet shaded area indicates the α -band. The band shaded in blue illustrates the region expected for tungsten recoil events. Besides the degraded alphas, a distribution of low-light events (events with only a small correlated light signal, as for example expected for tungsten recoils) around an energy of 103 keV tailing down to the region of interest is present in the data. This event distribution around 103 keV is located slightly below the band expected for W-recoil events.

Figure 5.14 shows the energy spectrum of these events from *all detector modules*. The distribution peaks at 103 keV; the peak energy allows to identify the heavy nuclei as ^{206}Pb from the decay of ^{210}Po . From this data we can determine directly the inverse value of the quenching factor for lead recoils to be 71.4 (1.4%).¹⁶

The long tail of the lead-event distribution suggests the radioactive decay does not only take place on the surface, it also has to occur in the sub-surface layers of the clamp. As lead recoils have a projected range of only about 15.4 nm, the silver layer has to be considered as the origin for the lead recoil events. In other words, ^{206}Pb recoil-events

¹⁵The projected range of a 5.5 MeV α -particle in silver has been calculated using the SRIM package [Zie+12].

¹⁶The inverse value of the quenching factor for tungsten recoils as used in Run 32 is 25.6.

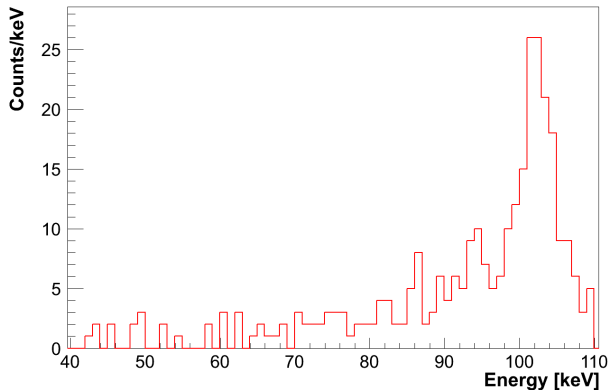


Figure 5.14. – Energy spectrum of ^{206}Pb -events from *all* detector modules in Run 32. The distribution shows a peak at 103 keV, the energy a ^{206}Pb -recoiling nucleus gains from the α -decay of ^{210}Po . The tail extending down to the signal region suggests the presence of a contamination not only at the surface of the clamp material but also in sub-surface layers of few 10 nm.

created from the α -contamination in the bulk material of the clamp are not able to escape the thick silver layer ($5.5 \pm 1.5 \mu\text{m}$).

No events with a different pulse-shape (longer decay/rise times) have been observed in Run 32 when using bare metal clamps. The no light events with a different pulse-shape observed in Run 31 are, therefore, due to the plastic interface used in between the clamps and the crystal, confirming the interpretation. The origin of the observed degraded α -events in the case of using bare metal clamps (Sabine/Josef in Run 31 and all detector modules in Run 32) has to be related to the bulk material of the clamps.

5.4. Origin of the Low Energy Alpha-background

The results and conclusions from observations made from the data of Run 31 and Run 32 when using *bare metal clamps* are summarized in the following:

- degraded α -events appear within the α -band and hence are emitted from a non-scintillating surface in the vicinity of the detector
- the energies of the degraded α -events range from the energy threshold of the detector up to 5 MeV and can only be explained due to a bulk effect
- the bare metal clamps in Run 31/Run 32 were covered with a thin, reflective layer consisting of aluminum/silver, respectively. The thickness of the layers

	Graphite [ppm]	NOSV [ppm]	Sn [ppm]	CuSn6 [ppm]
Pb	≤0.05	0.24	0.06	12/14
Bi	≤0.01	0.08	≤0.005	0.13/0.16

Table 5.2. – Results from the GDMS analyses of the components used for the production of the CuSn6-bronze. As two samples of the produced CuSn6 have been analyzed both values are given in case the obtained results were different [Maj+09].

is not sufficient to completely stop the alphas as has also been proven by MC simulations. Therefore, the bronze material has to be the origin of the observed α -background at low energies.

- the overall rate of degraded α -events detected is approximately 1-3 events per detector module and day (corresponding to about 10 decays per second and kilogram of clamp material).

5.4.1. Clamp Bulk Material

Material Studies

The raw material used for manufacturing the clamps used in Run 31 and Run 32 is bronze (CuSn6), as this alloy is known to be springy even at low temperatures. Due to the similar chemical properties of tin and lead commercial bronze is always contaminated with lead. The presence of lead implies the presence of its radioactive isotope ^{210}Pb , a contamination which should definitely be avoided.

Therefore, a low-background CuSn6 was produced at the Norddeutsche Affinerie AG using only very pure material components [Maj+09]. This alloy was produced in a top cast procedure using electrolytically refined NOSV copper and 99.9999% Sn from Alfa Aesar. Since the pulling takes place in ambient air (crucible at 1200 °C) a substantial layer of graphite was applied on top of the melt to prevent oxidation or rather to keep the oxygen content of the melt at about 5 ppm. A GDMS (Glow Discharge Mass Spectrometry) analysis was carried out for the NOSV copper, tin, and graphite powder as well as for two samples of the CuSn6 [Maj+09]. The contaminations with Pb and Bi are summarized in table 5.2.

The high amount of Pb and Bi found in CuSn6 can be attributed to a contamination from the crucible, the lid or the graphite nozzle of the Top Cast cooler, as all these parts were already used for the production of other samples.

It is to be clarified if the concentration of lead is sufficient to explain the number of observed α -events. Lead always contains some fraction of the radioactive isotope ^{210}Pb . Typical values are around 100 Bq/kg, corresponding to about 10^{-15} parts of

Decay-chain	Nuclide	Activity
^{232}Th	^{228}Ra	≤ 18 mBq/kg
	^{228}Th	$\leq (17\pm 8)$ mBq/kg
^{238}U	^{226}Ra	(25 ± 4) mBq/kg
	^{234}Th	≤ 0.12 Bq/kg
	^{234m}Pa	≤ 0.40 Bq/kg
^{235}U	^{235}U	≤ 6.0 mBq/kg
	^{40}K	(0.16 ± 0.04) Bq/kg
	^{210}Pb	(6.9 ± 0.9) Bq/kg

Table 5.3. – Results of a HPGe-measurement of rolled bronze produced by Norddeutsche Affinerie. The ^{210}Pb contamination showing an activity of 6.9 ± 0.9 Bq/kg could be verified. Results are given within 68% confidence limits.

^{210}Pb in pure lead.¹⁷ Assuming 100 Bq/kg of ^{210}Pb in Pb which corresponds to 35 ppq of ^{210}Pb in Pb, the clamp material yields an expected activity of about 4.4 mBq/kg. The rate of degraded α -events observed during Run 32 is approximately three orders of magnitude larger. Thus, another mechanism for the enhancement of the ^{210}Pb -fraction has to be present.

In order to verify that radioactive ^{210}Po is the source of the observed degraded alphas, a high-purity Germanium γ -spectroscopy measurement (HPGe) was carried out. In total 46.3 g of rolled CuSn6 material (strips of $(5 \times 10 \times 0.35)$ mm³) have been measured in a highly sensitive set-up at LNGS [Lau11]. The results obtained during a life time of 25.5 days are summarized in table 5.3: an excessive presence of the radioactive isotope ^{210}Pb could be verified. ^{210}Pb beta-decays into ^{210}Bi accompanied by the emission of a gamma of 46.5 keV. The sensitivity of the HPGe-detector was sufficient to measure the 46.5 keV from the gamma transition. The activity for ^{210}Pb as determined from the measurement is 6.9 ± 0.9 Bq/kg. This value is in agreement with the rate of observed degraded α -events in Run 32.

Optical Investigations

The excess of ^{210}Pb in CuSn6 is verified, however the process which enhances this isotope relative to the amount of stable Pb has to be clarified.

Examinations of the bronze material under the microscope revealed the presence of pieces of graphite (≤ 1 μm). Figure 5.15 shows the remnants found in three different

¹⁷The CRESST Pb-shield is made from low-background lead classified by its activity of ^{210}Pb of 30 Bq/kg

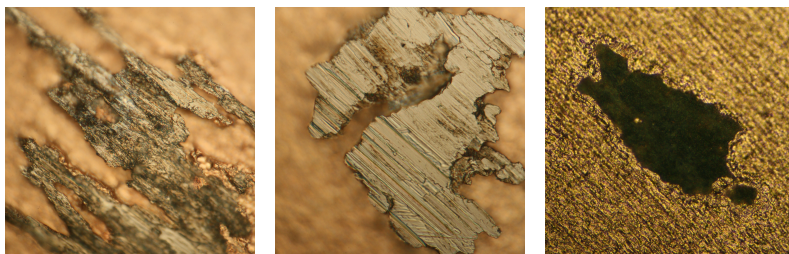


Figure 5.15. – Remnants from graphite powder in three different samples of CuSn6-bronze observed under the microscope. The size of the observed pieces is ($\leq 1 \mu\text{m}$).

samples. The bronze was etched in Piranha to remove approximately (1-2) μm of material, followed by an examination under the microscope. This procedure has been repeated up to 20 times. Some samples showed blackish remnants that could not be etched away and appear to be remnants from the graphite powder used to protect the melt from oxidation.

Due to its porous structure graphite has a huge surface area and is known for its good adsorption and catalytic reduction properties. Hence, one plausible scenario for the enhancement of ^{210}Pb in the melt is via the *adsorption of radon*. Radon is present in ambient air. The Top Cast procedure was carried out at ambient atmosphere, hence also the graphite powder was exposed to radon. Furthermore, the powder may have had an arbitrary exposure before being used for the production.

There are several ways in which radon can enter the melt. Due to the active surface of the graphite, radon and/or its progenies can be deposited directly onto the powder.¹⁸ Secondly, graphite also attracts moisture and radon and/or its progenies may be adsorbed by the carbon together with the moisture present in ambient air. As the melt is heated up to 1200 °C it is also possible that the adsorbed radon progenies are desorbed from graphite and enter the melt.

To complete the topic, a possible contribution from the silver coverage of the clamps also has to be discussed. The projected range of alphas of 5.3 MeV in silver is about 12 μm (calculated with SRIM [Zie+12]). Since the silver layer only has a thickness of $5.5 \pm 1.5 \mu\text{m}$, the silver coating is not sufficient to reproduce the observed degraded α -spectrum. This means the silver layer cannot be responsible for all observed degraded alphas. This was supported by MC simulations [Buc11].

¹⁸Filtering systems used to remove radon contributions from ambient air utilize activated carbon. Radon adsorption is most efficient at low temperatures. The charcoal filters have to be regenerated by heat treatment under the absence of oxygen.

5.5. Origin of the Pb-recoil Background in Run 32

The energy spectrum of the ^{206}Pb -recoil events in Run 32 (figure 5.14) shows a dominant peak at the nominal energy of 103 keV, as well as, a tail towards lower energies. The detected Pb-recoils from the ^{210}Po -decay can come from: a surficial implantation of α -recoiling nuclei from ^{222}Rn or its progenies, or from a direct enhancement of ^{210}Po in the clamp coverage.

In order to detect Pb recoil-events in the detector set-up of Run 32, the contamination of ^{210}Po has to be present on the surface and/or upper-surface layers of the silver coated bronze clamps. A contamination of ^{210}Po is also plausible directly on the surface of the crystal close, to the area where the clamps touch the crystal. The Pb-recoil in this special situation deposits its full nominal energy of 103 keV in the crystal and the escaping α -particle cannot be used as a veto since it hits the non-scintillating clamp surface.¹⁹

A contribution from the ^{210}Pb in CuSn6 can be excluded since the projected range of Pb-recoils in CuSn6/silver is calculated to be 15.9 nm/15.4 nm, respectively [Zie+12]. A Pb-recoiling nucleus originating from the CuSn6 cannot traverse the thick silver layer and only recoils from the upper most silver-layers can reach the crystal.

A ^{206}Pb background of three Pb-events per detector module and month can be estimated from the data. Thus, chemical analyses of assembled materials are not significant as the level of contamination is far away from the sensitivity of available instruments.

In the following section, the properties of the silver coating and the plating process are studied in more detail. Furthermore, possible reasons why a ^{210}Po contamination could have entered the plating process and how its deposition on the clamp material may have taken place are discussed.

5.5.1. Silver Coating of Clamps

The silver coating was applied onto the CuSn6 clamp via an electro-plating process. The plating solution is comprised of 2.5-7% potash (K_2CO_3), 2.5-7% potassium dicyanoargentate ($\text{KAg}(\text{CN})_2$), 10-25% potassium cyanide (KCN) and 74.5% H_2O . Two possible scenarios for an enhancement of ^{210}Po in the silver coating are:

- via the adsorption of radon in the potassium carbonate powder. Potassium carbonate is very hygroscopic, meaning that it accumulates water molecules from ambient air. Thus, radon and its progenies can also be enhanced in the K_2CO_3 powder.
- via accumulation of ^{210}Pb in the plating solution already during its production while being exposed to ambient air.

¹⁹In the case the α -particle hits the scintillating surrounding of the detector the event can be rejected by the additional light emitted by the scintillating foil.

The existence of other processes is, of course, not excluded. As found by [Fig61], ^{210}Po is solvable in most acid solutions and also in KCN. Furthermore polonium is known to spontaneously deposit on less noble metals. In 1986, Ehinger et al. studied the spontaneous deposition of ^{210}Pb - ^{210}Bi - ^{210}Po out of solution onto various metals [EPR86]. They found that ^{210}Po and ^{210}Bi deposit onto nickel whereas ^{210}Pb remains in solution. ^{210}Po only deposits remarkably on copper and silver surfaces, whereas most of the ^{210}Pb and ^{210}Bi remains in solution. Accordingly, a deposition of ^{210}Po is expected out of the solution onto the plated silver-layer of the clamps.

The plating-process has to be examined in greater detail under these conditions. For the electro-plating a voltage of 0.6 V was applied in the bath. Since the recoiling nuclei are not able to travel more than about 16 nm, only the last sub-layers of silver are of interest. After plating, the voltage is switched off while the clamps are still submerged in the plating solution. Only after some minutes the clamps were removed from the plating-solution and carefully rinsed in deionized water. In this special case the clamps were present in an electroless situation in a diluted KCN bath. Under these circumstances the spontaneous plating of Po is the favored process and ^{210}Po , if present in the solution, can be deposited onto the upper-most layers of the coated clamp.

Not only ^{210}Po -recoil background but also α -background is introduced via this process. Since the ^{210}Po -contamination is only expected on the surface of the clamps, slightly degraded α -events are possible. However, the maximum thickness the α -particles have to traverse is in the μm -range and therefore the energy of degraded alphas from this particular background source is quite high.

Therefore, the ^{210}Po -contamination in the silver-coating cannot obviously explain the observed spectrum of degraded alphas. However, it is an additional source along with ^{210}Pb present in the CuSn6 bulk material and contributes mainly in the higher alpha energy region.

5.5.2. Implantation of Daughters of Rn-222

Another possible mechanism to introduce a Pb-recoil background is the surficial implantation, in particular of $^{210}\text{Pb}/^{210}\text{Po}$ from ^{222}Rn . Such implantation can happen on the surface of the silver-plated clamps as well as on the surface of the crystal. Both processes can induce Pb-recoil events and will be discussed in the following section.

Pb-210 in Clamp Surface-Layers

An implantation of the recoiling radio-nuclides from ^{222}Rn in the silver-layer of the clamps will result in an accumulation of the radioisotope ^{210}Pb as it is the first isotope in the chain with a long half-life (22.3 y). The decay of lead nuclei establishes a population of ^{210}Po nuclides which alpha-decay (half-life of 138.4 d) inducing the observed ^{206}Pb recoiling nuclei. Depending on how deep it was implanted, the ^{206}Pb -recoils can show energies from 103 keV down to threshold energy.

This is plausible as *no radon prevention* has been undertaken, neither during the manufacturing process of the clamps nor during assembling and mounting of the detectors. Both at MPI in Munich as well as in the underground lab the detectors were handled over time periods of around 6 weeks (10 hours per day) in ambient air in a conventional clean room environment.²⁰ The radon concentration in unfiltered air depends on the geographical location and on the weather conditions as well as the ventilation situation.

In Hall A at LNGS radon activities up to approximately 100 Bq/m^3 have been measured. In the clean room at MPI concentrations up to 30 Bq/m^3 have been detected using a commercial radon monitor system. Definite values for the period of mounting for Run 32 are not known, however from recent radon concentration measurements at MPI and in Hall A at LNGS, a value of some 10 Bq/m^3 seems to be realistic.

Pb-210 on Crystal Surface

At the same time and by the same mechanism recoiling radio-nuclei from the ^{222}Rn -decay chain can also be implanted into the surface of the crystal. Here, two limiting cases have to be considered:

- the full energy of the α -particle can be detected in the crystal when the Pb-recoil escapes from it. In this case the event appears at high energies (MeV) and is far away from the WIMP signal region.
- the 103 keV of the recoiling ^{206}Pb nucleus are detected in the phonon detector and the α -particle escapes from the crystal. Here, again two cases have to be distinguished:
 - the escaping α -particle can hit a scintillating surrounding of the detector (e.g. foil) and the corresponding scintillation light will shift the event to higher light-yields far away from the WIMP-signal region
 - the α -particle hits the non-scintillating clamp. In this situation the Pb-recoil appears in the Pb-recoil band located slightly below the region expected for tungsten-recoil events (at lower LY). The escaping α -particle, as it might also deposit some of its initial energy in the crystal when escaping from it, generates a distribution of Pb-recoil events which from 103 keV extend to higher recoil energies (and by trend higher LY).²¹

²⁰The mounting of detectors for Run 32 was completed only few days before a strong earthquake in the region of L'Aquila (6. April 2009) occurred. Due to the earthquake some detectors lost electrical connections and the cryostat had to be warmed up and opened again to fix them. In this manner the detectors, for a second time were exposed to ambient air leading to about 6 weeks of mounting time.

²¹The α -particle while escaping from the crystal deposits energy in the crystal and also produces scintillating light. This light is detected together with the scintillation light produced by the ^{206}Pb -recoil.

Summary on the Pb-recoil Background

²⁰⁶Pb-recoil events from the silver coating:

- introduced via spontaneous deposition of ²¹⁰Po from the plating solution onto the upper most surface layer of the silver coating
- ²⁰⁶Pb-events from this background are expected to appear at 103 keV

²⁰⁶Pb-recoil events from radon implantation in the surface of the clamp:

- introduced via surficial implantation of recoil nuclei, in particular ²¹⁰Pb onto the clamp surface
- ²⁰⁶Pb-events from this background are expected to show energies down to threshold energy depending on the actual implantation depth of the nucleus

²⁰⁶Pb-recoil events from radon implantation into the crystal:

- introduced via surface implantation of ²¹⁰Pb recoiling nuclei into the crystal
- the mechanism found to be most important is the ²⁰⁶Pb-recoil which deposits its full energy in the crystal and the α -particle escapes from the crystal and hits the non-scintillating silver-coated clamp. ²⁰⁶Pb-events from this background are expected to appear mainly in the peak at 103 keV and even at slightly higher energies and light yields, in the case that the α -particle, while escaping, deposits some of its initial energy in the crystal

5.5.3. Time Dependence of Pb-recoil Events in Run 32

A separation of the ²⁰⁶Pb-recoil events produced by a contamination of ²¹⁰Po from the ²⁰⁶Pb-recoil events produced by a contamination of ²¹⁰Pb can be achieved by having a closer look to the decay properties of the two radio-nuclides.

²¹⁰Po has a half-life of 138.4 days whereas ²¹⁰Pb decays with a half-life of 22.3 years. In Run 32 about two years worth of data have been collected, a time scale long enough to study contributions from the two possible sources for the Pb-recoil background. In the case of a direct contamination of ²¹⁰Po on the silver coating of the clamp the detected rate of Pb-recoils should decrease during the data taking period. In the case of an enhancement of the radionuclide ²¹⁰Pb the situation is different as the population of ²¹⁰Po first has to be built up. Hence, the detected rate of ²⁰⁶Pb-recoil events should increase with the half-life of ²¹⁰Po.

Furthermore, the expected energy spectrum of the two background sources has to be considered. The spontaneous deposition of ²¹⁰Po onto the silver coated clamps takes place after the plating process when the voltage is switched off. Therefore, the recoiling nuclei are emitted from the uppermost surface-layers and are expected to appear at their maximum nominal energy or only slightly below.

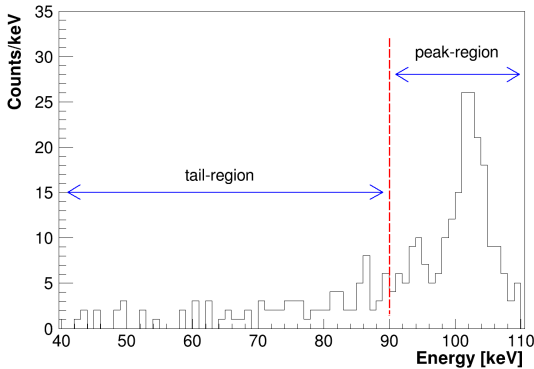


Figure 5.16. – Energy spectrum of ^{206}Pb -events from *all* detector modules in Run 32. The *tail-region* (40 keV to 90 keV) and the *peak-region* (90 keV to 110 keV) are indicated.

The energy spectrum of the Pb-events resulting from the implantation of ^{210}Pb in the clamp material is expected to be rather flat; the events in the tail of the observed distribution are good candidates for Pb-events introduced via implantation processes.

The Pb-recoils of all detectors in Run 32 were studied considering these aspects. As a first step the energy spectrum was subdivided (see figure 5.16), one spectrum includes the events from 40 keV to 90 keV and is referred to as the *tail-region*, whereas the spectrum of the *peak-region* is the energy window 90 keV to 110 keV. As the expected rate from the few recorded events is small (see figure 5.16), the data was binned in order to define a rate of the observed Pb-events versus measuring time. Ten data files were continuously added and a rate, given in counts/kg/day for each time bin, was calculated.²²

When dealing with low event rates (~ 1 event per detector and month) and long measuring times (years), effects that may influence the detector efficiency have to be taken into account. In this situation this is particularly important since the noise conditions of some of the detector modules varied during Run 32. Data cuts performed during the data selection are more likely to remove pulses from this high-noise periods and therefore a rate calculation would not be very significant. Thus, a method had to be found to account for the efficiency of every detector during the whole data taking period.

To measure the noise conditions, an artificial pulse is generated by a superposition of recorded empty baseline samples with a scaled template pulse for each detector. Empty baselines are records without a signal and, thus, are only influenced by the present

²²The data taking in CRESST has to be interrupted every 3 days for approximately 2 h to refill the liquid nitrogen and liquid helium tanks of the cryostat. Therefore a typical data file contains the data taken in about 65 h of measuring time.

	A_{Po} [events/kg/day]	A_{Pb} [events/kg/day]	Figure
tail-region			
40 keV-90 keV	0.05 ± 0.03	0.16 ± 0.02	figure 5.17
peak-region			
90 keV-110 keV	0.37 ± 0.07	0.26 ± 0.03	figure 5.18

Table 5.4. – The values of the different fit parameters are given within a 68% C.L.

noise. They are recorded every 6 min and in this way allow us to have a good measure of changing noise. The same cuts used for the analysis are applied to the artificial pulses. The cut-efficiency, or detector efficiency, is then given by the ratio of pulses that survived the cuts and the total number of artificial events in the considered period of measuring time. This method turned out to be a very efficient and elegant way to account for the efficiency changes of the detectors.

Fit Model

The calculated rate of Pb-events can be modeled as superposition of an exponential decay and an exponential rise for the two possible background sources:

$$R(t) = A_{Po} \cdot e^{-t/\tau} + A_{Pb} \cdot (1 - e^{-t/\tau}) \quad (5.1)$$

where A_{Po} is the initial activity (beginning of data taking) of ^{210}Po at the surface of the clamps while A_{Pb} is the initial activity of ^{210}Pb which builds up a ^{210}Po activity with the half-life of ^{210}Po . The life time τ for the decay of ^{210}Po is 199.63 days ($\tau = T_{1/2}/\ln 2$) and is used as a fixed parameter.

In figure 5.17 and figure 5.18 the measured rate of Pb-recoil events calculated for each bin is shown in form of a blue-colored cross-symbol. The red lines represent the fitted mean value according to equation 5.1. The uncertainty of the fitted mean is calculated assuming an underlying Poisson distribution. The grey-shaded boxes represent the 68% probability intervals for the observed number of events in each bin. The fit parameters for both the tail-region (40 keV to 90 keV) and the peak-region (90 keV to 110 keV) are summarized in table 5.4.

In figure 5.17 the data of the tail-region is shown. The fit indicates an increasing rate with time corresponding to a dominant contribution from the implanted ^{210}Pb in the surface of the clamp material. As the ratio of the amplitudes A_{Pb}/A_{Po} is about three, only one third of the events result from a direct contamination of ^{210}Po on the clamp. The dominant part of the rate is ascribed to ^{210}Pb . For the search of dark matter all events leaking into the signal region can mimic possible WIMP interactions. In this context

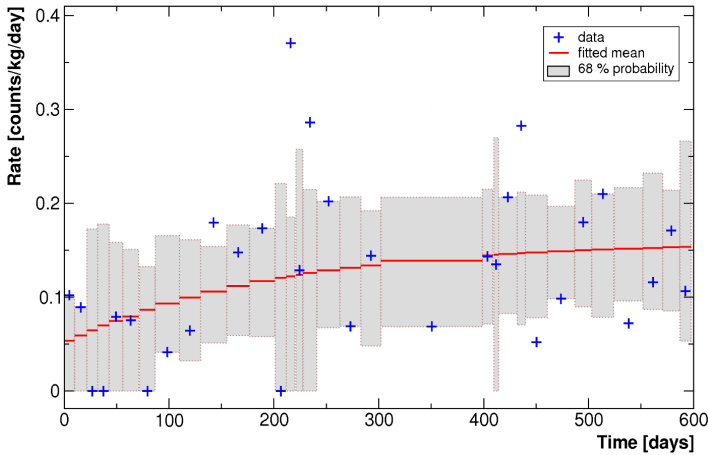


Figure 5.17. – The rate of observed Pb-recoil events (blue symbols) in the energy range from 40 keV to 90 keV, referred to as *tail-region*, is plotted versus time. The red line represents the fitted mean. In order to judge if the expectation fits to the number of observed events error bars are shown in form of 68% probability intervals. The fit shows an increase in rate originating from a dominant contribution of ^{210}Pb . Values of fit parameters are given in table 5.4.

the events present in the tail-region of the Pb-recoil event distribution are of great interest. The investigation of the time-dependence of the Pb-recoil data shows that 2/3 of the events of the tail-region result from ^{210}Pb , which was implanted into the surface via the decay of radon. This is a very meaningful information as it demonstrates the importance of preventing the exposure to radon of any non-scintillating components within the detector housing. par Figure 5.18 shows the data of the peak-region. The fit shows a decrease in rate with the parameters $A_{Pb}=0.26$ events/kg/day and $A_{Po}=0.37$ events/kg/day. As mentioned before, at least two competing effects have to be considered (implantation of ^{210}Pb into the crystal and deposition of ^{210}Po from the plating process on the surface of the clamps). Nonetheless, the decrease in rate points in the direction that the larger fraction of the events originates from an enhancement of ^{210}Po on the upper-surface layer of the clamps as for example introduced by deposition from the silver plating-solution.

5.6. Relaxation Events

Relaxation events summarize a class of events that feature a different pulse shape to the normal particle pulses (e.g. from calibrations) and, in addition, they have no correlated light signal. Relaxation pulses have only been observed in Run 31, when using the

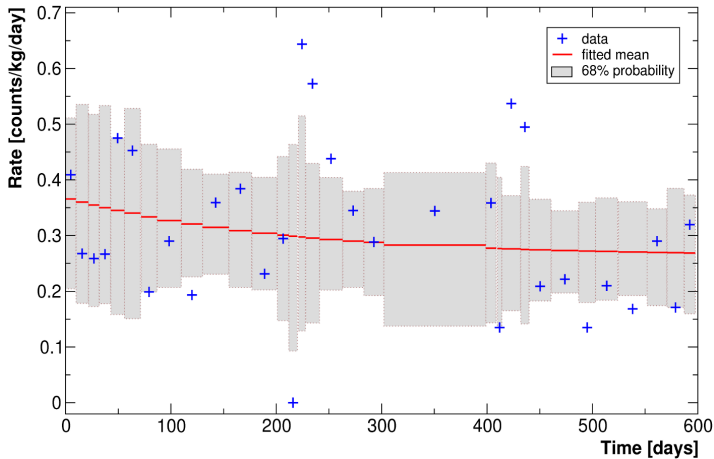


Figure 5.18. – The rate of observed Pb-recoil events (blue symbols) in the energy range from 90 keV to 110 keV, referred to as *peak-region* is plotted versus time. The grey-shaded boxes represent the 68% probability intervals for the observed number of events in each bin. The fit shows a decrease in rate over time. Parameters of the fit are summarized in table 5.4.

Araldite-covered clamps and the foil-covered clamps. As discussed in section 5.2, these events result from relaxation processes in the plastic-interface between the clamp and the crystal.

In Run 31 the Araldite-covered clamps and the foil-covered clamps have been introduced as an attempt to reach a completely scintillating surrounding of the detectors. In light of the results from Run 32, this is very important as the bare metal clamps are responsible for the observed degraded α -events and the Pb-recoil events, a serious background for the experiment. Both the alphas and the Pb-recoils could have been vetoed in Run 32, if a scintillating-coverage had been used for the clamps.

However, up to now, no functional scintillating coating has been found to meet all the requirements in matters of not introducing new backgrounds, as for example the events with different pulse-shapes. In general, pulses that show a different shape can be identified and removed from the data (rise/decay-time parameter), but this is only valid above a certain pulse amplitude. For very small pulses (low energies) the discrimination is not really efficient anymore and they cannot be distinguished from ordinary particle pulses. Therefore, low energy relaxation events with no associated light signal appear in the signal region and may mimic possible WIMP interactions.

In summary, to avoid relaxation events, a completely scintillating clamp design has to be developed which prevents a direct contact between the plastic-scintillating layer and the crystal.

5.7. Secondary Backgrounds

To be complete, the discussion in this section will give a short summary on *secondary backgrounds* that can be introduced by α -particles and ^{206}Pb -recoils from the contamination of ^{210}Po present on the pure metal clamps (Run 32).

5.7.1. Sputtering on the Clamps

M. Kuźniak, M.G. Boulay and T. Pollmann from Queen's University (Canada) propose that the *ion sputtering* caused by the ^{206}Pb -recoils on the clamp material, assuming a certain surface-roughness, can be a new, so far not considered source of background in the CRESST experiment [KBP12].

The sputtering process can be described in the following way: the ^{206}Pb -recoils hit the silver layer of the clamp and silver atoms are ejected by momentum exchange whereas the α -particle is stopped in the clamp due to some surface roughness. In the case that the α -particle reaches the scintillating housing or the CaWO_4 crystal, this background can be vetoed due to the extra light from the alpha.

The maximum energy a silver atom can obtain from the ^{206}Pb -recoiling nucleus (103 keV) is approximately 93 keV [KBP12]. Kuźniak et al. investigated the influence of the surface-roughness parameter (silver layer) on the final spectra of sputtered ions and Pb-recoils by using the GEANT4 simulation package. From their qualitative studies Kuźniak et al. conclude that a significant contribution to the number of events in the signal region in Run 32 data can come from sputtered silver ions.

For a definite statement on this possible new background a more sophisticated study has to be carried out, taking into account the correct surface-roughness parameters of the clamps used in Run 32 as well as the nature of radioactive contamination.

5.7.2. Sputtering on the Scintillating and Reflective Foil

Similar to the process described above, sputtering off the scintillating and reflective foil is also supposed to be a possible source of secondary backgrounds. Light elements may be ejected from the foil when hit by a ^{206}Pb -recoil, while the α -particle leaves the center of mass in the direction of the clamp and is lost for detection. Although the momentum transfer of the heavy Pb-nucleus to the light elements of the polymeric foil (hydrogen, carbon and oxygen) is not very efficient, there is a probability for light elements to be ejected, in particular for shallow incident angles of the Pb-nucleus. The characteristic light yield of such sputtered ions when hitting the crystal will depend on:

- the actual mass number of the sputtered elements
- the energy the light elements achieve from the interaction with the ^{206}Pb -nucleus
- the absolute number of sputtered elements ejected at the same time.

Diverse combinations of the afore mentioned aspects can lead to very different results concerning the light yield value of such sputtered events. In appendix C, the results from basic simulations carried out concerning surface sputtering of Pb-atoms of 103 keV on the PEN-layer of the foil are presented. The TRIM package was utilized for this simulations [Zie+12].

Not only the non-scintillating surfaces can be a source of ^{206}Pb -recoils, but also on the scintillating and reflective foil the deposition of α -emitters as for example from radon have to be prevented. This means the process described in this paragraph can also be induced from contaminations present on the foil itself, given the case that the escaping α -particle hits the non-scintillating clamp while the ^{206}Pb -nucleus may eject bunches of light elements (H-, C- and O-ions) from the foil.

From this simple simulation it can be shown that the sputtered bunches of ions induce by ^{206}Pb -nuclei can produce measurable signals in a CRESST detector. The sputtered ions can be vetoed in the case that the α -particle produces a scintillation light signal when hitting the foil. Only in the exclusive case where the α -particle escapes and hits the non-scintillating metal clamp surface are the sputtered bunches of ions expected to produce a signal which appears in the lower energy region.²³

For a final statement on the relevance of such a background in CRESST detectors, more detailed simulations would have to be carried out. However, simulations on this topic are very complex since many of the important input parameters are simply not known in detail. The right geometry of the detectors and their surroundings can be accounted for in the simulation, however the exact contribution and distribution of the α -emitters is unknown. In order to give an definite answer, a dedicated experiment to study possible sputtering processes is essential.

5.7.3. Conclusion

Secondary nuclear recoils coming from surface sputtering can be a very problematic background. Known sources of background can induce different kinds of secondary processes which might imply complex physics or simply have not been considered in the present analysis as they were completely unknown before.

It is most important to avoid α -emitters and their nuclear recoils on *all surfaces* close to the detectors by only using only very radiopure materials together with a strict radon-prevention in order to completely obviate secondary backgrounds.

The only effective approach to render both, the nuclear recoils and their secondary background harmless is by using a fully scintillating clamp concept. In the situation where only scintillating parts are present in the surrounding of the detector, these kind of background can be vetoed by the light emitted from the α -particle when traversing the scintillating surrounding.

²³Due to low statistics, no correlation between α -events and the identified signal events in the Run 32 data is observable.

Therefore, another main topic of this thesis is the investigation of next-generation clamping concepts to improve the current background situation of the CRESST experiment. Chapter 6 presents the different concepts investigated for future CRESST runs. In chapter 7 the results from measurements of these clamps are presented and discussed.

6. Development of New Clamping Concepts

The results of investigations made on clamp-induced background (chapter 5) are the basis for the development of new clamps. Two different strategies are followed: the development of a pure metal clamp design using radiopure materials to provide very low background conditions and, on the other hand, the development of a fully scintillating clamp concept to provide background identification.

For the pure metal clamp design, the bulk material, as well as its reflective coverage have to be manufactured from radiopure materials only. In order to prevent the implantation of $^{210}\text{Pb}/^{210}\text{Po}$ from ambient air, a consequent radon-prevention has to be provided during the fabrication of the alloy and the entire handling of the detectors.

For a scintillating clamp design, a coating for the clamps with a sufficient light output at low temperatures has to be found. In addition, no thermal relaxation events should result from this scintillating coating. This is realized by a crystal-clamp interface designed to prevent the direct transmission of relaxation phonons from the coating into the crystal.

In section 6.1, the main components of the clamps used to hold the crystal in position are introduced. Furthermore, the sections of this chapter are organized according to the different parts of a clamp. In section 6.2 the needs on the clamp-bulk material are presented. Section 6.3 provides information on the aluminum reflective coating of the bulk material. The light output of two scintillating coatings has been measured at low temperatures; results are presented in section 6.4. In section 6.5 three different crystal-clamp interfaces are introduced. The manufacturing of the different layouts as well as their advantages and limitations are demonstrated.

6.1. Overview

The schematic drawing in figure 6.1 introduces the possible components of a clamp for a new generation clamping concept developed within this work. The clamps consist of a radiopure and springy bulk material which is covered with a thin, highly-reflective layer. In the case of a fully scintillating clamping concept, an optional scintillating coating is applied onto the reflective layer to veto α -particles and recoiling nuclei. The contact between the clamp and the crystal is an important issue and can be provided in various ways. The dashed rectangle in figure 6.1 represents the different approaches investigated as crystal-clamp interface.

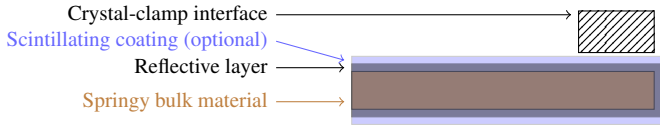


Figure 6.1. – Basic components of a clamp consisting of a bulk material, a reflective coating and an optional scintillating coating as well as an interface providing the contact to the crystal.

6.2. Bulk Material

6.2.1. Requirements

The following list summarizes the needs to be met by the next-generation bulk material:

- springiness at low temperatures to compensate different shrinkages of the materials. Springy materials keep the crystal tight enough to prevent microphonics but do not fracture the crystal because of too high pressure onto its surface.
- radiopurity, especially the presence of α -emitters has to be suppressed
- machinable
- diamagnetic as magnetic materials are known for their large specific heat which can prevent low temperature detectors from working due to a slow release of heat

Only few alloys meet at least some of these conditions: copper-beryllium (CuBe₂), bronze (CuSn₆) and an alloy of titanium-aluminum-vanadium (Ti90/Al6/V4). CuBe₂ was already used in a former CRESST run showing a high background-rate caused by ²¹⁰Pb. Beryllium cannot be obtained in high-purity quality and is known to be contaminated with lead. The titanium alloy is commercially produced with high-purity. However, its brittleness makes the shaping of the clamps impossible.

The most promising material is *bronze* because both tin and copper can be obtained in a high-purity grade and machining and handling of the alloy is standard. For the new clamp design, a dedicated sample of a CuSn₆ alloy was produced at the *Institut für Metallkunde und Metallphysik* in Aachen. The following section informs about the radiopurity measurements of the components of the alloy as well as the procedure adopted for its production.

6.2.2. NOSV Copper

Radiopurity

Bronze (CuSn₆) consists of copper (94 weight-percent) and tin (6 weight-percent). Both components have been analyzed concerning their radioactive contamination levels. Special interest is attributed to the radioactive isotopes ²¹⁰Pb/²¹⁰Po.

Electrolytically-refined NOSV copper from Aurubis AG has been used.¹ NOSV is also known as ETP1 copper (Electronic Tough Pitch). It has a very low hydrogen content and thus no heat leak caused by ortho-para-transitions of molecular hydrogen enclosures, a crucial aspect for low temperature applications.

Due to its electrolytic production, the radiopurity of the copper is very high [Heu95]. Two representative copper samples were analyzed by HR-ICPMS (High-Resolution Inductively Coupled Plasma Mass Spectrometry). A concentration of 342 ± 86 ppb and 337 ± 84 ppb of the stable isotope ^{208}Pb was found in these samples [Nis11].

The presence of stable lead does not necessarily imply the presence of ^{210}Pb in relevant amounts. However, the activity from ^{210}Pb in pure lead that has been refined recently can be as high as 2500 Bq/kg [BAH68], corresponding to 0.9 ppt of ^{210}Pb .

With the conservative assumption of a ^{210}Pb contamination in lead of 2500 Bq/kg, the corresponding contamination of the measured NOSV sample yields 3.3 mBq/kg (corresponding to an atomic ratio of $35 \cdot 10^{-19}$). This calculated value should be interpreted as a conservative upper limit.

The contamination of ^{210}Pb in the bronze material used in Run 32 was measured to be 6.9 ± 0.9 Bq/kg or about 0.8 ppq (HPGe-measurement at LNGS, [Lau11]) which is more than three orders of magnitude worse than the one estimated for the NOSV. Regarding the number of events present in the data attributed to this background source, a suppression of a factor of 1000 is desirable for a next-generation clamp material. Therefore, the NOSV meets the requirements for the production of the next-generation bronze material.

Cleaning and Passivating

The ^{210}Pb -activity in NOSV copper, as estimated above, is based on the valid and conservative abundance of ^{210}Pb found in a bulk of contemporary lead. Hence, this estimate is valid if there is no mechanism present that leads to an additional enhancement of ^{210}Pb relative to the amount of stable Pb.

Many low-background experiments use NOSV and so far no indications have been found for an enhancement of ^{210}Pb during production. However, care has to be taken when cleaning the copper surfaces, since radon daughters plate out on exposed surfaces and may lead to a residual ^{210}Pb background [WZ07].

All copper pieces used for the alloy production had machined surfaces and, thus, needed to undergo a chemical cleaning process: a concentrated nitric acid etch (1 HNO_3 (70%, supra-quality) : 3 H_2O) is used to remove the upper surface layers. Thereby, ^{210}Pb is also removed efficiently. However, ^{210}Po is known to return to the cleaned surface from the solution [WZ07]. In order to prevent a re-deposition of polonium, the etching-solution is exchanged repeatedly during the cleaning procedure. In addition,

¹In 2009 the Norddeutsche Affinerie AG rebranded itself as Aurubis.

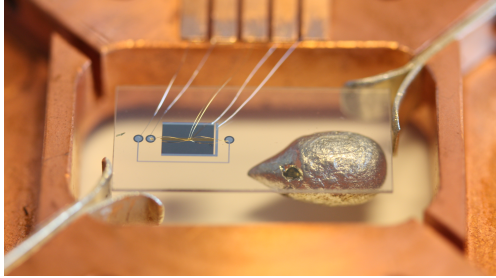


Figure 6.2. – In order to determine the radioactive contamination from ^{210}Pb in tin, a calorimetric method has been developed. A drop-shaped tin piece is glued onto a sapphire crystal. The sapphire is equipped with a TES to detect particle interactions in the tin absorber. The tin is both absorber and source of its own radioactive contaminations, in particular of ^{210}Po , showing a α -peak at around 5.4 MeV.

the cleaned copper surfaces are protected from oxidation [Hop+07] by passivation with a citric acid solution ($1 \text{ H}_2\text{O}_2 : 1 \text{ H}_2\text{O} + 5\%$ in weight of citric acid).

6.2.3. Tin

The tin used for the alloy-production has a purity of 99.99999% (Alfa-Aesar). Since tin is not commonly used in rare event searches, no information is available on its radiopurity, in particular on the abundance of $^{210}\text{Pb}/^{210}\text{Po}$. By all means, significant amounts of lead can be found in tin due to their chemical similarity.

The result from an ICPMS analysis gives an upper limit of 100 ± 25 ppb. Assuming again a maximal contamination of ^{210}Pb of 0.9 ppt [BAH68], the radiopurity of tin would be adequate for the production of the new alloy. However, since no direct measurements of the $^{210}\text{Pb}/\text{Pb}$ -ratio are available, the estimated values are not very reliable.

Calorimetric Method to Determine the ^{210}Pb -activity

For a direct measurement of a contamination with ^{210}Pb , tin was used as an absorber in a cryogenic calorimeter.² In this way the tin works as source and detector of its own intrinsic contamination with ^{210}Pb , since the α -decay of ^{210}Po deposits an energy of about 5.407 MeV. Besides, the 46.5 keV gammas from the β -decaying ^{210}Pb could also be used to identify the presence of ^{210}Pb .

The detector set-up is shown in figure 6.2. The tin absorber is drop-shaped and weighs 993 mg. It is glued onto a sapphire carrier crystal ($(20 \times 10 \times 1) \text{ mm}^3$) using

²Only because tin is a superconductor with vanishing electronic heat capacity at the operating temperature, it can be used as absorber.

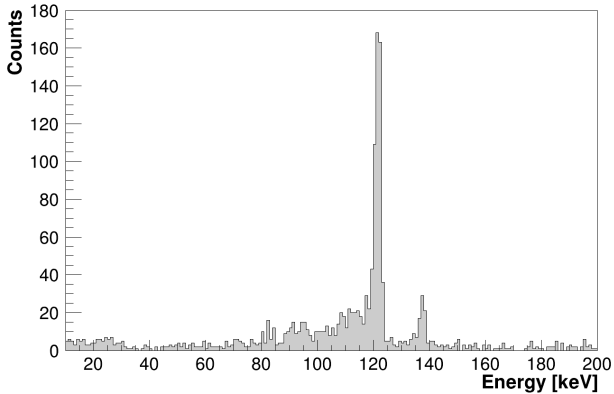


Figure 6.3. – Energy spectrum of the tin absorber when irradiated with a ^{57}Co -source. The lines at 122 keV and 136 keV are nicely separated.

epoxy resin (EpoTek[®] 301-2). The thermometer used to read out the absorber is a W-TES evaporated onto the carrier crystal. The TES is modified in geometry to meet the requirements of this measurement. Identical to a standard TES, it is equipped with a heater structure to allow for a stabilization within its superconduction transition as well as for calibrating the detector using heater pulses (see section 4.3.3).

The carrier crystal is fixed in its copper holder by two pairs of aluminum coated clamps. In order to ensure a low-background environment, all copper pieces have been chemically cleaned after machining.

Data Analysis Particles can deposit energy in the carrier crystal as well as in the tin absorber. Due to differences in pulse-shapes, events in the tin absorber can be well distinguished from those in the crystal. A cut on the decay-time or the peak-position parameter allows to remove all carrier hits down to threshold energy (10 keV).

Two different analyses were performed: one for the low energy region ([10-200] keV) and one for the high-energy region (>3 MeV). The operating point of the TES was set to allow for a large dynamic range in order to detect α -particle interactions. The response of the TES could be linearized up to an energy of 7 MeV by means of heater pulses.

For the low energy region from 10 keV to 200 keV a template fit was applied in order to determine the amplitude of the pulses (see section 4.3.3).

In the case of high-energy events from α -particle interactions (>3 MeV), the pulse-height parameter as determined by a moving average of 50 samples is used to determine the pulse amplitude instead. Particle pulses with a larger amplitude reveal slight

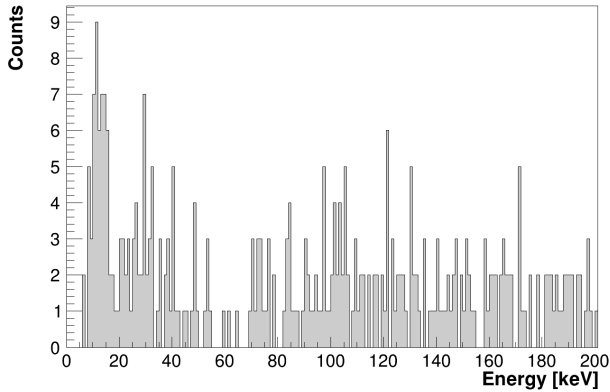


Figure 6.4. – Low energy spectrum of the tin absorber. No peak can be observed around 46.5 keV, the energy of the gamma-transition expected from a decaying ^{210}Pb -nucleus.

changes in pulse-shape.³ Typically, a change in pulse-shape is observed when leaving the linear range of the transition. Since only the particle pulses from the tin absorber show a change in their pulse-shape at high pulse amplitudes, whereas heater pulses remain unchanged, the effect is to be attributed to the physical properties of the tin absorber. The pulse height parameter filtered from a 50 sample moving average is not sensitive to pulse-shape and allows us to reliably reconstruct the amplitude of observed α -events. As explained in section 4.3.2, the moving average does not have the same precision as the template fit in the linear region of the transition curve. However, its accuracy is adequate and efficient to identify the α -events from ^{210}Po .

Calibration An external ^{57}Co γ -source was used to calibrate the energy response of the tin absorber. The calibration spectrum is shown in figure 6.3. The detector nicely separates the two lines at 122 keV and 136 keV, the resolution at 122 keV is 2.48 keV (FWHM). The left shoulder on both lines is caused by Compton scattering in the thermal shields of the cryostat [Kra12]. Gammas that scatter in the shielding under small angles may be seen in the detector. These gammas lose a small amount of their initial energy by the scattering process. When detected in the calorimeter, they form the observed shoulders extending to lower energies. Another effect correlated with ^{57}Co is Compton back-scattering. Back-scattering can explain the peak-like structure around 80 keV. The relevance of scattering is confirmed by a Monte Carlo simulation [Kra12].

³Pulses with large amplitudes show a slight change in the rise time. This leads to an underestimation of the amplitude if determined by a template fit. The moving average allows to evaluate the accurate pulse height.

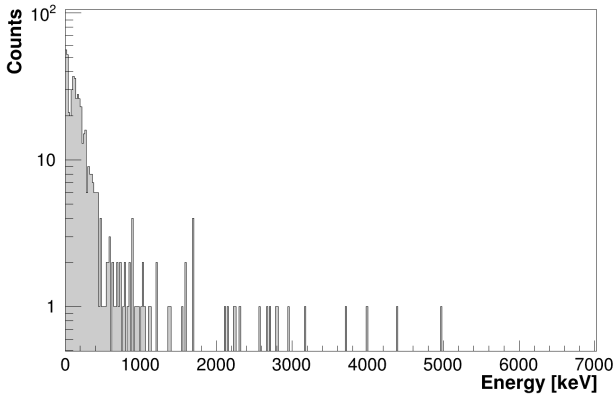


Figure 6.5. – High-energy spectrum of the tin absorber. Above an energy of 3000 keV the experiment is almost background-free. No events are observed around the Q-value of ^{210}Po of 5.407 keV. A 90% C.L. upper limit of 28.2 mBq/kg can be given for the tin bulk.

Results The acquired background data correspond to an exposure time of 81731 s (≈ 1 day). Figure 6.4 shows that the low-energy spectrum ([10-200] keV) does not provide any prominent structures. In particular, no peak is visible around an energy of 46.5 keV, where the gamma-line of ^{210}Pb would be expected. Due to the level of external e/γ -background, any peak containing only few events is hidden in the background. Moreover, to set an upper limit for the activity of ^{210}Pb from the 46.5 keV gamma-transition is not significant since, due to low statistics, there is no possibility to estimate the expected background from surrounding materials in this energy region. In the interval from 20 keV to 42 keV in total 57 events are observed. In order to look for events from ^{210}Pb , an interval of 44 to 66 keV (accounting for the energy resolution from test pulses) has to be considered. However, in this energy interval only 17 events are observed. This illustrates that without an estimation of the expected external e/γ -background there is no meaningful result in form of an upper limit for the ^{210}Pb -concentration possible.^{4,5}

A more sensitive and elegant approach in order to determine the activity expected from ^{210}Pb is to look for the decay products of the isotope ^{210}Po . ^{210}Po emits an α -

⁴The external e/γ -background would have to be described by an exponential at low energies as well as a Landau distribution accounting for the observed bump-like structure peaking around 150 keV which results from muon-bremsstrahlung generated from muon-induced electron-showers in the surrounding materials. However, in order to fit such data, a lot higher statistics has to be obtained.

⁵Assuming that *all* 17 events in the region from 44 keV to 66 keV originate from ^{210}Pb , this corresponds to an activity of about 210 mBq/kg in tin. The upper limit for tin found from the α -analysis is 28.2 mBq/kg. From a given activity of 28.2 mBq/kg one would expect to observe 2.3 events only.



Figure 6.6. – Rolled stripes of low-background CuSn6.

particle ($Q=5.407$ MeV; $T_{1/2}=138.38$ d) and the corresponding nuclear recoil has an energy of about 103 keV. Both the α -particle and its recoiling nucleus are absorbed in the tin.

Figure 6.5 shows the energy spectrum up to an energy of 7 MeV. The high energy region is background-free, only a few counts are visible above 3 MeV, the maximum energy observed from e/γ -background from the surrounding of the experimental set-up. Thus, in the case no counts are observed, the gained limit exclusively depends on the measuring time. This is a definitive advantage in comparison to radiopurity measurements carried out using HPGe-detectors.

Around the Q-value of ^{210}Po no events are observed. Taking into account the energy resolution in this energy region, as determined by heater pulses (5310 keV and $\text{FWHM}=7.4$ keV), a 90% C.L. upper limit of 28.2 mBq/kg can be derived for the activity of ^{210}Po in tin. This would correspond to 1.7 mBq/kg in bronze which is more than three orders of magnitude lower than the activity in the former bronze material (6.9 ± 0.9 Bq/kg from ^{210}Pb).

In order to keep the contamination with ^{210}Po for the bronze materials at such low levels as found for the pure tin and NOSV cooper, the alloying process has to be carried out in a controlled and clean way to not introduce further contaminations.

6.2.4. Production of CuSn6

The production of CuSn6 (6% Sn in weight) was carried out together with the *Institut für Metallkunde und Metallphysik* at RWTH Aachen in a *vacuum-inductance furnace* (chamber volume 900l, 70 kW at 10 kHz).

Preparation of Components The surface of the NOSV copper was machined and chemically cleaned in concentrated nitric acid etch. Tin was used, as delivered from Alfa Aesar (drop-shaped pieces), stored in a HDPE-container.

Preparation of the Crucible The crucible is made by SGL-Carbon from high-purity graphite (R6500). After production, the crucible was cleaned by heating in a chlorine atmosphere. The level of ash-remnants was measured to be <5 ppm (P5 quality). A second cleaning step was carried out at RWTH. The crucible was heated in the inductance furnace to 1800 °C under vacuum conditions ($< 10^{-3}$ mbar, 60 min). After this annealing the crucible was stored under vacuum.

Alloying Tin and NOSV copper were loaded in the crucible. The furnace was flushed by evacuating ($< 10^{-3}$ mbar) and venting with argon gas (Ar 6.0 quality).

The components were fused by gradually increasing the furnace power under the presence of 500 mbar of Argon. Since NOSV copper contains up to 300 ppm of oxygen, solidification of the melt in the crucible was carried out while evacuating the furnace. To ensure a complete degassing the procedure (melting under Argon atmosphere and evacuating) was repeated. As a last step the melt was cast into the chill-mold and cooled down in an argon atmosphere.

Preparation of the Chill-Mold The chill-mold is made out of copper which has also been extensively cleaned in concentrated nitric acid. The black wash used for coating the chill-mold is a boron nitride aluminum oxide mixture (LC25B).⁶ LC25B has been applied onto the chill-mold in subsequent steps to gain a sufficient thick coating. After applying the LC25B, the chill-mold was annealed at 180 °C.

Homogenization and Rolling The CuSn6-ingots were machined and rolled down to sheets of thickness of 0.38 mm, 0.45 mm and 0.50 mm (see figure 6.6). In between the rolling steps, the alloy was annealed again for homogenization. In order to prevent an introduction of radioactive contaminations from surface-diffusion, the CuSn6 stripes were extensively cleaned in nitric acid etch before annealing. In this way possible surface contaminations from the rolling were removed. The annealing was carried out at 750 °C for 14 h in a tempering oven within a new quartz tube.

6.3. Reflective Coverage of Clamps

Given the fulvous appearance of bronze, its reflectivity of the blue scintillation light from the CaWO₄ crystals is poor. In order to obtain better reflectivity, a *thin layer of aluminum* is deposited onto the clamps in a Magnetron sputtering system.

Applying a reflective layer by electroplating is no longer considered since it bears the risk of implementing radioactive contaminations. In particular, since available electroplating solutions are not of high-purity quality.

⁶The radiopurity of various black wash was checked by a HR-ICPMS analysis. The LC25B turned out to most suitable because it showed the lowest contamination level.

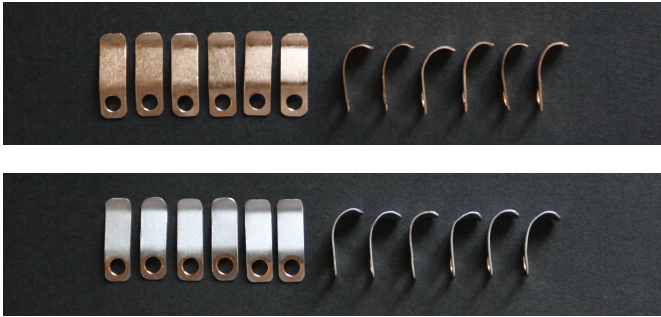


Figure 6.7. – The upper picture shows a set of bare CuSn6 clamps after chemical cleaning (front view, side view). In the lower photograph, the clamps are coated with a thin layer of highly-reflective aluminum.

6.3.1. Etching

Before the sputtering, the clamps have to pass a chemical cleaning process. First, the clamps are washed about 15 min in an ultrasonic bath of 1% of Micro90[®], an alkaline aqueous solution that removes oil, grease, biological materials and insoluble oxides from the machining process. Afterwards, the clamps are rinsed with deionized water.

The second step is the etching of the clamps in nitric acid (1 HNO₃ (70%, supra-quality) : 3 H₂O). During etching the clamps are agitated to ensure homogeneous etching of all surfaces. The etching rate strongly depends on the temperature of the etch solution, but also on the concentration of Cu-ions, which work as a catalyst. At a temperature of 21 °C, the time necessary to remove 25 μm was 6.5 min. The etching is followed by thorough rinsing with deionized water.

6.3.2. Passivating

The clamps are passivated in citric acid solution (1 H₂O₂ : 1 H₂O + 5% in weight of citric acid (supra-quality)) for 10 min and then the clamps are agitated again. After passivation, the clamps are rinsed exhaustively and sonicated in deionized water.

6.3.3. Sputtering

The Magnetron sputtering system at the Max-Planck-Institut (Munich) is equipped with an aluminum-target suitable for a radiopure reflective coating of the clamps. In the case that the target material is sufficiently radiopure no enhancement of radioactive isotopes is expected from the sputtering process.

In order to get an idea about possible radioactive contaminations in such sputtered layers, an ICPMS-analysis of a sputtered aluminum-film was performed. An aluminum

film was sputtered onto a sapphire wafer. For the analysis the aluminum was completely dissolved by etching. In order to account for possible contaminations from the substrate, a pure sapphire-wafer was also subjected to an identical treatment, followed by an ICPMS-analysis.

A contamination from ^{232}Th of 4 ppb was found in the aluminum. For ^{238}U only an upper limit of <5 ppb can be given. Uncertainties of given values are 30% [Nis11].

In order to judge if the level of radiopurity of the aluminum is sufficient a simple estimation can be devised. When assuming a thickness of about $1\ \mu\text{m}$ of aluminum on the surface of the clamps, this results in an upper limit for the expected activity of <70 nBq/set of clamps for uranium and about $0.45\ \mu\text{Bq/set}$ of clamps for thorium. This is sufficient for the next generation of clamps.

Before the deposition, the surfaces are cleaned by ion gun bombardment. After a pre-sputtering of 5 min, a coating thickness of about $1\ \mu\text{m}$ is obtained. A picture of a set of bare CuSn6 clamps as well as that of a set of clamps covered with aluminum can be seen in figure 6.7. These coated clamps are used for the “pure metal design”.

In the case of a scintillating clamp concept a scintillating coating has to be applied onto the surface of the clamps. Two different coatings have been tested, the results from these tests are discussed in the next section.

6.4. Scintillating Coating of Clamps

6.4.1. Motivation

The performance of the pure metal clamps, as shown in the lower photograph in figure 6.7, depends on reliable radon-prevention in order to obtain low background conditions. This also requires a handling of the clamps and assembling of the detector in a radon-free environment. Otherwise, radon and/or its progenies can get implanted from ambient air into the surface of the clamps and/or the reflective and scintillating housing and may mimic WIMP interactions.

In order to reject nuclear recoils, the *entire* surrounding of the detectors has to be scintillating. Thus, a completely scintillating clamp design is aimed for in order to render any background induced by α -emitters harmless.

A *scintillating coating* applied onto the clamp will work as a veto in the case where an α -emitter decays on its surface and the recoiling nucleus is traveling to the CaWO_4 crystal. The additional light signal produced by the α -particle in the scintillating coating is detected together with the small light signal emitted from the crystal when hit by the recoiling nucleus.⁷ In this way low-light signals from recoiling nuclei are prevented.

The principle can be illustrated by taking a look again at the light-yield energy plane from a detector module operated in Run 32 (see figure 6.8). All crystals in Run 32 were kept in position by bare metal clamps.

⁷The response time of the detector is orders of magnitude slower than possible time differences in the production of the scintillation light coming from both the foil and the crystal.

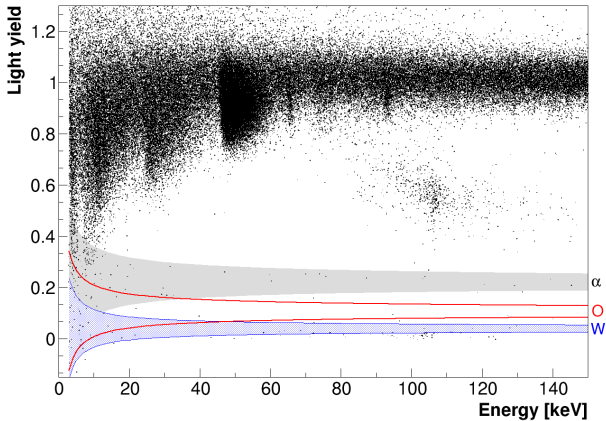


Figure 6.8. – Data in the light yield-energy plane for a detector module operated during Run 32. The blob around an energy of 100 keV and a light yield of 0.6 corresponds to ^{210}Po -events: the Pb-recoil hits the crystal and the α -particle hits the scintillating foil thereby producing additional scintillation light. If the surfaces of the clamps were also coated with a scintillator, the events inside (slightly below) the W-recoil band (blue) would also have been shifted to higher light yield-values, away from the WIMP signal region. The same is valid for degraded alphas (grey-band).

Two different cases have to be considered: ^{210}Po may be implanted into the surface of the crystal/reflective and scintillating foil or may be present on the pure metal clamps. In the following paragraphs only the relevant cases, where the recoiling nucleus is emitted in the direction of the crystal, are discussed.

^{210}Po present on the Crystal or on the Foil The ^{206}Pb -recoil deposits its energy (maximal 103 keV) in the crystal. The light emitted by the foil when hit by the α -particle is added to the small light signal of the crystal. Hence, the ^{206}Pb -recoils do not appear in the W-recoil band (blue-colored band) in figure 6.8 but are shifted to a higher light yield. In figure 6.8 these events are visible in form of a blob-like structure at an energy of roughly 103 keV and a light yield of about 0.6. Energies ≥ 103 keV can be detected in the case the ^{210}Po -nucleus is implanted into the crystal. The full energy of the lead nucleus of 103 keV plus a possible contribution from the α -particle before escaping from the crystal is detected. Instead if the ^{210}Po is present on the surface of the foils the energy absorbed in the crystal is ≤ 103 keV.

^{210}Po present on the Bare Metal Clamps ^{210}Po present on the clamp results in nuclear recoil events appearing in or slightly below the W-recoil band (blue band in figure 6.8). Depending on the implantation depth of the decaying nucleus, the energy

distribution of these events can go down to the energy threshold. Hence, these events may leak into the region of interest for WIMP search. In Run 32 this kind of events are identified to be responsible for a significant background contribution in the region of interest. A scintillating coating of the clamps could render this background harmless by shifting these events up to higher light yield values.

Properties of the Scintillating and Reflective Foil

In order to define the requirements on the scintillating coating for the clamps, it is useful to study the scintillation properties of the multi-layer foil (VM2002) from 3M used for the housing of the detectors. This foil has a scintillating surface and provides an effective veto for α -background induced by surface contaminations of the crystal or the foil itself. If hit by an α -particle of 5.4 MeV about 2 keV are emitted in the form of scintillation light.^{8, 9}

As a comparison the absolute energy measured in light for a 5.4 MeV α -particle interacting in CaWO_4 is about 22 keV.¹⁰ Although the value gained in CaWO_4 is about a factor of ten higher than in the foil, the emitted light by the foil is sufficient to shift the background from α -emitters to higher light yields, away from the region of interest. Thus, the scintillation light gained from any particular clamp coating should be at least as good as the multi-layer foil.

In the following section, the work effort to find a scintillator fitting all requirements for an efficient coating for the clamps is presented. The discussion starts with an introduction to the experimental set-up used to investigate different coatings at low temperatures.

6.4.2. Set-up to Study Scintillation Efficiencies

Figure 6.9 shows a scheme of the set-up used to investigate the scintillation properties of diverse coating materials at temperatures around 15 mK.

The coating to be tested is irradiated with a three-line α -source consisting of ^{239}Pu , ^{241}Am , ^{244}Cm corresponding to α -energies of 5.2 MeV, 5.5 MeV and 5.8 MeV. A collimator made out of copper adjusts the α -rate to about 0.5 s^{-1} . The light detector is facing the scintillator-sample and is calibrated by a ^{55}Fe -source. The whole set-up is surrounded by highly-reflective aluminum. In the following paragraph the results from ZnO and an epoxy based scintillator are discussed.

⁸The thickness of the foil is sufficient to stop alphas of some MeV but no information is available on the actual thickness of the scintillating surface layer of the foil. Since only one "peak" is observed although alphas of different energies interact in the foil, the thickness of the scintillating part is estimated to be only few 10 μm . Thus, the detected 2 keV may not correspond to full absorption of an alpha of 5.4 MeV (^{210}Po -decay).

⁹For an absolute energy calibration of the light detector, the light absorber is irradiated by low energy X-rays from ^{55}Fe . X-rays from ^{55}Mn show energies of 5.9 keV and 6.5 keV for K_α and K_β , respectively. As the attenuation length of 5.9 keV in copper is about 10 μm , the source is placed inside the cryostat.

¹⁰The overall detected scintillation light from CaWO_4 crystals for e/γ -interactions varies between 1% and 2%, depending on the quality of the crystal.

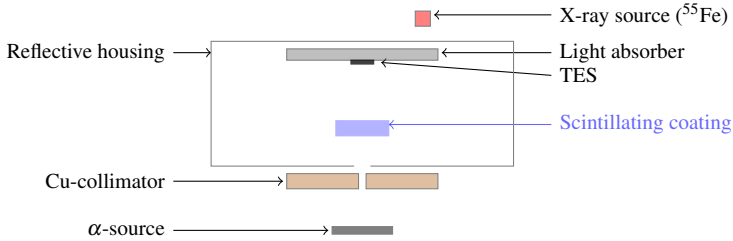


Figure 6.9. – Set-up used to investigate low temperature scintillation properties of a ZnO-layer and of a plastic scintillator coating. The amount of scintillation light produced by irradiating the sample with an α -source is determined. An absolute energy calibration of the light detector is obtained by low energy X-rays.

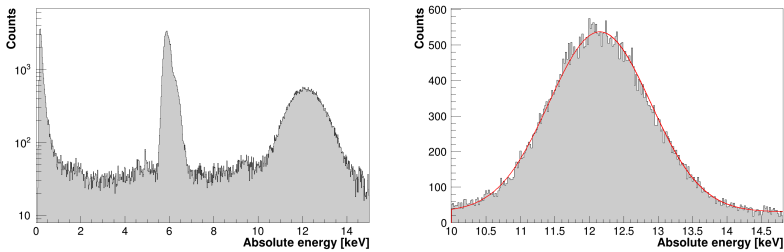


Figure 6.10. – Spectrum of a ZnO-layer facing the light detector and irradiated with an α -source (left picture). The scintillation-peak from ZnO is visible around 12 keV. The peaks at 5.9 keV and 6.5 keV come from ^{55}Fe and allow for an absolute energy calibration of the light detector. The right plot shows the scintillation-peak fitted with a Gaussian ($E=12.2\text{ keV}$ with $\text{FWHM}=1.7\text{ keV}$).

6.4.3. ZnO Layer

ZnO is known to be a scintillator also at low temperature. A ZnO-layer with a thickness of approximately $1\ \mu\text{m}$ was deposited onto a sapphire crystal ($(10 \times 10 \times 5)\text{ mm}^3$). The sample was produced in collaboration with the University of Leipzig via Pulsed Laser Deposition [Lor09].

Since the ZnO-layer is very thin, the alphas pass through it and finally stop in the sapphire crystal. As sapphire also scintillates weakly two measurements were performed. In a first measurement the ZnO-layer was facing the α -source, in the reference measurement the sapphire carrier was installed to face the α -source.

The logarithmic spectrum from the ZnO-layer facing the alpha-source is shown in figure 6.10. At an energy around 6 keV the ^{55}Fe is visible. Another peak appears at

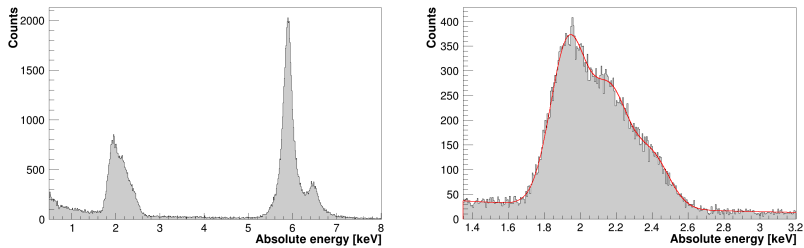


Figure 6.11. – Spectrum of the light detector obtained by irradiating the epoxy-based scintillator with a three line α -source (left plot). The scintillation-peak at around 2 keV can be fitted with three Gaussian at 1.9 keV, 2.2 keV and 2.4 keV (FWHM=0.2 keV) corresponding to α -energies of 5.2 MeV, 5.5 MeV, and 5.8 MeV (right plot). The K_{α} -line at 5.9 keV from ^{55}Fe is used for calibration.

12.2 keV (FWHM=1.7 keV). Since this peak is only present when irradiating the ZnO-layer, and disappears when irradiating the sapphire crystal (reference measurement), it is attributed to the scintillation of ZnO. Even though the ZnO-layer is too thin to fully absorb the alphas, the amount of scintillation light emitted from the ZnO is about a factor of six higher than detected from the VM2002 foil.

The thin ZnO-layer proved to be a very good scintillator at low temperatures. However, ZnO showed a porous and harsh surface after cooldown. Small pieces of the ZnO-layer were coming off. Furthermore, the manufacturing of the ZnO is done via PLD at temperatures around 500-700 °C. This is quite close to the melting point of CuSn6 and may influence its mechanical properties.

Alternative materials were searched for which do not show mechanical degradation by cooling and can be applied onto the clamps without the need of high temperatures.

6.4.4. Plastic Scintillator

A plastic scintillator coating based on an epoxy resin was developed: the epoxy resin Epo-Tek 301-2 (EpoxyTechnology) is not a scintillator by itself. Therefore, the organic powder 2,5-diphenyloxazole (PPO), that emits scintillation light in a wavelength region where CRESST light detectors are sensitive, was added to produce a scintillator. The PPO-powder (PerkinElmer, neutrino-grade), at a concentration of 0.1% in weight, was dissolved in the curing agent of the epoxy resin before mixing with the resin. The viscosity of the epoxy resin is very low and allows for thin coating layers. For the measurement, a slab (10 x 20 x 2) mm³ was machined out of a cast block. The sample was investigated using the same set-up as described before (figure 6.9).

Since the sample thickness is by far larger than the projected range of the alphas,

Element	Unit	Concentration
Pb	[ppb]	6
U	[ppt]	18
Bi	[ppt]	17
Th	[ppt]	18

Table 6.1. – Results of an ICP-MS analysis of PPO used to produce the plastic scintillator. The uncertainties are 25% of the given values [Nis11].

the total energy of the alphas is deposited in the sample. Figure 6.11 shows the results when irradiating the plastic scintillator sample with the α -source. The spectrum shows a scintillation peak at around 2 keV. A fit of three Gaussian to the scintillation peak is shown in the lower picture in figure 6.11. Accordingly, the α -energies of 5.2 MeV, 5.5 MeV and 5.8 MeV correspond to light energies of 1.9 keV, 2.2 keV and 2.4 keV (FWHM=0.2 keV).

Radiopurity To study the radiopurity of the epoxy resin and the PPO-powder, an ICP-MS analysis of the PPO powder, as well as a HPGe-measurement of a representative plastic scintillator sample was made [Nis11; Lau11]. The results from these studies are listed in table 6.1 and table 6.2, respectively.

The total amount of plastic scintillator applied onto a complete set of clamps of one detector module is about 200 mg (200 μ g of PPO). A rate <4 μ Bq per detector module is calculated assuming a contamination of ^{210}Po of <20 mBq/kg in the scintillator. Considering that events induced by α -emitters can be discriminated due to the produced scintillation light in the coating, this limit would be acceptable since it is of the same order of magnitude as determined for intrinsic contaminations in our CaWO_4 crystals. In other words, the coating would not introduce a dominant background.

The contamination of Pb in PPO examined by ICP-MS analysis is 6 ppb. Typical abundances of ^{210}Pb in pure Pb range from 0.04 to 1 ppt (see also section 6.2.2). Even assuming a very high abundance of 1 ppm, an activity of only 3.2 μ Bq per detector module is obtained. Hence, the PPO as well as the epoxy resin fulfill the radiopurity requirements.

6.4.5. Summary

The scintillation properties of the plastic scintillator are comparable to the scintillating foil used for the housing of the detectors. The plastic scintillator is favored for the coating as it does not show mechanical degradation by cooling and it can be applied onto the clamps with a simple brush-technique.

Decay chain	Nuclide	Activity
^{232}Th	^{228}Ra	< 25 mBq/kg
	^{228}Th	< 15 mBq/kg
^{238}U	^{226}Ra	< 25 mBq/kg
	^{234m}Pa	< 0.41 Bq/kg
^{235}U	^{235}U	< 24 mBq/kg

Table 6.2. – Results from a HPGe-measurement of the home-made plastic scintillator. Only upper limits can be given on contaminations from uranium-/thorium decay chains. Results are given within 68% confidence limits [Lau11].

So far the clamp bulk material and the scintillating coating which will be used to cover the main parts of the clamp surfaces have been discussed. The following section will introduce the different interfaces which have been developed and tested.

6.5. Crystal-clamp Interface

The interface between the crystal and the clamp is of crucial importance. From experiences made in Run 31 (see section 5.2), plastic is ruled out as interface material. Plastic scintillators in contact with the crystals gave rise to numerous events with various pulses-shapes, that are supposed to originate from relaxation processes in the plastic.

In Run 32 and also former runs pure metal clamps proved to work; no events with different pulse-shape have been observed. However, metal does not allow for an active discrimination of α -particles and their recoil background.

In this work four different types of clamp interfaces have been designed and will be introduced in the following sections.

6.5.1. Calcium Tungstate Balls

The first of two *complete scintillating* clamping concepts uses small balls made out of CaWO_4 (diameter 2 mm) as interface between clamp and crystal.¹¹

A layer of the epoxy-based plastic scintillator is applied onto all surfaces, including edges of the cleaned and coated clamps.¹² A hole in the clamp receives the CaWO_4 ball. In figure 6.12 a sub-set of this type of clamps is depicted. The picture on the left hand side shows the clamps in daylight conditions. On the right hand side the clamps

¹¹The small CaWO_4 -balls were produced by Kuhn-Edelsteinschleiferei.

¹²The thickness of the scintillator coating is around 40-60 μm , measured by a micrometer calipers.

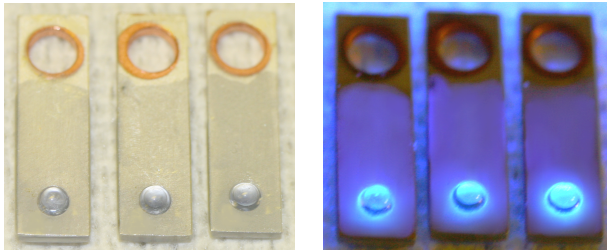


Figure 6.12. – A fully scintillating clamp design is obtained by covering the aluminum coated CuSn6 clamps with a thin layer of plastic scintillator. The balls providing the interface between clamp and crystal are made out of CaWO₄. The picture on the right hand side shows that both the CaWO₄-balls and the coating of the clamp scintillate when excited by UV light.

are excited by UV light. The plastic scintillator coating as well as the CaWO₄-balls scintillate in the blue regime of the visible spectrum.

6.5.2. Calcium Tungstate Half-cylinders

The second complete scintillating clamp design utilizes an interface of polished half-cylinders made out of CaWO₄: the aluminum coated CuSn6 clamps were covered with a thin layer of the epoxy-based scintillator before the CaWO₄ half-cylinders were glued onto the coated clamps by using a tiny amount of EpoTek 301-2. The half-cylinders measure 4 mm in diameter and height.¹³

Figure 6.13 shows two photographs of a complete set of these clamps. The upper picture shows the clamps in daylight. The lower picture was taken while exciting the clamps with UV light. Scintillation light is emitted from all surfaces, although the scintillation from the coating is less visible in the picture.

6.5.3. NOSV Half-cylinders

Since no relaxation events caused by the clamps were detected in previous measurements utilizing metal clamps, a set of clamps was tested which combines a metal interface with a partially scintillating clamp surface.

The aluminum covered CuSn6 clamps were coated with a thin layer of plastic scintillator. Small half-cylinders manufactured out of NOSV copper are used as interface between the clamps and the crystal. The NOSV half-cylinders measure 4 mm in diameter and height and have been chemically cleaned following the same procedures as established for CuSn6 (see section 6.3). During the chemical treatment the etch

¹³The half-cylinders were produced at the “Kristall-Labor“ at Technical University in Munich.



Figure 6.13. – A full set of clamps using CaWO_4 half-cylinders as interface. After applying a thin layer of plastic scintillator, the half-cylinders are glued onto the clamps by a tiny amount of epoxy resin. In the lower picture, the clamps are irradiated with UV light. Blue scintillation light is emitted from all surfaces. The small fissures in some of the half-cylinders were caused by cooling ((clamp 4, 6 and 9 counting from the left hand side; also see section 7.3.2).

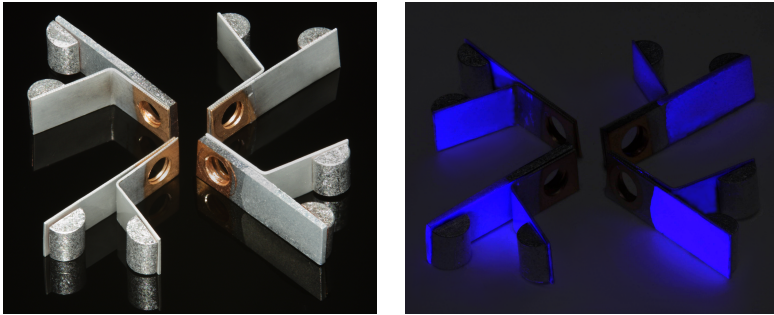


Figure 6.14. – A *partially* scintillating clamp design utilizing metal interfaces. A thin layer of plastic scintillator is applied onto the aluminum coating of the CuSn6 clamps. Al-coated half-cylinders providing the interface between crystal and clamps are made out of NOSV. The photograph on the left hand side shows a sub-set of these clamps in daylight whereas the photograph on the right hand side shows the clamps under excitation with UV light. The NOSV half-cylinders do not scintillate and can be recognized.

was renewed to prevent spontaneous out-plating of ^{210}Po from the solution. The half-cylinders were coated with a thin layer of aluminum by Magnetron-sputtering and glued onto the coated clamps using a small amount of EpoTek 301-2.

Figure 6.14 shows a sub-set of these clamps at day light (left photograph) and while being irradiated with UV light (right photograph). The NOSV half-cylinders, the only non-scintillating parts of the clamps, are clearly visible.

6.5.4. Pure Metal Concept

The background caused by silver-coated bronze clamps in Run 32 can be attributed to three main sources:

- the bulk material causes degraded α -events in the detector
- the highly-reflective silver-coating shows a contamination with ^{210}Po , most probably from spontaneous deposition out of the silver-solution used for plating
- implantation of ^{210}Po / ^{210}Pb from ambient radon onto the surface of the clamps and the reflective and scintillating foil surrounding the detector

In order to eliminate these backgrounds, a dedicated CuSn6 bulk material was alloyed (see section 6.2). The reflective coverage is radiopure as consisting of a sputtered aluminum film with a thickness of only $1\ \mu\text{m}$. Furthermore, radon-prevention methods are established in the manufacturing and handling process of the clamps in order to prevent implantation of radioactive nuclei from ^{222}Rn .

Therefore, besides the fully and partially scintillating clamping concepts, even pure metal clamps may be used again in a future CRESST run. In the case of an efficient radon-prevention during the entire handling of the clamps, the level of radioactive contaminations on the aluminum covered CuSn6 clamps should be at least three orders of magnitude lower than in Run 32 (see section 6.2). This is consistent with the requirements on a next-generation clamping concept. A picture of a sub-set of pure bronze clamps coated with aluminum was shown in figure 6.7.

7. Results for Different Clamp Concepts

In this chapter the results obtained by testing the different clamping concepts introduced in chapter 6 are presented.

The underground test-facility at LNGS, which was the precondition for all measurements and was set-up within this thesis, is introduced (section 7.1). In section 7.2 the detector module used for the measurements is described. Finally, section 7.3 gives detailed information on all tested clamping concepts. The different designs and corresponding observations, advantages and limitations, when being tested in a set-up providing identical conditions as in CRESST, are discussed in detail. The results are followed by a short summary (section 7.4).

7.1. Test-facility at Gran Sasso

Relevant information on the performance and functionality of the clamps can only be obtained if they are tested in a detector configuration which is identical to the one used in the main CRESST experiment. Hence, the crystal for the measurements had standard CRESST dimensions - a cylinder measuring 40 mm in diameter and height.

However, such large crystals cannot be operated above ground. The expected count rate from hadrons and muons originating from cosmic radiation would be as high as few 100 s^{-1} . Thus, at MPI in Munich only very small crystals ($(10 \times 20 \times 5) \text{ mm}^3$) can be tested, but do not allow to study clamp related background or radiopurity of surrounding materials.

In 2009, the proposal of the CRESST collaboration to build an underground test-facility in addition to the main CRESST experiment at LNGS was approved. In the framework of this thesis, this test-facility was installed in a service tunnel (close to Hall A) at LNGS (see figure 7.1). A $^3\text{He}/^4\text{He}$ -dilution refrigerator (MINIKELVIN 400-TOF, Leiden Cryogenics) is used to provide the low temperatures. The cryostat reaches temperatures as low as 7 mK and is equipped with two SQUIDs (Applied Physics Systems) allowing for an operation of one detector module. The readout electronics as well as the necessary DAQ is organized similar to the CRESST set-up (see chapter 4). A modified container provides the housing of the cryostat. Its infrastructure (pumps, water-chiller, ventilation) is located outside the container in an enclosed area. In order to shield against ambient e/γ -background, the cryostat is surrounded by 10 cm of lead. However, the dilution unit as well as the LHe-dewar are not made from radiopure materials. A detailed description of the experimental set-up and information on performance issues of the testcryostat can be found in appendix A.



Figure 7.1. – The test-facility of CRESST is located in a service tunnel connecting Hall A and Hall B (indicated with an red arrow) at LNGS. The housing of the test-facility is provided by a modified container. The infrastructure necessary to run the cryostat are placed outside the container in an enclosed area.

Thanks to this set-up, proof-of-principle measurements can for the first time be carried out independently from the main CRESST experiment, in order to study the performance of new developed clamp prototypes. This is a great advantage as it allows for R&D studies on short time scales which are necessary to optimize and improve the detectors.

For illustration, the ^{210}Pb -contamination found to be present in the bronze material used for the clamps of Run 32 (lasting 2 years) could have been detected in a few-weeks-measurement in the testcryostat.

7.2. Detector Module

7.2.1. Crystal and Light Detector

The crystal and the light detector used to investigate the different clamp prototypes are described in the following text. Since the clamps should, as mentioned before, be studied under similar conditions as in CRESST, a conventional detector module was prepared. The TES used to read out the phonon and the light detector are a standard design.

Crystal The CaWO_4 crystal (K09) has a cylindrical shape (about 40 mm in diameter and height) and weighs about 300 g. The TES was evaporated directly onto the crystal. To prevent light trapping, the surface of the crystal facing the light detector was mechanically roughened using boron-carbide powder.

Light Detector The light detector (Erwin) is of the SOS-type (silicon-on-sapphire). A TES was produced onto the sapphire-side of the wafer. In order to allow for an intrinsic energy calibration of the light detector an uncollimated ^{55}Fe -source (0.1 s^{-1}) is mounted close to the light absorber disc.

7.2.2. Holder Design

The crystal and the light detector are mounted in a holder made out of NOSV copper. Figure 7.2 shows a schematic drawing of a detector module. In comparison to the former holder (Run 32 and earlier), the new design includes the following major modifications:

- electrical connections to the detectors developed within the framework of this thesis are realized via plug-in connectors. Before, wires were soldered directly onto the bonding pad. The very rigid soldering joints were susceptible to mechanical stress and led regularly to open connections
- the clamping strength can be adjusted in order to deal with crystals of slightly different sizes
- the bonding pad of the light detector is standardized in order to mount all types of light detectors independently of the sensors' design
- the orientation of the light detector is fixed relative to the crystal and allows us to standardize the length of the superconducting wires used for heater and bias supply

7.3. Results of Tested Concepts

In this section the results obtained from proof-of-principle measurements of the new clamp prototypes are presented.

All clamp designs use the new produced bronze, covered with highly reflective aluminum. A thin layer of the plastic scintillator based on a mixture of epoxy resin with PPO serves as scintillating coating (see section 6.4.4). The crystal-clamp interfaces belong to the different types introduced in section 6.5:

- CaWO_4 balls
- CaWO_4 half-cylinders
- NOSV copper half-cylinders
- pure metal clamps

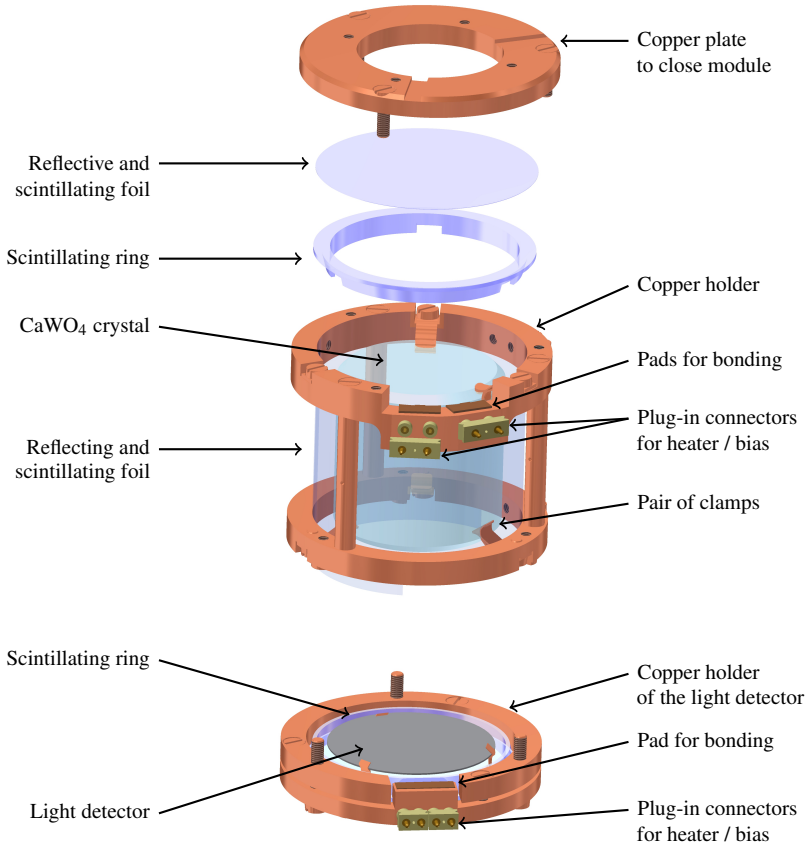


Figure 7.2. – Exploded view of the detector module. The main parts of the modified holder design are indicated. The crystal is depicted to be supported by pure metal clamps.

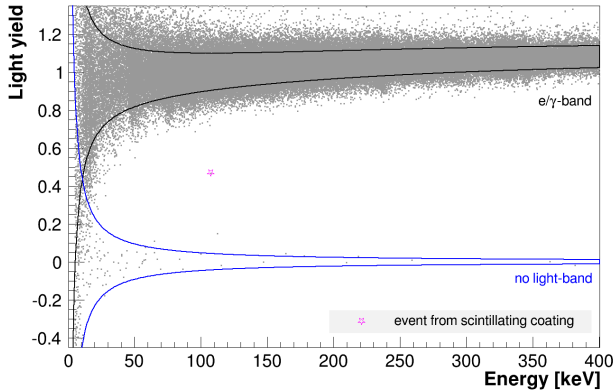


Figure 7.3. – Data in the light yield-energy plane for the detector module K09/Erwin using clamps with CaWO_4 balls as interface. A high number of no light events is observed, showing energies up to 360 keV. The bands which indicate the region expected for e/γ -interactions and for events with no associated scintillation light signal are shown as black and blue central 80% probability bands. This means, 80% of all corresponding events are expected to be contained within the respective boundaries. The event indicated with a star-like marker arises from the scintillating coating of the clamps.

For each measurement, a prototype version of the different clamp types was produced and mounted together with the before mentioned crystal and light detector. The measurements intend to investigate and study:

- microphonics due to an insufficient clamping strength
- no light events due to micro-fracturing of the crystal
- no light events of different pulse-shapes due to relaxation events in the interface material between the crystal and the clamps
- nuclear-recoils and α -background induced by the materials of the clamps

7.3.1. Calcium Tungstate Balls

No Light Events

This fully scintillating clamp design uses CaWO_4 balls (diameter of 2 mm) as an interface. A stable detector operation was achieved as no microphonics related to the clamping were present.

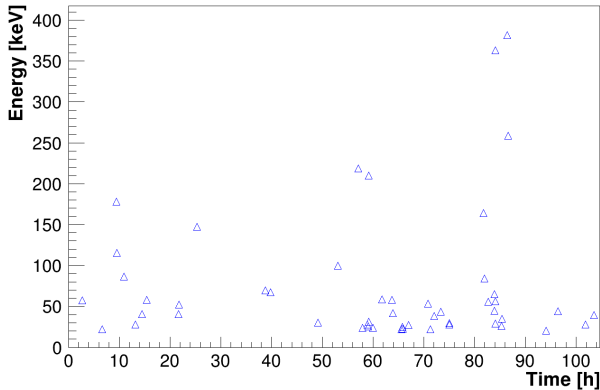


Figure 7.4. – Energy in the phonon channel versus measuring time for the no light events observed with CaWO_4 balls as interface. The high-energy no light events, since they are observed in a narrow window, appear rather to come in “avalanches”.

Figure 7.3 shows the light yield-energy plane for the detector module K09/Erwin utilizing these clamps. An exposure of 0.52 kg-days after data selection cuts was collected. In total, 51 no light events are observed in an energy range of 20 keV to 400 keV. The blue lines indicate the region where events with no associated light signal are expected. Each band is represented by two lines: 90% of events of a defined type (given QF) are expected below the upper boundary and 10% appear below the lower boundary. Hence, 80% of the events lie within the two boundaries. A detailed explanation on the model used for fitting the different event-distributions is given in section 8.4.

All no light events resemble the pulse-shape of ordinary particle pulses and thus, cannot be discriminated from particle pulses by any pulse-shape-analyses.

Origin of No Light Events The no light events have been investigated by an analysis of their time distribution. Since radioactive contaminations produce statistically independent events (constant rate), they follow Poisson statistics.¹ However, the no light events appear, in comparison, in “avalanches”.

In particular, the high-energy no light events often appear in narrow time windows. This correlation is shown in figure 7.4, where the measuring time (total 104.6 h) is plotted versus the energy in the phonon detector.

A sliding window correlation analysis was used to compare the rate of events from a γ -source to the rate of no light events. The correlation function C for a time difference

¹Decay-chains are an exception since their members show clearly correlated decays.

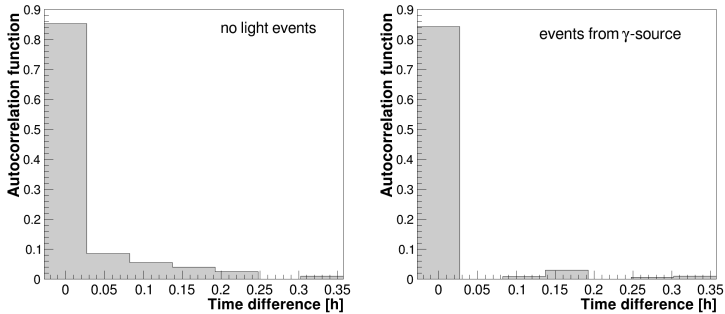


Figure 7.5. – Correlations function C for the event rate R from γ -events from a radioactive source (right side) as well as for no light events (left side). The γ -events follow a Poissonian distribution with $C = 0$ for $(t - t') \neq 0$ while the no light events reveal a small correlation in time lasting for some $\mathcal{O}(10 \text{ min})$.

$(t - t')$ is defined as the sum

$$C(t - t') = \overline{(R_t - \bar{R})(R_{t'} - \bar{R})} \quad (7.1)$$

where R_t denotes the event rate and \bar{R} is the calculated average. In the case that an increase in rate in comparison to the average rate can be observed and this increase also causes an increase at a time difference $\Delta t = t - t'$, then $C > 0$. For the absence of a correlation $C = 0$.

The γ -events are chosen from a γ -line in the energy spectrum of the data. For the γ -events a Poisson distribution is expected, hence $C = 0$ for $(t - t') \neq 0$, in accordance with the data (right figure in 7.5). The autocorrelation function C for the no light events is shown on the left hand side in figure 7.5. In comparison to the γ -induced events, there are correlations in time on the scale of a few $\mathcal{O}(10 \text{ min})$. Thus, the no light events do not seem to originate from a radioactive source. Of course, the results from the correlation calculations are weak since they are limited by the low statistics available.

During the early stage of the CRESST experiment, sapphire crystals were used as absorbers and an unexpectedly high rate of pulses was detected resembling the pulse-shape from particle pulses. These events were also found to be non-Poissonian. The origin of these events was finally traced to fracturing processes in the sapphire crystals due to a too tight clamping. This was also confirmed from an examination of the crystals under a microscope. In [Åst+06] these findings are summarized.

This strongly suggests that the no light events found are due to fracturing processes taking place either in the CaWO_4 -balls or the CaWO_4 crystal. As in the case of the sapphire absorbers during CRESST-I, an examination of the crystal and the clamps

under the microscope revealed that some of the CaWO_4 -balls showed small fissures on the surface, the large CaWO_4 crystal, on the other hand, did not show any apparent fracturing. However, this is only true for the polished surfaces of the large crystal. No statement can be given on the roughened top surface as tiny fractures are not visible. Thus, additional small fissures cannot be excluded.

A set of clamps consists of 12 single clamps. Three clamps are holding the crystal on the top and the bottom surface area, six clamps fix the crystal's side wall (see figure 7.2). All three balls of the clamps that keep the crystal on the roughened top surface area, which is facing the light detector, showed micro-fissures. All balls touching a polished surface remained completely undamaged.

The fissures on the surface of the concerned balls extend over an area of $\varnothing(100 \mu\text{m}^2)$. The expected energy released by fissures of this size can be determined by a simple estimation: fissures with the length of few $\varnothing(10 \mu\text{m})$ and assuming an atomic binding energy of 5 eV and an atomic spacing of about 0.5 nm result in energy deposits in the crystal of about 200 keV. This is in accordance with the energy range of observed no light events, since the calculated values assume that all phonons are transmitted into the crystal, but in reality a large fraction will leave the balls via the epoxy-layer into the clamp, resulting in a reduction of the detected energy.

The fracturing hypothesis is also supported by the fact that the high-energy no light events cannot be explained by any radioactive α -contamination, since for kinematic reasons the energy transferred to a recoiling nucleus in any α -decay cannot be as high as for example 260 keV.

Alpha-particles and Nuclear Recoils

Besides the no light events, no events are detected in the region where degraded α -particles are expected. One event at around 103 keV and a light yield value of about 0.5 is present in the data (figure 7.3). The energy signature of this event suggests that it originates from ^{210}Po present on the scintillating coating of the clamps where the recoiling ^{206}Pb nucleus hits the crystal while the α -particle leaves in the direction of the clamp, thereby traversing the scintillating coating and producing scintillation light. In this way, as discussed previously, the Pb-recoil event, which is expected to produce only a small scintillation light signal, is shifted to a higher light yield.

Another particle event has to be mentioned. At an energy of about 110 keV and a light yield of about 0.1 an event is observed, showing a small correlated light signal (see figure 7.3). This event appears in the region where neutrons are expected. In the testcryostat roughly 2-3 neutrons/kg/day are measured.² Thus, the observed event is in agreement with the expectation from neutron background. A more detailed discussion about the neutron background of the test facility is presented in section 7.3.3.

²From a sequence of measurements carried out in the testcryostat the neutron count rate is estimated to be about 2-3 neutron/kg/day.

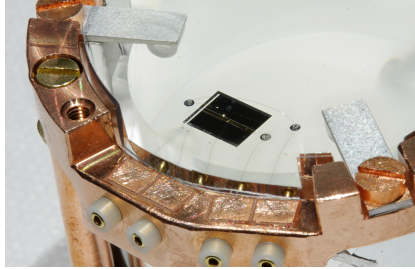


Figure 7.6. – Crystal K09 kept in position by clamps using CaWO_4 half-cylinders as interface.

Conclusions

The high number of observed no light events can be attributed to the fracturing of some of the CaWO_4 balls and possibly also of the roughened surface area of the large crystal which was in contact with the balls. This is supported by examining the balls under the microscope as well as by long-term correlations in time found by using an autocorrelation function. Taking into account that these events appear in the region where WIMP interactions are expected, this clamp design is not suitable.

However, since only the balls that hold the crystal on its roughened surface area revealed micro-fissures, whereas all others remained undamaged, a modification of the roughened surface may be successful in preventing this background. The surface area, where the balls touch the crystal can, for example, be optically polished.

No degraded α -events have been observed in the whole data set (up to 3000 keV) pointing to a radiopure bulk material. Such kind of events would be expected to show up above the region expected for α -particles due to the additional light signal from the coating, but still slightly below the e/γ -band. Furthermore, the scintillating coating is efficient to veto nuclear recoils from α -emitters, for example implanted from airborne ^{222}Rn . This is very promising since ^{206}Pb -recoils induced via ^{210}Pb (see section 5.5.3) were found to be the main background in the WIMP search region in Run 32. Thanks to its fully scintillating layout, this clamp design is able to veto all kinds of nuclear recoil-background.

7.3.2. Calcium Tungstate Half-cylinders

Motivation

In this design calcium tungstate half-cylinders are used as an interface to establish a fully scintillating clamp concept. Similar to the clamps utilizing CaWO_4 -balls, any possible α - and/or nuclear recoil-background is rendered harmless due to the fully scintillating layout.

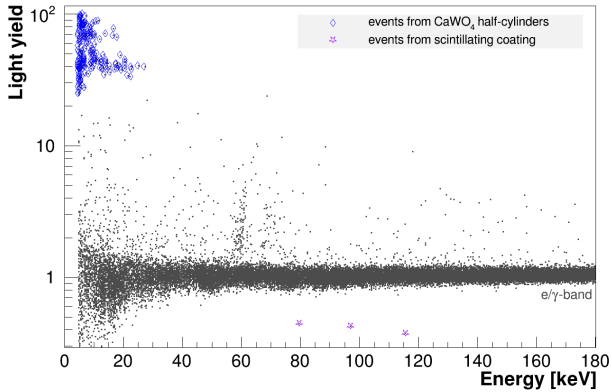


Figure 7.7. – Data in the light yield-energy plane for the detector module K09/Erwin with the crystal supported by clamps using CaWO_4 half-cylinders. The events from the half-cylinders appear at a very high light yield and are well separated from the region interesting for WIMP search. Events from the scintillating coating are marked as well.

The motivation for using CaWO_4 half-cylinders instead of the CaWO_4 -balls are as follows:

- larger contact area: the balls provided a point-like contact area which is more susceptible to break under stress by producing fissures. The half-cylinders distribute the keeping strength via a larger surface area
- polished surface: the geometry and bigger size of the half-cylinders allows for a defined, nicely polished surface. Since CaWO_4 is very brittle and soft, the manufacturing of the balls was very challenging and it was technically not possible to arrive at a perfectly polished surface of the spheres

Events Induced by the Half-cylinders

Figure 7.6 shows the crystal K09 mounted in its copper holder and supported by clamps with CaWO_4 half-cylinders as interface.³ Particle interactions in these small half-cylinders will produce phonons and a corresponding light signal. In the following paragraph, this new class of events is discussed in more detail.

The volume of all half-cylinders (4 mm in diameter and height) amounts to about 0.8% of the large crystal. Given their size, they introduce a class of signals seen in both

³The half-cylinders were produced out of a crystal called Hanna. Hanna was operated as the first composite detector in Run 31 and partially got damaged due to a bad gluing of its carrier. They were annealed in oxygen atmosphere after manufacturing to reduce stress induced via their manufacturing.

the phonon and the light detector. The light signal is given by the total energy deposited in the half-cylinders. However, from the phonons produced by particles interacting in the half-cylinders only a fraction is transmitted into the large crystal. Thus, the phonon signals are characterized by very small pulse-amplitudes. A main part of the energy escapes via the metal clamps.

Figure 7.7 shows the light yield-energy plane for the detector module K09/Erwin with the crystal kept by clamps using CaWO_4 half-cylinders. The light yield axis is plotted logarithmic. The class of events marked in blue color at a high light yield value far above the e/γ -band corresponds to events in the half-cylinders. These events, as mentioned before, are characterized by small pulse-amplitudes in the phonon channel and a large correlated scintillation light signal at the given energy detected in the crystal. The light yield for the half-cylinder events by itself has no relevance as there is no energy calibration for these events available. In the following a qualitative discussion on the characteristics and properties of these event class is carried out.

When looking at figure 7.7, the half-cylinders events can roughly be described by two band-like structures. In the band at a light yield around 70 the phonon signals from the half-cylinder events extend up to approximately 20 keV. In the second band, appearing at a light yield around 40, the highest phonon signals are at 30 keV.

The highest γ -energies from interactions in the large crystal extend to 3000 keV (Tl-line). Thus, the signals from the half-cylinders transmitted and detected in the big crystal are quenched by about a factor of 150/100, respectively. In other words, the phonon signals from the half-cylinders are a factor of 150/100 reduced in comparison to e/γ -interactions in the large crystal whereas the light signals are not. Given the typical threshold, only energy deposits in the half cylinders that are higher than 100 keV/150 keV are above threshold in the phonon channel of the big crystal. Therefore, assuming a light output of the small half-cylinders equal to that of the large crystal, this class of events from the half-cylinders should appear at a light yield around 100/150, whereas a gamma in the crystal appears at a light yield around unity. This very rough estimation agrees with the observation, in the data the events are present at light yields around 70/40 (see figure 7.7).

In principle the absolute transmission can be calculated from such data, however the correct light output of the small half-cylinders has to be known. This is not the case for the half-cylinders used. From measurements using smaller sized crystals it is known that their light output can be increased by up to a factor of three in comparison to a large crystal [Sch+12].⁴ Thus, no precise statement can be given on the transmitted fraction of phonons.

The reason why two and not only one band appear in figure 7.7 is discussed as follows: two equally populated bands point in the direction of two types of half-cylinders revealing different phonon transmission properties. The manufacturing of the half-

⁴Squared, small-sized crystals (5-6 g) are less susceptible to internal trapping of light and also the reduction in scintillation light due to absorption is reduced (absorption length).

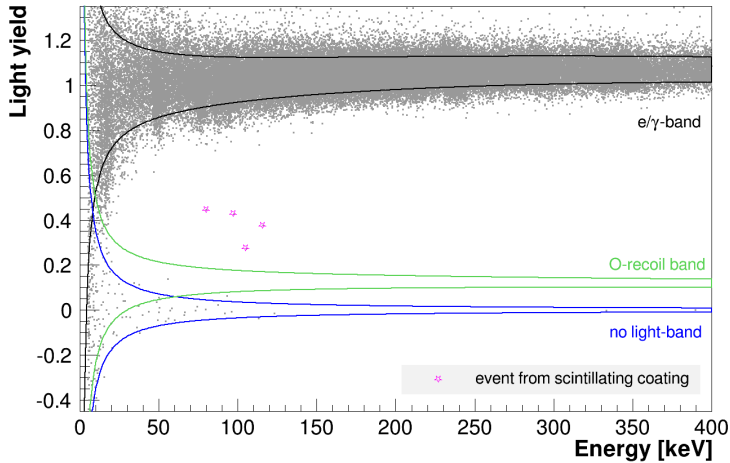


Figure 7.8. – Data in the light yield-energy plane for the detector module K09/Erwin using clamps with CaWO_4 half-cylinders. In the data a high number of no light events is observed, showing energies up to 380 keV. Events resulting from the scintillating coating are visualized using star-like markers. The bands indicate the central 80% probability region expected for γ/e -interactions (black), events with no associated scintillation light signal (blue) and O-recoil events as induced by neutrons (green).

cylinders was the same for the whole set of clamps, however the contact area between the half-cylinder and big crystal is expected to be different for the clamps holding the crystal on its flat surface or the clamps holding the crystal on its walls. Due to the curved surface area, the contact area of the half-cylinders from the side-clamps is reduced. This translates in a higher quenching of the phonon signal for particle-interactions taking place in these side-clamps. It is worth a mention that from the data the reduction can roughly be estimated resulting in a factor of about one third. This is plausible and in accordance with optical investigations of the contact area of a detector module with this type of clamps mounted.

Since the events from the half-cylinders appear at very high light yields, no background is expected from these events in the WIMP search region.

Excess Light Events Just above the e/γ -band, also so called *excess light events* are visible. These events appear mostly at low energies and show a higher light yield than the average of gammas and electrons at same energy. The origin of these events are for example back-scattered electrons which deposit energy in both the absorber crystal as

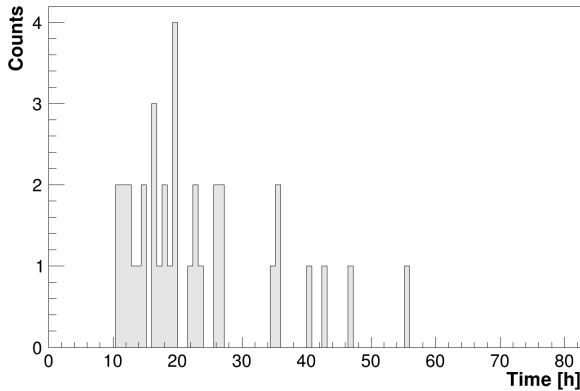


Figure 7.9. – No light events versus measuring time using clamps with CaWO_4 half-cylinders.

well as the scintillating foil and/or the light detector itself. Hence, the scintillation light signal is larger than that from interactions in the crystal, and the events appear above the e/γ -band.

As a consequence, the pulse-shape of these excess light signals is also different [Lan08]. Therefore they can easily be separated from the events in the half-cylinders.

No Light Events

The data shown in figure 7.8 corresponds to about 0.4 kg-days after data selection cuts. In total, 36 events with no associated scintillation signal are found in an energy interval of [20,400] keV. The blue band in figure 7.8 indicates the central 80% probability band expected for no light events.

The origin of the no light events can be investigated by an analysis of the time distribution as shown in figure 7.9. Most of the no light events, in particular the events at high energies, appear in a time window of about 20 h. This is shown in figure 7.10, where the energy in the phonon detector is plotted versus the measuring time (in total 81.6 h). In the first about 10 h of the measurement, zero no light events are detected. Later, an "avalanche" of events is detected followed again by a quieter period.

Therefore, the no light events are supposed to be related to fracturing processes in the CaWO_4 half-cylinders, similar to the measurement of the balls (see section 7.3.1). This was confirmed by optical examinations, showing quite invasive fracturing of some of the half-cylinders. However, the surface of all half-cylinders, including the ones which were in contact with the roughened top side of the large crystal remained undamaged. The fracturing of the half-cylinders started from the gluing layer. All surfaces of the

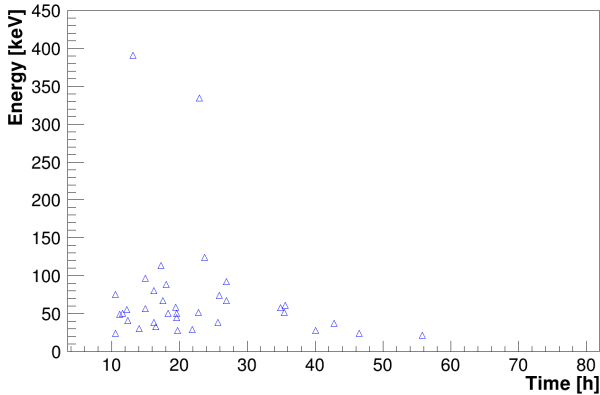


Figure 7.10. – Energy in the phonon channel plotted versus measuring time for the no light events observed while using clamps with CaWO_4 half-cylinders. Most of the, in total 36, events appear in a small time window of about 20 h duration.

CaWO_4 crystal did not show any damage or cracking.

Optical investigations of the half-cylinders give an idea for the reason behind the fracturing. The half-cylinders were attached onto the coated clamps using a tiny amount of epoxy resin. In total, three half-cylinders suffered from fracturing. All fissures start from the area where the half-cylinders were glued onto the clamp (see figure 7.11). Therefore, compressional stress onto the half-cylinder due to the clamping does not seem to be responsible for the fracturing but rather the difference of the thermal expansion coefficients of CaWO_4 and the epoxy resin EpoTek 301-2. Compressional and tensile stress builds up if two materials with different thermal expansions coefficients are attached to each other and cooled down. For the combinations of CaWO_4 and EpoTek 301-2 the thermal expansion coefficients differ by about an order of magnitude at 100 K [YB71; Cea+06].

Nuclear Recoil Background

Four events are observed around an energy of 100 keV and a light yield value of about 0.4 in figure 7.8. The energy signature of the events strongly suggests them to be caused by ^{206}Pb -nuclei interacting in the crystal.⁵ As they appear at a quite high light yield value, the origin of these events is the scintillating coating of the clamps.

⁵The presence of radon and/or its progenies is expected as the clamps have been produced and handled in ambient air conditions. Furthermore, before the measurement the clamps have even been stored for some time in the clean room at LNGS. The radon concentrations there can be as high as 100 Bq/m³.

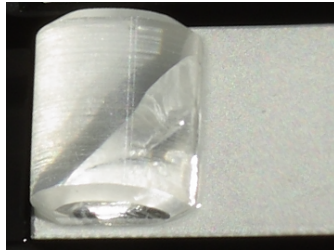


Figure 7.11. – One of the in total three half-cylinders that suffered from fracturing after cooling down to low temperatures. The fissures are responsible for the observed no light events.

If the decaying ^{210}Po is implanted into the surface of the epoxy coating, the Pb-recoils are not expected to deposit their maximum recoil energy in the CaWO_4 , but extend down to lower energies. The event with the lowest energy shown in figure 7.8 appears at around 75 keV.

This measurement proved the functionality of the fully scintillating concept. A nuclear recoil background induced for example via radon from ambient air can be vetoed successfully.

The event at an energy of 50 keV and a light yield of 0.15 can be explained by the interaction of a neutron. This event is present within the band of oxygen recoils as expected for neutrons. The O-recoil band is also shown in figure 7.8.

Conclusions

Scintillation of the epoxy coating is efficient to discriminate background from nuclear recoils, as for example from implantation of radon and its progenies on the surfaces of the clamps.

A high number of no light events caused by fracturing of some of the half-cylinders are observed. Tensile and compressional stress, building up while cooling down to low temperatures due to different thermal expansion coefficients of CaWO_4 and EpoTek 301-2, is suggested to be responsible for the fracturing.

Following the results of simulations carried out in [Kie12], the use of a thinner layer of epoxy resin attaching the half-cylinders may prevent them from cracking. Furthermore, applying a thin layer of vacuum grease (Apiezon N) instead of the epoxy resin, might be another solution for a smooth attachment of the half-cylinders onto the clamp. Besides, also a fitting of the half-cylinders as realized for diamond rings might be a good concept to be considered in the future.

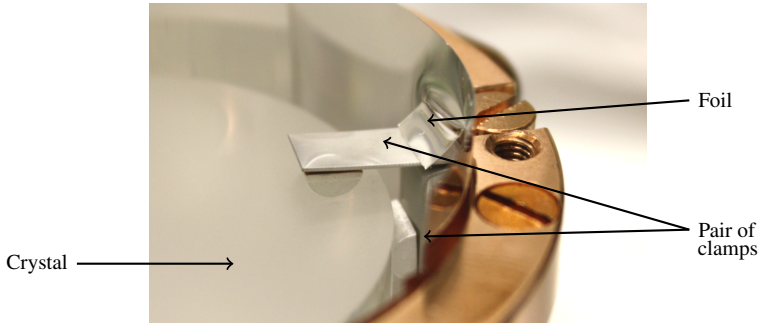


Figure 7.12. – K09 mounted with clamps using NOSV copper half-cylinders as interface. The copper half-cylinders are the only non scintillating material in the vicinity of the detector. The cylinders (4 mm in diameter and height) are covered with highly-reflective aluminum.

7.3.3. NOSV Copper Half-cylinders

In difference to the clamp designs described above, the following concept is based on an only partially scintillating layout: aluminum coated bronze clamps are covered with a thin layer of plastic scintillator (EpoTek 301-2 mixed with PPO) and small aluminum coated half-cylinders (4 mm in diameter and height) made out of NOSV copper serve as interface. These half-cylinders are the only non-scintillating parts in the surrounding of the detector. Figure 7.12 shows a pair of these clamps being used to mount the K09 crystal.

Due to the only partially scintillating concept, the following background contributions and, as a result, requirements for the handling of the clamps have to be considered:

- NOSV half-cylinders: progenies from ambient ^{222}Rn on the surface of the half-cylinders produce nuclear recoil events which, depending on their implantation depth, can appear in the WIMP signal region. Furthermore, secondary backgrounds (see section 5.7) can be induced by this kind of nuclear recoil background. Thus, the half-cylinders have to be handled exclusively in a radon-pure environment to obviate any radioactive contamination.

In addition, α -emitters, if present in the bulk material of the NOSV copper, may produce degraded α -events. However, the corresponding recoiling nuclei are not able to reach the crystal since their projected range is not sufficient to escape from the highly-reflective aluminum layer. Furthermore, the NOSV copper is known for its high radiopurity.

- scintillating and reflective housing: the radon progeny ^{210}Po , when present on the surface of the scintillating and reflective housing of the detectors (Radiant Mirror

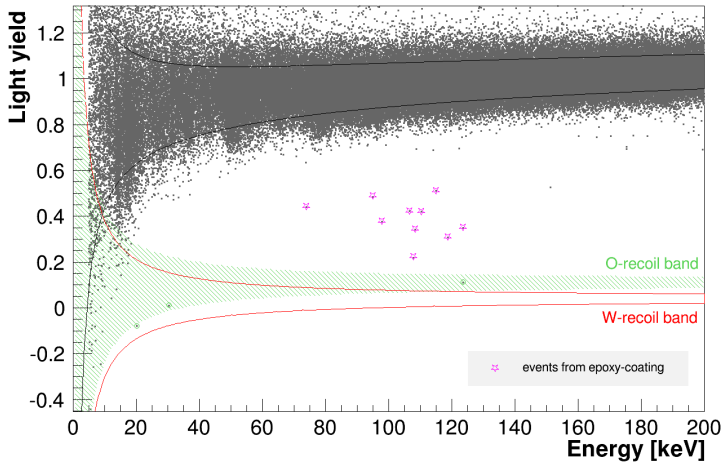


Figure 7.13. – Data in the light yield-energy plane for the detector module K09/Erwin using clamps with NOSV copper half-cylinders. The bands indicate the central 80% probability region expected for e/γ -interactions (black), oxygen recoils (green) from neutron-interactions as well as tungsten recoils (red). The events supposed to result from the scintillating coating are visualized using star-like markers.

Film VM2002 by 3M), is expected to produce secondary particles by sputtering (see section 5.7). The background from sputtered light elements is vetoed as long as the α -particle hits a scintillating surface or the crystal. A problematic situation occurs if the escaping α -particle hits the non-scintillating NOSV half-cylinder. In this case the α -particle is lost as a veto for the sputtered ions. In order to prevent this secondary background, the reflective and scintillating foil has to be thoroughly cleaned and handled in a radon-free environment only.

It is worth noting that a high sputter-yield may only be obtained if shallow angles are provided. Thus, due to geometrical reasons, the afore mentioned process is not a dominant background source. See appendix C for supplemental information on sputtering off the scintillating and reflective foil.

Nuclear Recoil Background

With this clamp type a net exposure of 1.2 kg-days after data selection was collected for the detector module K09/Erwin.

In figure 7.13 the data in light yield-energy plane is shown. The central 80% band ex-

pected for oxygen recoils is indicated in green. The red lines define the tungsten recoil band. Due to the large e/γ -background, the discrimination threshold of all measurements carried out in the testcryostat is quite high. The e/γ -leakage finally determines the discrimination threshold.

Another class of events, indicated with star-like markers, is visible in figure 7.13. As in the measurement with the CaWO_4 half-cylinders, these events are suggested to result from a ^{210}Po contamination on the scintillating coating of the clamps.

The following events are discussed:

- three events in the O-recoil band expected to be induced by neutrons
- ten events around an energy of 100 keV and a light yield of 0.4 resulting from a ^{210}Po contamination on the epoxy-coating of the clamps.

Neutrons Out of the three events being present in or slightly on the border of the O-recoil band, only the event at around 120 keV shows a clear scintillation light signal. The two events at around 20 keV and 30 keV do not show any correlated light signal within the resolution of the light detector. Nonetheless, these events are assumed to be neutrons: in the beginning of CRESST-II no neutron shield was present resulting in a measured neutron rate of 0.87 neutron/kg/day [Ang+05]. Since no copper shield is installed at the testcryostat and the lead shielding is thinner compared to CRESST, a doubling or tripling of the neutron rate is plausible for the testcryostat. Indeed, a sequence of measurements carried out in the test-facility results in a rate of about 2-3 neutrons/kg/day. Thus, the three events detected within an exposure of 1.2 kg-days are consistent with neutrons.

Events from the Epoxy-coating The ten events clustering at an energy around 100 keV and a light yield of about 0.4 are assumed to come from a ^{210}Po contamination on the epoxy-coating of the clamps. In the following section an explanation is given on the variations in detected phonon energies and light yield values as well as on the remarkable high number of those events.

The tail extending to lower energies is caused by the actual implantation depth of the decaying ^{210}Po -nucleus. Depending on how much energy the Pb-nucleus loses while escaping from the scintillating surface, the energy detected in the crystal can reach down to the energy threshold of the detector.

The significant differences in the observed light-yield of this class of events might be attributed to thickness variations in the scintillating epoxy layer. The coating has been applied onto the clamp using a small brush. Thus, thickness-variations cannot be excluded completely. Since the layer is thin, the path length which the α -particle can travel through it also varies. Depending on the actual path length of the alpha, the amount of produced scintillation light also differs. Last but not least, the light collection

might suffer in the case the scintillation light is produced on the less accessible parts of the clamp, resulting in a decreased light yield for such kind of events (see figure 7.12).⁶

Within an exposure of about 1.2 kg-days, a number of ten events is detected. Since the measurement was carried out in the testcryostat, a contamination by ^{210}Po from radon on the surface of the clamps and the surrounding of the detectors is expected as the test-facility does not provide a radon-pure environment. The air for ventilating is not purified and the detector module, while being mounted in the testcryostat, is exposed to normal air. Furthermore, the manufacturing of the clamps as well as the assembling of the detector module was carried out in a non radon-pure clean room.

There it is important to note that the same coating was used for the measurements of the other clamping concepts, however, the manufacturing of each prototype version was done independently, thus, variations in the level of contamination present from, for example, radon implantation are expected.

A bulk contamination of the scintillating coating can be excluded by the results from HPGe-measurements and ICP-MS analysis which arrive at far lower limits than found in this measurement (see section 6.4.4). However, it cannot be excluded that the scintillating layer causes radon and/or its progenies to deposit onto its surface.

The role of electrostatics and electro-chemical attraction on the deposition of radon progenies onto the epoxy layer was not studied. In order to avoid a deposition of radon progenies the coated clamps should only be handled under radon-pure conditions, which are also available now in CRESST.

Conclusions

In approximately 1.2 kg-days of net exposure the partially scintillating clamp concept did not show unexpected background events (no light events, nuclear recoils). A class of events around a light yield parameter of 0.4 is observed which can be attributed to a ^{210}Po contamination present on the scintillating coating of the clamps. This contamination may come from ambient air and is supposed to be introduced while assembling and mounting the detector module. Since the main part of the clamps, especially the area facing the scintillating and reflective housing of the detector, are covered with a scintillator, the probability for inducing secondary backgrounds via sputtering off the multi-layer foil are suppressed for geometrical reasons.

7.3.4. Pure Metal Clamps

To be complete, this section gives some information on the pure metal clamp design. The main aspects to be studied are:

- radiopurity: background from the radon progeny ^{210}Pb

⁶From the parts of the clamps which are not facing the light detector the collection and transport of the produced scintillation light is supposed to be less efficient.

- springiness: microphonics or micro-fracturing due to a too weak/tight fixing of the crystal

The mechanical properties of bare metal clamps were successfully tested in several measurement in the testcryostat: all measurements carried out in order to study the response of the detector to low energetic α -particles (see chapter 8) were performed while using the new type of bare metal clamps. No microphonics on the signals nor micro-fissures on the crystal could be observed. Thus, the material properties in the context of springiness and clamping strength are optimal.

There was no long background measurement carried out in the testcryostat in order to study the radiopurity of the bare metal clamps. There are two main reason for this: firstly, the radiopurity studies done on the CuSn6 clamp bulk material (see section 6.2) as well as on the reflective aluminum coating (see section 6.3) provide an upper limit for the activity expected from ^{210}Pb which is few $\varnothing(10\text{ mBq/kg})$. This means roughly that one event is expected from ^{210}Pb every three years, a background which if at all can only be measured during a long run in the CRESST experiment. Secondly, in order to gain a significant result from a measurement, the clamps have to be exclusively handled in a radon-pure environment in order to not introduce additional background. The test facility does not provide radon-free conditions and thus, does not allow for measurements which have to ensure very low background conditions.

In summary, the expected radioactive contamination of ^{210}Pb in the recently produced CuSn6 bulk is about a factor of 10^3 lower than in the old bronze used in Run 32. This level of radiopurity is sufficient for a future run. In the case of using this clamp type it is most important to assemble and handle detectors exclusively in a deradonized environment in order to prevent additional background from radon progenies on the clamps or the scintillating surrounding of the detectors from ambient air.

7.4. Résumé

Table 7.1 gives a short summary on the advantages and limitations of the different clamp concepts that have been investigated in this work.

Concept	Advantages	Disadvantages	Results	Conclusion/Outlook
CaWO ₄ balls	<ul style="list-style-type: none"> • fully scintillating • no plastic in contact with crystal 	<ul style="list-style-type: none"> • surface of balls not sufficiently polished 	<ul style="list-style-type: none"> • high number of no light events due to micro-fissures on the surface of some balls 	<ul style="list-style-type: none"> • no CaWO₄ balls on roughened surfaces of crystal • improve finish of the surface of the balls
CaWO ₄ half-cylinders	<ul style="list-style-type: none"> • fully scintillating • no plastic in contact with crystal 	<ul style="list-style-type: none"> • appropriate attachment of half-cylinders onto the clamps 	<ul style="list-style-type: none"> • high number of no light events due to fracturing of some of the half-cylinders 	<ul style="list-style-type: none"> • use only tiny amount of glue to attach half-cylinders
NOSV half-cylinders	<ul style="list-style-type: none"> • absence of no light events due to relaxation processes • absence of fracturing of the crystal-clamp interface 	<ul style="list-style-type: none"> • only partially scintillating • requires mounting in radon-pure atmosphere 	<ul style="list-style-type: none"> • radioactive contamination of scintillating coating due to radon-implantation • requires assembling and mounting in radon-pure atmosphere 	<ul style="list-style-type: none"> • if handled in radon-pure air a functional design • back-side of clamps facing the foil is covered with scintillator, important to veto processes that involve sputtering off the scintillating foil

Table 7.1. – Summary on the different clamp concepts that have been investigated in this work.

8. Low Energy Alpha Analysis

Chapter 8 is dedicated to the study of low energy α -events, another background observed in the CRESST Run 32 data. In order to allow for an event-by-event identification of particles as well as to calculate their expected contribution to the WIMP search region, the quenching factor (QF) of the respective particle has to be known precisely.

A special experimental set-up was designed in order to study the response of the detector to α -particles with a continuous energy distribution going down to lowest energies. Results are presented for CaWO_4 as well as for CdWO_4 , both showing a significant energy-dependence of the quenching factor.

The chapter is organized in the following way: after motivating the study of the quenching factor of low energetic α -particles, section 8.2 gives an overview on the interaction of heavy ionizing particles in matter. Furthermore, the scintillation response of the detector is discussed and a phenomenological model to describe the light quenching mechanism is introduced.

The experimental set-up used to determine the α - QF for CaWO_4 and CdWO_4 is the topic of section 8.3, including information on the dedicated source used to provide a continuous distribution of α -particles.

The subsequent sections give an introduction of the formal description of the data. In CRESST, the region in the light yield-energy plane where different particles are expected are described by central probability bands. The aim of section 8.4 is to explain how these bands are defined and obtained from the data. The e/γ -band, since it is sufficiently high populated, is used to determine the parameters describing the mean and the width of the light yield of the e/γ -distribution from a fit. The values of the parameters allow us to calculate the position of the bands for other particle types (α -particles, O-recoils, Ca-recoils), given the case that their respective quenching factors are known. In order to arrive at a description of the α -band directly from the data, the fit was extended to allow for a simultaneous fitting of the e/γ -events and α -events.

In section 8.5 and section 8.6 the results for the description of the α -band as obtained from the fit to the data are given for CaWO_4 and CdWO_4 respectively.

8.1. Motivation

In Run 32 a significant number of events caused by degraded α -particles is observed. Alphas which do not show the nominal decay-energy but rather a continuous energy spectrum extending to very low energies are referred to as degraded α -particles. The

origin of this background was the topic of chapter 5 and was discussed in detail in section 5.4.

Alphas, in comparison to heavier ions (e.g. O- and Ca-recoils), appear at a relatively high light yield-value in the light yield-energy plane. In other words, the inverse quenching factor (see section 2.4.3) for α -particles is small in contrast to the inverse quenching factor for tungsten-recoils. Therefore, in the light yield-energy plane, the region of α -particles should not overlap with the region expected for O-, Ca- or W-recoiling nuclei. However, due to the finite energy resolution of the detectors, the different recoil-bands do overlap at low energies (typically around 50 keV; see figure 2.17). Thus, to model a possible background contribution of degraded α -particles to the WIMP signal region, the knowledge of their quenching factor at low energies is fundamental.

In former CRESST analyses, the quenching factor for α -particles has been used as determined from α -emitters being present within the crystal. It was defined at MeV-scale and assumed to be constant. However, phenomenological theories predict an energy-dependence of the quenching factor for light charged particles as alphas.

In order to study the energy dependence of the quenching factor for alphas in CaWO_4 , a dedicate experiment was carried out. To rule out effects that might affect the results, the following requirements on the experimental set-up should be respected:

- use a conventional CRESST detector module
- provide experimental conditions as in the CRESST experiment
- apply an α -source providing a continuous energy spectrum in the energy range of interest (10 keV to 400 keV)

Before starting to introduce the experimental set-up, an overview on the interaction mechanism of ionizing particles in matter is given.

8.2. Interaction of Ionizing Particles in Matter

The first part of this section gives an overview on the description of the interaction of ionizing particles (protons, α -particles, heavier ions) in matter. Thereafter, existing concepts on how to describe the quenching mechanism of scintillation light observed with ionizing particles are reviewed in short.

8.2.1. Stopping of Charged Particles

Charged particles traversing a solid are slowed down continuously due to interactions with the electrons and screened nuclei. A discussion on the general concepts of slowing-down of ions in matter can be found in the work of [Boh48] and [Lin69].

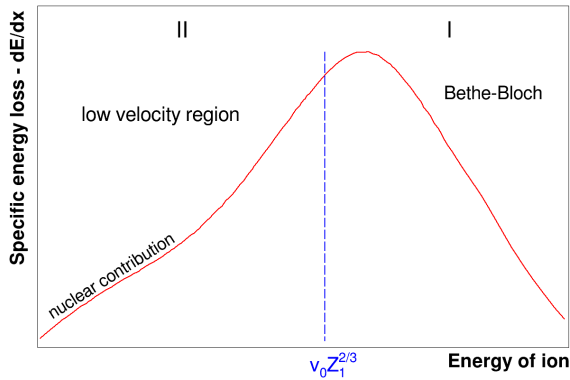


Figure 8.1. – Qualitative classification of the specific energy loss versus the energy of an arbitrary charged particle. The specific energy loss is composed of a nuclear and an electronic contribution, whereas nuclear collisions can only compete with the electronic component at very low velocities.

The stopping process is generally described by the specific energy loss dE/dx , the energy loss per unit path length of the ion. The stopping is composed of a nuclear and an electronic component, whereas nuclear collisions can only compete with electronic collisions at very low velocities/energies. In figure 8.1 a qualitative classification of the stopping process for arbitrary charged particles is depicted, where the specific energy loss dE/dx is shown versus the energy of the incident ion. The energy range of the charged particle is divided into two regions:

Region I It is referred to as *high velocity region*. The incident ion possesses high energies when impinging onto the target. At this high velocities the Bohr criterion for classical trajectory calculations is not fulfilled and the relativistic *Bethe-Bloch formula* is used. Depending on the properties of the ion, corrections have to be applied to the Bethe-Bloch based calculations. Fano introduced various extensions as for example the shell correction term and the density effect correction [Fan63].

This high-energy region is not of particular interest for the CRESST experiment.

Region II The Bethe-Bloch formula used to describe the energy loss at high velocities assumes a constant charge of the ion, but at ion velocities smaller than the orbital velocity of its atomic electrons, electrons from the target solid can be captured by the moving ion, thereby changing its charge or even neutralizing it.

For a correct description of the stopping, an understanding of both the energy loss of low-velocity charged particles and the neutralization mechanism of the ions by electron

capture is necessary. The characteristic velocity at which the charge of the ion starts to change and, thus, a limit for the Bethe-Bloch theory is reached, can be estimated as $v < v_0 Z_1^{2/3}$, where v_0 denotes the Bohr velocity given by $v_0 = e^2/\hbar$ and Z_1 is the charge of the ion. Lindhard and Scharff described the low-energy electronic stopping by assuming an interaction of the ion with the target electrons that were modeled as free electron gas. However, shell oscillations create a discrepancy between experimental data and this model and have to be corrected.

At the very low end of this region, nuclear stopping starts to compete with electronic stopping, as indicated in figure 8.1.

Calculating the Specific Energy Loss

The stopping for anticipated high velocities of heavy ionizing particles is described reasonably by the Bethe-Bloch theory. Though an understanding of the intermediate region around $v = v_0 Z_1^{2/3}$ is very complex due to a partial neutralization of the ion caused by picking up electrons from the target. Further complexity arises in the case of a compound target material.

Ziegler et al. gave a formal description of the whole regime based on the Bethe-Bloch-theory including various correction terms ([ZBL85], [Zie99]). Interpolation formulas with an adequate parameterization for the low- and the high-velocity regions including experimental data are used. An effective charge concept is applied to describe the charge state of the ion within the target to allow for a low-velocity extrapolation.

The SRIM software-package [Zie+12] provides a semi-empirical approach for determining the energy loss of charged particles in various elementals as well as in compound targets by combining calculations and experimental stopping data arriving at accurate data on stopping powers.

Stopping of Alpha-particles in CaWO₄

The specific energy loss of α -particles in CaWO₄ was calculated using the SRIM package [Zie+12]. In figure 8.2 the nuclear and the electronic contribution to the stopping are shown. Only at energies as low as 1 keV the nuclear component becomes the dominant stopping process. In the subsequent section the scintillation response to α -particles in a scintillating material is discussed.

8.2.2. Scintillation Response to Highly Ionizing Particles

As described by Birks already in 1964, the amount of scintillation light emitted from highly ionizing particles in a scintillating material is lower than that produced by e/γ -interactions of the same energy [Bir64]. The coefficient that describes this reduction in scintillation light is the *quenching factor* (QF , see section 2.4).

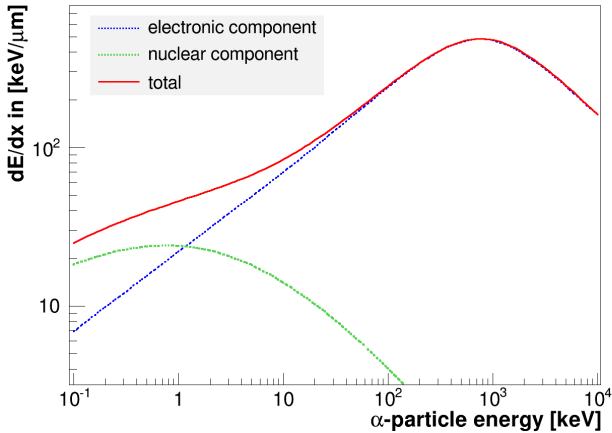


Figure 8.2. – Specific energy loss of an α -particle in CaWO_4 versus its energy on a double logarithmic scale [Zie+12]. The nuclear and the electronic contribution to the overall stopping of the incident α -particle are shown. Only at very low velocities/energies of the α -particle, nuclear collisions starts to compete with the electronic part.

In the CRESST experiment, WIMPs are expected to scatter elastically off the target nuclei. Depending on the mass of the hypothetical WIMPs, these interactions are expected to be detected via oxygen-, calcium- and/or tungsten-recoiling nuclei. Thus, the accurate knowledge of the corresponding quenching factors is necessary in order to define the WIMP sensitive region in the light yield-energy plane.

A lot of experimental effort is put into the investigation of quenching factors of particular particles in a certain scintillating material. This is necessary as so far no common theory is able to predict or describe quenching factors in different target materials with sufficient accuracy.

When carrying out experimental studies of quenching factors, the following aspects are important:

- QF measurements should be carried out under identical experimental conditions as in the physics experiment itself. Temperature dependencies of the light output of scintillators are an experimentally well established finding. The determination of a quenching factor at room temperature, therefore, does not necessarily reflect the quenching factor at low temperatures.
- the scintillator material employed for the QF determination should be from the same quality as the target material used in the physics experiment. Different

concentrations and types of dopants are observed to influence the QF [Bar08]. Furthermore, even scintillators considered to consist of high-purity material, often contain contaminations and defects that might influence the QF [Tre10].

- an energy-dependence of the quenching factors is suggested by semi-empirical descriptions of the light quenching mechanism. Chapter 9 focuses on this topic. In order to experimentally arrive at accurate QF -values, they should be studied in the energy range of interest.
- the light output of a crystal may also depend on the direction of the incident ion relative to the crystal axes [Bir64]. For α -particles in CdWO_4 a dependence of the QF on the particles' direction relative to the crystal axes was found [Dan+03].

Scintillation Light Quenching Mechanism

The parameter used to describe the slowing-down of ions in matter is the specific energy loss per unit path length dE/dx , as already discussed in section 8.2. However, the amount of scintillation light in a scintillator does not only depend on the stopping power, since two different particles at same dE/dx do not show the same light output [Bir64]. In order to allow for a correct description of the quenching factor, the ionization density in the crystal also has to be taken into account.

A summary on the data and theoretical approaches before 1963 is given in [Bir64]. More recently, a number of quantitative models have been developed. Michaelian et al. gives a short historical review on a selection of different models (see [MM94] and references). All these models are very extensive due to the complexity of the electron production cross section and low energy electron scattering and back-scattering.¹

Additionally, at high specific energy losses non-linearities in the production of scintillation light are observed. Meyer and Murray ascribed this behavior to a depletion of available luminescence centers (saturation effect) in the effective reach of the incident particle [MM62]. Later on, however, experimental investigations have ruled out the mechanism of a saturation of activator centers [GM63]. Nowadays, non-radiative electron-hole pair or exciton-exciton annihilation and damaged molecular structures working as electron or hole traps are suggested to be responsible for the observed non-linearities at high dE/dx values [SA81].

Summarizing, a universal description to calculate and predict the scintillation response induced by ions in scintillating crystals is still absent. The very complex physics underlying the processes of interaction of ions in matter followed by the production of scintillation light so far does not allow for an ion independent treatment.

The parameters of influence concern the nature of the incident ion and the target and are summarized in table 8.1.

¹None of these models allows for a universal description. Ion dependent parameters as charge and energy have always to be accounted for.

Incident ion	Target Material
• energy	• elemental/compound material
• charge	• organic/inorganic scintillator
• mass	• activated/non-activated scintillator
	• scintillation mechanism

Table 8.1. – The parameters that are suggested to influence the production of scintillation light concerning the nature of the incident ion and the target material are listed.

Therefore, experiments using scintillators tend to determine their quenching factors in dedicated experiments and/or by using calibration-sources (e.g. neutron source). The data acquired for the scintillation response of a particular ion in the crystal is then fitted by a multi-parameter fit.

Semi-empirical calculation methods of the quenching factors can also be used in order to describe the scintillation response of inorganic crystals as for example proposed by Birks ([Bir51], [Bir64]). The phenomenological method proposed by Birks will be introduced and also used in chapter 9 in order to describe the energy-dependence of the quenching factor of α -particles in CaWO_4 . Furthermore, this model is also applied to CRESST data from a neutron calibration taking place during Run 32.

8.3. Experimental Arrangement

The experimental set-up utilized for the study of low energy α -particles in a CaWO_4 and a CdWO_4 crystal is explained in the following. Both measurements have been carried out in the testcryostat at LNGS using the identical experimental set-up.

8.3.1. Detector Module

A slightly modified CRESST detector holder was used to allow for positioning of the α -source close to the target crystal. The flat surface of the crystal facing the light detector was mechanically roughened. The scintillating and reflective housing on the lateral area of the crystal was provided by the common V2002 Radiant Mirror Film.

The source providing the degraded α -particles was irradiating the flat surface of the crystal which also carries the TES. It was aligned in a way to not directly shine onto the thermometer. The scintillating and reflective foil enclosing the flat surface area was replaced by a metal foil consisting of reflective silver. It is important that α -particles have

no line of sight to the scintillating surrounding since the produced scintillating light of α -particles, when hitting the foil, may falsify the result of the measured scintillation light produced by α -particles hitting the crystal coincidentally at the same moment. The detectors as well as the type of α -source used for the measurement are introduced in the following paragraphs.

CaWO₄ crystal

The CaWO₄ crystal used for the measurement is called *K09*.² This crystal was already operated in order to study new clamping concepts (see chapter 7). The crystal is of conventional CRESST size (40 mm in diameter and height, 307 g) and equipped with a W-TES. The thermometer was evaporated directly onto the surface of the crystal.

CdWO₄ crystal

The CdWO₄ crystal (40 mm in diameter and height, 397 g) used for the measurement is called *HilgerI*, since it was purchased from Hilger Crystal. A composite detector design was used. A small ((20 x 10 x 2) mm³) CdWO₄ carrier crystal, equipped with a W-TES, was glued onto the large absorber using Epo-Tek 301-2.

CdWO₄ was studied in order to have the possibility to compare the results found for CaWO₄ to a chemically similar material. Further information on the properties of the target material CdWO₄, results from low temperature measurements of such a crystal in conventional CRESST size and a discussion on the advantages of this material as an alternative scintillator for the CRESST experiment are presented in appendix B.

Light Detector

For both measurements the same light detector is used. It is of the SOS-type and is named WII-133. The layout of its TES is different in comparison to the light detector used for the measurements of the various clamp designs. It implies a separated heater structure [Huf10], which is less susceptible to electromagnetic interferences.

8.3.2. Degraded Alpha Source

The requirements on the source providing the α -particles for the study of their energy-dependent quenching factor in the energy range of interest are:

- pure α -emitter (no accompanied gammas) as CRESST cryogenic detectors can only cope with low rates $\mathcal{O}(1 \text{ s}^{-1})$
- specified to be used at low temperatures
- continuous energy spectrum of α -particles ranging from 1 keV to 400 keV

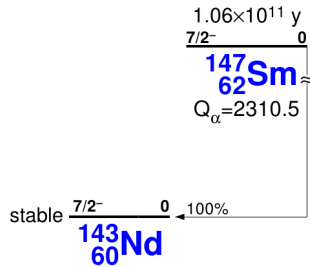


Figure 8.3. – ^{147}Sm decay scheme, from [Fir+99].

Conventional α -sources as ^{241}Am or ^{238}U are ruled out due to their accompanied γ -transitions causing high count rates. Pure α -emitters as ^{210}Po or ^{233}U were only available in form of open sources, consisting of a thin layer of the radioactive isotope, producing a perfect line-spectrum. Some layers of a sufficient thin but hole-free material (for example gold foil) would have had to be fixed in front of the source in order to downgrade the alphas and produce a continuous energy spectrum. However, none of the available sources was certificated for the usage at mK-temperatures.

The natural choice for a material providing degraded alphas is a bulk consisting partially of an α -emitting isotope. About 15% of ^{147}Sm is present in natural samarium. ^{147}Sm is a pure α -emitter decaying to ^{143}Nd while emitting an alpha with 2.31 MeV. The decay scheme is shown in figure 8.3. The α -spectrum expected from a natural piece of samarium bulk is continuous due to the homogeneous distribution of the radioactive isotope over its volume, thus α -particles, while traversing the surface close area of the bulk, lose a part of their initial energy before escaping from it.

In order to stop the recoiling Nd-nuclei which are emitted from the most upper surface layers, the samarium bulk was covered by about 200 nm of gold. Since the evaporated gold film was not sufficient in covering all parts of the samarium, two additional layers of a thin gold foil (<100 nm) were placed in front of the bulk. These foils succeeded in removing the major part of the Nd-recoils seen by the crystal.³

The samarium piece used for the measurement has an area of about 0.5 cm². It was mounted to face the surface area of the crystal which is also carrying the W-TES. The samarium had no line of sight to the lateral housing of the crystal since it was surrounded by a collimator made out of a thick silver foil. With the gold foils in place a

²The crystal K09 was bought from KARAT company in Lviv (Ukraine).

³Since such thin metal foils always reveal some tiny holes, still few counts from Nd-recoils are observed in the data. Thicker gold foils of a few ℓ (μm) would reduce the rate of alphas as a thicker layer is efficient in stopping the Nd-nuclei but also reduces the energy of the alphas without being itself a source of α -particles. Thus, the highest possible α -energy is reduced and also the overall event rate.

continuous energy spectrum from threshold energy up to about 1800 keV was observed. The overall rate of degraded α -particles during detector operations was about 0.1 s^{-1} .

Before the results of the response of a CaWO_4 and CdWO_4 crystal to degraded α -particles are presented, the model used to describe the data in a formal way is explained in detail.

8.4. Data Description Model

The data in CRESST is typically depicted in a plot of light yield versus energy. In order to define the region interesting for WIMP search, the accurate position and behavior of the probability bands for the different interacting particle types in this light yield-energy plane has to be known.

Such bands for the various interacting type of particles in CRESST detectors have already been shown in chapter 5 and chapter 7, but an exact description of the definition of these bands was so far absent. Thus, in this section the way how these bands are defined is explained and the parameters used to describe the data are introduced.

8.4.1. Fitting the Electron/Gamma-event Distribution

In CRESST, two functions are used to define a band: the average amount of produced scintillation light for a particular particle relative to the average amount of produced scintillation light of electrons/gammas as a function of the deposited energy in the crystal is described by the *mean value of the light yield*, a dimensionless quantity. The other function describes the energy-dependent *width* of the band around the mean value which is set by the finite energy resolution of the detectors.

Since the e/γ -band is highly populated both the parameters used to describe the mean and the parameters used to describe the width of the band can be extracted directly from a fit to the data.

The following notation is used: the energy deposited in the crystal is E , the corresponding energy emitted in form of scintillation light from an interaction in the crystal is L and the mean value of the light yield of a particle k is referred to as Υ^k .

Mean

In this data-oriented model the mean of the light yield of the e/γ -event distribution is a function of the form

$$\Upsilon^{e/\gamma}(E) = (L_0E + L_1E^2) \left[1 - L_2 \exp\left(-\frac{E}{L_3}\right) \right], \quad (8.1)$$

with the four parameters L_0 , L_1 , L_2 and L_3 .

L_0E is the term describing the center of the band in the case that the scintillator can be assumed to have a linear light response over the whole energy range of interest.

The value of L_0 is typically around 1 since the light yield parameter gained for e/γ -interactions after calibration is close to unity (section 4.3.3).

The crystals used in CRESST show a non-linear behavior since e/γ -interactions at low energies appear at lower light yield-parameters in the light yield-energy plane. This property of electrons and gammas is referred to as *scintillator non-proportionality* [Huf10; Lan+09]. There are two parameters introduced to model this effect: L_3 can be interpreted as the decay length describing the development over the energy range where the non-proportionality has an impact, whereas L_2 quantifies the overall fraction of the effect in comparison to L_0 .

Furthermore, in some detectors the fit of the e/γ -band could be improved by introducing another term ($L_1 E^2$), which allows for further deviations from the linearity of the band. This empirical extension is only interesting when looking at high energies. The effect of L_1 is negligible in the WIMP signal region.

Width

The width of a band is given by the energy resolution of a detector module. Again, due to the high statistics, the energy dependence of the resolution can be extracted from a fit to the e/γ -band. According to [Sch10], the width of the e/γ -band can be described by a Gaussian function with the width

$$\sigma^{e/\gamma}(L) = \sqrt{S_0 + S_1 L + S_2 L^2}, \quad (8.2)$$

whereas S_0 , S_1 and S_2 account for three effects that can contribute to the accuracy of the measured signals in the light channel and L is the energy of the detected scintillation light. The three contributions are:

- S_0 : baseline noise of the light signal
- S_1 : statistical fluctuations in the number of detected scintillation photons (Poisson statistics)
- S_2 : other contributions revealing a proportionality to L at high energies (e.g. position dependence in the light production of a crystal [Lan08]).

During detector operation, testpulses are sent to the detector (section 4.2). The resolution of a testpulse in principle determines the S_0 parameter, since testpulses, in comparison to particle pulses, only suffer from the baseline noise. Therefore, testpulses are expected to be an ideal estimate for this parameter. In this work, S_0 was determined from the testpulses and always kept fixed. S_1 and S_2 were determined from the fit.

So far the resolution of the phonon channel was ignored. However, since the phonon detector also exhibits a finite energy resolution its influence on the width of the band, even though very small, has to be accounted for. The uncertainty on the deposited energy E in the crystals translates for electrons and gammas (LY about unity) into a

fluctuation of the produced scintillation light of the same amount. In [Sch10] it was found that the small influence of the phonon channel on the width of the band can be included by defining S_0 as

$$S_0 = (\sigma_0^L)^2 + (\sigma_0^P)^2 \quad (8.3)$$

where σ_0^L and σ_0^P are the resolution of the testpulses for the light channel and the phonon channel respectively.

Excess Light Events

In order to properly describe the e/γ -band, another class of events produced from e/γ -background has to be considered. These events appear mainly at low energies and are characterized by a higher light yield-value. Back-scattered particles as for example electrons are suggested to be a possible source of these events, depositing energy in the surrounding of the foil or the light detector itself before or after being detected in the crystal. In this way, the detected light signal is increased in comparison to the signal induced from the amount of scintillation light emitted from the crystal only. Thus, these events are referred to as *excess light events*.

To account for these excess light events another three parameters are added to model their contribution:

- X_0 : the fraction of excess light events from all events (at zero energy)
- X_1 : the fraction of excess light events decreases when going to higher energies. An exponential function with an decay length of X_1 is used to infer this distribution.
- X_2 : the number of excess light events decreases when going to higher light yield values. Another exponential function, starting at the middle of the e/γ -band and revealing a decay length X_2 is used to describe this distribution. In order to account for the finite energy resolution of the light channel, this exponential has to be convolved with the Gaussian function describing the width of the e/γ -band.

The formal description used in order to account for the excess light events is discussed in detail in [Sch10].

8.4.2. Fitting the Alpha-particle Distribution

The experimental set-up designed to study low energy α -particles in a CRESST detector allows us to gain high statistics in the energy range of interest. In order to determine the quenching factor for α -particles directly from the data, three parameters were added to simultaneously fit both the e/γ - and the α -particle distribution.

A completely phenomenological model is used to describe the energy dependence of the center of the band of α -particles in the light yield-energy plane. As already mentioned before, a band is typically characterized by a mean value and its width. The function used to describe the mean of the light yield for α -particles is discussed in the following paragraph. Since the width of a bands accounts for the finite energy resolution of the detectors, it is defined by the same parameters as found for the e/γ -band.

Mean

The mean of the light yield of the α -particle distribution is defined as

$$\Upsilon^\alpha(E) = QF^\alpha(E) \cdot (L_0E + L_1E^2) \quad (8.4)$$

where again L_0E is the term which, as for the e/γ -band, would describe the center of the band in the case of having a perfectly linear scintillator. The contribution of L_1E^2 allows for deviations from strict linearity, only important when dealing with a large energy range. The parameter QF^α is the function used to describe the energy-dependence of the α -quenching factor. It shall be given by

$$QF^\alpha(E) = \frac{A_0}{1 - A_1 \exp\left(-\frac{E}{A_2}\right)}, \quad (8.5)$$

where the parameter A_0 can be interpreted as the value for the quenching factor exclusively at very high energies (MeV-range). In the data a significant increase of the QF appears towards lower energies. This increase of QF is parameterized by the exponential function (denominator in equation 8.5): A_2 can be interpreted as a decay length while A_1 quantifies the overall magnitude of the effect. Thus, the quenching factor is maximal at zero energy showing a deviation of $(1 - A_1)^{-1}$ from A_0 . At higher energies the QF approaches the value of A_0 .

The extension of the fit by the three parameters A_0 , A_1 and A_2 is only applied for the data collected while studying low-energy α -particles using the special designed α -source.

Generally, the bands for α -particles, oxygen-, calcium- or tungsten-recoils are not highly populated and, therefore, do not allow to determine their quenching factors from a fit to the background data.

To be complete, the formalism on the calculation of quenched bands on the basis of constant quenching factors as carried out in the CRESST analysis of Run 32 is presented in appendix D.

8.4.3. Maximum Likelihood Fit

It is either possible to bin data in the light-energy plane and make an usual likelihood fit or use the extended likelihood formalism which allows us to work with unbinned data.

For the analyses presented within this work an extended maximum likelihood fit is used to extract from the data the different parameters for the e/γ -band and also the α -band, as introduced above.

In order to describe the observed event distribution in the light yield-energy plane (E, Υ) (again E denotes energy deposited in the crystal and Υ the light yield) a model in form of a two-dimensional probability density function is formulated for all possible background contributions, generally described by

$$\rho_i(E, \Upsilon). \quad (8.6)$$

All density functions ρ_i depend on a set of parameters (resolution, QF, as introduced before). These parameters are summarized in form of a vector \mathbf{p}_i leading to $\rho_i(E, \Upsilon | \mathbf{p}_i)$.

Each density function is defined as a product of the expected recoil energy spectrum dN_i/dE and a Gaussian describing the expected distribution of events in the light yield coordinate. The components of such a density function are described by [Ang+12]

$$\rho_i(E, \Upsilon) = \frac{dN}{dE}(E) \cdot \text{Gaussian}(\Upsilon | \mathbf{p}_i). \quad (8.7)$$

The center of the Gaussian is given by the quenching factor and the width is mainly determined by the resolution of the light detector. All these parameters have been discussed in detail in the previous sections.

Considering the two main contributions in the data from the measurement of low-energy alphas, the total density is given by ⁴

$$\rho = \rho_\gamma + \rho_\alpha. \quad (8.8)$$

The total number of events expected from the contribution of e/γ s and α -particles in (E, Υ) is given by the integral of the total density function over the whole range of observation:

$$\iint \rho(E, \Upsilon | \mathbf{p}) dE d\Upsilon = \mathcal{N}(\mathbf{p}) \neq 1 \quad (8.9)$$

Due to an unconstrained normalization condition, a difference in the number of expected events to the actual number of observed events is allowed.

This function can be used to formulate a likelihood function with the help of the *extended maximum likelihood* formalism [Bar90]

$$\mathcal{L}(\mathbf{p}) = \left[\prod_k \rho(E_k, \Upsilon_k | \mathbf{p}) \right] \cdot \exp^{-\mathcal{N}(\mathbf{p})} \quad (8.10)$$

where the product is running over all events k observed at (E_k, Υ_k) . Using this formalism and applying it to the experimental data allows us to find the best fit by maximizing

⁴The model in principle can also be extended for O-recoils in the case of a highly populated band in e.g. from a neutron calibration.

the likelihood.⁵ In this way, the most likely values to all the parameters can be assigned. It is worth mentioning that the density function ρ is evaluated for every observed event in (E, Y) and no binning of the data in the two-dimensional plane as used in other methods is involved.

In section 8.5 and section 8.6 the results from the study of low energy α -particle interactions in a CaWO_4 and CdWO_4 crystal are presented. For both crystals, an energy-dependence of the quenching factor for α -particles is found, increasing towards low energies.

8.5. Results from Calcium Tungstate

In this section the results from the study of the quenching factor for α -particles in the detector module K09/WII-133 (see section 8.3) using CaWO_4 as target material are presented. The results from the fit and the qualitative agreement of data and fit are discussed. The energy interval considered for the study of α -particles is 4 keV to 400 keV. The overall exposure collected for the detector module K09/WI-133 after data selection is 1.43 kg-days.

8.5.1. Fitting the Gamma- and Alpha-particle Distribution

The selected data set was fitted with the model described in detail in section 8.4. In figure 8.4 data and fit in the light yield-energy plane for the detector module K09/WII-133 is depicted. The band description for e/γ -interactions and the α -particles is shown with the obtained mean-line and the $\pm 1.28\sigma$ boundary lines respectively. The results for the parameter values received from the fit are listed in table 8.2. In the following some comments on the parameters are made:

Excess Light Events It deserves a mention that the parameter X_1 , describing the decrease of the excess light fraction when going to higher energies was set to 90 keV. The overall high e/γ -background in the test-facility leads to a highly populated e/γ -band. However, the observed excess light events are only few in comparison. In order to allow for a correct proportion of the excess light fraction despite the low statistics a fixed value for the parameter X_1 was necessary.

Scintillator Non-proportionality The crystal K09 was produced by Karat in Ukraine. Crystals from this producer typically appear to show a less dominant non-proportionality effect which only becomes important at lower energies. In other words, the parameter L_2 has a value in the order of 10 keV. CaWO_4 crystals from another producer show values for L_2 around 30 keV to 50 keV instead. At low energies the contribution from the non-proportionality in most of the crystals is of the order of 20%.

⁵Technically the likelihood function is not maximized but its negative logarithm is minimized.

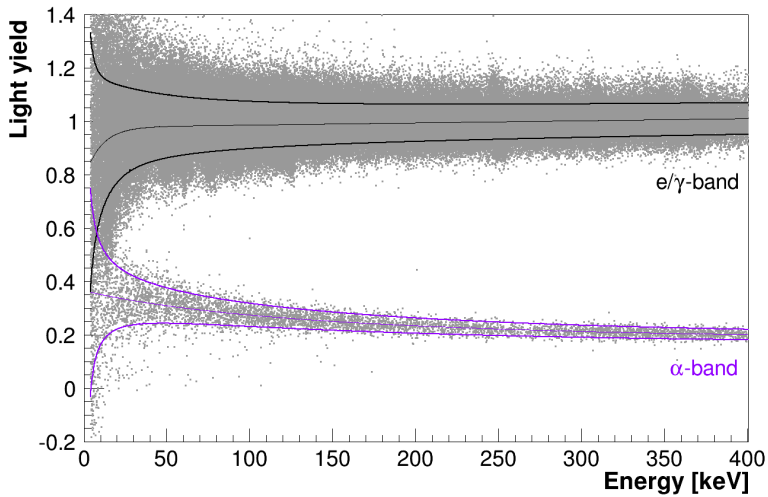


Figure 8.4. – Data in the light yield-energy plane recorded with the detector module K09/WII-133 while being irradiated with α -particles revealing a continuous energy spectrum. The band descriptions obtained for e/γ -interactions and α -particles are shown. For both distributions the mean line and the respective $\pm 1.28\sigma$ boundary lines are plotted. A clear energy-dependence of the quenching factor for α -particles, increasing towards lower energies, is observed. The events present below the α -band are mainly due to Nd-recoils from the α -emitter ^{147}Sm . Since the gold foil placed in front of the samarium is very thin, it reveals some tiny holes which are responsible for the observed Nd-recoils. Furthermore, a background from neutrons is also expected in this region.

Parameter	CaWO ₄ K09/WII-133	CdWO ₄ HilgerI/WII-133
L ₀ [keV ⁻¹]	0.98	0.99
L ₁ [keV ⁻²]	0.08 · 10 ⁻⁴	0.38 · 10 ⁻³
L ₂	0.20	0.39
L ₃ [keV]	10.0	10.92
S ₀ [keV _{ee} ²]	1.09	1.14
S ₁ [keV _{ee}]	0.35	0.64
S ₂	1.26 · 10 ⁻³	2.14 · 10 ⁻³
X ₀	0.22	0.19
X ₁ [keV] (fixed)	90.0	93.0
X ₂ [keV _{ee}]	4.91	12.09
A ₀	0.171	0.163
A ₁	0.54	0.56
A ₂ [keV _{ee}]	290.9	290.45

Table 8.2. – Parameter values as obtained from the fit to the data of the detector module K09/WII-133 using a CaWO₄ crystal and the detector module HilgerI/WII-133 using a CdWO₄ crystal. The exact meaning of the parameters is explained in section 8.4. For an discussion on the statistical error see section 8.5.4 and section 8.6.3.

Here it is worth to note that the non-proportionality effect does not seem to be a constant effect and is suggested to depend on the crystal. Moreover, it is suggested to depend on the actual background in the respective energy range in the crystal. See section 9.2 and appendix E for more information on this topic.

Alpha Quenching Factor A clear energy dependence of the mean light yield of α -particles is observed. As mentioned in section 8.4.2, the parameters describing the trend of the quenching factor for the α -particles are A_0 , A_1 and A_2 . To illustrate this, two limiting cases can be contemplated: at zero energy, the obtained value for QF is $1/2.7$ whereas the value for QF at 200 keV is $1/4.3$. At high energies, the value approaches the value of A_0 of $1/5.8$.

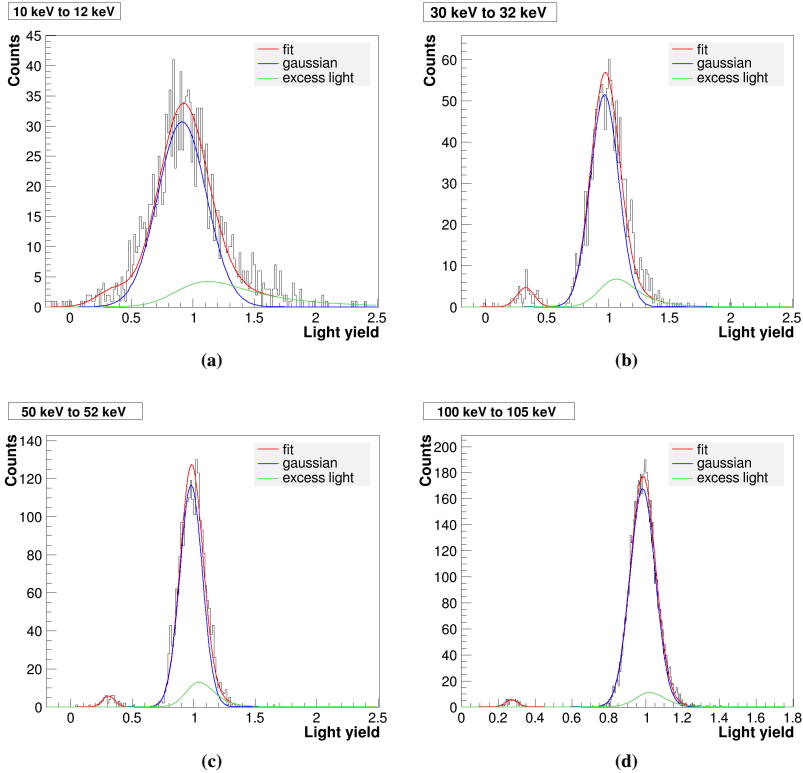


Figure 8.5. – Histogramming the light yield of the observed event-distribution at different energy intervals is used in order to judge the qualitative agreement between data and fit. The distribution of the e/γ -events (blue line) and the contribution of the excess light events (green line) as obtained from the fit are shown in each histogram. The total event distribution (sum of all contributions) including the α -particles as inferred from the fit is shown by the red colored line. The fit matches well with the observed events in all histograms.

8.5.2. Qualitative Agreement of Data and Fit

In order to judge the qualitative agreement between data and fit, the light yield of the observed events from e/γ -interactions and α -particles is histogrammed for a certain energy interval. Such histograms for energy intervals of 10 keV to 12 keV, 30 keV to 32 keV, 50 keV to 52 keV and 100 keV to 105 keV are shown in figure 8.5. In each histogram, the distribution of e/γ -events (blue line) and the excess light events (green line) are depicted. The red colored line is the description of the total event distribution as obtained from the fit also including the distribution of the α -particles.

In figure 8.5 (a) the α -band overlaps due to the finite energy resolution of the detectors with the highly populated e/γ -band. However, the contribution from the α -particles is already visible in form of a small bump at a light yield around 0.4. In figure 8.5 (b)-(d) the distribution of α -particles is separated from the e/γ -events and the fit agrees well with the observation.

8.5.3. Comparison to Run 32

The quenching factor for α -particles in Run 32 was determined directly from the data with much smaller statistics. Its inverse value is 4.5 and was assumed to be constant over the whole energy range in the analysis of Run 32 [Ang+12].

Figure 8.6 shows the light yield-energy plane for the detector module K09/WII-133. The band descriptions for e/γ -interactions and α -particles as inferred from the fit are plotted in form of central $\pm 1.28\sigma$ boundary lines in black and violet color respectively. In addition, the α -band calculated for $QF = 1/4.5$ as used in former analyses is shown (green colored band, central $\pm 1.28\sigma$ boundary lines).

Obviously, at low energies the calculated α -band with the constant QF does not match the α -particle distribution. In particular, in the energy range interesting for WIMP search (10 keV to 40 keV), the observed deviation is very large. Since the α -particle distribution bends to higher light yields, the expected background contribution from α -particles to the WIMP search region in the dark matter analysis of Run 32 was overestimated and thus conservative. As a consequence, the number of extra-events in the signal region in Run 32 (see table 2.2) which cannot be explained by known background sources is supposed to be slightly higher than found in [Ang+12].

Implementing the energy-dependent QF for α -particles as found in this work and re-running the dark matter analysis of Run 32 will allow to give concrete numbers for the different expected background contributions in the signal region of Run 32. This is not only valid for the spectral distribution of alphas in the WIMP signal region but also for the reference region used to estimate the expected contribution. However, this is beyond the scope of this work. Nonetheless, it is also interesting, to gain a better insight on the impact of possible secondary backgrounds (see section 5.7) which have not been accounted for in the latest CRESST analysis.

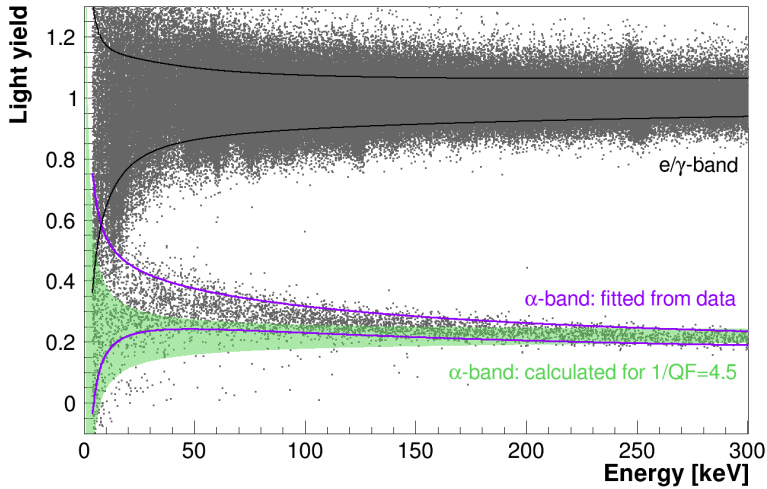


Figure 8.6. – Data in the light yield-energy plane for the detector module K09/WII-133. The band descriptions for e/γ -interactions and α -particles as obtained from the fit are shown in black and violet color respectively. In green color, the α -band calculated for a constant quenching factor is plotted. The value is given by $QF = 1/4.5 = \text{const}$ as determined from the Run 32 data set. Bands are plotted with central $\pm 1.28\sigma$ boundary lines. Note, the few events below the α -band are due to recoiling Nd-nuclei as well as induced by neutron-interactions in the crystal.

8.5.4. Statistical Error of the QF

In order to evaluate if the fit model gives an appropriate description of the data, also the statistical error for the inverse value of the QF while accounting for correlations between the parameters was determined. In figure 8.7 the mean value of $1/QF$ is plotted versus energy. In the upper picture an energy range from 5 keV to 400 keV is chosen whereas the lower picture only shows a detailed view up to 100 keV. In both figures the 1σ confidence contours are shown together with the mean value for the inverse QF (black line). The prominent energy dependence of the QF is clearly visible from these plots. The small errors indicate that the data is well described by the fit model.

8.6. Results from Cadmium Tungstate

In the following section the results from the study of the quenching factor for α -particles in the detector module HilgerI/WII-133 (see section 8.3), using $CdWO_4$ as target material, are presented. $CdWO_4$ was studied as an alternative target material (see appendix B for results) and also gives us the possibility to investigate the response to α -particles and compare the results to that ones obtained for $CaWO_4$. $CdWO_4$ and $CaWO_4$ are chemically similar and it is interesting to prove by measurement an expected similar developing of the α -band.

The overall exposure collected for the detector module HilgerI/WI-133 after data selection is 0.46 kg-days in an energy interval from 5 keV to 400 keV.

8.6.1. Fitting the Gamma- and Alpha-particle Distribution

Figure 8.8 shows data in the light yield-energy plane for the detector module HilgerI/WII-133 in form of a color-coded histogram. This illustration was chosen to visualize the high event rate. The intrinsic isotope ^{113}Cd is responsible for the highly populated e/γ -band. The band description for the α -particles as obtained from the fit is depicted with the mean and the central $\pm 1.28\sigma$ boundary lines (green). The parameter values are listed in table 8.2. The main observations to these parameters are:

Excess light Events The parameter X_1 , describing the decrease of the excess light events when going to higher energies was set to 93 keV. Also the parameter X_0 , describing the overall fraction of excess light events was kept fixed at 0.19 keV. The already high e/γ -background observed in the test-facility was further increased due to the presence of the beta-emitter ^{113}Cd , causing additional 100 events/kg/keV/day in an energy range up to 300 keV. To allow for a correct proportion of the excess light fraction in comparison to e/γ -events, despite their low statistics, a fixed value for this parameter was necessary.⁶

⁶Forcing the excess light contribution to 0 had no significant effect on the results of the fit.

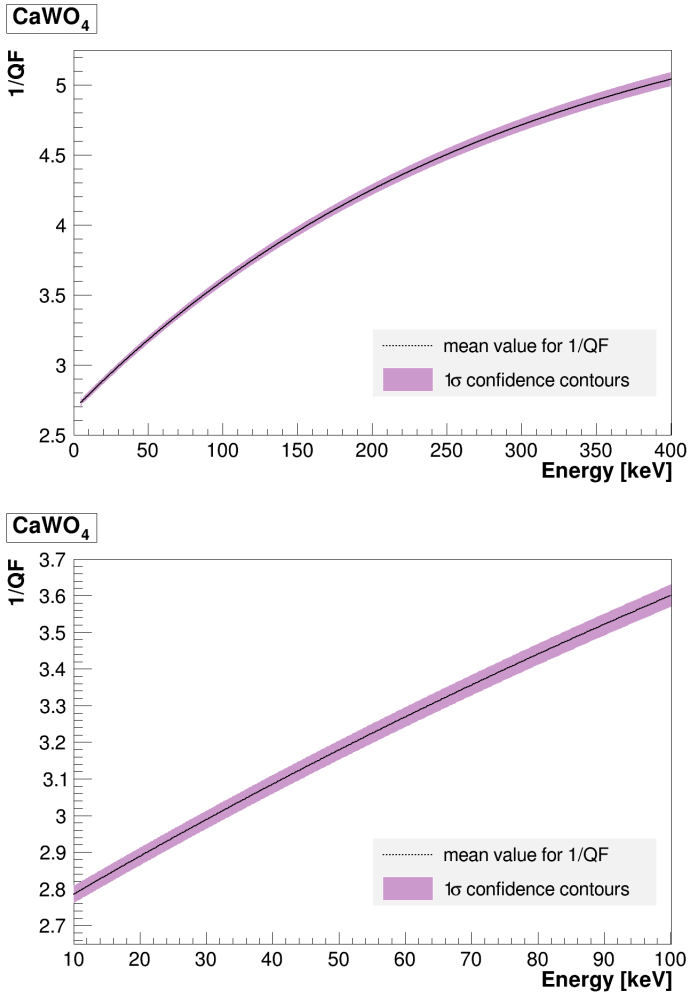


Figure 8.7. – Energy-dependence of the inverse value of QF for α -particles in CaWO_4 . The upper picture shows an energy range from 5 keV to 400 keV. The lower picture provides a detailed view to the low energy region, relevant for WIMP search. In both the mean value for $1/QF$ is plotted in form of a black line. The 1σ confidence contours for the statistical correlated errors are shown as violet bands.

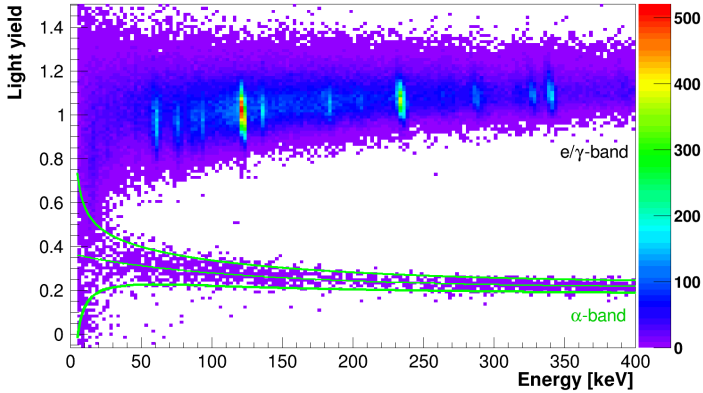


Figure 8.8. – Binned data of the detector module HilgerI/WII-133 in the light yield-energy plane while being irradiated with α -particles revealing a continuous distribution. The color-coded plot allows to evaluate the high e/γ -background observed in CdWO_4 due to the beta-decay of its intrinsic isotope ^{113}Cd . Furthermore, an external ^{157}Co -source and a ^{241}Am -source were applied for means of calibrating the detectors. The obtained band description for α -particles is shown as green lines. Both, the mean and the central $\pm 1.28\sigma$ boundary lines are plotted.

Alpha Quenching Factor As in the case of CaWO_4 , a clear energy dependency of the mean of the light yield-distribution of α -particles is observed. The parameters A_1 and A_2 are very similar to the ones obtained for the CaWO_4 crystal. The parameter A_0 obtained from the fit is 0.163 whereas $A_0 = 0.171$ was found for CaWO_4 . This means that the scintillation light quenching for α -particles in CdWO_4 is slightly higher than that found for α -particles in CaWO_4 .

8.6.2. Qualitative Agreement of Data and Fit

As before, histogramming the light yield of the observed events from e/γ -interactions and α -particles for a certain energy interval allows to judge the agreement between data and fit. Histograms at energy intervals of 12 keV to 14 keV, 24 keV to 28 keV, 48 keV to 50 keV and 100 keV to 104 keV are shown in figure 8.5. The red line is the description of the total event distribution including α -particles, whereas the contribution of e/γ - and the excess light-events are depicted as blue and green lines respectively.

At low energies (see figure 8.9 (a)) the α -band overlaps with the e/γ -band due to the high gamma-leakage caused by the very high event rate. In figure 8.5 (b)-(d) the distribution of α -particles is separated from the e/γ -band and matches well the observation.

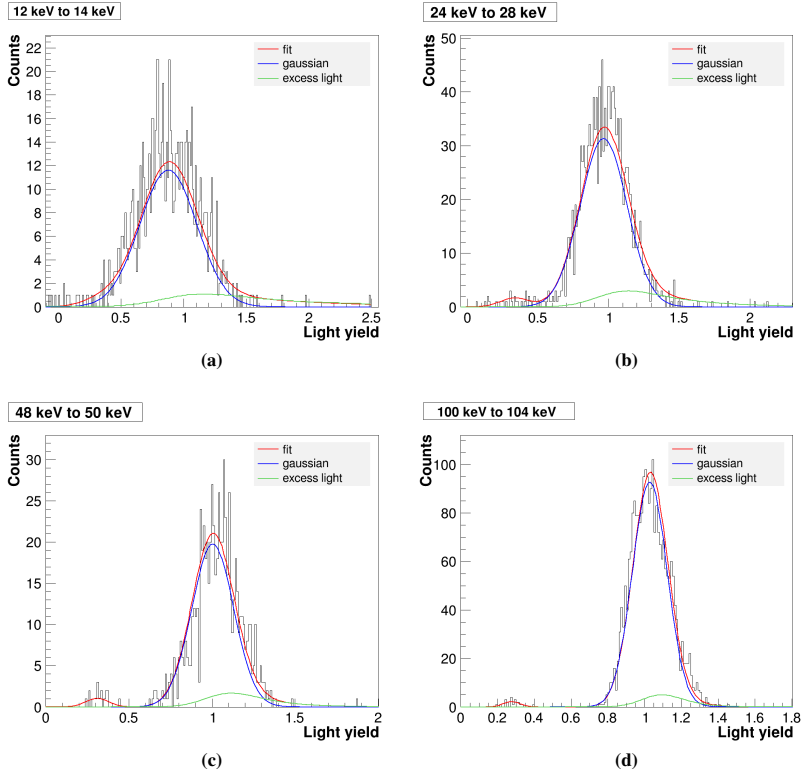


Figure 8.9. – Histogramming the light yield of the observed distribution at different energy intervals is used in order to judge the agreement of the CdWO_4 data and the fit. In each histogram the contribution of e/γ -events (blue line) and the contribution from the excess light events (green line) as obtained from the fit are shown. The red line is the summed event distribution including the α -particles as inferred from the fit. The fit agrees with the observed events.

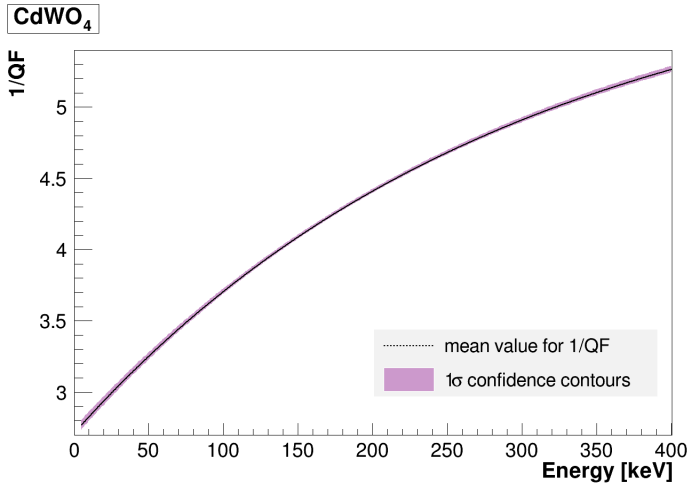


Figure 8.10. – Energy-dependence of the inverse QF for α -particles in CdWO_4 . The mean value for $1/QF$ is shown (black line) together with the 1σ confidence contours for the statistical correlated errors (violet band). As for CaWO_4 , a prominent energy dependence is visible.

8.6.3. Statistical Error of the Fit

As before, the statistical error of the inverse QF was calculated. Figure 8.10 shows the mean value of $1/QF$ (black line) together with the 1σ confidence contours for CdWO_4 . As for CaWO_4 , a prominent energy dependence is observed and clearly visible from the plot. Furthermore, the values for $1/QF$ in CdWO_4 are, as expected, similar to the ones obtained for CaWO_4 .

8.7. Summary

The scintillation light response to α -particles with a continuous energy spectrum in the energy range of interest (4 keV to 400 keV) in a CaWO_4 crystal and a chemically similar CdWO_4 crystal have been investigated by performing dedicated experiments. For both target materials an energy dependence of the quenching factor for α -particles at low energy was found. This is also predicted by semi-empirical models as explained in detail in chapter 9.

In the analysis of the Run 32 data a constant quenching factor for α -particles as determined at high energies from intrinsic α -emitters was used ($QF=1/4.5$). Due to the prominent increase of the QF towards lower energies there is a significant discrepancy observable, in particular in the energy range of interest for WIMP search.

In order to judge the effect on the results obtained from the latest data [Ang+12], the analysis of Run 32 has to be repeated taking into account the energy-dependent QF for α -particles as determined in this work. This is an interesting future project and beyond the scope of this work.

It is worth mentioning that for the first time the energy-dependent QF for α -particles has been measured with high statistics in the keV-energy range while using a CaWO_4 and CdWO_4 crystal in a CRESST calorimeter configuration at around 8 mK.⁷ The result will allow us to improve the background model of α -particles in a future CRESST run.

⁷Typically α - QF s are studied at MeV-scale and at higher energies by often using PMTs.

9. Semi-empirical Description of Quenching Factors

Nowadays, many experiments in the field of particle and astro-particle physics use scintillators as target materials. Typically the light response of the scintillating materials to the various types of interacting particles is described by a n -parameter fit. These fits are mainly phenomenological descriptions of the data and do not involve fundamental physics.

The bands used to describe the CRESST data are also determined by using a mainly data-oriented fit as explained in detail in section 8.4.

Given the popularity of scintillating materials in experimental physics, considerable effort from the theoretical side was taken to understand the underlying physical processes that are responsible for the scintillation light production in order to arrive at a fundamental and physical description of the scintillation mechanism. Although, numerous theoretical models exist today, so far no model has been able to describe the light response for different scintillator materials with high accuracy over a large energy range (keV to MeV-scale) and without the necessity of ion dependent corrections accounting for mass and charge of the interacting particle. The lack of a fundamental description and the disadvantage of the existing models to depend on complex corrections terms makes the implementation of such kind of models as a routine for data analysis in experiments an unattractive task.

As discussed in section 8.4, the increase in light yield for α -particles towards lower energies is well described by the data oriented model involving an exponential term (see equation 8.5). Nonetheless, a physical motivated model would satisfy the need on a more fundamental description of the experimentally proven energy-dependence of the QF of alphas in CaWO_4 and CdWO_4 (see section 8.5 and section 8.6). This is of particular interest in the light of former analyses, where the QF for alphas as well as nuclear recoils was always assumed to be constant. Thus, investigations in the direction of applying a physics oriented fit to the data which account for the energy dependence of the QF are well motivated and justified.

As early as 1951, Birks proposed a semi-empirical model to describe the quenching factors of heavy ionizing particles in scintillators [Bir51]. In this chapter the approach of Birks is followed to fit the energy dependence of the α -band in CaWO_4 . Furthermore, this model is also applied to CRESST data from a neutron calibration taking place during Run 32 describing the QF for O-, Ca- and W-recoils.

The chapter is organized in the following way: section 9.1 outlines the semi - empiri-

cal method proposed by Birks. Since this model is based on the energy loss of particles per path length, section 9.2 specifies the stopping powers for electrons, α -particles, O-, Ca-, and W-ions obtained from the respective software packages. Section 9.3 gives information on the fit and the parameters which describe the experimental data using this semi-empirical approach. Results for α -particles as well as O-, Ca- and W-recoils from a neutron calibration by using this method are presented and discussed in section 9.4 and section 9.5. The chapter concludes with a summary and outlook (section 9.6).

9.1. Semi-empirical Method

The amount of light produced in a scintillator following the phenomenological description proposed by Birks [Bir51] in differential form is given by:

$$\frac{dL}{dx} = \frac{A \frac{dE}{dx}}{1 + kB \frac{dE}{dx}} \quad (9.1)$$

where A is the absolute scintillation factor, BdE/dx is the density of the luminescence centers along the track of the ion and k is a factor accounting for saturation. Generally, kB is treated as a single parameter and referred to as Birks factor. dE/dx is the stopping power and was already introduced in 8.2. The stopping powers of various ions for a large selection of materials can be obtained from the SRIM software-package [Zie+12].

The general formula for the amount of produced scintillation light shall be described by

$$L(E) = \int_0^E \frac{A dE'}{1 + kB \frac{dE'}{dx}}. \quad (9.2)$$

This formula can be used to describe the scintillation response for every particle by simply using the correct stopping powers dE/dx . The only free parameters are A and kB , where kB , if determined once, is the same for all different particle types assuming identical experimental conditions.

In order to define the quenching factor for a particular ion from this method, the scintillation light detected from ions has to be divided by the scintillation light detected from electrons of the same energy.¹ Thus, the quenching factor QF shall be calculated as [Tre10]:

$$QF^i(E) = \frac{L_i(E)}{L_e(E)} = \frac{\int_0^E \frac{dE'}{1 + kB(\frac{dE'}{dx})_i}}{\int_0^E \frac{dE'}{1 + kB(\frac{dE'}{dx})_e}}. \quad (9.3)$$

The ratio is independent of the factor A and only depends on the factor kB , which is supposed to be constant.

¹The definition of a quenching factor in principle is obsolete in the case it is energy-dependent.

In CRESST we are used to display data in the light yield-energy plane. The light yield Υ is defined as the ratio $L(E)/E$. As mentioned before, CRESST detectors are calibrated with the response of the detector to the 122 keV γ s from a ^{57}Co -source. This means $L_e(E_0)/E_0 = 1$ by definition with $E_0 = 122$ keV.

The detected light of an ion L_i at energy E is normalized to the detected light of electrons L_e at energy E . Thus, Υ^i and QF^i are identical in the case the light detected from electrons and gammas L_e is proportional to the deposited energy in the crystal in the energy range of interest.

From the latter discussion, the following properties of quenching factors can be deduced [Tre10]:

- the quenching factors depend on energy
- the quenching factor is minimal when dE/dx is maximal
- the quenching factor for ions increases at low energies due to the decrease of dE/dx

The semi-empirical model of Birks shall be applied to the data obtained for α -particles in the low energy regime as well as to CRESST data from a neutron calibration taking place during Run 32.

9.2. Stopping Powers for Ions in Calcium Tungstate

The stopping powers of diverse ions for a large choice of materials are, nowadays, available from public software packages. The stopping power for electrons in CaWO_4 , as used in this work, was calculated by using the ESTAR package [Ber+05]. The stopping powers for α -particles and oxygen-, calcium-, and tungsten-ions were calculated with the SRIM package [Zie+12].

Figure 9.1 shows the calculated values for the total stopping powers (electronic and nuclear component) of different ions (1 keV to 10 MeV) in CaWO_4 .

Using stopping powers of electrons in order to describe the e/γ -distribution in the CRESST detectors is justified - but only at some level of approximation. The background spectrum of a typical crystal as used in CRESST allows to identify the main components of the background. The low energy region is typically dominated by beta-emitters. Thus, the observed electrons and gammas follow a variable distribution, depending on the present intrinsic and extrinsic background sources. See appendix E for an elaborated discussion on the background of the crystal VK33, the detector used for the description of the data from a neutron calibration during Run 32.

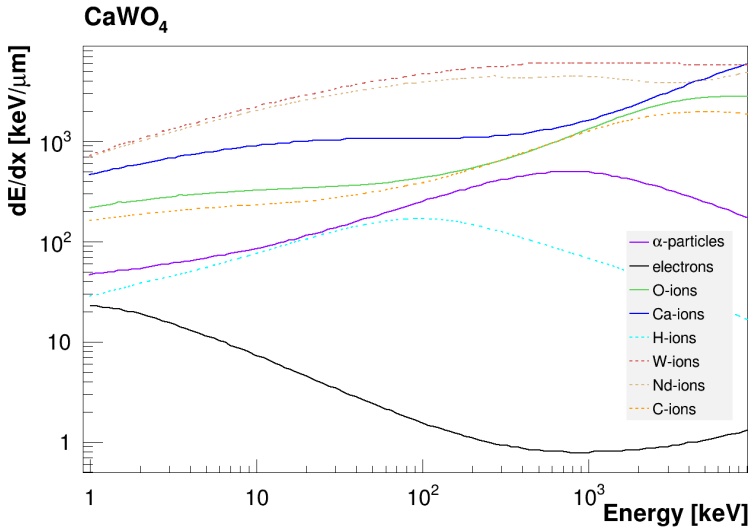


Figure 9.1. – Stopping powers for electrons, α -particles, O-, Ca-, W-, C-, H- and Nd-ions in CaWO₄. Note, the total stopping powers are given including the electronic and the nuclear contribution for an energy range from 1 keV to 10 MeV. The density of CaWO₄ used for calculations was chosen to be 6.12 g/cm³.

9.3. Fitting the Data

Identical to the fit introduced in section 8.4, two functions are used to define a band: the *mean value* and the energy-dependent *width* of the band around this mean value. The width is described in the same way as before whereas the mean value of the light yield is determined by applying the method proposed by Birks.

The relevant parameters of the fit are introduced in the following. The extended maximum likelihood formalism is used in order to find the best fit to the data and to assign the most likely values to all parameters.

9.3.1. Mean of the Distribution of Electron/Gamma-events

In Birks semi-empirical model, the mean of the light yield distribution of e/γ -events is defined from the integral

$$\Upsilon^e(E) = \frac{L_e(E)}{E} = \frac{1}{E} \int_0^E \frac{AdE'}{1 + kB(\frac{dE}{dx})_e} \quad (9.4)$$

The stopping power $(dE/dx)_e$ is used as determined from the ESTAR package.

Since some crystals do show a non-linear behavior of the e/γ -band going to higher energies, an entirely empirical term $L_1 E^2$ is added. To date, the reason for the tilt of the band is not known. It may be induced by a not understood property of the scintillating material or may also be related to a non-linearity in the calibration of the light detector. Typically, the value for L_1 is very small. Only when considering large energy intervals (up to 200 keV or higher), does this parameter become more important.

As before, a contribution of excess light events is allowed and modeled by three additional parameters:² X_0 , X_1 and X_2 . The meaning of these parameters was explained in section 8.4.1.

9.3.2. Mean of the Distribution of Alphas and Nuclear Recoils

The mean of the light yield distribution of α -particles and nuclear recoils is defined in the same way as the mean of the light yield distribution of e/γ -events

$$\Upsilon^\alpha(E) = \frac{\frac{L_\alpha(E)}{E}}{\frac{L_\alpha(E_0)}{E_0}} \approx \frac{L_\alpha(E)}{E} \quad (9.5)$$

$$= \frac{1}{E} \int_0^E \frac{AdE'}{1 + kB(\frac{dE}{dx})_\alpha} \quad (9.6)$$

²Excess light events appear mainly at low energies and are characterized by a higher light yield-value.

by using the values for $(dE/dx)_\alpha$ as calculated from the SRIM package. As mentioned before, $L_e(E_0)/E_0 = 1$ by definition with $E_0 = 122$ keV and E is in the region where detected scintillation light L_e is proportional to E to a good approximation.

Applying the model proposed by Birks to the α -data and fitting the α - and e/γ -event distribution allows to assign values to kB and A . In principle, the value kB , once determined from experimental data for one particular particle type, then will be the same for all particles.

Thus, it is meaningful not only to determine kB from electrons and α -particles but also, if possible, determine it for another particle type in order to allow for the validation of this method. Such an approach was already suggested by Birks [Bir64] and recently shown by Tretyak [Tre10] for α -particles and light ions in diverse scintillators for the intermediate and higher energy range (0.5 MeV to 10 MeV). However, relevant data in the energy region of interest of the CRESST experiment is absent.

In this context, the model of Birks shall also be applied to the data collected during a neutron calibration in Run 32. Neutrons interact in CaWO_4 by scattering off the O-, Ca- and W-nuclei. The spectral distribution for the neutron-induced events is described by three exponentials accounting for the contributions from the three nuclei given by

$$\frac{dN_i}{dE} = A_i \cdot e^{-\frac{E}{A_i^{dec}}} \quad (9.7)$$

where the parameter A_i is the fraction of events of the particular particle at zero energy and A_i^{dec} is the decay energy. The index i stands for O-, Ca- and W-recoils.

Moreover, stopping powers for O-, Ca- and W-ions were calculated by SRIM (see figure 9.1). The calculation of the mean for the light yield distribution of O-, Ca- and W-recoil events is carried out using the same formalism as in the case of the alphas.

9.4. Results for Alpha-particles

In figure 9.2 the description of the e/γ -band and the α -band as obtained from fitting the experimental data with the model proposed by Birks is shown in the light yield-energy plane. For both distributions the mean line and the respective $\pm 1.28\sigma$ boundary lines are plotted. The e/γ -band is well described by the fit. For the α -particles the situation is different: while the fit describes the observation well at energies >150 keV, the fast rise of the fitted α -band towards low energies is not reflected in the data.

9.4.1. Qualitative Agreement of Data and Fit

The discrepancy between data and fit at low energies can be judged when looking at the histogrammed light yield of the event-distributions. Figure 9.3 shows two histograms for energy intervals of 25 keV to 26 keV and 100 keV to 105 keV. In both histograms the e/γ -events are described well by the fit. For the α -particles, however, a deviation of

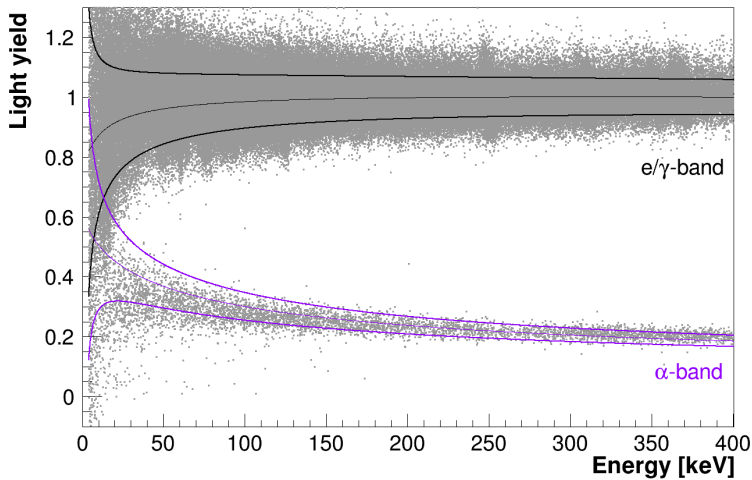


Figure 9.2. – Light yield-energy plane for the detector module K09/WII-133. The band descriptions for e/γ -interactions and α -particles, as obtained by using the semi-empirical method from Birks, are shown. The mean line and the respective central $\pm 1.28\sigma$ boundary lines are plotted. Towards low energies the fitted band reveals a prominent rise which is not reflected in the experimental data. Thus, below 150 keV the data is not sufficiently well described by the fit.

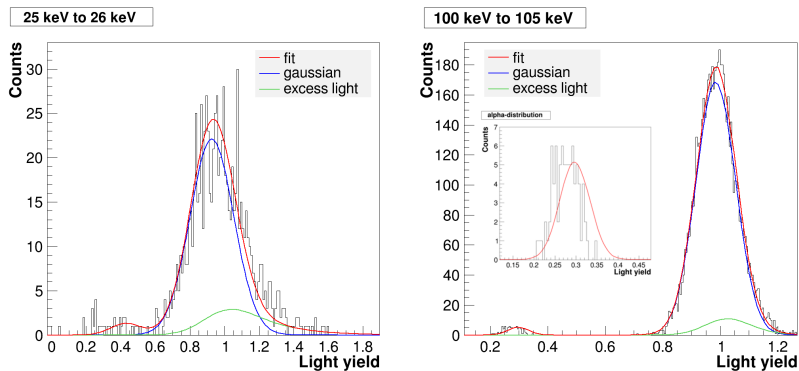


Figure 9.3. – Histogramming the light yield of the observed event-distribution at different energy intervals is used in order to evaluate the quality of the fit. In each histogram the distribution of e/γ -events (blue line) and the excess light events (green line) as obtained from the fit are shown. The red line is the total event distribution including the α -particles as inferred from the fit.

the fit from the data appears, overestimating the amount of produced scintillation light, as clearly visible in both histograms.

9.4.2. Discussion and Interpretation

A possible explanation for the discrepancy may arise from the values for the stopping powers used for α -particles. To gain an idea about the accuracy of stopping powers, the way they are calculated within the SRIM package has to be investigated [Zie+12]. In SRIM the approach is to establish methods that describe the stopping powers of ions based on accurate experimental data and on extending these values to regions where no experimental data is available so far by using unified theoretical models. In this context two main aspects seem to be important:

- stopping powers were calculated for CaWO_4 , a compound material
- energies of the incident He-ions (α -particles) are very low ([1-400]keV).

Stopping powers for compound materials are calculated following Bragg's rule: the total stopping power may be estimated as a linear combination of the stopping powers of the individual elements [BK05]. The correct density and stoichiometry of the compound are taken into account. The accuracy of the Bragg rule depends on the way the ion interacts and loses its energy in the target. Depending on the material and its atomic structure, bonding effects (in particular in case of plastics) and the excitation structure may strongly influence the interaction mode and thus, the stopping powers of the ion. However, in Ziegler et al. it is shown that for heavy compound materials the deviations from Bragg's rule are typically $< 2\%$ [Zie+12]. A definite answer for CaWO_4 , however, cannot be given but similar values are expected.³

The energy region of interest for the α -measurement is at low energies in comparison to the energy range of typical solid state physics experiments (mid and high MeV-scale). For light ions as helium and hydrogen the Bethe-Bloch theory is assumed to give accurate results only for energies $> 1 \text{ MeV/u}$ [Zie99]. Correction terms (density effect corrections, mean ionization energy, shell corrections) have to be implemented to be able to use the high-energy stopping power formula for low energies [ZBL85].

As mentioned previously, the stopping powers for α -particles in CaWO_4 are calculated on the basis of its individual elements. On the SRIM-homepage, the stopping powers for He-ions in O, Ca, and W are available [Zie+12]. In the plots accessible via the SRIM homepage, the stopping powers from experimental data as well as the SRIM results are shown versus ion energy. Very few experimental data points are available in the energy range below 100 keV for all relevant elements, whereas on the MeV-scale a lot of experimental data points are present and efficiently described by the model.

³The deviation from Bragg's rule for Al_2O_3 is $< 1\%$ and for WO_3 $< 2\%$. No concrete statement can be made on the accuracy of the calculated stopping powers for α -particles in CaWO_4 in the low energy region, however, deviations larger than 20% are not expected (see [Zie+12] and references).

Fit parameter	α-source data from K09/WII-133 testcryostat	neutron-source data from VK33/Franz CRESST Run 32
A	1.05	1.11
kB [$\mu\text{m}/\text{keV}$]	$1.65 \cdot 10^{-2}$	$2.25 \cdot 10^{-2}$
L_1 [keV^{-2}]	$-4.91 \cdot 10^{-5}$	$-7.82 \cdot 10^{-5}$

Table 9.1. – Parameter values as obtained from the semi-empirical method suggested by Birks. For the meaning of the parameters see section 8.2.

Furthermore, the presence of an additional saturation effect for light and highly ionizing particles as alphas at low energies is possible and not excluded. In this case, the description of the light response by using the simple saturation model of Birks is clearly not sufficient and an extension is strongly suggested.

Without making a claim to be complete, in the latter intercept some arguments have already been discussed that may explain the observed discrepancy between the data and the fit using Birks' model for α -particles towards low energies (< 150 keV). In table 9.1 the results for the parameters kB , A , and L_1 are listed, including the results from the neutron-calibration data, as explained in detail in the following section.

9.5. Results for O-, Ca- and W-recoils

The description of the e/γ -band by using the semi-empirical method suggested by Birks is in good agreement with the data (see section 9.4).

The light yield distribution of α -particles was overestimated by the fit at low energies (see figure 9.2). In the light of the findings from the fit of this model to the α -particle distribution, it is also interesting to evaluate the method for heavier ions in order to judge the relevance of this model for the CRESST experiment.⁴

In Run 32 a calibration of the detectors by using a neutron-source was carried out. Neutrons interact in the CaWO_4 by scattering off the oxygen, calcium and tungsten nuclei. Depending on the energy spectrum of the neutrons, different individual contributions from the three nuclei are expected. The event-distributions from the three nuclei in the light yield-energy plane can be described by three bands referred to as O-, Ca- and W-recoil-bands. In order to use the model of Birks for the description of the neutron-data, the stopping powers of O-, Ca- and W-ions in CaWO_4 have to be known (section 9.2).

⁴As discussed in section 9.4.2, there are relevant arguments which may explain the observed discrepancy between data and fit for light ions as α -particles.

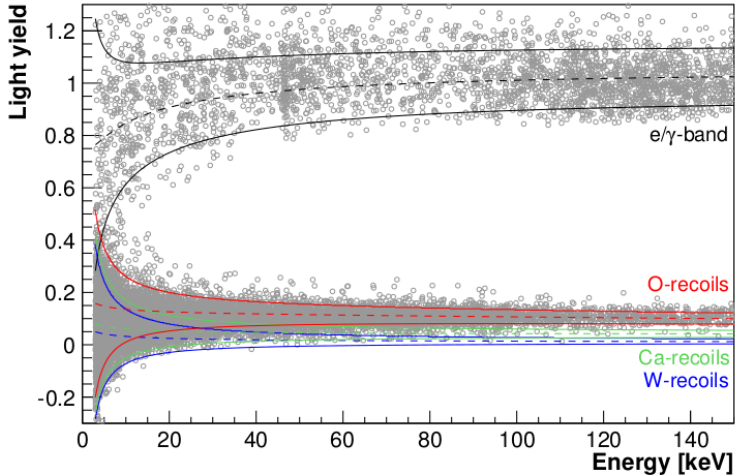


Figure 9.4. – Data from a neutron-calibration during Run 32 shown in the light yield-energy plane for VK33/Franz. The physical position of the neutron-source was on the coldbox. The obtained band descriptions for e/γ -events and the neutron-induced O-, Ca- and W-recoil events by using the semi-empirical method of Birks are shown. The mean lines (dashed line) and the respective central $\pm 1.28\sigma$ boundary lines are plotted. Different colors have been chosen for the different bands: red for the O-recoil-band, green for the Ca-recoil-band, and blue for the W-recoil-band. The e/γ -band is shown in black.

9.5.1. Neutron Source

During Run 32, two independent neutron-calibrations were carried out. In both an AmBe-source was used but placed at two different positions. For the data presented within this work, only the data recorded while having the source mounted on the coldbox of the experiment was considered (see section 2.2 and figure 2.2). The energy spectrum of neutron-induced events goes up to approximately 300 keV. Taking into account the mass differences between the three nuclei, the events at highest energies are supposed to be O-recoils, whereas Ca-recoils are expected to contribute up to about 100 keV. W-recoils only show a prominent fraction at very low energies, in the range of a few keV.

9.5.2. Discussion on Results

In figure 9.4 the description of the e/γ -band and the neutron-induced O-, Ca- and W-recoil-bands in the light yield-energy plane as obtained from fitting the model of Birks

Recoiling nucleus	Parameter	Value
oxygen	A_O	0.05
	A_{dec} [keV]	57.5
calcium	A_{Ca}	0.12
	A_{dec} [keV]	12.7
tungsten	A_W	0.83
	A_{dec} [keV]	2.0

Table 9.2. – Parameter values for the description of the spectral distribution of the neutron-induced events. For the meaning of parameters see section 9.3.

to the neutron-calibration data are shown. For all bands the mean line (dashed line) and the respective central $\pm 1.28\sigma$ boundary lines are plotted. From section 9.4 it was deduced that the e/γ -distribution is well described by the model. This is also verified by the fit to the e/γ -band of the neutron-data.

In order to evaluate the fit to the neutron-induced events, the event-distributions have to be looked at in greater detail. Figure 9.5 shows detailed plots of figure 9.4. Only the event-distribution induced by the neutrons is depicted together with the obtained central probability bands for O-, Ca- and W-recoil events.

In figure 9.5 (a) energies up to 150 keV are shown. The O-recoil-band is plotted in red, green and blue are used for the Ca- and W-recoil-band, respectively.

Figure 9.5 (b) shows instead a color-coded plot (grey-scale) of the event-distribution induced by neutrons in the low energy range up to 50 keV, the energy range interesting for WIMP search.

Figure 9.5 (b) visualizes that the distribution cannot simply be described by one single band: an increase in events, both towards lower recoil energies and light yield values is observed. This increase can be taken into account by introducing contributions from all nuclei present in the compound as also physically expected. As discussed in the latter section, neutrons interacting in CaWO_4 scatter of O-, Ca- and W-nuclei. Depending on the energy spectrum of the neutrons, the contributions from the respective nuclei in the considered energy range are expected to vary.

It deserves a mention that the upper boundary line for the O-recoils well represents the observation (see figure 9.5 (b)). This can be interpreted as a first and strong indication of a correct description of the different contributions.

The values for kB and A as assigned from the fit to the neutron-data as well as the α -data are summarized in table 9.1. Values for the parametrization of the energy spectrum for the neutron-induced events as obtained from the fit are presented in table 9.2.

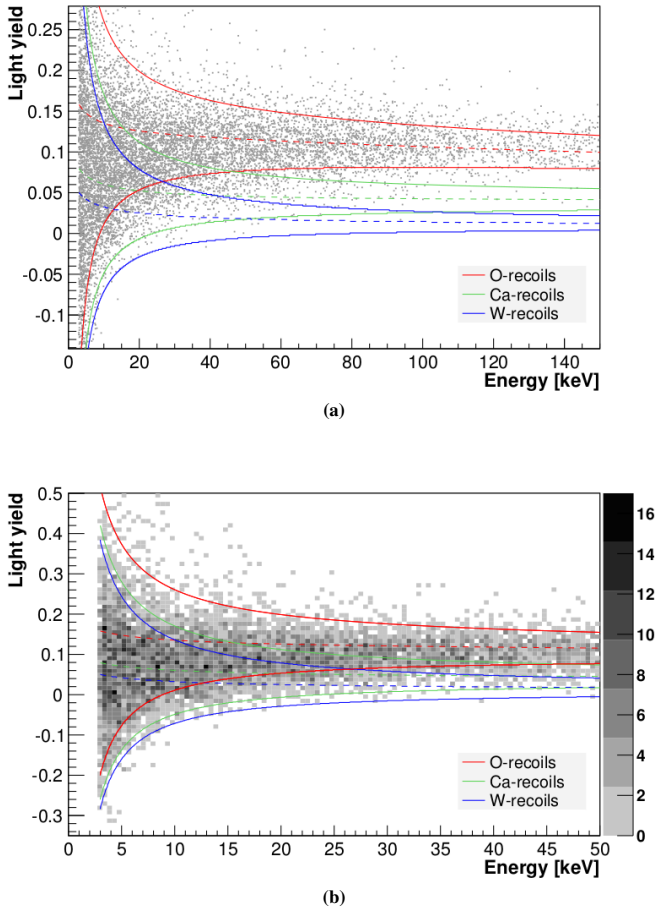


Figure 9.5. – Event-distribution induced by neutrons in the light yield-energy plane for the detector module VK33/Franz. Both figures depict detailed data from a neutron-calibration taking place during Run 32. In (a) recoil energies up to 150 keV are plotted. The central 80% probability bands expected for the corresponding recoiling nuclei are shown for: O-recoils (red), Ca-recoils (green) and W-recoils (blue). In (b) the binned data in the region of interest for WIMP search is presented. In comparison to the scatter plot, the color-coded illustration allows us to judge the three contributions from O-, Ca- and W-recoils.

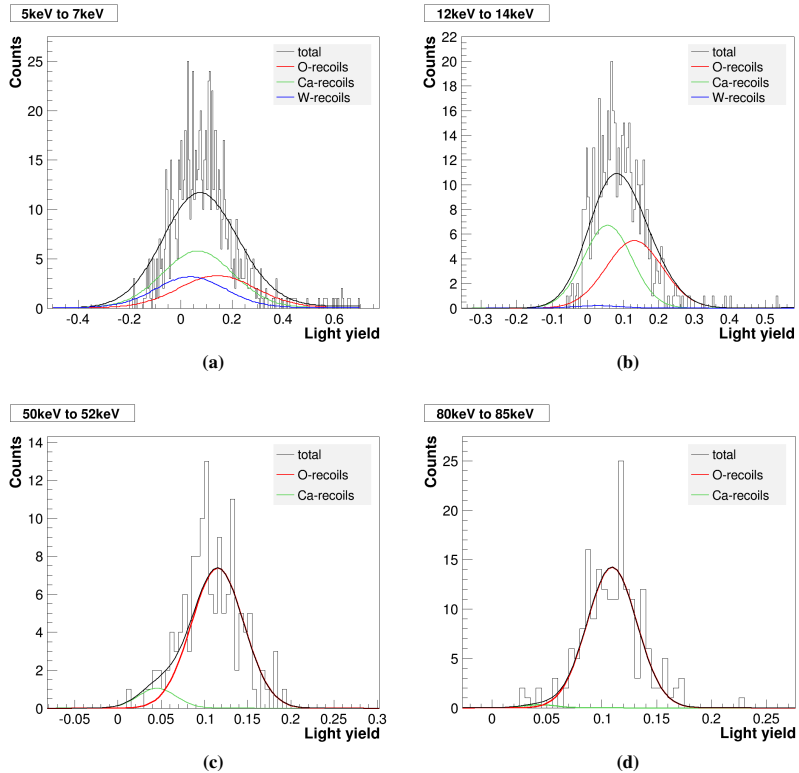


Figure 9.6. – Histogramming the light yield of the event-distribution resulting from neutrons interacting in CaWO_4 for different energy intervals is used in order to judge the qualitative agreement of data and fit. For every histogram the contributions from O-, Ca- and W-recoils are shown in different colors. In all four histograms, the complete distribution of events is well described by the black line, the sum over all contributions. See text for further information.

9.5.3. Qualitative Agreement of Data and Fit

In order to judge the agreement of data and fit, the light yield of the neutron-induced event-distribution was histogrammed at four different energies. In the histograms (see figure 9.6) the contributions from O-recoils (red), Ca-recoils (green) and W-recoils (blue) to the summed band description (black) are shown.

Some comments on the different histograms follow:

- figure 9.6 (a): a prominent contribution from W-recoils is only present at this low energies
- figure 9.6 (b): Ca- and O-recoils are almost equally contributing. Due to the small value for A_W^{dec} (see table 9.2) already at around 15 keV the fraction of tungsten becomes negligible whereas calcium-recoils are responsible for the main contribution to the overall event number.
- figure 9.6 (c): the contribution from tungsten-recoils is not shown as it is negligible. The observation is well described by the fit assigning a dominant O-contribution as well as a small fraction still coming from Ca-recoils.
- figure 9.6 (d): the distribution is almost only described by one component, the O-recoils. This approves the expectations since, because of kinematics, mainly interactions on the lightest element of the compound, namely oxygen, are expected at energies above 100 keV.

To summarize, there is a good agreement between data and fit. The energy spectra of the contributions from the different involved nuclei are described by three exponentials. The fitted energy spectra reflect the values obtained from simple kinematics.

9.5.4. Statistical Error of the QF

The statistical error of the inverse value of QF while taking into account correlations between the parameters was calculated for all three recoils.

The results from the error calculation are shown in figure 9.7. The mean value of $1/QF$ is plotted versus energy. The 1σ confidence contours are shown in different colors: figure 9.7 (a) for O-recoils, figure 9.7 (b) for Ca-recoils and figure 9.7 (c) for W-recoils.

From this plots the energy-dependence of the QF present for all three recoils is clearly visible. This is very interesting, since in former CRESST analyses QF s were assumed to be constant (see section 2.4.3 and table 2.1). In table 9.3 the inverse QF -values at 40 keV are listed for comparison.

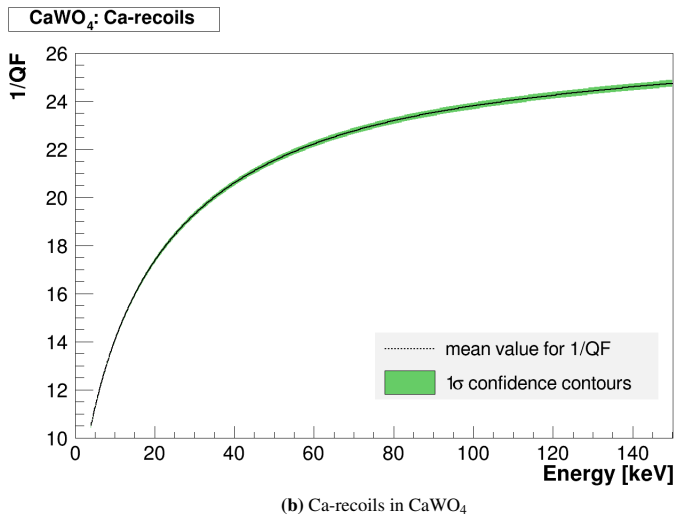
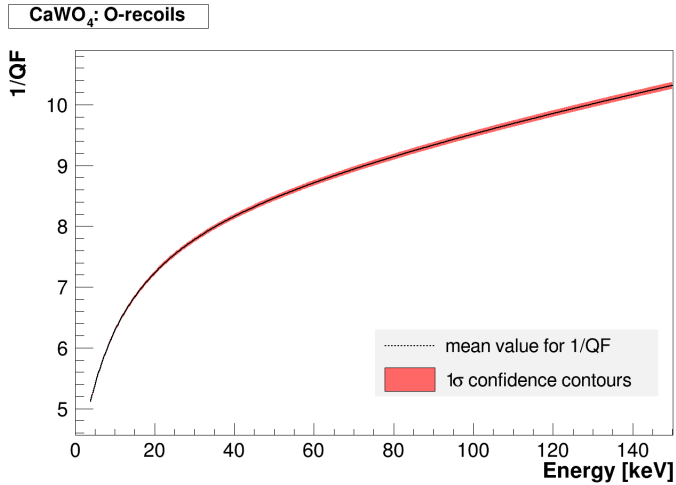
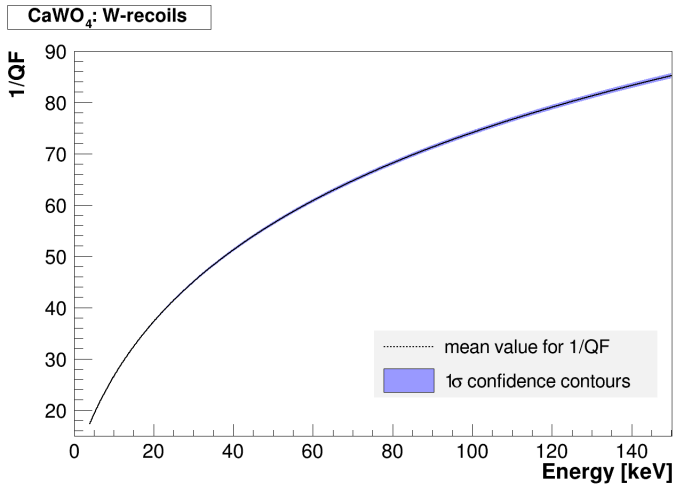


Figure 9.7. – Energy-dependence of the inverse values for the quenching factors for O-, Ca- and W-recoils in CaWO₄ as determined from fitting the semi-empirical model of Birks to the data from a neutron-calibration taking place during Run 32. The mean value for $1/QF$ are shown together with the 1σ confidence contours for the statistical and correlated errors.

(c) W-recoils in CaWO₄**Figure 9.7.** – continued

particle type	1/QF
O-recoils	8.1
Ca-recoils	20.5
W-recoils	51.1

Table 9.3. – Inverse values of quenching factors determined at 40 keV by using the semi-empirical model proposed by Birks in order to describe the neutron-data.

9.6. Summary and Outlook

In both analyzed data sets (α -data and neutron-data), the e/γ -event distribution is very well described by the semi-empirical model suggested by Birks. To account for the event class of excess light events an additional phenomenological term was added to the model (see section 9.3).

For the α -particle distribution the situation is different. For energies >150 keV the observation is well described by the fit, however, towards lower energies the fit overestimates the produced amount of scintillation light and is not in agreement with the data. In section 9.4.2 possible explanations for the observed discrepancy are discussed.

Bearing in mind the simplicity of the model of Birks, the fit to the neutron-induced events agrees astonishingly well with the data. The neutron-induced events do not appear as isolated distributions, but overlap due to the limited resolution of the light detector. Furthermore, no information on the spectral distribution of the neutron-induced events in form of for example a Monte Carlo simulation is available for the case of the neutron-source mounted on the coldbox. The combination of these two aspects was considered to make a fitting of the corresponding O-, Ca- and W-recoil-bands a difficult task. However, the corresponding values for the energy spectrum of the three nuclei assigned by the fit (see table 9.2) are in good agreement with simple estimations on the basis of the mass difference of the three nuclei. O-recoils, since they are the lightest constituent, are the dominant contribution at higher energies, reaching up to approximately 300 keV. As expected from simple kinematics, the Ca-recoils contribute up to 100 keV whereas W-recoils show a relevant contribution only in the few keV-range.

So far it was not taken into account that neutrons do not only lead to single-scatter events in the CaWO_4 crystals but also double-scatterings are possible. Such double scatterings result in an event-distribution which does not correspond to that of pure O-, Ca- or W-recoil events but rather leads to an additional distribution, depending on the actual nuclei involved in the double scattering. Therefore, the event distributions cannot be described by the three bands but would need a separate treatment. The fraction of double-scatterings expected in a conventional CRESST detector for an energy range of 10 keV to 280 keV was determined by simulations to be 0.31 [Sch11]. However, the simulation is carried out for the situation of having the neutron source outside of the shielding, thus, the double to single scattering fraction for the data presented in this work is expected to be different.

Nonetheless, the large fraction of double-scatterings shows that data from the neutron calibration of Run 32 has its limitations in the scope of studying QFs .

In order to judge the possible impact of this semi-empirical model in the CRESST experiment further investigations are necessary. Dedicated experiments would have to be carried out fulfilling the following requirements:

- separation of the O-, Ca- and W-recoil-event distribution
- experiment with small crystal to exclude double scattering

- high statistics
- identical experimental conditions as in CRESST (temperature, energy range)

A separation of O-, Ca- and W-recoil events can be realized by using a light detector with an increased energy resolution by a factor of five (see figure 2.17). Since there are no arguments for operating a conventional CRESST detector module consisting of a large light detector together with a large CaWO_4 crystal for the purpose of studying the energy-dependence of quenching factors, the experiment may be reduced in size to arrive at this sensitivity level.

The reduction in size (volume) of the light detector will result in an increased sensitivity. An absorber with an geometry of approximately $(10 \times 20 \times 0.5) \text{ mm}^3$ is suggested since it shows a reduction in volume by a factor of about six. In addition to the light detector, there are several other reasons arguing for a small crystal: in order to ensure that the light emitted from the crystal is sufficiently absorbed in the small-sized light detector, the crystal should have similar dimensions as the light detector to not suffer from the light collection efficiency of the surrounding reflector. Furthermore, small crystals have the advantage that up to twice the amount of scintillation light can be detected.⁵ The smaller dimensions of the crystal reduce the number of reflections inside the crystal and, therefore, reduce the loss of light due to self-absorption.⁶

Last but not least the size of the crystal should be chosen in order to suppress double scatterings of neutrons. The actual scattering length depends on the energy of the neutron and is about (2-3) cm for the energy range of interest in CRESST.⁷ Thus, a crystal with the dimensions of $(10 \times 20 \times 2) \text{ mm}^3$ fulfills the requirements.

Relative to the α -measurement presented in chapter 8, dedicated experiments as described in the latter intercept would allow us to study quenching factors of O-, Ca- and W-recoils in the energy range of interest, with large statistics and consequently higher accuracy. Moreover, such a set-up would also give us the chance to investigate the response of the detector to external electrons from for example a ^{90}Sr -source in order to give an answer on the quenching of gamma-radiation in comparison to electrons.

In addition, such conditions would allow us to evaluate the semi-empirical model proposed by Birks and successfully used to describe the neutron-data as presented in this chapter. In the case that the semi-empirical approach could be proven to accurately describe event-distributions from heavy ions, it would be a great profit to the CRESST experiment in the sense of implementing a more physically accurate model for the description of the data.

⁵ CaWO_4 , CdWO_4 and CsI (pure) crystals with the size of $(10 \times 20 \times 5) \text{ mm}^3$ were investigated within this work and showed 3.1%, 2.7% and 7.1% of the deposited energy in the crystal detected in form of scintillation light.

⁶The impact of self-absorption depends on the quality of the crystal and might be influenced by its opacity. The transport efficiency of the light in conventional CRESST detector modules was studied within [Kie12].

⁷The scattering length of neutrons can be calculated by using data available from the National Nuclear Data Center (NNDC).

10. Conclusion and Perspective

In this work, different key backgrounds of the CRESST-II experiment have been studied. The background involves degraded α -particles as well as the nuclear recoil background from recoiling Pb-nuclei. Any nuclear recoil background in the energy region of interest is very problematic and can mimic WIMP signal events. The origins of these backgrounds have been investigated and measures have been taken to avoid them in a future CRESST run. Moreover, degraded α -particles have been studied in the relevant energy range in order to arrive at a correct description of their light yield. From the data, an energy dependence of their quenching factor was found. Motivated by this finding, a semi-empirical model of quenching factors was applied for the description of neutron induced O-, Ca- and W-recoils from a neutron calibration taking place during Run 32. The results are quite promising as they point in the direction of a more physical description of the CRESST data including an energy-dependency of the quenching factor.

Run 32 was the first long physics run of the CRESST-II dark matter search. In approximately two years of measuring time, the data collected, from eight detector modules, after cuts corresponds to a net exposure of about 730 kg-days. In total 67 events have been observed in the region where low energy nuclear recoils from elastic WIMP nucleus scattering are expected. Not all of these events can be explained by the sources of known background but rather an additional origin of these events has to be considered. One possibility might be WIMPs. However, due to the overall high background contribution and the large uncertainties in the background models, it is important to work on a significant reduction of the present background to clarify in a future run if the excess above known background events still remains.

The backgrounds in the Run 32 data include degraded α -particles as well as a lead recoil background (see chapter 5) and have been studied within this work. The silver coated bronze (CuSn6) clamps, which are used to keep the target crystals in their copper holders were identified as the source of these two types of background. These clamps are the only non scintillating surfaces inside a detector module and therefore, do not provide an active veto for any α -related backgrounds.

The origin of the degraded α -particles could be attributed to a significant contamination of ^{210}Pb in the CuSn6 bulk material introduced by the production process. For the observed lead recoils the situation is somewhat more difficult since two possible mechanisms for the presence of ^{206}Pb -recoils have to be considered: on the one hand, ^{210}Pb nuclei may be present on the uppermost surface layers of the silver-coated clamps due to an exposure to radon from ambient air during the assembling and mounting of

detectors. On the other hand, a contamination with ^{210}Po may be introduced via the electroplating process in the moment before the clamps were removed from the plating solution. According to reference [EPR86] after disconnection of the voltage applied for plating, spontaneous plating of Po is the favored process and ^{210}Po , if present in the solution, can be deposited onto the upper-most layers of the coated clamp. In order to distinguish between both contaminations, an analysis of the time dependence of the rate of detected ^{206}Pb -recoils was carried out. The fit to the data strongly argues for the presence of both mechanism. Moreover, it argues for a significant fraction of the low energetic ^{206}Pb -recoils to come from radon deposits. This is a meaningful result in the light of future CRESST runs as it underlines the importance of the prevention of radon-exposure during the whole assembling and mounting phase of the detectors.

Within this work, a new bronze material for the manufacturing of the clamps was fabricated. Copper, due to its production method, is available in high-purity quality tin, however, is known to contain significant amounts of lead due to their chemical similarity. In order to test for a possible ^{210}Pb contamination, a cryogenic calorimeter using a tin piece as absorber was made to determine the ^{210}Po -activity by measuring the energy deposits of α -particles in the volume of the tin. This is a very sensitive technique to gain information about the radiopurity of a material and it sets a limit on the ^{210}Po -activity of the tin bulk of $<28.2\text{ mBq/kg}$ (90% C.L.). Moreover, the whole production procedure was carefully controlled (ICP-MS analysis and HPGe-measurements) and thus, in the new bulk material the degraded alpha background is expected to be eliminated.

In addition to utilizing a radiopure bulk material for the clamps, any nuclear recoil background from the metal clamps can be avoided if the clamp material is covered with a scintillating material.

The concept of fully scintillating clamps was already tested in Run 31 by using two different designs: one type of the bronze clamps was covered by an scintillating epoxy layer and for the other type, the bronze clamps were wrapped in the scintillating and reflective foil which is also used for the housing of the detectors. Analyzing the Run 31 data allowed us to judge the performance of the these clamp concepts. Two different types of relaxation events introduced by these clamps have been found. Whenever a plastic is in contact with the crystal, pulses with no correlated light signal and a different pulse-shape were observed. These no light events were induced by relaxation processes taking place in the epoxy layer or the scintillating foil right at the position where the clamps touch the crystal. Furthermore, a further class of background events was observed and can be attributed to a micro-fracturing of the crystal due to a too tight holding. These crack-events are a very severe background as they also do not show a correlated light signal, and appear in the region of interest for WIMP search. Since they reveal the same pulse-shape they cannot be distinguished from good particle pulses as for example from a calibration source. On the basis of these results (see chapter 5) the requirements on a future clamping concept have been defined.

In chapter 6, new clamping concepts involving two fully scintillating clamp designs and a partially scintillating design have been developed and tested. In order to evaluate

the performance of new clamps they have to be tested in a conventional CRESST detector module (large CaWO_4 crystal) which, due to the cosmic background, can only be operated in an underground laboratory. In the framework of this work a test-facility has been installed and set-up at LNGS, equipped with a dilution refrigerator and a CRESST equivalent readout electronics and data taking for two SQUID channels, in order to be able to operate one complete detector module. The availability of the test facility was the pre-condition for all measurements carried out within this thesis. The partially scintillating clamp design was successfully tested. The scintillating resin used to coat the main parts of the clamp showed a sufficient light output in order to render any recoil background harmless. Additionally, two fully scintillating clamp concepts have been investigated, utilizing small CaWO_4 balls or half-cylinders as an interface between clamp and crystal. Both concepts suffered from no light events induced by micro-fissures in the balls or half-cylinders respectively. Further studies are necessary in order to find a fully scintillating clamp design which actively rejects any nuclear recoil background produced within the housing of the detector module.

On the same topic, two different detector designs have now been developed within the collaboration: one design uses CaWO_4 sticks in order to keep the crystal in position [Str13]. The other concept relies on a completely different approach. In this design the light detector no longer consists of a disc but is made out of a quite large silicon beaker. The crystal is exclusively held by clamps on the carrier (disc with the diameter of the crystal) and is inserted into the beaker. The carrier is shaped in a way to not allow for a direct line of sight between clamp and crystal. Since the events in the carrier can be distinguished by pulse-shape from events in the crystal, there is a complete active surrounding of the crystal which should allow for a rejection of any nuclear recoil background. A prototype version of both designs will be implemented in the next CRESST run.

However, the majority of detectors in the upcoming CRESST run will be equipped again with bare metal clamps using the new fabricated radiopure bronze material. In order to prevent surface contamination with ^{210}Po from the silver plating, a thin layer of aluminum is sputtered onto the surface of the clamps instead for a better light reflection. Furthermore, the clamps during detector assembling and mounting are exclusively handled in deradonized air and/or stored in a nitrogen flushed environment.

Apart from the degraded α -particles and the lead recoil background, secondary nuclear recoils can also be a very problematic background since the recoiling lead nuclei may introduce secondary particles by sputtering off surrounding materials of the detector.

M. Kuźniak et al. propose that the ion sputtering caused by the ^{206}Pb -recoils on the silver coating off the clamps can produce a so far not considered background in the CRESST experiment [KBP12]. In the present work, the effect of ^{206}Pb ions sputtering of the scintillating and reflective foil has been studied by simulation using the TRIM package [Zie+12] (see chapter 5 and appendix C). For shallow angles ($> 75^\circ$) the distribution of the sputtered set of ions consisting of O-, Ca- and H-ions shows a peak at

an energy higher than 10 keV. Thus, these events are supposed to produce measurable signals in a CRESST detector. However, only in the exclusive case where the α -particle escapes from the foil and hits the non-scintillating metal clamp surface, the sputtered bunches of ions are expected to produce a signal which appears in the low energy and low light region. Otherwise they are vetoed by the additional light produced by the alpha in the scintillating foil. In order to give an answer on the region where the sputtered ions are supposed to appear in the light yield-energy plane, their light yield-value has to be determined. Therefore, recently a measurement was started in the test-facility in order to study the light yield value of such sputtered sets of ions. The results of this measurement might allow to get a first opinion on the relevance of such sets of sputtered educts as a background for WIMP search.

The second part of this work dealt with the question where the previously discussed backgrounds show up in the light yield-energy plane. Thus, in chapter 8 the quenching factor of α -particles in the energy range of interest has been determined. A dedicated experiment was carried out in order to study the response of the detector to low energetic alphas in a conventional CRESST detector module. The measurement has been performed for a CaWO_4 crystal and a chemically similar CdWO_4 crystal (a study of CdWO_4 as an alternative scintillating material in CRESST is available in appendix B). For both target materials an energy dependence of the α -quenching factor at low energy was found. In the analysis of the Run 32 data and earlier runs a constant value for the quenching factor for α -particles as determined at high energies from intrinsic α -emitters was used. Due to the prominent decrease of the QF towards lower energies there is a significant discrepancy observable, in particular in the energy range of interest for WIMP search.

Semi-empirical models as proposed by Birks predict an energy-dependence of the QF . In chapter 9 the approach of Birks is used in order to describe the data from the α -measurement as well as the data from a neutron calibration taking place during Run 32. As found from a fit of this model to the data the α -particle distribution is only well described by the fit at energies >150 keV, however, towards lower energies a discrepancy is observed. The fit overestimates the amount of scintillation light produced and is not in agreement with the observation.

For the neutron induced O-, Ca- and W-nuclear recoils the situation is different. Although the model of Birks is very simple, the fit agrees unexpectedly well with the data. In order to evaluate the impact of this semi-empirical model in the CRESST experiment further investigations are necessary. An experiment with a highly sensitive light detector and a crystal with small dimensions to suppress double-scatterings would have to be carried out. There is hope that in such an experiment the contributions from oxygen, calcium and tungsten appear as separate distributions. Providing these conditions, the accuracy and relevance of the semi-empirical approach of Birks could be proven for neutron-induced events in the region of interest for WIMP search in the CRESST dark matter search.

A. Test Cryostat at Gran Sasso

A.1. Underground Site

The installation of the test-facility started in December in 2009 and first relevant data could be recorded in spring 2011. The facility is located in a service tunnel connecting hall A to hall B (see figure 7.1). A modified container provides the housing of the cryostat. The technical equipment and infrastructure (pumps, water-chiller, ventilation system) is placed outside of the container in a separate enclosed area.

A.2. Dilution Refrigerator

The $^3\text{He}/^4\text{He}$ -dilution refrigerator (see figure A.1) is of the type MINIKELVIN 400-TOF bought from Leiden Cryogenics B.V. together with a gas handling system (GHS). The base temperature of the cryostat in the current set-up is 7 mK. There are four thermal shields present: an outer vacuum chamber (dewar) at ambient temperature, an inner vacuum chamber anchored at liquid helium temperature and two additional radiation shields at 700 mK and 50 mK (optional).

In order to install detectors, the cryostat has to be lifted out of the LHe-dewar using a manual crane. In parking position the inner vacuum can, as well as the radiation shields can be dismantled. The experimental volume available for detector mounting measures 190 mm in height and about 90 mm in diameter.

The cryogenic calorimeters used in CRESST are very sensitive to vibrations from the laboratory and/or mechanical vibrations introduced by the cryostat itself (pumps for $^3\text{He}/^4\text{He}$ -mixture, 1K-pot, boiling LHe). The installation of the housing of the facility was followed by a time-intensive period to study the origin of the different sources of vibrations that prevented the cryogenic detectors from operation. In a first attempt the roof of the container was modified as well as the suspension of the cryostat to gain a more rigid construction which is less sensitive to vibrations from the surrounding and the laboratory.

After this modifications, the main mechanical disturbances were introduced by the turbo-molecular pumps (825 Hz) used to circulate the ^3He as well as the membrane pump, used to provide the temperature of the first cooling stage (about 1 K) of the cryostat. Furthermore, the 1K-pot introduces vibrations by the phase transition happening if liquid helium changes from the normal to the superfluid phase.

To most effectively damp all possible kind of mechanical vibrations the intuitive position for introducing a decoupling system is as close to the detector module as possible.



Figure A.1. – The picture on the left hand side shows the test-facility of CRESST, including the gas-handling system, a rack providing all necessary electronics as well as the cryostat. In the picture on the right hand side the testcryostat is depicted while inserted in dewar. The pumping tubes used to circulate the ^3He -mixture are visible. On the head of the cryostat the feed through for the bias- and heater leads (copper shielded) are visible. The brass boxes fixed by a bar-clamp are the processor electronics of the SQUIDS. The cryostat is mounted inside a conventional dewar which is placed inside a Pb-shielding (10 cm), as visible in the foreground (right picture taken by E. Sacchetti).

The crystal and the light detector disc are mounted with bronze clamps. The crystal is mounted tightly to avoid vibrations induced by friction between the clamps and the crystal.

The microphonics observed on the signals of the detectors showed a frequency spectrum ranging from few 10 Hz to some 100 Hz. The level of disturbances is of course different for the light detector and the crystal due to their huge mass-difference.

Following the observations, a decoupling system was implemented based on the idea of suppressing all vibrations above a few Hertz. A special bronze-spring was manufactured showing a resonance frequency of about 1.8 Hz if loaded with 1 kg. Furthermore, the suspension of the spring was chosen similar to a pendulum suspension. The upper eye of the spring was inserted into a drilled hole of a threaded bolt. The threaded bolt is screwed in the mixing chamber plate of the dilution unit. The same was done with the lower eye of the spring however, the threaded bolt was screwed onto a thick plate made out of NOSV copper. Figure A.2 shows a photograph of the decoupling system together with a detector module.

This design succeeded in eliminating all microphonics on the signals and allowed to operate big CaWO_4 crystals with excellent data quality.

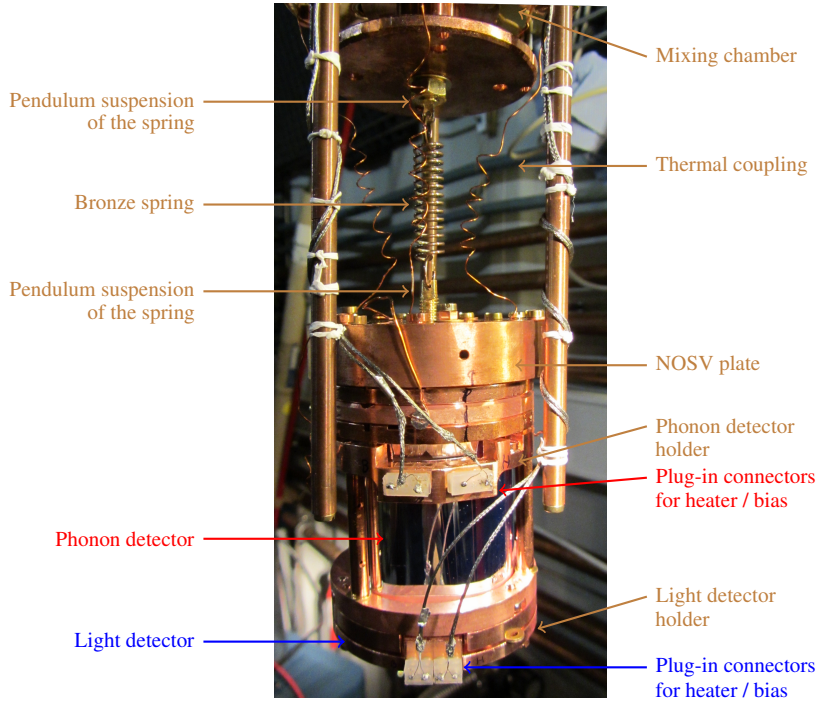


Figure A.2. – Decoupling-system together with a mounted detector module in the testcryostat at LNGS. A bronze spring suspended like a pendulum is utilized to damp vibrations coming from the laboratory or the cryostat itself. The main parts of the decoupling system and the detector module are indicated.

A.3. Electronics and DAQ

All electronic equipment necessary to operate the facility is placed inside the container. In order to measure the temperature of the cryostat, a LR-400 temperate bridge is used. During detector operation the temperature of the mixing chamber is stabilized. A software-based PID-controller is used for this purpose.

To read out the transition edge sensors (TES) dc-SQUIDs from Applied Physics Systems (APS) are used. The processor electronics necessary to operate the SQUID probes are run at ambient temperature (Model 581H). A control/display console (Model 581S) from APS is used to provide the necessary power-input; it also allows to adjust various parameters of the SQUIDs.

The grounding scheme is realized in the following way: the power-supply of the heater-modules and the floating-current sources for biasing the TES, the temperature bridge and the control console of the SQUIDs are connected to the same ground. The cables bringing the bias and heater lines to the cryostat are shielded by two braided strands of copper. This shields reduce electromagnetic interferences and provide a low-inductive grounding. The cables connecting the control console of the SQUIDs to the actual processor electronics are also shielded by braided strands of metal. The SQUID processor electronics is enclosed in a brass box and located very close to the head of the cryostat and the feedthrough connectors (see figure A.1). The cables running from the processor electronics to the feedthrough have a length of only about 30 cm and are double shielded by braided strands of metal. In order to prevent ground loops both the SQUID and the heater-bias-cables are guided physically close to each other to the head of the cryostat.

Inside the dilution unit, twisted pairs of superconducting wires (NbTi-wire with CuNi-mesh) are used for the bias- and heater-leads as well as for the wiring between the input-coil on the SQUID probe and the readout circuit of the TES (see figure 4.1). Furthermore, in the bias- and heater leads low pass filters (cutoff at 10 kHz) are installed to block high frequency interferences. The SQUID-probes are mounted at the 1 K-pot plate and the shunt resistors are located at the mixing chamber.

The DAQ is very similar to the one used in CRESST (see chapter 4).

A.4. Performance

A.4.1. Conditions for Detector Operation

The particle induced event-rate for a standard CRESST crystal (cylinder with 40 mm in diameter and height) is about 0.8 1/s.

The rate expected from neutrons is estimated from a series of measurement to about 2-3 neutrons/kg/day. This is also plausible when comparing to the neutron rate measured in the first stage of CRESST-II, where a rate of about 0.8 neutrons/kg/day was measured [Ang+05]. In the beginning of CRESST-II still no neutron-shield was present

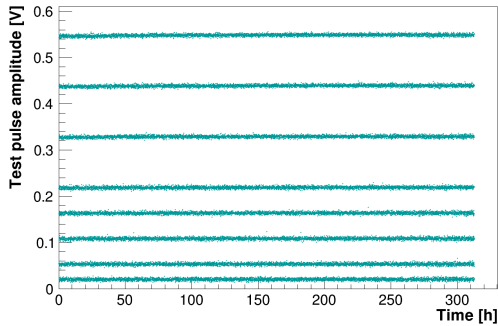


Figure A.3. – The detector response to different test pulses amplitudes recorded as a function of measuring time. The pulses are injected via a heater.

and the detectors where enclosed by a 14 cm copper shield (10 t of weight) followed by 20 cm of low background lead (24 t of weight).

The testcryostat is not surrounded by a Faraday cage. Nevertheless, the noise conditions achieved with the present set-up allow to efficiently trigger on test pulses in the phonon and light detector as low as $5 \text{ keV}_{(ee)}$.

A.4.2. Long Term Stability

With the decoupling in place a very stable and reliable long-term operation of detectors is possible in the testcryostat. In figure A.3 the response of a light detector to different test pulses amplitudes is shown as a function of time. The time period displayed in figure A.3 corresponds to a measurement of almost two weeks showing very stable running conditions.

A.4.3. Gamma-background

A relatively large e/γ -background contribution is observed. In the CRESST experiment typically 1100 events/kg/day are detected (in an energy range of [10,200] keV). This translates to about 6 events/keV/kg/day.

In the testcryostat, the event-rate is about a factor of 100 higher. In the same energy range 118500 events/kg/day or approximately 620 events/keV/kg/day are recorded.

The dominant part of the e/γ -background comes from non-radiopure materials used for manufacturing the cryostat and the LHe-dewar. Furthermore, the Pb-shield does not completely enclose the experiment. The Pb-bricks (10 cm thickness, total mass about 4 tons) are placed below and around the LHe-dewar arriving until its upper end. However, the top area where the cryostat is inserted remains unshielded (see figure A.1).

In figure A.4 the γ -spectrum for a CaWO_4 and a CdWO_4 are shown. Prominent γ -lines from members of the natural decay-chains appear in both crystals. This argues for an external origin of these background sources.¹

As visible in the spectra, a dominant contribution comes from the thorium decay-chain (^{212}Pb observed at approximately 238 keV). The LHe-dewar as well as main parts of the cryostat are manufactured from glass fiber reinforced plastics. These materials are known to be contaminated with thorium [Heu95]. Furthermore, two lines at around 13 keV and 16 keV are present (see last spectrum in figure A.4). The origin of these lines is unknown, most likely this are X-rays produced in the surrounding of the detectors (thermal shields, parts of the cryostat).

The bump-like structure peaking at roughly 150 keV is induced by muon bremsstrahlung generated from muon-induced electron-showers in the neighboring materials of the detectors [Heu95]. This background contribution can be described by using a Landau-distribution.

¹The only exception is ^{210}Pb . It is present as a line in the CdWO_4 spectrum and therefore can be attributed to an external background. In the case of the CaWO_4 , the 46 keV γ -line is recorded together with the accompanied beta-spectrum. Thus it is caused by an intrinsic contamination of the CaWO_4 crystal with ^{210}Pb .

B. Alternative Scintillators

Advantageously, in the CRESST experiment target materials can be exchanged while leaving the experimental set-up unaltered. Therefore, studies are undertaken to investigate alternative materials. The main motivations are:

- a material with a higher light output improves the background discrimination
- as a consequence, a lower discrimination threshold increases the expected WIMP count rate due to the sharp rise of the WIMP spectrum at low energies
- alternative materials allow to study WIMP interactions on different target nuclei, an important signature to confirm a positive WIMP signal

The results from low-temperature studies of CdWO_4 and CsI (pure) are presented. Small (see [Sch+12]) as well as large crystals have been investigated. Here, only the results from measurements of large CdWO_4 and a large CsI (pure) crystals, carried out in the test-facility at LNGS, are presented.

The crystals have been studied with respect to their light output and overall performance as a CRESST detector module. Emphasis was also put on active background discrimination and energy resolution. Table B.1 lists some of the key properties of CaWO_4 , CdWO_4 and CsI (pure).

Properties	CaWO_4	CdWO_4	CsI(pure)
Density (g/cm^3)	6.12	8.0	4.5
Melting point ($^\circ\text{C}$)	1650	1325	621
Structure	Scheelite	Wolframite	CsCl
λ_{max} at 300 K	420-425	480	310
Hygroscopic	no	no	slightly
Θ_D	335	-	125
Refraction index	1.94	2.25	1.74

Table B.1. – Properties of CaWO_4 , CdWO_4 and CsI (pure) [Zde+05; Woo+90; BP66; Sen+04].

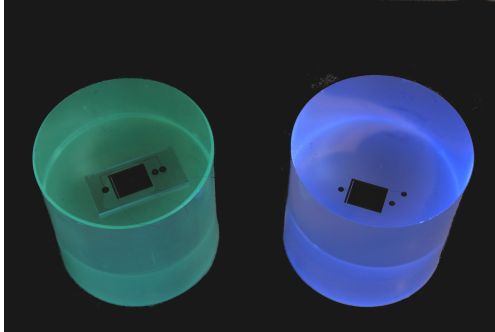


Figure B.1. – CdWO_4 (left hand side) crystal with its TES on a small carrier crystal and a conventional CaWO_4 crystal (right hand side, called K09). The crystals are excited with UV light to demonstrate the differences in their scintillation light wavelength.

B.1. Cadmium Tungstate

B.1.1. Properties

Emission Spectra

CaWO_4 and CdWO_4 reveal different crystal structures (see table B.1), also affecting the scintillation centers and explaining their different emission spectra. The knowledge of the emission wavelength of the target crystals is important as both the efficiency of the light absorber as well as the reflective housing are wavelength dependent.

Recoil Spectrum

The recoil spectra for CsI (pure), CdWO_4 and CaWO_4 were calculated for WIMP masses of $30 \text{ GeV}/c^2$ and $100 \text{ GeV}/c^2$ under the assumption of (see section 1.4.3):

- an energy threshold of 0 keV
- normalized to an exposure of 1 kg-day
- a Helm form factor with Lewin/Smith parametrization

In CdWO_4 , a non negligible fraction of WIMP scatterings is expected to happen on cadmium, leading to a higher expected WIMP-rate in CdWO_4 crystals in comparison to CaWO_4 (see figure B.2). In addition to tungsten, cadmium is another heavy element in the compound resulting in an enhanced rate due to the A^2 proportionality in the cross section. Furthermore, the recoil spectrum for CdWO_4 is more flat in comparison to CaWO_4 . Hence, the WIMP-sensitivity is less dependent on the energy threshold of the detector.

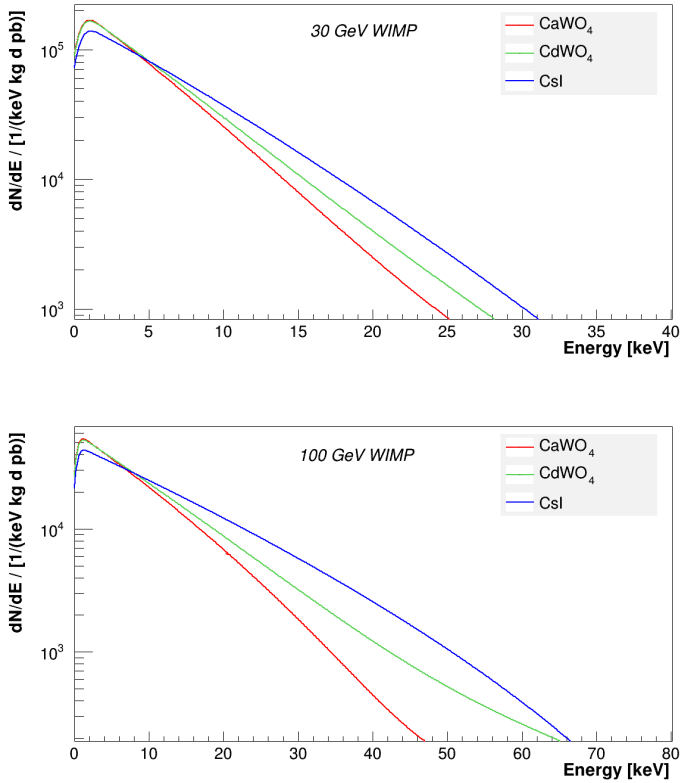


Figure B.2. – Differential event rate for WIMP masses of $30 \text{ GeV}/c^2$ and $100 \text{ GeV}/c^2$ in CaWO_4 (red), CdWO_4 (green) and CsI (blue). The rates are given in units of a WIMP-nucleon cross section of 1 pb .

B.1.2. Experimental Set-up

Afore to the measurement, the large CdWO₄ crystal (40 mm in diameter and height, Hilger Crystal) was annealed in oxygen atmosphere at 950 °C for 48 h.¹

A composite detector design was used for the production of the CdWO₄ detector. A small ((20 x 10 x 2) mm³, WI-287) CdWO₄ carrier crystal, equipped with a TES, was glued onto the large absorber using Epo-Tek 301-2 (see figure B.1, left hand side). The surface of the crystal, which is facing the light detector was roughened as usual to reduce light trapping.

The light detector used is of the SOS-type (silicon-on-sapphire, WII-133). The layout of the TES implies a separated heater structure which is less susceptible to electromagnetic interferences [Huf10]. In order to allow for an absolute energy calibration of the light detector, a ⁵⁵Fe-source is mounted close to the light absorber.

In addition, an α -source was installed inside the cryostat to study the QF of low-energetic α -particles as discussed in detail in chapter 8.

B.1.3. Light Output at Low Temperatures

We characterize the *light-output* of a crystal as the fraction of the energy deposited in the crystal, which is detected in the light detector. The measured amount of scintillation light is not absolute since only a part of the overall produced scintillation light (total about 6% in CaWO₄) is seen by the light detector. The sum of different effects as internal absorption or trapping of the light as well as a non 100% efficient light reflection in the module may be responsible for this discrepancy. However, as different crystals are tested by always using the same experimental set-up as well as an identical geometrical shape of the crystal a comparison among one another is valid.

In order to calibrate the light detector it was irradiated with a ⁵⁵Fe-source. The spectrum of the Mn K α - and K β -line at 5.9 keV (FWHM = 164 eV) and 6.5 keV is shown in figure B.3.

When irradiating the CdWO₄ crystal with 122 keV from a ⁵⁷Co source, the light-output of the CdWO₄ crystal is found to be 1.48%. This value is comparable to that of CaWO₄, showing a light output around 1-2%, depending on the quality of the crystal.

Figure B.4 shows the spectra of the phonon- and the light detector while exciting the crystal with an external ⁵⁷Co- and ²⁴¹Am-source. The lines from ⁵⁷Co at 122.1 keV and 136.5 keV (FWHM = 2 keV) are separated in the phonon detector (red spectrum). The light detector (blue spectrum) cannot resolve these lines. The absolute energy detected in the light detector from the absorption of 122.1 keV and 136.5 keV gammas in the crystal are 1.8 keV and 2.0 keV, respectively, resulting in about 1.5%, as previously mentioned.

¹CaWO₄ crystal are typically annealed at 800 °C. Investigations proved that the higher temperature for CdWO₄ resulted in a higher light output measured at room temperature by using a PMT set-up. For CaWO₄ an increase in annealing temperature did not show an improvement of the light output at room temperature. A more detailed description of this measurements is given in the diploma thesis of R. Kleindienst [Kle10].

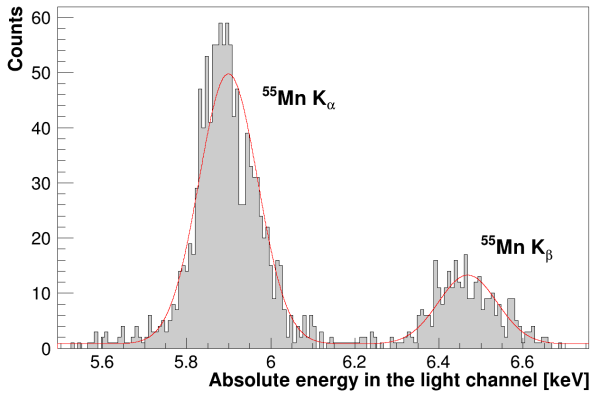


Figure B.3. – Spectrum of the light detector while being irradiated by a ^{55}Fe -source. The Mn K_{α} - and K_{β} -line at 5.9 keV and 6.5 keV show a resolution of 164 eV (FWHM). These lines are used to establish an intrinsic energy calibration of the light detector.

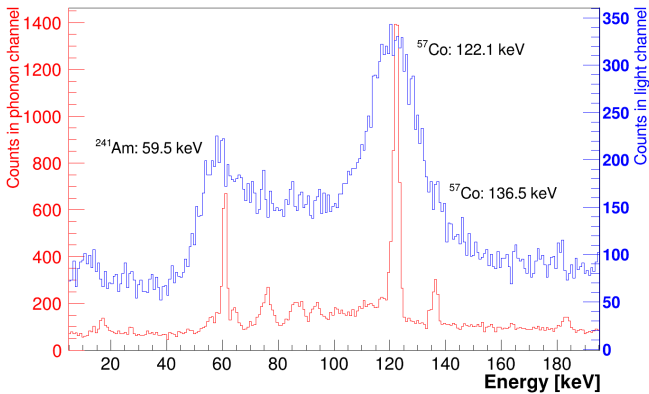


Figure B.4. – Energy spectrum of a CdWO_4 detector module while being excited by an external ^{57}Co - and ^{241}Am -source. The spectra of the phonon- and light-channel are depicted in red- and blue color respectively. The phonon channel shows an energy resolution comparable to CaWO_4 crystals measured in the same set-up; both lines from ^{57}Co are well separated.

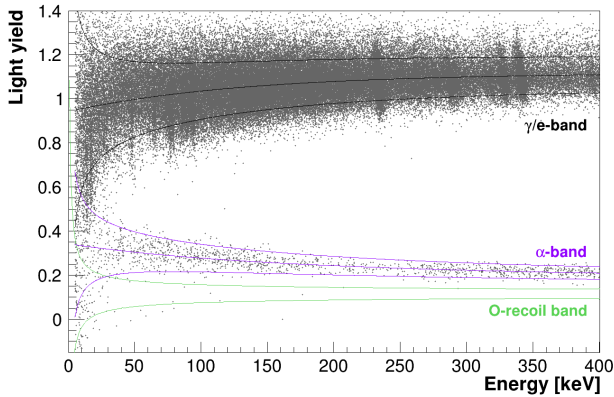


Figure B.5. – Data in the light yield-energy plane for the CdWO_4 crystal. The bands which indicate the region expected for γ/e -interactions, α -particles and oxygen-recoils (e.g. from neutron-interactions) are shown in form of central probability bands. 80% of all events are expected to be contained within the two boundaries. The e/γ -events are well separated from the nuclear-recoil region, where WIMP interactions are expected. The high population of the α -band is due to the presence of a dedicated α -source.

B.1.4. Event Discrimination

Figure B.5 shows data in the light yield-energy plane of the detector module using CdWO_4 . The bands where e/γ -interactions, α -particles and oxygen-recoils induced by for example neutrons are depicted. The bands are determined applying the fit as described in section 8.4. Each band is represented by at most three lines: a mean line (dashed line) and two boundary lines. 80% of the events are expected to lie within the two central boundaries ($\pm 1.28 \sigma$). Gammas and electrons (black-colored band) from mainly external background sources can be very well distinguished from nuclear recoils (green-colored band and below). Due to the presence of a degraded α -source, the α -band is highly populated. It was used to study the QF of low energetic alphas. Further explanations and detailed information on the low-energy α -analysis can be found in section 8.6.

The events appearing in the oxygen-recoil band are caused by neutrons. The test-facility at Gran Sasso does not feature a neutron-shielding, therefore the number of background neutrons interacting in the absorber is increased in comparison to the main CRESST experiment.

Furthermore, a number of events is present below the O-recoil band. These events are generated by the α -source (see section 8.3.2). In order to prevent recoil nuclei from the source reaching the crystal, it was covered with a thin foil of gold. However, the

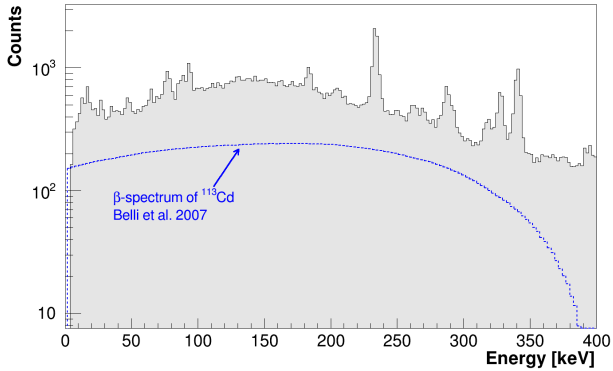


Figure B.6. – Energy spectrum of gammas and electrons in CdWO_4 . In addition, as a blue-dotted line the β -spectrum of ^{113}Cd is shown (from [Bel+07]). Due to the high external e/γ -background in the test-facility, the contribution from the beta-decay of ^{113}Cd is not the dominant background in the low energy region. However, the count rate from ^{113}Cd is about ten times higher than the overall event rate in the low energy region of a CaWO_4 operated in the main CRESST experiment.

thin gold foils revealed tiny holes that are responsible for the observed events showing no or only little associated light in the region below 80 keV.

To summarize, the CdWO_4 crystal is as good as CaWO_4 concerning the energy resolution and the discrimination power. In the next section, the background level from intrinsic radioactive contaminations inside the crystal is studied.

B.1.5. Radioactivity in Cadmium Tungstate

^{113}Cd Isotope So far CdWO_4 has not been used as target. Natural cadmium consists of 12.22% of the unstable ^{113}Cd isotope decaying via beta-decay to stable ^{113}In ($Q_\beta=318$ keV, $T_{1/2}=7.7\cdot 10^{15}$ y) [MPG06]. As the separation of e/γ -events and nuclear recoils works efficiently, this is not a limiting constraint. Nevertheless, due to the low Q -value, the overall background in the low energy-region is significantly increased. From the beta-decay of ^{113}Cd around 100 events/kg/keV/day are expected in an energy range of 10 keV to 300 keV, which is a factor of about 10 higher than observed in CaWO_4 in the low energy region. A higher e/γ -background will result in an increased γ -leakage, finally determining the lower energy threshold of the WIMP acceptance region.

Figure B.6 shows the energy spectrum of gammas and electrons in CdWO_4 measured in the test-facility at LNGS. Besides, also the β -spectrum caused by ^{113}Cd is indicated (blue-dotted line) [Bel+07].

The dominant background observed in figure B.7 comes from external e/γ -radiation

from the testcryostat and its surrounding.² Hence, the contribution from the ^{113}Cd beta-decay to the spectrum is only a small fraction of all detected gammas and electrons. However, in the main CRESST experiment, CaWO_4 crystals show a 10 times lower total event-rate in the energy range from 10 keV to 300 keV in comparison to the number of events only expected from ^{113}Cd in CdWO_4 .

In the case of using a target material with an increased count rate due to the presence of an intrinsic radionuclide, the loss of live time has to be accounted for. For a CdWO_4 crystal of 400 g the count rate from ^{113}Cd is about 0.23 s^{-1} , resulting in about 11.5% loss of live time considering a record length of 328 ms, the pre-trigger intervals and the time for reading out, summing up to about 500 ms.

Natural Decay Chains The radioactive contamination with uranium and thorium can be derived from an α -analysis. Alpha-emitters being present in the CdWO_4 crystal will, due to their short projected range, deposit their full energy in the crystal. They appear as lines in the energy spectrum at the Q-value of the decay (MeV-scale).

The exact energy reconstruction of high-energetic α -events in this measurement is limited by the overall high event-rate. Most pulses reveal a decaying baseline resulting in a decrease in energy resolution. Therefore, in this analysis all events in the energy window of 3.5 MeV to 7 MeV are summed up in order to calculate the limit for contributions from all natural decay chains.

This is a valid approach, as the relevant energy region is known to be quasi background free; practically all events detected in this energy regime have to come from an internal α -contamination of the crystal. Taking into account the effective exposure, a count rate of $1.54 \pm 0.15 \text{ mBq/kg}$ is calculated. This is one order of magnitude less as found in CaWO_4 crystals operated in the latest CRESST run.

Summary

The following list summarizes the results from the study of CdWO_4 as target material:

- CdWO_4 shows a light output of 1.5%. This is in the region of the best CaWO_4 crystals (up to 2%). The tested CdWO_4 crystal had a lutescent appearance. This may be attributed to a deficiency of oxygen in the crystal lattice which may be cured by annealing at high temperatures in oxygen atmosphere. In CaWO_4 crystals the light output could be improved by up to 50% by this procedure. Therefore, there may still be room for improvement of the light output of CdWO_4 .
- The level of radioactive impurities coming from natural decay chains was found to be $1.54 \pm 0.15 \text{ mBq/kg}$. This is a factor of ten better than in CaWO_4 .
- CdWO_4 crystals are commercially available, a pre-requisite when thinking about an upgrade of the present experiment.

²A more detailed discussion on the background situation of the test-facility can be found in section A.4.

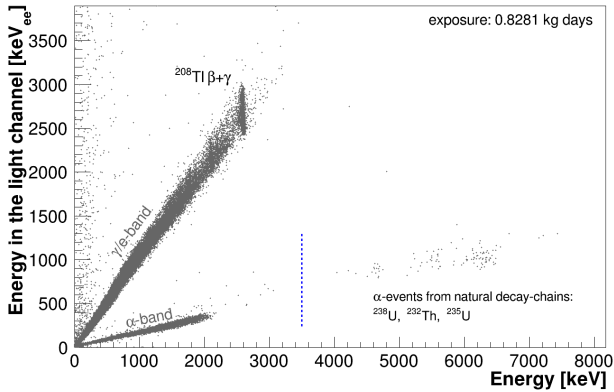


Figure B.7. – Energy in the light channel plotted vs. energy in the phonon channel for the CdWO₄ detector module. The γ/e -band as well as the α -band are visible. The high number of events in the α -band below 2400 keV is due to a samarium α -source irradiating the crystal. The rate coming from $^{238}\text{U}/^{232}\text{Th}/^{235}\text{U}$ in an energy window of 3500 keV to 7000 keV was calculated to be 1.54 ± 0.15 mBq/kg.

- The WIMP sensitivity of CdWO₄ is increased in comparison to CaWO₄ due to the contribution of the cadmium nuclei.
- The high natural abundance of the ^{113}Cd isotope results in an additional event rate of 0.23 s^{-1} in the low energy region ([10-350]keV).

B.1.6. Neutrino Physics and Perspectives

CdWO₄ crystals are also interesting for the search of the Neutrinoless Double Beta Decay (0 ν DBD) [Gir+09]. The existence of the 0 ν DBD would clarify the nature of the neutrino (Dirac or Majorana) and its mass scale would be set.

In CdWO₄, the isotope ^{116}Cd ($\eta=7.5\%$) is a known DBD-emitter with a transition energy of $Q_{\beta\beta}=2805$ keV [MPG06]. As this Q-value exceeds the highest natural 2615 keV γ -line from ^{208}Tl , very low background levels can be expected in the region of interest for 0 ν DBD.³

Besides germanium diodes, massive bolometers are used nowadays to study neutrino properties. The CUORICINO experiment [And+11], the most massive bolometric experiment realized so far, studied the 0 ν DBD of ^{130}Te in TeO₂ crystals reaching

³The natural gamma-activity drops significantly above the ^{208}Tl -line allowing for extremely low background conditions.

an energy resolution of 0.2-0.5% in the region above the ^{208}Tl γ -line as well as extremely low background (0.1 counts/keV/kg/year). CUORE will operate up to 1 ton of detector mass and aims for a further reduction of external background of one order of magnitude [Arn+04]. The main background of these kind of experiments comes from α -contaminations on the surfaces facing the crystals. If implanted in the surrounding material, these α -emitters reveal a flat energy spectrum between the Q-value of the decay down to threshold energy. Therefore they add a background-contribution in the region of interest for 0vDBD.

Scintillating bolometers provide an active veto for such kind of degraded α -events and render this background harmless. The LUCIFER experiment plans to use scintillating bolometers [Pir+06] to study the 0vDBD of ^{82}Se . In total, ten ZnSe crystals enriched in ^{82}Se shall be operated in the near future at LNGS.

The operation of for example enriched CdWO_4 crystals in the CRESST experiment would allow to search for dark matter, as well as for 0vDBD in one experiment. The requirements that have to be met by an experiment of this kind are:

- DBD-isotope with high abundance and a transition energy above the ^{208}Tl γ -line
- excellent energy resolution in the region interesting for WIMP search, as well as in the region of >2600 keV
- an absorber crystal showing good scintillation properties
- low background conditions
- a low energy threshold (around 10 keV)
- very low level of intrinsic impurities from natural decay chains

The CRESST experiment fulfills all pre-requisites in terms of low-background and detector performance. The detector modules are sensitive to a wide energy range (keV to MeV) and combine a low energy threshold with an excellent energy resolution.

Despite the overall high event-rate in the test-facility the CdWO_4 measurement performed within this work shows an energy resolution of the ^{208}Tl line of 25.6 keV (FWHM $\sim 1.0\%$). At the same time, the detector was sensitive in the region for WIMP search ([15-40] keV), showing a discrimination power comparable to that of CaWO_4 .

Therefore, CdWO_4 crystals are a good candidate for a combined experiment as they reveal a high light-output and a sufficient abundant DBD-emitter (^{116}Cd , 7.5%) with a transition energy exceeding the ^{208}Tl γ -line.

The only disadvantage of this material is the beta-decaying isotope ^{113}Cd (12.22%, corresponding to 0.23 s^{-1} in a CRESST sized detector), which significantly increases the background in the lower energy region.

Succeeding in a feasible and affordable depletion process of ^{113}Cd , CdWO_4 crystals would turn to be the most suitable target material in the scope of searching for both, dark matter and 0vDBD in the same experiment.



Figure B.8. – CsI(pure) crystals mounted in a copper holder. The small carrier crystal providing the TES was attached to the large CsI by using a tiny amount of grease (small round spot below the W-TES). The crystal has a transparent appearance.

B.2. Cesium Iodide

B.2.1. Experimental Set-up

The tested CsI (pure) crystal has a cylindrical shape (40 mm diameter and height) and was produced by Hilger Crystal. Since CsI is hygroscopic, it had to be handled in a nitrogen flow box during the entire detector production.

A composite detector design was used since the melting point of CsI (undoped) is very low and does anyhow not allow for a direct evaporation of the W-TES onto the crystal. The carrier consists of a small sapphire wafer ($20 \times 10 \times 2 \text{ mm}^3$) which was attached onto the CsI crystal using Apiezon N grease. Using grease instead of an epoxy resin for gluing the carrier onto the large crystal was tested before while using CaWO_4 crystals. No change in signal amplitude is observed.⁴

The crystal was mounted in a conventional detector holder and paired with a silicon-on-sapphire light detector (Erwin). The light detector was equipped with an ^{55}Fe -source. In figure B.8 a picture of the mounted CsI crystal is shown. To enclose the detector module a reflective silver foil was used.

Table B.2 gives information on the radiopurity of the CsI crystal as measured by a HPGe-measurement.

B.2.2. Light Output at Low Temperatures

CsI(pure) is a poor scintillator at room temperature but its scintillation properties are known to improve significantly at low temperatures .

The light output for the CsI (undoped) crystal determined via calibration with the

⁴Grease has the advantage that it allows to remove the carrier again after the measurement.

Decay chain	Nuclide	Activity
^{232}Th	^{228}Ra	< 7.7 mBq/kg
	^{228}Th	< 6.7 mBq/kg
^{238}U	^{226}Ra	< 3.2 mBq/kg
	^{234m}Pa	< 0.2 Bq/kg
^{235}U	^{235}U	< 12 mBq/kg
	^{137}Cs	(64 ± 7) mBq/kg
	^{134}Cs	(54 ± 4) mBq/kg
	^{60}Co	< 0.82 mBq/kg

Table B.2. – Results of a HPGe-measurement of the CsI(pure) crystals. Limits are given for the radioactive nuclides of cesium. Only upper limits can be given on contaminations from uranium-/thorium decay-chains. Results are given within 68% confidence limits [Lau11].

122 keV γ -line from an external ^{57}Co source was 4.9%.⁵. This is a very promising result as it is about a factor of three more than commonly achieved from CaWO_4 . Results from this measurement are also reported in [Sch+12].

B.2.3. Performance of the Phonon Channel

Despite the very large scintillation light signal, the achieved detector performance is not convincing since the detected phonon signals showed very small signal amplitudes.

In figure B.9 the response of the light and the phonon detector to 122 keV gammas of ^{57}Co for a conventional CaWO_4 crystal and a CsI crystals are shown. In both measurements the light detector was operated in the same operating point. The phonon signal in CsI (pure) is a factor of ten smaller than the comparable signal in CaWO_4 . Such small signal amplitudes translate into a bad energy resolution. This becomes more clear having a look at the resolution of directly injected heater pulses. A test pulses with an amplitude of 0.032 V, corresponding to an equivalent particle energy of 139 keV showed an energy resolution of 11.6 keV. This is more than an order of magnitude less than recorded with CaWO_4 .

In addition, there is a strong light-phonon anti-correlation detected in CsI. Assuming a detector with an infinite good energy resolution, monochromatic γ -events are supposed to produce a point-like spot in the light yield-energy plane. Due to the finite energy resolution of the light detector and phonon detector, events introduced by for

⁵The light detector could separate sufficiently K_α and K_β from the ^{55}Fe X-ray source having a FWHM = 260 eV at 5.9 keV.

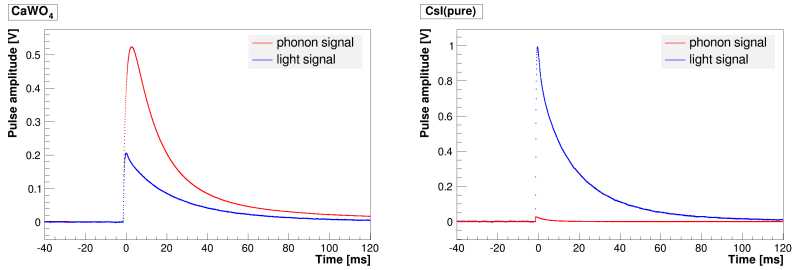


Figure B.9. – Phonon and light signals due to energy deposition of gammas of 122 keV for a CaWO_4 and a $\text{CsI}(\text{pure})$ crystal. The phonon signal in CsI is a factor of ten smaller than the comparable signal in CaWO_4 . The same light detector operated at the identical operating point was used for both measurements.

example the 122 keV gammas appear as lines in the light yield-energy illustration of a typical CaWO_4 crystal.

In figure B.10 data from the $\text{CsI}(\text{pure})$ crystal in the light yield-energy plane is depicted. The afore mentioned 122 keV γ -line does not appear as a straight line but shows a negative slope. This might be an indication of fluctuations: the fraction of deposited energy in the crystal that is converted into phonons and scintillation light varies. However, due to energy conservation, the fluctuations have to compensate each other. This means that the energy that is not converted into scintillation light has to lead to an increased signal amplitude in the phonon channel and vice versa. This effect obviously increases with an increased relative light output of the crystal.

Another explanation for the observed behavior may be *position dependent effects*. CsI crystals are hygroscopic and a degradation of its upper surface layers might result in such variations since such degraded or slightly damaged surfaces can modify the light emission or self absorption of the scintillation light.

Further investigations on this interesting target material are necessary: an understanding of the mechanism(s) that are responsible for the loss of phonons resulting in small signal amplitudes as well as the observed negative slope of the calibrations lines has to be established. The lower Debye temperature of CsI as well as the hygroscopicity may also play some crucial role in this context. It deserves a mention that the results from the CsI measurement are the first results ever obtained by using a CsI crystal in a scintillating calorimeter configuration at such low temperatures.

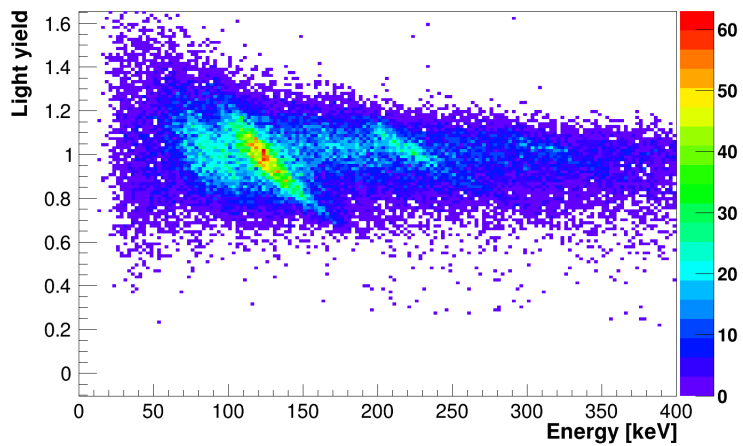


Figure B.10. – Light yield-energy plane for CsI(pure). The 122 keV γ -line from an external ^{57}Co -source appears with a negative slope. See text for discussion.

C. Sputtering

This appendix presents the principle and basic results from simulations carried out concerning surface sputtering of Pb-atoms (103 keV resulting from ^{210}Po) on the detectors scintillating and reflective surrounding by using the TRIM package [Zie+12]. Since the actual reflective layers of the foil (VM2002 from 3M) are very thin, they are protected by a supporting foil consisting of PEN (polyethylene naphthalate). Thus, sputtering processes are expected to happen on this material by releasing bunches of carbon, oxygen and hydrogen atoms. In the simulation, Pb-ions with 103 keV are fired onto a layer of PEN (10 μm thickness). The PEN material is cataloged in TRIM and available from the compound data base.

C.1. Energy Spectrum of Sputtered Set of Ions

In figure C.1 the histogrammed results for different incident angles (70° , 75° , 80° , 85°) of the Pb-ions are depicted. The incident angle is defined in the following way: an angle of 90° means the ions is traveling parallel to the foil, whereas an angle of 0° means that the ions hits the foil at an angle of 90° . The entries in the histogram correspond to the summed energies over all sputtered ions per incident Pb-ion which reveal an energy higher than the surface binding energy. The surface binding energy for all three types of sputtered ions (hydrogen, oxygen and carbon) was set to 4 eV.

For shallow angles ($> 75^\circ$) the distribution of the sputtered set of ions shows a peak at an energy higher than 10 keV. Thus, these events are supposed to produce measurable signals in a CRESST detector. Because of geometrical constraints, not all sputtered ions will be able to reach the crystal. Since from the simulation also information on the direction of the sputtered ions is available, an angular distribution can be defined that has a high probability to be seen in the crystal. For the data presented in figure C.1 a simplified angular correction was applied.

9999 Pb-ions were always simulated for all incident angles. For angles $> 75^\circ$, every incident Pb-ion gives rise to a set of sputtered educts. If calculating the integral over all incident angles and considering only entries that exceed an energy of 10 keV (lower energy threshold in CRESST) a fraction of about 15% may be seen in the detector. However, this does not consider the important aspect that these events can be vetoed as long as the α -particle produces a scintillation light signal in the foil. Only in the exclusive case where the α -particle escapes from the foil and hits the non-scintillating metal clamp surface, the sputtered bunches of ions are expected to produce signals in the low energy region. Thus, the fraction that may contribute is $\ll 15\%$.

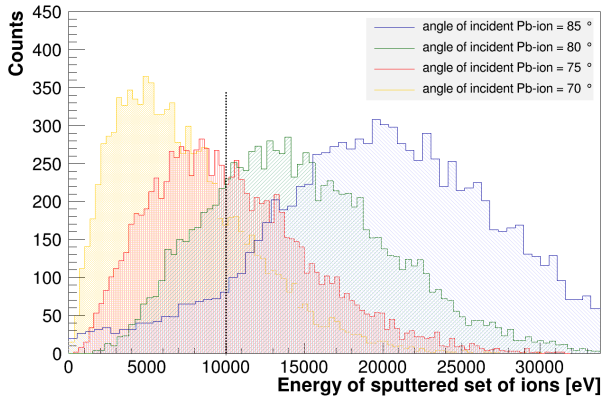


Figure C.1. – Energy spectrum of sputtered sets of ions produced by shooting Pb-ions (103 keV) onto a PEN layer as calculated with the TRIM package [Zie+12]. Each entry in the histogram corresponds to the summed energy over all sputtered ions per incident Pb-ion. Only sputtered ions with an energy larger than the surface binding energy (4 eV) are considered. The sputtered sets consist of hydrogen-, oxygen- and carbon-ions.

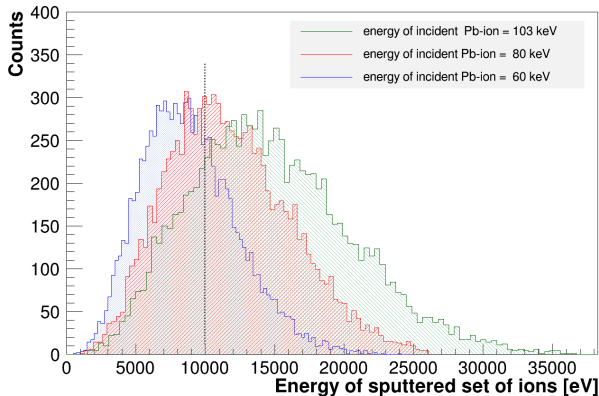


Figure C.2. – Energy spectrum of sputtered sets of ions for shooting Pb-ions onto a PEN layer. The results for different energies of the Pb-ions are histogrammed. The angle of the Pb-ions relative to the PEN-layer was set to 80°.

It is worth mentioning that, depending on the implantation depth of ^{210}Po , the energy of the Pb-recoil available for sputtering may be smaller than 103 keV. Thus, in figure C.2 the energy spectrum of sets of sputtered ions for Pb-ions of different energies (60 keV, 80 keV, 103 keV) is shown. The angle in this case was set to 80° .

C.2. Energy Spectrum of Sputtered O-, C- and H-Ions

Although the scintillation light produced by the single sputtered ions is detected simultaneously, it is interesting to have a look at the actual energy distribution of the single sputtered O-, C- and H-ions. Thus, in figure C.3 the spectra for the relevant three ions are shown for an incident angle of 80° using the data from the simulated 9999 Pb-ions, as mentioned before.

C- and O-ions are responsible for the main sputtered educts and all three spectra show an increase towards lower energies. Thus, a set of sputtered ions is made out of many single ions, typically showing energies in the few keV-range. This can be advantageous, as depending on the actual energy-dependence of the particular quenching factor, the overall light yield-value of the sputtered bunches of ions may be higher. In other words, the light detected from five C-ions with an energy of 2 keV may be higher than the light produced by a C-ion of 10 keV. This would provide a possibility to discriminate such kind of background from possible signal events.

C.3. Conclusion and Outlook

In order to give an answer on the region where the sputtered ions are supposed to appear in the light yield-energy plane, their light yield-value has to be calculated. The simulation provides information on the type of sputtered ion. However, in order to calculate the light yield for each set of sputtered ions, the quenching factors for carbon- and hydrogen-ions in CaWO_4 have to be known. In the case this information would be available for such low energies, the corresponding light yield for all sputtered ions of every bunch could be determined.¹ This is an interesting project, beyond this work.

To summarize, these basic simulations showed that sputtering off the PEN-layer of the scintillating and reflective foil has to be considered as an additional process which is expected to produce measurable signals in the low energy region of CRESST detectors. In order to get information on the light-yield distribution of these sputtered set of ions, the quenching factors for hydrogen- and carbon-ions in CaWO_4 have to be known.

Further investigations are necessary in order to clarify the relevance of such sets of sputtered educts as a background contribution to the WIMP sensitive region in the CRESST experiment.

¹ Sputtered ions per incident Pb-ion are detected simultaneously. They produce a signal in the phonon detector corresponding to the sum over all single ion energies. The same applies for the light produced by these ions.

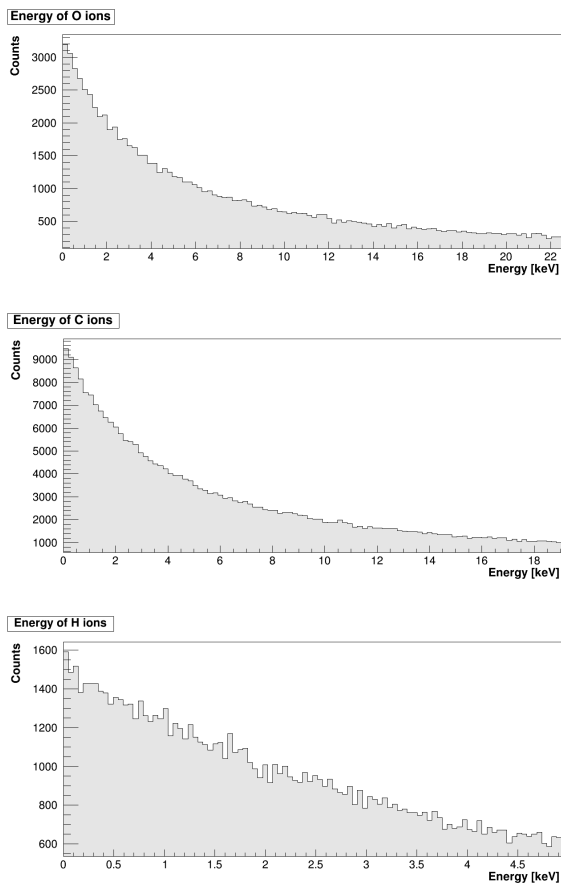


Figure C.3. – Simulated energy spectra of O-, C- and H-ions produced by shooting Pb-ions (103 keV) onto a PEN layer. Only ions with an energy larger than the surface binding energy (set to 4 eV) are histogrammed.

D. Calculation of Quenched Bands

In case the QF for a particular particle is known, its light yield-distribution can be calculated on the basis of the fit to the light yield-distribution of the e/γ -events.

Mean The mean of the light yield of a quenched band is given by

$$\Upsilon^{QF}(E) = QF \cdot (L_0E + L_1E^2) \quad (\text{D.1})$$

where L_0 and L_1 are the same parameters as already introduced in section 8.4.1. The QF provides in this case a constant value. An energy dependence of the QF was not foreseen in this procedure, as used for the analysis of Run 32.

Width The width of a quenched band can be described very similar to the width of the e/γ -band. Taking into account the resolution of the phonon and the light channel, the width of the e/γ -band is given by [Sch10]

$$\sigma^\gamma(L) = \sqrt{[\sigma_L^\gamma(L)]^2 + [1 \cdot \sigma_p^\gamma(E(L))]^2} \quad (\text{D.2})$$

where σ_L^γ is the resolution of the light channel at L and σ_p^γ is the resolution of the phonon channel at energy $E(L)$. The factor of one indicates that the light yield of the e/γ -band is about unity. The resolution of the light and phonon channel for the quenched bands can be determined in the same way as before for the e/γ -interactions since the processes that determine the resolution (baseline noise, photon statistics) are identical. Due to the fact that these processes depend on energy (of the detected scintillation light), the resolution has to be multiplied by QF . Thus, the width of a quenched band can be calculated by [Sch10]

$$\sigma^{QF}(L^{QF}) = \sqrt{[\sigma_L(L^{QF})]^2 + [QF \cdot \sigma_p(E)]^2}. \quad (\text{D.3})$$

In the e/γ -band the relation $L^\gamma \simeq E$ is valid. For the quenched bands this relation turns into $L^{QF} \simeq QF \cdot E$. Therefore, also the uncertainty in the phonon channel measurement is reduced by the quenching factor.

It should be emphasized that the procedure of calculating quenched bands to present knowledge is only justified to some level of approximation.¹

¹In the case of a highly populated O-recoil-band (as e.g. from a neutron calibration) the band for O-recoils can be determined directly from the data, similar to the α -band (see section 8.4.2). However, the knowledge of the correct distributions of W-, Ca- and O-recoils has to be taken into account in order to correctly parameterize the energy spectrum.

E. Description of the Electron/Gamma-distribution

In order to describe the light yield distribution of e/γ -events in a CRESST detector by using the model of Birks, stopping powers for the respective interacting particle have to be known. In the case of the e/γ -events one might rise the question if it is justified to exclusively use the stopping powers for electrons in order to describe the distribution which, however, definitely includes both type of interactions.

Gammas in the energy region of interest will dominantly interact via photoelectric effect and also Compton scattering. Thus, electrons introduced via such interaction processes have definitely lower energies than the energy deposited and detected in the crystal.

The stopping powers for electrons are calculated using the Bethe-Bloch formula. Hence, the stopping power are calculated with the assumption that one single electron of a certain energy is slowed down in the material to zero energy. This means using, in case of an energy deposition in the crystal from a gamma of 60 keV, the corresponding value for the stopping power for a electron of 60 keV will not produce the correct result. The amount of produced scintillation light for γ -interactions (see figure 9.1) will be overestimated.¹

However, if the dominant background contribution in the low energy region of the e/γ -distribution can be attributed to be due to electrons, a description of the e/γ -band by using the stopping power for electrons would approximately be justified.

In this context it is helpful to look at the background spectrum of the crystal VK33 operated in Run 32 (see figure E.1).² A dominant feature in this spectrum comes from ^{210}Pb . Since the γ -line at 46.5 keV is visible together with the beta-spectrum (Q-value: 63.5 keV), the contamination is supposed to come from an internal or maybe a combination of intrinsic and extrinsic contamination. Besides the lead contribution, another two dominant features around 10 keV and 25 keV are present in the spectrum. These features were identified by [Lan08] to be due to an internal contamination of the crystal with ^{227}Ac . A level scheme of the decay of this actinium isotope is depicted in figure E.3. According to the decay scheme three beta spectra are expected: one beta spectrum extends to the Q-value of the decay at 44.8 keV. A second beta spectrum starts

¹Subsequent, this would also mean that the scintillating light emitted from γ s is slightly quenched in comparison to that of electrons of same energy.

²The detector module VK33/Franz was used in order to describe the data from a neutron calibration carried out during Run 32 by applying the model of Birks (see section 9.5).

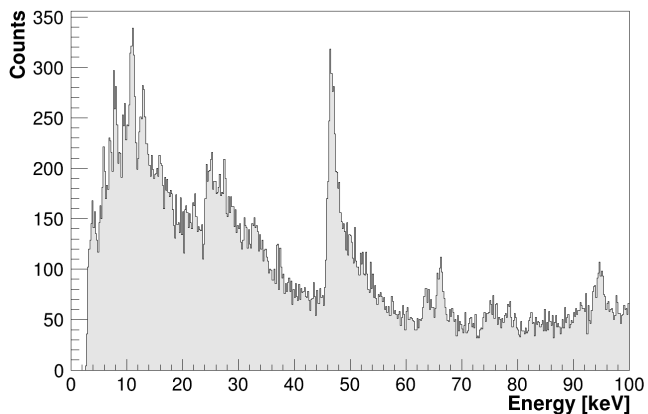


Figure E.1. – Background spectrum recorded with the phonon detector VK33 in Run 32.

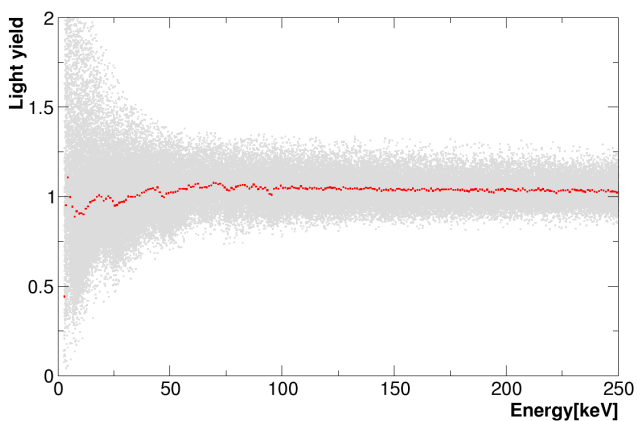


Figure E.2. – Data in the light yield-energy plane of the detector module VK33/Franz. The red points are the mean of the counts in each 1 keV energy bin.

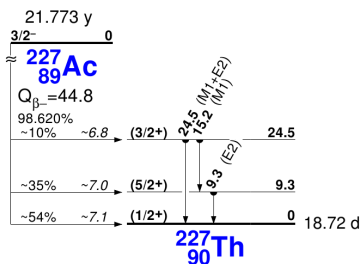


Figure E.3. – The level scheme of the ^{227}Ac decay. Taken from [Fir+99].

at the first excited state of ^{227}Th at 9.3 keV and the third beta spectrum starts at the second excited daughter state at 24.5 keV. Thus, in the lower energy region the background is given by the before mentioned γ -transitions which are overlaid by four beta spectra, as clearly visible in figure E.1.

To summarize, in a typical CaWO_4 crystal there is a variable distribution of electron and gammas present in the low energy region. The distribution depends on the intrinsic and extrinsic background. This can also be visualized by plotting the mean of the counts per energy bin in the light yield-energy plane. A scatter plot of the detector VK33 including the mean for each energy bin of 1 keV is depicted in figure E.2. The mean (red points) shows small dips at the energy intervals where the gamma-transitions (9.3 keV, 24.5 keV and 46.5 keV) from the aforementioned beta-spectra appear. This points in the direction of a reduced light yield for gamma-interactions, as already stated in [Lan08; Lan+09]. However, electrons are responsible for the dominant background contribution in this low energy regime.

Thus, applying Birks' model by using stopping powers of electrons in order to describe the distribution of the e/γ -events is justified, but only at some level of approximation.

Bibliography

- [Aal+11a] C.E. Aalseth et al. “Results from a Search for Light-Mass Dark Matter with a p-Type Point Contact Germanium Detector”. In: *Phys. Rev. Lett.* 106 (2011), p. 131301.
- [Aal+11b] C.E. Aalseth et al. “Search for an Annual Modulation in a p-Type Point Contact Germanium Dark Matter Detector”. In: *Phys. Rev. Lett.* 107 (2011), p. 141301.
- [Aal+13] C.E. Aalseth et al. *CoGeNT: A Search for Low-Mass Dark Matter using p-type Point Contact Germanium Detectors*. 2013. arXiv:1208.5737 [astro-ph.CO].
- [Abb+12] R. Abbasi et al. “Multiyear search for dark matter annihilations in the Sun with the AMANDA-II and IceCube detectors”. In: *Phys. Rev. D* 85 (2012), p. 042002.
- [Ack+12] M. Ackermann et al. “Measurement of Separate Cosmic-Ray Electron and Positron Spectra with the Fermi Large Area Telescope”. In: *Phys. Rev. Lett.* 108 (2012), p. 011103.
- [Adr+09] O. Adriani et al. “An anomalous positron abundance in cosmic rays with energies 1.5–100 GeV”. In: *Nature* 458 (2009), p. 607.
- [AFW49] D.H. Andrews, R.D. Fowler, and M.C. Williams. “The Effect of Alpha-particles on a Superconductor”. In: *Phys. Rev.* 76 (1949), pp. 154–155.
- [Agl+89] M. Aglietta et al. “Neutron Flux Generated by Cosmic Ray Muons at 5200 hg/cm⁻² Underground. Depth – Neutron Intensity Curve.” In: *Il Nuovo Cimento C12* (1989), pp. 467–477.
- [Agu+13] M. Aguilar et al. “First Result from the Alpha Magnetic Spectrometer on the International Space Station: Precision Measurement of the Positron Fraction in Primary Cosmic Rays of 0.5–350 GeV”. In: *Phys. Rev. Lett.* 110 (2013), p. 141102.
- [Ahm+10] Z. Ahmed et al. “Dark matter search results from the CDMS II Experiment”. In: *Science* 327 (2010), p. 1619.
- [Ake+13] D.S. Akerib et al. “The Large Underground Xenon (LUX) experiment”. In: *Nucl. Instr. Meth. Phys. Res. A* 704 (2013), pp. 111–126.

- [Aki+12] D. Akimov et al. *Light Yield in DarkSide-10: a Prototype Two-phase Liquid Argon TPC for Dark Matter Searches*. 2012. arXiv:1204.6218 [astro-ph. IM].
- [Ale+98] A. Alessandrello et al. “Measurements of internal radioactive contaminations in samples of Roman lead to be used in experiments on rare events”. In: *Nucl. Instr. Meth. Phys. Res. B* 142 (1998), pp. 163–172.
- [Amb+95] M. Ambrosio et al. “Vertical muon intensity measured with MACRO at the Gran Sasso laboratory”. In: *Phys. Rev. D* 52 (1995), pp. 3793–3802.
- [And+11] E. Andreotti et al. “ ^{130}Te neutrinoless double-beta decay with CUORICINO”. In: *Astropart. Phys.* 34 (2011), pp. 822–831.
- [Ang+05] G. Angloher et al. “Limits on WIMP dark matter using scintillating CaWO_4 cryogenic detectors with active background suppression”. In: *Astropart. Phys.* 23 (2005), pp. 325–339.
- [Ang+09] G. Angloher et al. “Commissioning run of the CRESST-II dark matter search”. In: *Astropart. Phys.* 31 (2009), pp. 270–276.
- [Ang+11] J. Angle et al. “Search for Light Dark Matter in XENON10 Data”. In: *Phys. Rev. Lett.* 107 (2011), p. 051301.
- [Ang+12] G. Angloher et al. “Results from 730 kg days of the CRESST-II Dark Matter Search”. In: *Eur. Phys. J. C* 72 (2012), p. 1971.
- [Ang+13] R. Angese et al. *Dark Matter Search Results Using the Silicon Detectors of CDMS II*. 2013. arXiv:1304.4279 [hep-ex].
- [Apr+10] E. Aprile et al. “First Dark Matter Results from the XENON100 Experiment”. In: *Phys. Rev. Lett.* 105 (2010), p. 131302.
- [Apr+12] E. Aprile et al. “Dark Matter Results from 225 Live Days of XENON100 Data”. In: *Phys. Rev. Lett.* 109 (2012), p. 181301.
- [Arm+12] E. Armengaud et al. “Search for low-mass WIMPs with EDELWEISS-II heat-and-ionization detectors”. In: *Phys. Rev. D* 86 (2012), p. 051701.
- [Arn+04] C. Arnaboldi et al. “CUORE: a cryogenic underground observatory for rare events”. In: *Nucl. Instr. Meth. Phys. Res. A* 518 (2004), pp. 775–798.
- [Arp92] C. Arpesella. “Background Measurements at Gran Sasso Laboratory”. In: *Nucl. Phys. B (Proceedings Supplements)* 28 A (1992), pp. 420–424.
- [Åst+06] J. Åström et al. “Fracture processes observed with a cryogenic detector”. In: *Phys. Lett. A* 356 (2006), pp. 262–266.
- [BAH68] R. de Boeck, F. Adams, and J. Hoste. “Determination of ^{210}Po in Lead”. In: *Radioanalyt. Chem.* 1 (1968), pp. 397–412.

- [Bar08] L. Bardelli. “Pulse-shape discrimination with PbWO_4 crystal scintillators”. In: *Nucl. Instr. Meth. A* 584 (2008), pp. 129–134.
- [Bar90] R. Barlow. “Extended maximum likelihood”. In: *Nucl. Instr. Meth. A* 297 (1990), pp. 496–506.
- [Bav+08] I. Bavykina et al. “Investigation of ZnWO_4 Crystals as Scintillating Absorbers for Direct Dark Matter Search Experiments”. In: *IEEE Trans. Nucl. Sci.* 55 (2008), pp. 1449–1452.
- [Bav09] I. Bavykina. “Investigation of ZnWO_4 and CaMoO_4 as target materials for the CRESST-II dark matter search”. PhD thesis. Ludwig-Maximilians – Universität München, 2009.
- [BCS57] J. Bardeen, L.N. Cooper, and J.R. Schrieffer. “Theory of Superconductivity”. In: *Phys. Rev.* 108 (1957), p. 1175.
- [Bel+07] P. Belli et al. “Investigations of beta decay of ^{113}Cd ”. In: *Phys. Rev. C* 76 (2007), p. 064603.
- [Bel+89] P. Belli et al. “Deep underground neutron flux measurements with larger BF3 counters”. In: *Il Nuovo Cimento* 101 A (1989), pp. 956–966.
- [Ber+05] M.J. Berger et al. *ESTAR, PSTAR, and ASTAR: Computer Programs for Calculating Stopping-Power and Range Tables for Electrons, Protons, and Helium Ions*. <http://physics.nist.gov/PhysRefData/Star/Text/ESTAR.html>. Version 1.2.3. 2005.
- [Ber+10a] R. Bernabei et al. “New results from DAMA/LIBRA”. In: *Eur. Phys. J. C* 67 (2010), pp. 39–49.
- [Ber+10b] G. Bertone et al. *Particle Dark Matter*. Cambridge University Press, 2010.
- [BG06] L. Bergström and A. Goobar. *Cosmology and Particle Astrophysics*. 2nd Edition. Springer Verlag, 2006.
- [Bir51] J.B. Birks. “Scintillations from Organic Crystals: Fluorescence and Relative Response to Different Radiations”. In: *Phys. Proc. Soc. A* 64 (1951), pp. 874–877.
- [Bir64] J.B. Birks. *The Theory and Practise of Scintillation Counting*. Pergamon Press, 1964.
- [BK05] W.H. Bragg and R. Kleemann. “On the alpha particle of radium, and their loss of range in passing through various atoms and molecules”. In: *Philosoph. Mag. Ser. 6* 10 (1905), pp. 318–340.
- [Boh48] N. Bohr. “The Penetration of Atomic Particles Through Matter”. In: *Mat. – fys. Meddr.* 18 (1948).

- [Bos81] A. Bosman. “21-cm line studies of spiral galaxies. I – Observations of the galaxies NGC 5033, 3198, 5055, 2841, and 7331. II – The distribution and kinematics of neutral hydrogen in spiral galaxies of various morphological types”. In: *Astrophys. J.* 86 (1981), pp. 1791–1846.
- [BP66] A.J.F. Boyle and G.J. Perlow. “Debye-Waller Factor for the Cesium Ion in the Cesium Halides by Measurements of the Mössbauer Effect in Cs133”. In: *Phys. Rev.* 151 (1966), pp. 211–214.
- [Buc11] C. Bucci. private communication. 2011.
- [Cea+06] H. Cease et al. *Measurements of mechanical properties of three epoxy adhesives at cryogenic temperatures for CCD construction*. <http://lartpc-docdb.fnal.gov/0002/000249/001/fermilab-tm-2366-a.pdf>. Fermi National Accelerator Laboratory, 2006.
- [Cir12] M. Cirelli. *Indirect Searches for Dark Matter: a status review*. 2012. arXiv:1202.1454 [hep-ph].
- [Clo+06] D. Clowe et al. In: *Astrophys. J. Lett.* 648 (2006), pp. L109–L113.
- [Coz+04] C. Cozzini et al. “Detection of the natural α decay of tungsten”. In: *Phys. Rev. C* 70 (2004), p. 064606.
- [Dan+03] F.A. Danevich et al. “ α activity of natural tungsten isotopes”. In: *Phys. Rev. C* 67 (2003), p. 014310.
- [Deb12] P. Debye. “Zur Theorie der spezifischen Wärmen”. In: *Annalen der Physik* 39 (1912), pp. 789–839.
- [DFS98] F. Donato, N. Fornengo, and S. Scopel. “Effects of galactic dark halo rotation on WIMP direct detection”. In: *Astropart. Phys.* 9 (1998), pp. 247–260.
- [DiT+92] J. F. DiTusa et al. “Role of phonon dimensionality on electron-phonon scattering rates”. In: *Phys. Rev. Lett.* 68 (1992), pp. 1156–1159.
- [Eng91] J. Engel. “Nuclear form factors for the scattering of weakly interacting massive particles”. In: *Phys. Lett. B* 264 (1991), pp. 114–119.
- [EPR86] S.C. Ehinger, R.A. Pacer, and Romines. “Separation of the radioelements ^{210}Pb – ^{210}Bi – ^{210}Po by spontaneous deposition onto noble metals and verification by Cherenkov and liquid scintillation counting”. In: *J. Radioanalyt. Nucl. Chem.* 68 (1986), pp. 39–48.
- [Fan63] U. Fano. “Penetration of Protons, Alpha Particles, and Mesons”. In: *Annu. Rev. Nucl. Sci.* 13 (1963), pp. 1–66.
- [Fen10] J.L. Feng. “Dark Matter Candidates from Particle Physics and Methods of Detection”. In: *Ann. Rev. Astron. Astrophys.* 48 (2010), pp. 495–545.

- [Fig61] P.E. Figgins. *The radiochemistry of polonium*. Nuclear Sciences Series NAS-NS 3037. National Academy of Science (U.S.A.), 1961.
- [Fir+99] R.B. Firestone et al. *Table of Isotopes (CD ROM Edition)*. 8th ed. John Wiley & Sons, 1999.
- [FN84] E. Fiorini and T. O. Niinikoski. “Low Temperature Calorimetry for Rare Decays”. In: *Nucl. Instr. Meth. Phys. Res. A* 224 (1984), pp. 83–88.
- [Fra02] T. Frank. “Development of Scintillating Calorimeters for Discrimination of Nuclear Recoils and Fully Ionizing Events”. PhD thesis. Technische Universität München, 2002.
- [FST06] J.L. Feng, S. Su, and F. Takayama. “Lower Limit on Dark Matter Production at the CERN Large Hadron Collider”. In: *Phys. Rev. Lett.* 96 (2006), p. 151802.
- [Gir+09] L. Gironi et al. “CdWO₄ bolometers for double beta decay search”. In: *Opt. Mat.* 31 (2009), pp. 1388–1392.
- [GM63] R. Gwin and R.B. Murray. “Scintillation Process in CsI(Tl). I. Comparison with Activator Saturation Model”. In: *Phys. Rev.* 131 (1963), pp. 501–508.
- [Har79] J.P. Harrison. “Review paper: Heat transfer between liquid helium and solids below 100 mK”. In: *J. Low Temp. Phys.* 37 (1979), pp. 467–565.
- [Hel56] R.H. Helm. “Inelastic and Elastic Scattering of 187-MeV Electrons from Selected Even-Even Nuclei”. In: *Phys. Rev.* 104 (1956), pp. 1466–1475.
- [Heu95] G. Heusser. “Low-Radioactivity Background Techniques”. In: *Annu. Rev. Nucl. Part. Sci.* 45 (1995), pp. 543–590.
- [Hop+07] E.W. Hoppe et al. “Cleaning and passivation of copper surfaces to remove surface radioactivity and prevent oxide formation”. In: *Nucl. Instr. Meth. Phys. Res. A* 579 (2007), pp. 486–489.
- [Huf+] P. Huff et al. *Quenching factors of CaWO₄ and their microscopic explanation*. to be published.
- [Huf10] P. Huff. “The Detector Parameters Determining the Sensitivity of the CRESST-II Experiment”. PhD thesis. Technische Universität München, 2010.
- [JKG96] G. Jungman, M. Kamionkowski, and K. Griest. “Supersymmetric dark matter”. In: *Physics Reports* 267 (1996), pp. 195–373.
- [KBP12] M. Kuźniak, M.G. Boulay, and T. Pollmann. “Surface roughness interpretation of 730 kg days CRESST-II results”. In: *Astropart. Phys.* 36 (2012), pp. 77–82.

- [Kie07] M. Kiefer. “Optimierung szintillierender Tieftemperaturkalorimeter für den direkten Nachweis von Teilchen der Dunklen Materie”. MA thesis. Julius – Maximilians – Universität Würzburg, 2007.
- [Kie12] M. Kiefer. “Improving the Light Channel of the CRESST–II Dark Matter Detectors”. PhD thesis. Technische Universität München, 2012.
- [Kle10] R. Kleindienst. “Light Yield Measurements of Cadmium Tungstate and Titanium Doped Sapphires for the CRESST Dark Matter Search”. MA thesis. Technische Universität München, 2010.
- [Kom+11] E. Komatsu et al. “Seven – year Wilkinson Microwave Anisotropy Probe (WMAP) Observations: Cosmological Interpretation”. In: *Astrophys. J. Supp. Ser.* 192 (2011), pp. 18–65.
- [Kra12] H. Kraus. private communication. 2012.
- [Lan08] R.F. Lang. “Search for Dark Matter with the CRESST Experiment”. PhD thesis. Technische Universität München, 2008.
- [Lan+09] R. Lang et al. *Scintillator Non-Proportionality and Gamma Quenching in CaWO₄*. 2009. arXiv:0910.4414 [nuc1-ex].
- [Lau11] M. Laubenstein. High–purity Germanium Gamma Spectroscopy at LNGS. 2011.
- [LG91] J. Liu and N. Giordano. “Electron-phonon scattering times in thin Sb films”. In: *Phys. Rev. B* 43 (1991), pp. 3928–3932.
- [Lin69] J. Lindhard. “Slowing–down of ions”. In: *Proc. Roy. Soc. A* 311 (1969), pp. 11–19.
- [LNG12] LNGS. <http://www.lngs.infn.it/>. Homepage of the laboratory. 2012.
- [Lor09] M. Lorenz. Universität Leipzig. 2009.
- [LS96] J.D. Lewin and P.F. Smith. “Review of mathematics, numerical factors, and corrections for dark matter experiments based on elastic nuclear recoil”. In: *Astropart. Phys.* 6 (1996), pp. 87–112.
- [Maj+09] B. Majorovits et al. “Production of low-background CuSn₆–bronze for the CRESST dark-matter–search experiment”. In: *Applied Radiation and Isotopes* 67 (2009), pp. 197–200.
- [Mar+11] A. Marchionni et al. “ArDM: a ton-scale LAr detector for direct Dark Matter searches”. In: *J. of Phys.: Conf. Ser.* 308 (2011), p. 012006.
- [Meu+99] P. Meunier et al. “Discrimination between nuclear recoils and electron recoils by simultaneous detection of phonons and scintillation light”. In: *Appl. Phys. Lett.* 75 (1999).

- [MM62] A. Meyer and R.B. Murray. “Effect on Energetic Secondary Electrons on the Scintillation Process in Alkali Halide Crystals”. In: *Phys. Rev.* 128 (1962), pp. 98–105.
- [MM94] K. Michaelian and A. Menchaca-Rocha. “Model of ion-induced luminescence based on energy deposition by secondary electrons”. In: *Phys. Rev. B* 49 (1994), p. 15550.
- [MPG06] J. Magill, G. Pfennig, and J. Galy. *Karlsruher Nuklidkarte*. 7th ed. 2006.
- [MR01] C.A. Mahieux and K.L. Reifsnider. “Property modeling across transition temperatures in polymers: a robust stiffness-temperature model”. In: *Polymer* 42 (2001), pp. 3281–3291.
- [Nak10] K. Nakamura. “Review of Particle Physics”. In: *J. Phys. G: Nucl. Part. Phys* 37 (2010), p. 075021.
- [Nis11] S. Nisi. High Resolution Inductively Coupled Plasma-Mass Spectrometric (HR-ICP-MS) analysis, Chemistry Department at LNGS. 2011.
- [Pan08] E. Pantić. “Performance of Cryogenic Light Detectors in the CRESST-II Dark Matter Search”. PhD thesis. Technische Universität München, 2008.
- [Pet05] F. Petricca. “Dark Matter Search with Cryogenic Phonon-Light Detectors”. PhD thesis. Ludwig-Maximilians-Universität München, 2005.
- [Pfi10] S. Pfister. “Suche nach Dunkler Materie mit dem CRESST-II Experiment”. PhD thesis. Technische Universität München, 2010.
- [Pip55] A. B. Pippard. “Ultrasonic Attenuation in Metals”. In: *Philos. Mag.* 36 (1955), pp. 1104–1114.
- [Pir+06] S. Pirro et al. “Scintillating Double Beta Decay Bolometers”. In: *Phys. Atom. Nucl.* 69 (2006), pp. 2109–2116.
- [Pob92] F. Pobell. *Matter and Methods at Low Temperatures*. Springer Verlag, 1992.
- [Prö+95] F. Pröbst et al. “Model for Cryogenic Particle Detectors with Superconducting Phase Transition Thermometers”. In: *J. Low Temp. Phys.* 100 (1995), pp. 69–104.
- [Rei11] F. Reindl. “Analysis of CRESST Dark Matter Search Data”. MA thesis. Technische Universität München, 2011.
- [RF70] V.C. Rubin and W.Jr. Ford. “Rotation of the Andromeda Nebula from a Spectroscopic Survey of Emission Regions”. In: *Astrophys. J.* 159 (1970), pp. 379–403.
- [Rod97] P.A. Rodnyi. *Physical Processes in Inorganic Scintillators*. CRC Press LLC, 1997.

- [SA81] M.H. Salamon and S.P. Ahlen. “NaI:Tl response to relativistic Ne, Ar, and Fe ions”. In: *Phys. Rev. B* 124 (1981), pp. 5026–5036.
- [Sav+09] C. Savage et al. “Compatibility of DAMA/LIBRA dark matter detection with other searches”. In: *J. Cosmol. Astropart. Phys.* 0904 (2009), p. 010.
- [Sch10] J. Schmalzer. “The CRESST Dark Matter Search - New Analysis Methods and Recent Results”. PhD thesis. Technische Universität München, 2010.
- [Sch11] S.M. Scholl. “Neutron Background Simulation for the CRESST–II Experiment”. PhD thesis. Universität Tübingen, 2011.
- [Sch+12] K. Schaeffner et al. “Alternative Scintillating Materials for the CRESST Dark Matter Search”. In: *J. of Low Temp. Phys.* 167 (2012), pp. 1075–1080.
- [Sek+10] H. Sekiya et al. *XMASS*. 2010. arXiv:1006.1473 [astro-ph].
- [Sen+04] A. Senyshyn et al. “Lattice dynamics and thermal properties of CaWO₄”. In: *Phys. Rev. B* 70 (2004), p. 214306.
- [Sim35] F. E. Simon. “Application of Low Temperature Calorimetry to Radioactive Measurements”. In: *Nature* 135 (1935), p. 763.
- [Smi+07] M.C. Smith et al. “The RAVE Survey: Constraining the Local Galactic Escape Speed”. In: *Mon. Not. Roy. Astron. Soc.* 379 (2007), pp. 755–772.
- [Str13] R. Strauss. “in preparation”. PhD thesis. Technische Universität München, 2013.
- [Tan+11] T. Tanaka et al. “An Indirect Search for Weakly Interacting Massive Particles in the Sun using 3109.6 Days of upward-going Muons in Super – Kamiokande”. In: *Astrophys. J.* 742 (2011).
- [Tan11] A. Tanzke. “Optimization of Light Detectors for the CRESST Experiment”. MA thesis. Technische Universität München, 2011.
- [Tre10] V.I. Tretyak. “Semi-empirical calculations of quenching factors for ions in scintillators”. In: *Astropart. Phys.* 33 (2010), pp. 40–53.
- [Woo+90] C.L. Woody et al. “Readout Techniques and Radiation Damage of Undoped Cesium Iodide”. In: *IEEE Trans. Nucl. Sci.* 37 (1990), pp. 492–499.
- [WZ07] M. Wójcik and G. Zuzel. “Behavior of the ²²²Rn daughters on copper surfaces during cleaning”. In: *AIP Conf. Proc.* 897 (2007), pp. 53–58.
- [YB71] B. Yates and A.C. Bailey. “The low-temperature anisotropic thermal expansion of calcium tungstate”. In: *J. Low Temp. Phys.* 4 (1971), pp. 117–125.

- [ZBL85] J.F. Ziegler, J.P. Biersack, and U. Littmark. *The Stopping and Ranges of Ions in Matter*. Vol. 1-6. Pergamon Press, 1977-85.
- [Zde+05] Y.G. Zdesenko et al. "Scintillation properties and radioactive contamination of CaWO_4 crystal scintillators". In: *Nucl. Instr. Meth. Phys. Res. A* 538 (2005), pp. 657–667.
- [Zie+12] J. Ziegler et al. *Stopping and Range of Ions in Matter*. <http://www.srim.org>. SRIM-2012.03. 2012.
- [Zie99] J.F. Ziegler. "The Stopping of Energetic Light Ions in Elemental Matter". In: *J. Appl. Phys. / Rev. Appl. Phys.* 8 (1999), pp. 1249–1272.
- [Zim12] K. Zimmermann. "Study of Zinc Tungstate as Target Material for Cryogenic Dark Matter Search". MA thesis. Julius–Maximilians–Universität Würzburg, 2012.
- [Zwi33] F. Zwicky. "Die Rotverschiebung von extragalaktischen Nebeln". In: *Helvetica Physica Acta* 6 (1933), pp. 110–127.

Acknowledgments

First of all I want to thank my Ph.D. supervisor Prof. Dr. Allen Caldwell for giving me the possibility to start this work in the CRESST group supervised by Dr. Franz Pröbst at the Max-Planck-Institut für Physik. Thank you very much for your interest and the fruitful comments which definitely improved this work. I am grateful to Prof. Dr. Stefan Schönert who kindly offered to be my second referee.

Many and special thanks I want to express to Dr. Franz Pröbst. Thank you for your continuous help, for your interest in my work and the patient supervision. You were always willing to discuss and you had a solution to almost all kind of problems and questions which came to my mind — your expertise and comprehensive knowledge was of inestimable value! Thank you, Franz, for your support and for being such a remarkable physicist!

Many thanks go to Dr. Wolfgang Seidel. His engagement and interest in setting up the infrastructure of the testcryostat was the precondition for all my work which followed. Thank you very much for the practical skills, for sharing of your knowledge, for useful discussions and for trying to give me an insight in a completely different way of looking at things and the world!

Dieter Hauff was the person who made me plucking up courage to take the decision of doing a Ph.D. thesis. Thank you very much for your interest and for your essential help concerning detector production.

Many thanks go to my office-mate Dr. Federica Petricca. I do not know where to start and stop, your help in really any respect was invaluable: thank you for always listening to all my ideas and constantly supporting my work, for your feedback and advice, for sharing your enthusiasm and thoughts, for pushing in the same direction, for the Nougatine, for plenty of discussions on many topics of life besides physics, for your phone calls during my long stay at Gran Sasso, for your patience, especially when proof-reading my thesis. Federica, ti ringrazio tanto per l'amicizia che c'è stata e che spero andrà oltre il nostro rapporto di lavoro e soprattutto oltre i confini.

Equal thanks go to Dr. Jens Schmalzer for all the experiences and things we achieved in the period of the preparation and the detector mounting for Run 32. Thank you for sharing your thoughts and time and all the unforgettable moments.

I am indebted to my colleague and friend Dr. Michael Kiefer. You were always willing and patient to help me with any computing problems. Thank you for all the discussions and the nice and very pleasant atmosphere. And as you anyhow already know, it did not pass one single day since you left on which I did not miss you :)

I also want to express my gratitude to Florian Reindl. First of all for helping me with

all kind of root-related problems. Without you, non of these plots could have ever been produced. Furthermore for sorting my thoughts, in particular in the last months, for plenty of discussions and for sharing the enthusiasm for the new run!

Special thanks I want to express to Dr. Godehard Angloher. Gode, I am deeply impressed by your enthusiasm, by your creativity and the endurance you show in following your beliefs. Thank you very much for all the productive ideas, discussions and the good time we had at Gran Sasso. Moreover, thank you very much for proof-reading and the detailed comments that helped me to clear my mind while writing this thesis.

Thanks also go to Rafael Kleindienst. He was diploma student during my second year as a Ph.D. student. I am grateful for the productive and funny time we had!

The same goes to my colleague Dr. Patrick Huff: thank you for your support in producing the samarium α -source, for sharing your knowledge and the many discussions and debates in our daily coffee breaks.

Thanks also go to Dr. António C. S. Miguel Bento. Antonio, thank you for the many discussions, your onest advice, your interest in my work and for the always very funny excursions around Munich!

Many, many thanks I also want to express to *all* current and former members of the group. Too many names for a list and I do not want to miss someone! Thank you all very much for the nice working atmosphere, for serious and not-so-serious discussions, for cookies and cakes. You all, in various ways did contribute to this work!

Equal thanks go to all my colleagues working at TU München and Universität Tübingen. In particular I want to thank Dr. Sebastian Pfister. Sebastian, thank you for your support at Gran Sasso and the many discussions, not only on physics-related topics which helped me to always again find the strength to face the problems with the testcryostat. Your advice was very important for me! Special thanks also go to Raimund Strauss. Raimund, thank you for being such an example of optimism!

Many thanks to my proof-readers: Gode, Federica, Florian, Antonio, Vanessa and Tom!

Ein Dank geht an alle Mitarbeiter der verschiedenen Max-Planck-Werkstätten ohne deren Hilfe und Bereitschaft die experimentelle Arbeit nicht möglich gewesen wäre. Danken möchte insbesondere Peter Mühlbauer für seinen große Hilfe und die Ausdauer beim Aufbau des Testkryostaten sowie die vielen gemeinsamen Erfahrungen! Ein Dankeschön geht auch an Günther Tratzl für die vielen guten Ratschläge bzgl. Epoxidharzklebern und die immer präzise Anfertigung der benötigten Bauteile.

Ein ganz besonderes Dankeschön geht an Walter Kosmale. Walter, du hattest immer in offenes Ohr für mich und Interesse an meiner Arbeit. Ich möchte dir für die sehr angenehme und produktive Zusammenarbeit danken. Ohne deine immer zeitnahe und akkurate Fertigung der Bauteile und deinen großen Einsatz wären viele Dinge für mich nicht zu schaffen gewesen! Ich werde dich vermissen!

Weiterhin möchte ich dem Kristall-Labor der TU München danken. Insbesondere gilt mein Dank Michael Stanger und Katarzyna Danielewicz: herzlichen Dank an euch für

die hervorragende Bearbeitung der Kristalle, die Pfefferminztee und die so angenehme Arbeitsatmosphäre.

I am indebted to people working at the Laboratori Nazionali del Gran Sasso. I want to thank Carlo Bucci who always supported and helped during my time at Gran Sasso. Knowing that you will have a solution for any organizational problem and always some good advice was very important for my work. Grazie mille!

Un ringraziamento molto speciale al mitico Marco Guetti. Marco, non so se troveró le parole giuste ma proveró a ringraziarti per il tuo inestimabile supporto tecnico, in ogni momento del giorno e per qualsiasi evenienza. Grazie mille per il tuo accurato ed eccellente lavoro; senza il tuo aiuto, costante impegno ed ottimismo non avrei mai potuto risolvere alcun problema tecnico riguardo il testcriostato. Grazie per avermi insegnato l'italiano ("... mó vedi quanto parleró!"), per i caffè con i biscotti nei momenti piú opportuni, per aver condiviso i tuoi pensieri ed entusiasmi con me ed infine per lo stile di vita italiano. In definitiva, ti rivolgo il ringraziamento piú grande per la tua amicizia!

Un ringraziamento davvero sentito alla famiglia D'Archivio! Grazie per la vostra ospitalità, la fiducia e per la positività che mi avete trasmesso nei momenti piú pesanti della mia esperienza al Gran Sasso. Grazie per aver condiviso pensieri, pareri e momenti di famiglia. In particolare, Pietro e Gianna voglio ringraziarvi per tutti i consigli nei vari aspetti della vita, per avermi fatto sentire come a casa in un posto a mille chilometri da Monaco. Sara, grazie per il bel tempo passato insieme, per le lunghe chiacchierate, e per avermi fatto affrontare le giornate con un bel "Hakuna Matata". Ti ringrazio per la bella amicizia che c'è stata!

Bastian, dir möchte ich für deine große Unterstützung während unserer gemeinsamen Zeit danken. Du hast mich in schwierigen Situationen bestärkt meinen Weg weiterzugehen, das werde ich dir nie vergessen!

Kathi, oft hast du unsere Freundschaft mit meiner Arbeit teilen müssen. Danke für deine erfrischend "andere Sicht" auf die Dinge und dein Verständnis.

*Am Schluss möchte ich den Menschen danken,
die für mich an erster Stelle stehen — meiner Familie.
Ihr habt mich immer unterstützt und mich meine Träume verfolgen lassen.
Diese Sicherheit war die Voraussetzung für diese Arbeit!
Für euer Vertrauen, eure Geduld und eure Liebe möchte ich euch von Herzen danken!*

Amore, grazie per avermi dato la giusta grinta nell'affrontare il mio dottorato e per essere stato, con tanto affetto, sempre al mio fianco.